ALMA MATER STUDIORUM - UNIVERSITÀ DI BOLOGNA

Dipartimento di Fisica e Astronomia

Dottorato di Ricerca in Fisica
Ciclo XXXIV

Non Perturbative Aspects of Non Equilibrium Physics in Two Dimensional Models

Candidato: Octavio Pomponio

Coordinatore Dottorato:
Prof. Michele Cicoli

Supervisore:
Prof. Francesco Ravanini
Co-supervisore:
Prof. Gábor Takács

Settore Concorsuale di afferenza: 02/A2
Settore Scientifico disciplinare: FIS/02

Esame Finale Anno 2022

Abstract

The present manuscript focuses on out of equilibrium physics in two dimensional models. It has the purpose of presenting some results obtained as part of out of equilibrium dynamics in its non perturbative aspects. This can be understood in two different ways: the former is related to integrability, which is non perturbative by nature; the latter is related to emergence of phenomena in the out of equilibirum dynamics of non integrable models that are not accessible by standard perturbative techniques. In the study of out of equilibirum dynamics, two different protocols are used througout this work: the bipartitioning protocol, within the Generalised Hydrodynamics (GHD) framework, and the quantum quench protocol. With GHD machinery we study the Staircase Model, highlighting how the hydrodynamic picture sheds new light into the physics of Integrable Quantum Field Theories; with quench protocols we analyse different setups where a non-perturbative description is needed and various dynamical phenomena emerge, such as the manifistation of a dynamical Gibbs effect, confinement and the emergence of Bloch oscillations preventing thermalisation.

"Ford... you're turning into a penguin. Stop it."

Douglas Adams, *The Hitchhiker's Guide To The Galaxy*

Declaration

This manuscript is based on the results presented in the following papers published during the Ph.D. studies of the candidate:

[1] Michele Mazzoni, Octavio Pomponio, Olalla A Castro-Alvaredo, and Francesco Ravanini. "The staircase model: massless flows and hydrodynamics". In: *Journal of Physics A: Mathematical and Theoretical* 54.40 (Sept. 2021), p. 404005. DOI: 10.1088/1751-8121/ac2141. URL: https://doi.org/10.1088/1751-8121/ac2141

[2] O. Pomponio, L. Pristyák, and G. Takács. "Quasi-particle spectrum and entanglement generation after a quench in the quantum Potts spin chain". In: *Journal of Statistical Mechanics: Theory and Experiment* 1.1 (Jan. 2019), p. 013104. DOI: 10.1088/1742-5468/aafa80. arXiv: 1810.05539 [cond-mat.stat-mech]

[3] Máté Lencses, Octavio Pomponio, and Gabor Takacs. "Relaxation and entropy generation after quenching quantum spin chains". In: *SciPost Physics* 9.1, 011 (July 2020), p. 011. DOI: 10.21468/SciPostPhys.9.1.011. arXiv: 2004.09550 [cond-mat.stat-mech]

[4] Octavio Pomponio, Miklós Antal Werner, Gergely Zaránd, and Gabor Takacs. "Bloch oscillations and the lack of the decay of the false vacuum in a one-dimensional quantum spin chain". In: *SciPost Physics* 12.2, 061 (Feb. 2022), p. 061. DOI: 10.21468/SciPostPhys.12.2.061. arXiv: 2105.00014 [cond-mat.stat-mech]

Contents

Introduction

Due to recent developments in experimental techniques, non-equilibrium behaviour of quantum many-body systems is at the forefront of contemporary research. Within this framework, closed quantum systems, described by pure states and subject to the time dependent Schrödinger equation, play an essential role. It is clear that quantum statistical mechanics must arise from such time-evolving pure states. But how and in what sense?

When a whole new range of methods in the field of ultracold atomic and molecular gases was developed, allowing the engineering of strongly-interacting quantum systems, a massive theoretical interest in questions concerning out of equilibrium dynamics arised.

In particular quantum integrable models play an important role: in the first place, some of the systems that have been explored experimentally are described by integrable theories with small perturbations; secondly, integrable models allow the derivation of exact results. This in turn has proved extremely useful for revealing general features of non equilibrium dynamics.

The present manuscript is set within this context. Its aim is to present some results obtained as part of out of equilibrium dynamics in its non perturbative aspects. This can be understood in two different ways: the former is related to integrability itself, which is non perturbative by nature; the latter is related to emergent phenomena in the out of equilibirum dynamics of non integrable models that are not accessible by standard perturbative techniques. In this case other approaches are needed and numerical methods that allow the study of the properties of many-body quantum systems constitute a main tool. In particular in recent years increasing attention has been paid to algorithms that express the state of the system as a tensor network. Among them, for the simulation of time evolution, the *Time Evolving Block Decimation* (TEBD) algorithm is particularly popular and extensively used in this thesis. The work is structured as follows.

In Chapter 1 we start by recollecting some useful notions about out of equilibrium dynamics in one dimensional systems. It is explained in what sense an isolated quantum system may relax to a stationary state at late times. The concept of quantum integrablity

is introduced and compared with the well established classical counterpart, analysing the role of the infinitely many conserved quantities. Finally the relation between (non) integrability and equilibration is explored.

One of the leading approaches to compute out-of-equilibrium dynamical quantities is introduced in Chapter 2: *Generalised hydrodynamics* (GHD). The original GHD proposals considered the partitioning protocol. In this set up two independently thermalised systems are put into contact at time zero. The presence of multiple conserved quantities gives rise to ballistic transport, meaning that, after a transient period, steady state currents flowing between the right and left sub-systems emerge; GHD provides a method to compute such currents by combining the hydrodynamic principle, generalised to infinitely many conservation laws, with an effective description of quasi-particles, which for integrable Quantum Field Theories is based on the Thermodynamic Bethe Ansatz (TBA).

In Chapter 3 we apply GHD formalism to the integrable staircase model (SM), a generalisation of the sinh-Gordon model obtained by Al. B. Zamolodchikov. After investigating hydrodynamic properties of the model, we focus on the expectation values of conserved densities and currents, both at and away from equilibrium. We evaluate these for several values of spin higher than $s = 1$ and investigate the temperature dependence in the CFT limit. This chapter gathers the results published in [1].

Chapter 4 aims at reviewing some key aspects of another protocol used to drive systems out of equilibirum: the *quantum quench*. An isolated quantum system composed of many particles and ruled by a Hamiltonian H is prepared in a state that is not an eigenstate of the latter, and it is let to evolve. Even in this simple set up it is not trivial at all to describe the system dynamics. The example of quench dynamics in the paradigmatic Transverse Field Ising Chain is finally provided.

The last two chapters have the purpose of exploring some non perturbative effects in the framework of quench dynamics. Chapter 5 presents the results obtained in [2] and [3], where the first non perturbative effect of the work is introduced: the dynamical Gibbs Effect. After proving the existence of such mechanism for the Potts model, we analyze the relation between relaxation and entropy generation in quantum spin chains and provide a characteristic signature of the phenomenon that can be observed in experimental environments.

In Chapter 6 we consider the decay of the false vacuum realised within a quantum quench into an *anti-confining* regime of the Ising spin chain with a magnetic field opposite to the initial magnetisation. We observe that time evolution is in stark contrast with the field theory predictions and after comparing this scenario with *dynamical confinement*,

another highly non-perturbative effect already studied within the quench framework, we find that the relevant mechanism responsible for the suppression of correlations is the emergence of Bloch oscillations. This results can be found in [4].

Finally, we draw our conclusions and discuss the outlooks for future inquiries.

1

A Prelude to out of equilibrium systems

In this chapter the problem of quantum many body systems out of equilibrium is introduced together with the role played by integrability (for reviews see [5–7]). Our understanding of the out-of-equilibrium dynamical properties of many-body quantum systems has vastly expanded over the past decade [6, 8]. In the context of 1+1D quantum integrable models, a lot of interest was triggered by the results of the quantum Newton's cradle experiment [9] which showed that dimensionality in conjunction with integrability give rise to a distinct kind of dynamics: one in which there is no long-term thermalization. This result was later related to the presence of infinitely many conserved quantities in integrable models. The dynamics is then determined by all conserved quantities, leading to the concept of generalised Gibbs ensembles (GGEs) [10]. As a consequence, quantum integrable models do not thermalise to Gibbs ensembles but they equilibrate to GGEs. Thanks to this fundamental understanding, non-equilibrium dynamics has become a powerful way of studying strongly correlated many-body systems [6, 7, 11–17].

The Chapter is organised as follows. We start in Sec. 1.1 by specifying in what sense an isolated quantum system may relax to a stationary state. In Sec. 1.2 we discuss thermalisation in generic systems and finally in Sec. 1.3 we introduce the concept of *equilibration* in integrable systems, after reviewing the key points of integrability.

1.1 Relaxation in isolated quantum systems

In statistical mechanics of classical systems, a generic isolated system in the thermodynamic limit prepared in a generic initial state evolves, in the long time limit, towards a well defined stationary state. The latter is the one that maximises the entropy [18, 19] and the whole system is described by a microcanonical ensemble with total energy equal to the initial one.

Since we are considering an isolated quantum system, it is necessary to specify in what sense it may relax to a stationary state al late times after we have driven it out of equilibrium. If we prepare the system in a pure state $|\psi_0\rangle$ that is not an eigenstate of the Hamiltonian of the system H, it will remain in a pure state, since evolution is unitary

$$|\psi(t)\rangle = e^{-iHt} |\psi_0\rangle \tag{1.1}$$

instead of a statiscal ensemble, which is by definition a mixed state. Consider, for instance, the following class of hermitian operators

$$\mathcal{O}_{kl} = |k\rangle \langle l| + |l\rangle \langle k| . \tag{1.2}$$

Expanding the pure state in the energy eigenstates

$$H |n\rangle = |n\rangle E_n \tag{1.3}$$

$$|\psi(t)\rangle = \sum_n \langle n|\psi_0\rangle e^{-iE_n t} |n\rangle , \tag{1.4}$$

the expectation values in the state $|\psi(t)\rangle$ of these operators can be expressed as

$$\begin{aligned} \langle\psi(t)| \mathcal{O}_{kl} |\psi(t)\rangle &= \langle\psi(t)|k\rangle \langle l|\psi(t)\rangle + c.c. \\ &= e^{i(E_k - E_l)t} \langle\psi_0|k\rangle \langle l|\psi_0\rangle + c.c.. \end{aligned} \tag{1.5}$$

We see that generically it exhibits periodic oscillatory behaviour in time. Hence the observables $\mathcal{O}_{kl}$ do not relax at late imes. In general the whole evolution is periodic or quasi-periodic, that is, the system will return to its initial state or arbitrary close to it: the whole isolated system cannot relax to a steady state.

Figure 1.1: Finite subsystem A and rest of the system.

Locality plays a crucial role (note that operators like $\mathcal{O}_{kl}$ are generally non-local). Even if the whole system cannot relax, subsystems of a much larger system are not isolated and they may therefore thermalise due to the thermal bath with the rest of the system. Isolated quantum many-body systems can namely relax *locally* in space. Using the density matrix formalism, this is equivalent to saying that the density matrix of the whole system is pure while the density matrix of the subsystem is mixed and the latter can be therefore described by a statistical ensemble [20–23]. To clarify these concepts, let's consider a quantum spin chain of N sites initially in a pure state $|\psi_0\rangle$, whose time

evolution is ruled by an Hamiltonian H. We partition the system into an arbitrary but finite subsystem A and its complement $\bar{A}$ (Fig. 1.1). The density matrix of the entire system at a certain time t is given by

$$\rho_{A\cup\bar{A}}(t) = |\psi(t)\rangle \langle\psi(t)| = e^{-iHt} |\psi_0\rangle \langle\psi_0| e^{iHt} \tag{1.6}$$

which is a pure state. The reduced density matrix of the subsystem A is obtain by tracing out the degrees of freedom of the rest of the system:

$$\rho_A(t) = \mathrm{Tr}_{\bar{A}} \left[\rho_{A\cup\bar{A}}(t)\right] \tag{1.7}$$

The question is if it exists a "virtual" mixed state $\rho^{\mathrm{SS}}_{A\cup\bar{A}}$ capable of describing the stationary state of $\rho_A(t)$, i.e.

$$\lim_{t\to\infty}\lim_{N\to\infty} \rho_A(t) = \lim_{N\to\infty} \mathrm{Tr}_{\bar{A}} \left[\rho^{\mathrm{SS}}_{A\cup\bar{A}}\right]. \tag{1.8}$$

If such virtual mixed state exists for any finite subsystem A, then the system is said to relax *locally* and $\rho^{\mathrm{SS}}_{A\cup\bar{A}}$ describes the stationary state of the system.

Any expectation value of a local observable $\mathcal{O}_A$ having its support on A can be now computed in the long time limit with a statistical ensamble as

$$\lim_{t\to\infty} \mathrm{Tr}\left[\rho(t)\mathcal{O}_A\right] = \mathrm{Tr}\left[\rho^{\mathrm{SS}}_{A\cup\bar{A}}\mathcal{O}_A\right]. \tag{1.9}$$

It is important to remark that the thermodynamic limit is taken keeping the subsystem A finite, and that it has to be done before the long time limit, otherwise quantum recurrences are impossible to avoid.

1.2 Non-integrability and thermalisation

An important question about the dynamics of a closed many-body quantum system is if interactions within the system are sufficient to make the system behave *ergodically*,which is at the basis of statistical mechanics.

Let us consider a classical system with N particles in d spatial dimensions, represented by a point in the $2dN$ dimensional phase space; given an initial condition $\mathbf{X_0} = (\mathbf{q_0}, \mathbf{p_0})$, the Hamiltonian $H(\mathbf{q}, \mathbf{p})$ is ergodic if the trajectory of the system in the phase space covers uniformly the constant energy hypersurface selected by the initial condition, for almost every initial state. This condition allows the replacement of time averages with

phase space averages weighted with the microcanonical ensemble; hence for any operator $\mathcal{O}$:

$$\begin{aligned}\langle O\rangle_{\text{time}} &\equiv \lim_{T\to\infty}\frac{1}{T}\int_0^T dt\mathcal{O}(\mathbf{q}(t),\mathbf{p}(t)) \\ &= \int d^{dN}qd^{dN}p\mathcal{O}(\mathbf{q},\mathbf{p})\delta[H(\mathbf{q},\mathbf{p})-H(\mathbf{q_0},\mathbf{p_0})] \equiv \langle O\rangle_{mc}\end{aligned} \tag{1.10}$$

Equations of motions for classical non integrable systems are not exactly solvable and non linear equations. KAM's theory [24] states that if the non linear amplitudes overcome a certain threshold, chaos emerges and the ergodic hypothesis is satisfied for these systems.

The most straightforward generalization of ergodicity to quantum system was performed by von Neumann [25]. We can define a microcanonical ensemble for quantum systems with the following procedure: given an Hamiltonian H with eigenstates $|n\rangle$ of energy E_n, we can coarse grain the spectrum on energy shells of width δE, in such a way that it remains small on macroscopic scales but it contains many states. Denoting with $\mathcal{S}(E)$ the set of eigenstates of H with energy between E and $E+\delta E$, we can define the microcanonical distribution as

$$\rho_{mc}(E) = \sum_{n\in\mathcal{S}(E)}\frac{1}{N(E)}|n\rangle\langle n|, \tag{1.11}$$

where $N(E)$ is the number of states in the shell. But given now a generic initial condition in a microcanonical shell

$$|\psi_0\rangle = \sum_{n\in\mathcal{S}(E)} c_n|n\rangle, \tag{1.12}$$

the long time average of the density matrix of the system is not given, in general, by the microcanonical ensemble (1.11). Assuming the eigenstates of the system not to be degenerate, we indeed obtain

$$\begin{aligned}\lim_{T\to\infty}\frac{1}{T}\int_0^T dt\,|\psi(t)\rangle\langle\psi(t)| &= \sum_{m,n} c_m\bar{c}_n|m\rangle\langle n|\lim_{T\to\infty}\frac{1}{T}\int_0^T dte^{-i(E_m-En)t} \\ &= \sum_n |c_n|^2|n\rangle\langle n| \equiv \rho_{\text{diag}},\end{aligned} \tag{1.13}$$

where the last step follows from a stationary phase approximation. This is the so called *diagonal ensemble* [10, 26, 27]. Note that this ensemble depends on the choice of the initial states through the overlaps $c_n = \langle n|\psi_0\rangle$ and the requirement $\rho_{mc} = \rho_{\text{diag}}$ implies that $|c_n|^2 = 1/N(E)$ for every n, which is obviously not satisfied for any initial state. Quantum ergodicity in the sense above is therefore almost never realizable. The reason

is in the linearity of Schrödinger's equation, hence we cannot expect an emergence of quantum chaos.

However there are many evidences of both experimental [28, 29] and numerical nature [10, 30] that shows that thermalization can occur. The commonly accepted explanation for this behaviour is the ETH (Eigenstate Thermalization Hypothesis) [31–33]: instead of explaining the ergodicity of a thermodynamic system through the mechanism of dynamical chaos, one should instead examine the properties of matrix elements of observable quantities $\mathcal{O}_k$ in individual energy eigenstates of the system. The requirement

$$\mathrm{Tr}\left[\rho_{mc}\mathcal{O}_k\right] = \mathrm{Tr}\left[\rho_{\mathrm{diag}}\mathcal{O}_k\right] \tag{1.14}$$

implies that matrix elements of these observables are constant on the energy shell and equal to the microcanonical average:

$$\mathrm{Tr}\left[\rho_{\mathrm{diag}}\mathcal{O}_k\right] = \sum_n |c_n|^2 \langle n|\mathcal{O}_k|n\rangle = \mathrm{Tr}\left[\rho_{mc}\mathcal{O}_k\right] \sum_n |c_n|^2 = \mathrm{Tr}\left[\rho_{mc}\mathcal{O}_k\right]. \tag{1.15}$$

In this picture even the initial state is a thermal one but the coherence between the eigenstates initially hides it (Fig. 1.2) and time dynamics reveals it through dephasing [26].

It is important to remark, though, it has been proof that ETH is not a necessary condition to quantum thermalization [34] and that it does not apply to all cases, for example to many body localised states [35].

1.3 Integrability and equilibration

1.3.1 Integrable systems

First of all, what does *integrability* mean for quantum systems? And how integrability of a certain model implies its *solvability*? A physical system is commonly identified as a topological space of states $\mathcal{M}$ (usually a manifold, albeit often infinite dimensional) with a bijective evolution map

$$U_t : \mathcal{M} \to \mathcal{M} \tag{1.16}$$

parametrised by a real parameter t identified as time. Every state in $\mathcal{M}$ encodes physical observable predictions, while the evolution map depicts how these predictions change in time.

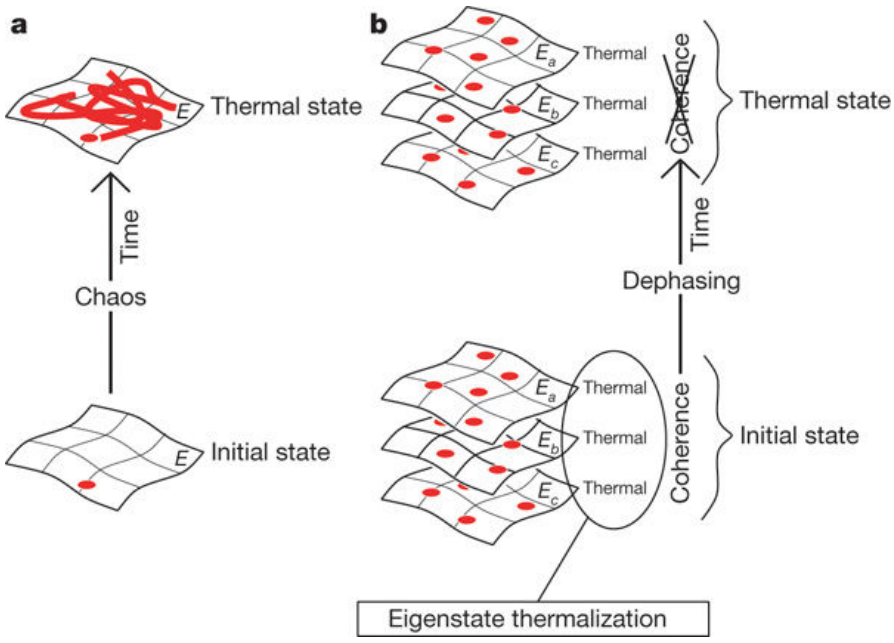

Figure 1.2: In classical mechanics (left), time evolution constructs the thermal state from an initial state that generally bears no resemblance to the former. In quantum mechanics (right), according to the ETH, every eigenstate of the hamiltonian always implicitly contains a thermal state. The coherence between the eigenstates initially hides it, but time dynamics reveals it through dephasing. Figure taken from [26].

Classical integrability

For classical one dimensional systems, $\mathcal{M}$ is a $2n$ simplectic manifold described by the coordinates $(q_i, p_i) \in \mathbb{R}^2$, $i \in \{1, \ldots, n\}$, with canonical Poisson brackets

$$\{q_i, p_j\} = \delta_{ij}. \tag{1.17}$$

A physical observable is then a real (smooth) function F of these coordinates. Denoting by $\mathcal{F}$ the real linear space of observables, we have for any $F, G \in \mathcal{F}$

$$\{F, G\} = \sum_k \frac{\partial F}{\partial q_k}\frac{\partial G}{\partial p_k} - \frac{\partial F}{\partial p_k}\frac{\partial G}{\partial q_k}. \tag{1.18}$$

The bijective map U_t is related to a particular function on phase space, the Hamiltonian $H = H(q, p)$, that gives the equations of motion of the system

$$\frac{dF}{dt} = \{F, H\}. \tag{1.19}$$

The operator

$$D_H F(\mathbf{q}, \mathbf{p}) = \{F, H\}\Big|_{(\mathbf{q},\mathbf{p})} \tag{1.20}$$

acts as infinitesimal generator of the evolution map and U_t can be expressed as Lie series

$$U_t = \sum_{n=0}^{\infty} \frac{t^n}{n!} D_H^n \equiv \exp\{tD_H\}. \tag{1.21}$$

The evolution equation is such, in most physical cases, that time evolution of a given state is continuous. However the map U_t can be very complicated. In particular, although it may be almost everywhere continuous, this continuity is almost nowhere uniform in time. In many cases, two nearby states map to states that are very far apart, and that become exponentially further apart as t is increased (*chaos*). Integrability is essentially the opposite of chaos: the map U_t is as nice as it can be. It possesses infinitely many invariant submanifolds that foliate $\mathcal{M}$, parametrised by as many continuous parameters as there are "degrees of freedom", and on these submanifolds, states that start nearby stay nearby uniformly in time. To clarify these concepts we introduce the definition of *Liouville integrability* [24].

Definition 1 (First integral)**.** *A function $F \in \mathcal{F}$ is a* first integral *of a system with hamiltonian function H if its Poisson bracket with H itself is identically equal to zero.*

$$\{F, H\} = 0 \tag{1.22}$$

Definition 2 (Involution)**.** *Two functions $F_1, F_2 \in \mathcal{F}$ are* in involution *if their Poisson bracket is equal to zero.*

$$\{F_1, F_2\} = 0 \tag{1.23}$$

Definition 3 (Liouville integrability)**.** *A dynamical system (of $2n-$dimensional phase space) is* Liouville integrable *if there exists n independent first integrals I_k, with $k \in \{1, \dots, n\}$, in involution.*

The independence of the latter means that at generic points on the symplectic manifold, the tangent space of the surface defined by $I_k = const.$ exists $\forall k$ and is $n-$dimensional.

It is now possible to state the Liouville theorem on integrable systems.

Theorem 1 (Liouville theorem)**.** *Consider a Liouville integrable system with a set of first integrals $\{F_k\}$. Consider the set*

$$M_{\mathbf{f}} = \{(\mathbf{q}, \mathbf{p}) : F_i(\mathbf{q}, \mathbf{p}) = f_i = const.,\ \ i \in \{1, \dots, n\}\}. \tag{1.24}$$

Then

1. *$M_{\mathbf{f}}$ is a smooth manifold, invariant under the phase flow with hamiltonian function $H = F_1$*

2. *If the manifold $M_{\mathbf{f}}$ is compact and connected, then it is diffeomorphic to the $n-$dimensional torus*

$$T^n = \{(\phi_1, \dots, \phi_n), \phi_i \in [0, 2\pi[\}$$

3. *The evolution map with hamiltonian function H determines a conditionally periodic motion on $M_{\mathbf{f}}$, i.e., in angle variables$\{\phi_j\}$ and their canonical conjugate action variables $\{I_j\}$, $j = 1, \dots, n$,*

$$\{\phi_j, I_k\} = \delta_{j,k}$$

we have that action variables are purely functions of the first integrals, hence are invariant under time evolution. This implies that angles evolve linearly with time:

$$\{\phi_j, H\} = \frac{\partial H}{\partial I_j} \qquad \Rightarrow \qquad \phi_j(t) = \frac{\partial H}{\partial I_j} t + \phi_j(0)$$

4. *The canonical equations with hamiltonian function H can be integrated by quadratures.*

Quantum integrability

When it comes to quantum theory, the definition of integrability it is not straightforward. One may wish to emulate the classical case following canonical quantization [36], supplanting Poisson brackets by commutators

$$\{F, G\} \to -i[F, G] \tag{1.25}$$

and ask for many integrals of motions (in involution) as there are degrees of freedom. Having a lattice model with N sites in mind and a local Hilbert space of dimension 2, the problem is that for any finite N, its Hamiltonian is a finite-dimensional Hermitian matrix $2^N \times 2^N$ and can be diagonalised. In the diagonal basis, any other matrix that is diagonal will commute with the Hamiltonian. There are 2^N of such matrices, all independent from each other. Hence, we have automatically a greater number of conserved quantities then the number of degrees of freedom. Obviously this doesn't mean that every quantum chain is integrable: since these conserved quantities exist for every system, they can't have any profound meaning or impact. There is no universally accepted definition of integrability for quantum spin chains (see for example [37, 38]). One of the main concepts that is commonly accepted as being fundamental, however, is that of *locality*. We now introduce some concepts related to this feature [39].

Definition 4 (local quantum spin chain)**.** *A quantum spin chain model is* local *if the Hamiltonian H, as the thermodynamicl limit is taken, is always on the form*

$$H = \sum_k h_k, \tag{1.26}$$

with $[h_l, h_k] = 0$ for $|l - k|$ large enough.

Definition 5 (local operator)**.** *An operator $\mathcal{O}_n$ is* local *around the site n*[1]

$$\exists r > 0 : [\mathcal{O}_n, h_m] = 0 \quad \forall m : |n - m| > r. \tag{1.27}$$

Two operators $\mathcal{O}_n, \mathcal{O}'_m$ are said to be local with respect to each other *if they commute for $|n - m|$ large enough.*

Definition 6 (local conserved quantity)**.** *A* local conserved quantity *(or charge) is an operator Q supported on the whole chain, such that it commutes with the hamiltonian function*

$$[Q, H] = 0 \tag{1.28}$$

[1] The meaning of index n can be introduced through the unitary algebra automorphism that generates space translations, formally e^{iPn}.

and such that Q is a sum over n of uniformly *local operators around n:*

$$Q = \sum_n q_n, \qquad \exists r > 0 : [q_n, h_m] = 0 \qquad \forall |n - m| > r \tag{1.29}$$

Using these concepts we can define integrability as follows:

Definition 7. *(quantum integrability) A local quantum spin chain model is integrable if, in the thermodynamical limit, there exist infinitely many local conserved quantities $Q^{(k)}$ that are in involution,*

$$[Q^{(k)}, Q^{(l)}] = 0 \qquad \forall k, l \tag{1.30}$$

and whose densities are local with respect to each other.

We remark that in the thermodynamic limit the Hamiltonian H can be written as [37]

$$H = \sum_k \epsilon(k) \eta_k^\dagger \eta_k + E_0 \tag{1.31}$$

where $\eta_k^\dagger$ and η_k are the creation and annihilation operators for asymptotic particles of momentum k and produce quasi particle excitations with dispersion relation $\epsilon(k)$ and E_0 is the ground state energy. Furthermore in integrable models $n_k = \eta_k^\dagger \eta_k$ are extensive observables. It is important to remark that the existence of a quasi-particle description is not a sufficient condition for integrability. It is indeed necessary that the quasi-particles mantain their identity upon scattering between each other. This is ensured by the complete factorization of many-body scattering amplitudes into $2-$body scattering processes [40]. In this picture the conserved charges are simply the occupation number of each single-particle eigenmode n_k.

1.3.2 Equilibration

Considering now integrable quantum systems out of equilibrium, expectation values of the conserved quantities $Q^{(k)}$ are time independent

$$\mathrm{Tr}\big(\rho(t) Q^{(k)}\big) = \mathrm{Tr}\big(e^{-iHt} \rho(0) e^{iHt} Q^{(k)}\big) = \mathrm{Tr}\big(\rho(t) Q^{(k)}\big) \equiv E^{(k)}, \tag{1.32}$$

where the invariance of the trace under cyclic permutations and the fact that $[Q^{(k)}, H] = 0$ were used.

An immediate consequence is that such systems cannot thermalise because the system retains memory of the initial expecation values of all conserved quantities at all times. The works of Jaynes [18, 19] on the maximum entropy ensemble then suggest

that the stationary state density matrix is given by a *generalised Gibbs ensemble* (GGE) [10]

$$\rho^{\mathrm{SS}} \equiv \rho^{\mathrm{GGE}} = \frac{e^{\sum_n \lambda_n Q^{(n)}}}{\mathrm{Tr}\left(e^{\sum_n \lambda_n Q^{(n)}}\right)}. \tag{1.33}$$

The Lagrange multipliers λ_k are fixed by the initial conditions (1.32), requiring

$$\lim_{N\to\infty} \frac{E^{(k)}}{N} = \lim_{N\to\infty} \frac{1}{N} \mathrm{Tr}\left(\rho^{\mathrm{GGE}} Q^{(k)}\right) \tag{1.34}$$

To distinguish this process from thermalization it has been given the name of *equilibration*. This conjecture motivates the need of a clear characterization of quantum integrable systems and it also recovers part of the analogy with the classical case: even if the thermalization mechanism may be different, integrability is still a sufficient condition for non-thermalization.

Nevertheless, this definition of GGE suffers from the same ambiguities of the definition of integrability. Instead of using local conserved quantities, GGE are often formulated using conserved mode occupation numbers [10]. The crucial point is that conservation laws are usually linearly related to the mode occupation number. This implies that the GGE describing the stationary state can be constructed either from the local conservation laws or from the mode occupation number. There are though cases in which this is not valid. In this cases the stationary state is not always locally equivalent to a GGE [41–43].

Furthermore it was found in [44, 45] that a GGE formed of local conserved charges fails to describe thermalization after a quantum quench in the gapped XXZ model. These results hinted at the existence of additional effectively local conserved charges linearly independent from the strictly local ones. The first progress to solve this dilemma was perfermoed in [46] where the importance of a *quasilocal conservation law* is pointed out. In a subsequent study [47], a connection to certain non-standard solutions to Yang–Baxter equation has been uncovered, permitting a systematic construction of a large set of quasilocal conservation laws directly from commuting transfer matrices associated to complex spin (non-unitarty) representations. As stated in [12] it became clear that in a generic case the GGE has to be appropriately extended by incorporating quasilocal conservation laws which are viable for the whole range of anisotropies, invariant under spin-reversal transformation (i.e., of even parity), but still distinct from the canonical ones obtained from expanding the fundamental transfer matrix. Such quasilocal charges have been constructed (for the isotropic case) in [48], invoking transfer matrices built from unitary but non-fundamental spin representations of the auxiliary spin. Soon after, a study [49] confirmed that those charges exactly explain the GGE puzzle.

2

Generalised Hydrodynamics

Generalised hydrodynamics (GHD) is one of the leading approaches to computing dynamical quantities in non-equilibrium steady states and non-stationary settings [16, 50, 51]. The basic idea is that hydrodynamics emerges as a consequence of local entropy maximisation and scale separation on individual fluid cells containing a mesoscopic quasi-particle number. In a practical sense GHD allows us to evaluate exact expectation values of currents in GGEs. This current formula has been subject to increasingly rigorous and general derivations [52–61].

The original GHD proposals considered the partitioning protocol. In this set up two independently thermalized systems are put into contact at time zero. The presence of multiple conserved quantities gives rise to ballistic transport, meaning that, after a transient period, steady state currents flowing between the right and left sub-systems emerge [11, 13]. As mentioned above, GHD provides a method to compute such currents by combining the hydrodynamic principle, generalised to infinitely many conservation laws, with an effective description of quasi-particles, which for IQFTs is based on the Thermodynamic Bethe Ansatz (TBA) [62–64]. The energy current and density in the partitioning protocol admit simple exact expressions in conformal field theory (CFT) [65–67]. These constitute a useful benchmark when studying IQFTs, whose ultraviolet limits are described by CFT.

The chapter, following [16], is organized as follows: In Sec. 2.1 we review the main concepts of hydrodynamics. After introducing the Thermodynamic Bethe Ansatz technology in Sec. 2.2, we apply it to obtain Generalised Hydrodynamics in Sec. 2.3. Finally in Sec. 2.4 we consider the Riemann problem (or partitioning protocol) in the new GHD framework.

2.1 Hydrodynamics: A Short Review

The main assumption of standard hydrodynamics lies in the possibility of reducing the complex behaviour of a many particle system with small range interaction to a small set of equations. In this perspective, the dynamics and the states of the system are specified by the value and the evolution of some fields, so that the knowledge of the trajectory of each particle is not required. In order to understand when this drastic simplification is actually viable, we need to distinguish four types of time scales in which phenomena of different nature occur:

- **Microscopic regime**: At very short time scales the individual particles of the system propagate ballistically between collisions and the dynamics is reversible;
- **Boltzmann equation regime**: after many collisions, some mixing occurs. At this stage, one reverts to an approximate description where, instead of individual particles' trajectories, one uses the coarser density of particles in the single-particle phase space. This description is valid only after this coarse graining has actually occurred. This leads to the Boltzmann equation, with contains a collision integral that accounts for the change of phase space densities due to collisions. This is famously an irreversible dynamics, the passage from reversible to irreversible being attributed to the coarsening and arguments about microscopic phase space volumes occupied by coarse states;
- **Hydrodynamics regime**:

  Collisions – or the collision integral in the Boltzmann equation – lead to relaxation, whereby the system tends to maximise entropy. Entropy maximisation occurs at large scales compared to the microscopic scales, but can still occur at small scales compared to laboratory scales. Thus we divide the system into "fluid cells", where each cell, small on laboratory scales, is considered thermodynamically large, and is considered to have (nearly) reached a state in which entropy has been maximised. These are local thermodynamic states, and local entropy maximisation is often referred to as the reaching of a local thermodynamic equilibrium (although in integrable systems this nomenclature is not entirely accurate). This change in the degrees of freedom used to describe the local states – from densities in single-particle phase space to the degrees of freedom of entropy-maximised thermodynamic states – is one of the most important assumptions of hydrodynamics.

- **Thermodynamics regime**: At even larger time scales the entropy maximisation tends to involve all the system and one recovers thermodynamics.

2.1.1 Maximal Entropy States and Hydrodynamic Matrices

Let us consider a homogenous many-body one dimensional system with short range interactions, which is isolated from any external environment. Let H be its (conserved) total energy and $\mathcal{Q}_i$ be a (finite) set of conserved charges in involution expressed in terms of some local or quasi-local densities $q_i(x,t)$. We can write:

$$\begin{aligned} \mathcal{Q}_i &= \int dx q_i(x,t), \\ \partial_t \mathcal{Q}_i = 0 \implies \partial_t q_i(x,t) + \partial_x j_i(x,t) &= 0. \end{aligned} \tag{2.1}$$

Now the question is: if the system starts in some arbitrary, generic, homogeneous state, what happens to a typical finite region after long enough times? Physically, we expect such finite regions to "relax" to some state, the rest of the infinite system playing the role of a bath. By ergodicity, the density matrix ρ that describes all local or quasi-local observables $\mathcal{O}$,

$$\langle \mathcal{O} \rangle = \mathrm{Tr}\left[\rho \mathcal{O}\right], \tag{2.2}$$

will maximise the entropy

$$S = -\,\mathrm{Tr}[\rho \ln \rho]. \tag{2.3}$$

As averages of conserved densities cannot change, entropy maximisation is with respect to the available conservation laws. Constraints for the conserved quantities $\mathcal{Q}_i$ impose a density matrix of the Gibbs form:

$$\rho \propto \exp\left\{ -\sum_i \beta^i \mathcal{Q}_i \right\}, \tag{2.4}$$

where β^i is the Lagrange multiplier associated to $\mathcal{Q}_i$. The set of β^i form a system of coordinates in the manifold of maximal entropy states (MESs) and they are the only parameters encoding information about the initial, generic state after relaxation has occurred. These are the "generalised inverse temperatures". Let $\boldsymbol{\beta}$ be the array of all the inverse temperatures, the averages evaluated in MESs satisfy

$$-\frac{\partial}{\partial \beta_i} \langle \mathcal{O} \rangle_{\boldsymbol{\beta}} = \int dx \, \langle \mathcal{O} q_i(x,0) \rangle^c_{\boldsymbol{\beta}} \tag{2.5}$$

where the upperscript c denotes the connected correlation function. In particular (2.5) constitues an appropriate definition of the inverse temperatures and contains most of the information encoded in (2.4).

Notice that, by denoting

$$\bar{\mathcal{O}} = \langle \mathcal{O}(0,0) \rangle_{\boldsymbol{\beta}}\,, \tag{2.6}$$

we have

$$\frac{\partial}{\partial \beta^i} \bar{q}_j = \frac{\partial}{\partial \beta^j} \bar{q}_i. \tag{2.7}$$

This implies the existence of a free energy $\mathcal{F}(\boldsymbol{\beta})$ such that:

$$\bar{q}_i = \frac{\partial \mathcal{F}}{\partial \beta^i}. \tag{2.8}$$

We can now define an inner product on the space of local and quasi-local observables as

$$(\mathcal{O}_1, \mathcal{O}_2) = \int dx \, \langle \mathcal{O}_1(0,0) \mathcal{O}_2(x,0) \rangle^c_{\boldsymbol{\beta}} \tag{2.9}$$

From this, it is convenient to introduce the symmetric **static covariance matrix** C, whose elements are defined by the inner product of the densities of the local conserved charges:

$$C_{ij} = (q_i, q_j). \tag{2.10}$$

This matrix is positive and symmetric, in fact (2.5, 2.7) imply:

$$C_{ij} = \int dx \, \langle q_i(0,0) q_j(x,0) \rangle^c_{\boldsymbol{\beta}} = -\frac{\partial}{\partial \beta^j} \langle q_i \rangle_{\boldsymbol{\beta}} = -\frac{\partial}{\partial \beta^j} \bar{q}_i = -\frac{\partial}{\partial \beta^i} \bar{q}_j = C_{ji}, \tag{2.11}$$

thus the free energy $\mathcal{F}(\boldsymbol{\beta})$ is a strictly convex function of the inverse temperatures (note that C is precisely the Hessian of the free energy). This observation is extremely useful: the very same matrix can be seen as the Jacobian

$$C_{ij} = -\frac{\partial}{\partial \beta^j} \bar{q}_i, \tag{2.12}$$

hence the map

$$\boldsymbol{\beta} \to \bar{\boldsymbol{q}} \tag{2.13}$$

is a bijection. This allow us to fully characterise maximal entropy states in terms of the averages of conserved densities. As a consequence, all averages of local or quasi-local observables in maximal entropy states can be seen as functions of $\bar{\boldsymbol{q}}$. In particular for the average currents we may write the **equations of state** of the model

$$\bar{j}_i = \bar{j}_i(\bar{\boldsymbol{q}}). \tag{2.14}$$

Equations of state satisfy quite surprising relations. Indeed, there is a symmetry (see [16] for proof) mimicking (2.7):

$$\frac{\partial}{\partial\beta^i}\bar{j}_j = \frac{\partial}{\partial\beta^j}\bar{j}_i. \tag{2.15}$$

The related hydrodynamic matric B follows up:

$$B_{ij} = (j_i, q_j) = \frac{\partial}{\partial\beta^j}\bar{j}_i \tag{2.16}$$

and as a consequence there must exist a free energy flux $\mathcal{G}$ such that

$$\bar{j}_i = \frac{\partial\mathcal{G}}{\partial\beta^i}. \tag{2.17}$$

Finally we define the so-called **flux Jacobian** as:

$$A_i^j = \frac{\partial\bar{j}_i}{\partial\bar{q}_j}. \tag{2.18}$$

The flux Jacobian plays an essential role in identifying some of the fundamental quantities in hydrodynamics and it satisfies the identity:

$$B = AC = CA^T. \tag{2.19}$$

Writing an arbitrary conserved density as a linear combination $\sum_{i,j} v_i C^{ij} q_j(x,t)$, where C^{ij} is the inverse of C_{ij}, the inner product defined in (2.9) induces an inner product on the coefficient vector $\boldsymbol{v}$ with components v_i

$$\langle \boldsymbol{v}, \boldsymbol{w}\rangle = (\boldsymbol{v}\cdot C^{-1}\boldsymbol{q}, \boldsymbol{w}\cdot C^{-1}\boldsymbol{q}) = \boldsymbol{v}\cdot C^{-1}\boldsymbol{w} = \sum_{ij} v_i C^{ij} w_j. \tag{2.20}$$

In particular this defines a metric in which the flux Jacobian is symmetric:

$$\langle \boldsymbol{v}, A\boldsymbol{w}\rangle = \boldsymbol{v}C^{-1}A\boldsymbol{w} = \boldsymbol{v}A^TC^{-1}\boldsymbol{w} = \langle A\boldsymbol{v}, \boldsymbol{w}\rangle . \tag{2.21}$$

Since A is symmetric, it is diagonalisable and its eigenvectors $h_{j;l}$ can be interpreted as the normal modes of hydrodynamics and its real eigenvalues as generalised sound velocities (we will simply refer to them as effective velocities v_l^{eff}):

$$\sum_j A_i^j h_{j;l} = v_l^{\text{eff}} h_{i;l}. \tag{2.22}$$

2.1.2 From Microscopic Regime to Hydrodynamics: Local Entropy Maximisation and Euler Hydrodynamics

In the previous section we have introduced a set of important mathematical objects to describe the hydrodynamics of maximal entropy states. Now we want to use that formalism to obtain a generalised version of the Euler equation for local averages and, starting from such equation, we aim to find a privileged frame, where the description of hydrodynamics looks simpler.

To begin with, let us consider some initial inhomogeneous state of a quantum many body system. In general, average values of observables in this kind of states depend on the position and the time in which they are computed. In the assumption of local entropy maximisation, however, we can state with a good approximation that:

$$\langle \mathcal{O}(x,t) \rangle \approx \langle \mathcal{O}(0,0) \rangle_{\boldsymbol{\beta}(x,t)} \,, \tag{2.23}$$

that is, any average of an arbitrary operator $\mathcal{O}(x,t)$ can be evaluated as the average of $\mathcal{O}(0,0)$ in a maximal entropy state with (x,t)-dependent inverse temperatures.

The choice $(x,t) = (0,0)$ is completely arbitrary and follows from the homogeneity and stationarity of MESs, moreover (2.23) does not depend on the observable itself, so the same state can be used to describe any (quasi)local observable.

The downside of this approach is that the validity of such approximation has to be checked case by case and so far there are no general rules for non trivial systems. However we can expect to obtain exact results in the limit where the typical sizes over which the variations of local average occur become infinitely large. We will refer to this situation as the **Euler scaling limit** or mesoscopic scale (see Fig. 2.1).

Once the local entropy maximisation is assumed, one can derive, from the microscopic dynamics, the Euler equations for the model under consideration. First consider the conservation laws (2.1) in their integral form over some contour (say $[0,X] \times [0,T]$):

$$\int_0^X dx (q_i(x,T) - q_i(x,0)) + \int_0^T dt (j_i(X,t) - j_i(0,t)) = 0. \tag{2.24}$$

By taking the averages and using the entropy maximisation hypothesis we get:

$$\int_0^X dx (\bar{q}_i(x,T) - \bar{q}_i(x,0)) + \int_0^T dt (\bar{j}_i(X,t) - \bar{j}_i(0,t)) = 0. \tag{2.25}$$

If such equations are differentiable, they can be re-casted in the local form:

$$\partial_t \bar{q}_i(x,t) + \partial_x \bar{j}_i(x,t) = 0. \tag{2.26}$$

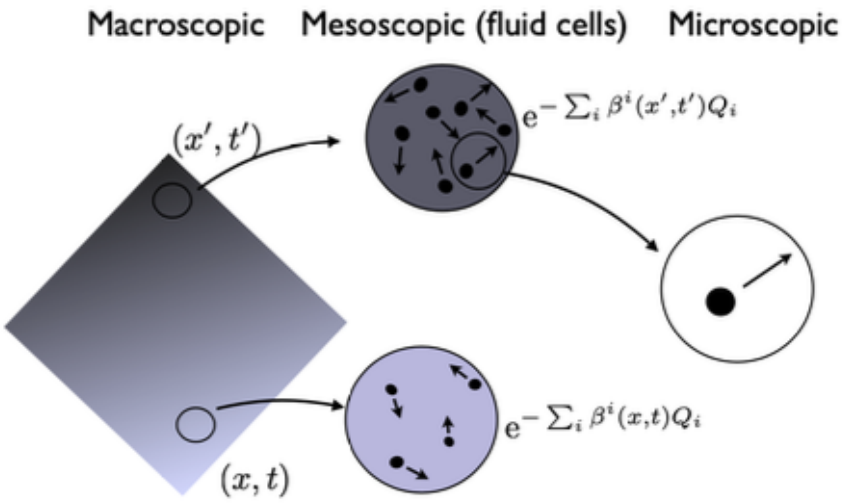

Figure 2.1: The local entropy maximisation hypothesis. At mesoscopic scales the behaviour of each fluid cell is dictated only by the value of the local inverse temperatures.

We can now use the flux Jacobian (2.18) to re-write the second term in the l.h.s. obtaining:

$$\partial_t \bar{q}_i(x,t) + \sum_j A_i^j(\bar{\boldsymbol{q}}(x,t))\partial_x \bar{q}_j(x,t) = 0. \tag{2.27}$$

These "wave equations" for all space-time dependent coordinates $\bar{q}_i(c,t)$ characterising the local MESs represent the **Euler hydrodynamic equations**. They depend on the equations of state of the model and the number of conserved quantities, but on nothing else: at the emerging Euler scale, very little of the microscopic dynamics remains. Once such equations are solved, then the exact local state at every space-time point (x,t) is known and, in particular, we can evaluate the average of any observable at any point lying within the fluid cell through (2.23).

Let us now investigate in more detail the properties of the flux Jacobian. In the previous section we argued that, being it symmetric with respect to the inner product (2.20), it is diagonalisable. Then there must exist a matrix R such that

$$RAR^{-1} = \mathrm{diag}(v_i^{\mathrm{eff}}), \tag{2.28}$$

where the effective velocities v_i^{eff}, defined by (2.22), are its eigenvectors. Since R depends on $\bar{\boldsymbol{q}}$, let us suppose that we can find a set of functions $n_j(\bar{\boldsymbol{q}})$, whose Jacobian is precisely R:

$$\frac{\partial n_i}{\partial \bar{q}_j} = R_i^j(\bar{\boldsymbol{q}}). \tag{2.29}$$

Then (2.27) becomes:

$$\partial_t n_i + v_i^{\text{eff}} \partial_x n_i = 0. \tag{2.30}$$

If R is invertible, so are the functions $n_j(\bar{\boldsymbol{q}})$ and, in such a case, we have found a new set of coordinates which can characterise all the maximal entropy states. Moreover, in these coordinates, the dynamics governed by the generalised Euler equation looks simpler, so we will refer to them as normal modes of the hydrodynamics. In this perspective, (2.30) simply means that the i^{th} normal mode is convectively transported at the velocity v_i^{eff}.

We conclude this section by pointing out that Euler equations only involve first-order derivatives, so they must describe a reversible dynamics. This fact can be checked also by considering the macrocanonical entropy:

$$s = \sum_i \beta^i \bar{q}_i - \mathcal{F}\bar{\boldsymbol{q}}. \tag{2.31}$$

Using the Euler hydrodynamic equation (2.26) and the free energy flux (2.17), it is a simple matter to observe that there exists a conserved entropy current j_s such that

$$\partial_t s + \partial_x j_s = 0, \tag{2.32}$$

with

$$j_s = \sum_i \beta^i j_i - \mathcal{G}. \tag{2.33}$$

Thus, Euler hydrodynamics conserve entropy.

2.2 Thermodynamic Bethe Ansatz

In the previous sections we discussed the main properties of hydrodynamics in absolute generality. Now we want to specialise our results in the case in which the number of conserved commutating charges is infinite, that is when the system under consideration is integrable.

Natural questions that arise are: How can we extend the previous results? The diagonalisation problem (2.29) is in general a difficult task: how is it expressed in this context? What are the normal modes? To answer these questions we need to introduce the Thermodynamic Bethe Ansatz machinery. With TBA's help, in the next section the answers to those questions will come quite naturally.

Let's consider a relativistic Integrable Quantum Field Theeory (IQFT). To avoid irrelevant complications we consider first the simplest scattering theory with a single

neutral particle of mass m and pair scattering amplitude $S(\theta_{12} = \theta_1 - \theta_2)$. Rapidities $\theta_{1,2}$ of particles parameterize their on-shell energies and momenta.

$$e_i(\theta) = m \cosh \theta_i, \quad p_i(\theta) = m \sinh \theta_i. \tag{2.34}$$

Amplitude $S(\theta)$ satisfies unitarity

$$S(\theta)S(-\theta) = 1 \tag{2.35}$$

and crossing symmetry

$$S(\theta) = S(i\pi - \theta). \tag{2.36}$$

$S(\theta)$ satisfies the quantisation equations for the momenta p_i, $i = 1, \ldots, N$, of N particles in a periodic box of length L given by

$$e^{ip_iL} \prod_{j \neq i} S(\theta_{ij}) = 1; \quad i = 1, \ldots, N, \tag{2.37}$$

or, by defining

$$S(\theta) = e^{i\delta(\theta)}, \tag{2.38}$$

we have the **Bethe ansatz equations**

$$mL \sinh \theta_i + \sum_{j \neq i} \delta(\theta_{ij}) = 2\pi n_i, \tag{2.39}$$

with N integer numbers n_i.

Additional selection rules on rapidity sets are to be taken into account if the particles are identical. The Bethe wave function should be symmetrized or antisymmetrized depending on their statistics. The unitarity condition (2.35) specifies that $S^2(0) = 1$. Two different cases are possible:

- $S(0) = -1$: This leads to a wave-function that is antisymmetric under the exchange of two particles with the same rapidity. If the two particles are bosons, this is clearly in conflict with their Bose statistics. This implies that two bosons cannot have the same value of the rapidity, namely each value of θ can be assigned at most to one particle only. Hence all integers n_i must be different. Vice versa, if the identical particles are fermions, the antisymmetry of the wavefunction perfectly matches their Fermi–Dirac statistics and there is no restriction on the integers n_i. In the context of the Bethe ansatz, the condition $S(0) = -1$ is called **fermionic type**, independently of the bosonic or the fermionic nature of the particles.

- $S(0) = 1$: In this case the situation is inverted. this condition gives rise to a symmetric wavefunction under the exchange of two particles of the same species with the same rapidity. Hence, if the two particles are bosons, this is compatible with their Bose statistics and there is no restriction on the integers n_i. Vice versa, if the two particles are fermions, each value of the rapidity can be taken only by one particle, i.e. all integers n_i must necessarily be different. In the context of the Bethe ansatz, the condition $S(0) = +1$ is called **bosonic type**, independently of the bosonic or the fermionic nature of the particles.

Thermodynamic limit and Thermodynamics

The quantisation conditions (2.39) for the rapidities of the particles form a complicated set of transcendental equations. They simplify in the thermodynamic limit, on which both $L \to \infty$ and the total number of particles $N \to \infty$ but keeping their ratio fixed. The spectrum of rapidities condenses and the distance between adjacent levels behaves as $\theta_i - \theta_{i+1} \sim 1/mL$. It makes sense in this limit to introduce a continuous rapidity density of *roots* $\rho^{(r)}(\theta)$ defined as the number particles with rapidity between θ and $\theta + \Delta\theta$ divided by $L\Delta\theta$. The phase sum in (2.39) is nearly constant when varying from θ to θ_{i+1} and can be estimated as an integral. Eq. (2.39) acquires the form

$$mL \sinh \theta_i + \int d\gamma \delta(\theta_i - \gamma)\rho^{(r)}(\gamma) = 2\pi n_i \tag{2.40}$$

and can be considered as the equation for rapidity levels, defined as solutions to this equation for all integer numbers n on the r.h.s. but not only n_i corresponding to actual states. In fact, these equations admit solutions in θ_i also for integer values of n that are necessarily in relation to the occupie d states. Such solutionsthat do not correspond to the admissible quantum numbers, are called *holes*, and their density around the value θ is denoted by $\rho^{(h)}(\theta)$.

The total density $\rho(\theta)$ of the occupied and empty levels of the particle is equal to

$$\rho(\theta) = \rho^{(r)}(\theta) + \rho^{(h)}(\theta) = \frac{1}{L}\frac{dn_i}{d\theta}, \tag{2.41}$$

which leads to

$$\rho(\theta) = \frac{m}{2\pi}\cosh\theta + \int d\gamma \varphi(\theta - \gamma)\rho^{(r)}(\gamma), \tag{2.42}$$

where

$$\varphi(\theta) = \frac{\partial\delta(\theta)}{\partial\theta} = -i\frac{\partial}{\partial\theta}\ln S(\theta) \tag{2.43}$$

It is convenient to define *pseudo-energies* $\varepsilon(\theta)$ through the ocupation numbers $n_{F/B}(\theta)$ as:

$$\frac{\rho^{(r)}(\theta)}{\rho(\theta)} = n_{F/B}(\theta) = \frac{1}{e^{\varepsilon(\theta)} \pm 1}, \tag{2.44}$$

where the sign $+(-)$ stands for fermions (bosons).

The equations abocve can be manipulated to generate equations for the pseudo-energies $\varepsilon(\theta)$. This is achieved by requiring thermodynamic equilibrium, or minimisation of the free energy per unit length. To do so we have to define the total energy of the system and entropy. The former is simply given by

$$h(\rho^{(r)}) = m \int d\theta \rho^{(r)}(\theta) \cosh\theta, \tag{2.45}$$

while for the latter a little bit of work is needed. It should be realized that in the thermodynamic limit a large number of quantum states correspond to every consistent pair of densities $\rho(\theta)$ and $\rho^{(h)}(\theta)$. Consider a partition of the rapidity axis in small intervals $\Delta\theta$ such that $1 \ll \Delta\theta \ll 1/mL$. In this case there is a large number $N \sim \rho(\theta)\Delta\theta$ of levels in each interval and about $n \sim \rho^{(r)}(\theta)\Delta\theta$ particles are distributed between them.

Since these densities are not strongly influenced by the local redistributions of the particles, the number of different ways of distributing the particles among these levels is given by

$$\Omega_F = \frac{[L\rho(\theta)\Delta\theta]!}{[L\rho^{(r)}(\theta)\Delta\theta]![L\rho^{(h)}(\theta)\Delta\theta]!} \tag{2.46}$$

in the fermionic case and by

$$\Omega_B = \frac{[L(\rho(\theta) + \rho^{(r)}(\theta) - 1)\Delta\theta]!}{[L\rho^{(r)}(\theta)\Delta\theta]![L(\rho(\theta) - 1)\Delta\theta]!} \tag{2.47}$$

in the bosonic case. Correspondingly, the entropy per unit length $s = \ln\Omega$ is expressed by

$$\begin{aligned} s_F[\rho, \rho^{(r)}] &= \int d\theta [\rho \ln\rho - \rho^{(r)} \ln\rho^{(r)} - (\rho - \rho^{(r)}) \ln\big(\rho - \rho^{(r)}\big)], \\ s_B[\rho, \rho^{(r)}] &= \int d\theta [(\rho + \rho^{(r)}) \ln\big(\rho + \rho^{(r)}\big) - \rho \ln\rho - \rho^{(r)} \ln\rho^{(r)}]. \end{aligned} \tag{2.48}$$

Minimizing the free energy

$$f(\rho, \rho^{(r)}) = h(\rho^{(r)}) - \frac{1}{\beta} s_{F,B}(\rho, \rho^{(r)}), \tag{2.49}$$

and taking into account (2.44)w e obtain the **Thermodynamic Bethe Ansatz (TBA) Equation**

$$\varepsilon(\theta) = m\beta\cosh\theta \mp \frac{1}{2\pi}\int d\gamma\varphi(\theta-\gamma)\ln\big(1\pm e^{-\varepsilon(\gamma)}\big), \tag{2.50}$$

where the upper sign refers to the fermionic case and the lower one to the bosonic case. The extremal free energy is given by

$$f(\beta) = \mp\frac{1}{2\pi m\beta}\int d\theta\cosh\theta\ln\big(1\pm e^{-\varepsilon(\theta)}\big), \tag{2.51}$$

where again the upper sign refers to the fermionic case and the lower sign to the bosonic case. The term $\ln\big(1\pm e^{-\varepsilon(\theta)}\big)$ is usually referred to as the $L(\theta)$ function:

$$L(\theta) = \ln\big(1\pm e^{-\varepsilon(\theta)}\big). \tag{2.52}$$

In the more general case there are several types of particles A_a with masses a. The purely elastic scattering theory is described by a symmetric matrix of pair transition amplitudes $S_{ab}(\theta)$. In this case, TBA equations can be rephrased as

$$\varepsilon_a(\theta) = m_a\beta\cosh\theta \mp \sum_b \frac{1}{2\pi}\int d\gamma\varphi_{ab}(\theta-\gamma)\ln\big(1\pm e^{-\varepsilon_b(\gamma)}\big), \tag{2.53}$$

where

$$\varphi_{ab}(\theta) = -i\frac{\partial}{\partial\theta}\ln S_{ab}(\theta). \tag{2.54}$$

Relation to QFT on a Torus

Consider a (1+1)-dimensional euclidean quantum field theory defined on a cylinder, with periodic boundary conditions. Now let L and R be respectively the lengths of the two geodesics Γ_L and Γ_R generating the torus (see Fig. 2.2). There are two equivalent ways to quantize the theory on such a geometry: from the symmetry of the two directions, one can equivalently choose as the time direction one of the two axes and consider the other as the space direction. Hence, the partition function can be written either as

$$Z(R,L) = \operatorname{Tr} e^{-LH_R}, \tag{2.55}$$

or as

$$Z(R,L) = \operatorname{Tr} e^{-RH_L}, \tag{2.56}$$

where H_R and H_L are the Hamiltonians of the system quantized along the R and L direction respectively. The quantisation scheme in which the role of the time direction is played by the L axis will be denoted as the L-channel, while the other one is the R-channel.

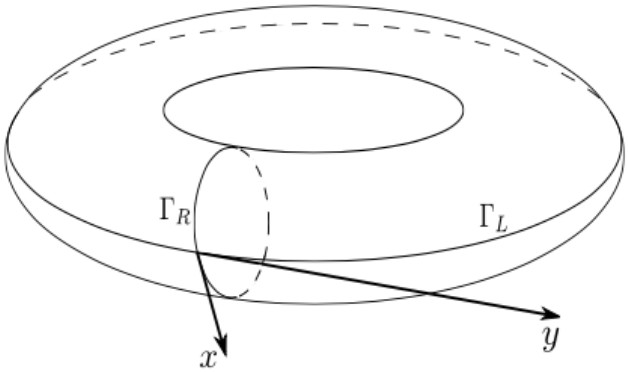

Figure 2.2: Graphical representation of the torus with circumferences Γ_L and Γ_R.

- In the L-channel, taking $L \to \infty$ and keeping R finite we have a compactified system whose partition function is led by the term $e^{-e_0(R)L}$, where $E_0(R)$ is the ground state energy.
- In the R-channel we have instead a theory where time is periodic and space infinite. If we identify R with β, then we can think of this as a description of a QFT at finite temperature. The partition function is now dominated by the term $e^{-RLf/R}$, where $f(R = \beta)$ is given by (2.51).

It is straightforward that

$$E_0(\beta) = \beta f(\beta) = \mp \frac{1}{2\pi m} \int d\theta L(\theta) \cosh\theta \tag{2.57}$$

where the function $L(\theta)$ is defined by (2.52). For generic values of β we may define a *scaling function* $c(\beta)$ by the ground state energy parameterisation

$$E_0(\beta) = -\frac{\pi c(\beta)}{6\beta}. \tag{2.58}$$

From (2.57) it follows that

$$c(\beta) = \frac{3\beta}{\pi^2 m} \int d\theta L(\theta) \cosh\theta. \tag{2.59}$$

Taking the ultraviolet limit $\beta \to 0$ we expect to approach the underlying CFT and so the ground state energy is related to the central charge in the usual way:

$$\lim_{\beta\to 0} E_0(\beta) = -\frac{\pi c_{\text{eff}}}{6\beta}, \quad \text{where } c_{\text{eff}} = c - 24\Delta_{\min}, \tag{2.60}$$

being Δ_{min} the lowest negative conformal weight of the theory. Notice that this limit establishes an important relation between the scattering theory of a massive quantum field theory and the conformal theory that rules its short-distance behavior. The confirmation and the validity of many scattering theories proposed to describe the deformations of conformal field theories can be accomplished thanks to the relation above.

2.3 Generalised Hydrodynamics

The aim is now to specialize the concepts of hydrodynamics to systems with an infinite number of conserved charges using the TBA technology. We will begin our discussion by assuming that the system under study can be described by a set of TBA equations. For semplicity we will assume they are of the fermionic type. A more general version of this equation takes the form

$$\varepsilon(\theta) = \nu(\theta) - \int \frac{\mathrm{d}\theta'}{2\pi} \varphi\left(\theta - \theta'\right) \underbrace{\ln\left(1 + e^{-\varepsilon(\theta')}\right)}_{L(\theta')} \tag{2.61}$$

where now the so called *driving term* is given by: $\nu(\theta) = \sum_i \beta^i h_i(\theta)$, where $h_i(\theta)$ are the one-particle eigenvalues of the conserved quantities in the model. For instance $h_0(\theta) = 1$ (particle number), $h_1(\theta) = e(\theta) = \cosh\theta$ (energy), $h_2(\theta) = p(\theta) = \sinh\theta$ (momentum) and more generally

$$h_{2s-1}(\theta) = \cosh(s\theta) \qquad h_{2s} = \sinh(s\theta), \qquad \text{for} \quad s \in \mathbb{Z}_{\geq 0}. \tag{2.62}$$

By taking the derivative of eq. (2.61) with respect to the inverse temperature β^i we obtain:

$$\frac{\partial\varepsilon(\theta)}{\partial\beta^i} = h_i(\theta) + \int \frac{d\theta'}{2\pi} \varphi\left(\theta - \theta'\right) \frac{\partial L\left(\theta'\right)}{\partial\varepsilon} \frac{\partial\epsilon\left(\theta'\right)}{\partial\beta^i}. \tag{2.63}$$

We define:

$$\begin{aligned} h_i^{\text{dr}}(\theta) &= \frac{\partial\varepsilon(\theta)}{\partial\beta^i} \qquad \text{Dressed charge density.} \\ n(\theta) &= -\frac{\partial L(\theta)}{\partial\varepsilon} \qquad \text{Occupation function.} \end{aligned} \tag{2.64}$$

And we observe that:

$$n(\theta) = \frac{1}{1 + e^{\varepsilon(\theta)}} \tag{2.65}$$

With these new variables, eq. (2.63) becomes:

$$h_i^{\text{dr}}(\theta) = h_i(\theta) + \int \frac{d\theta'}{2\pi} \varphi\left(\theta - \theta'\right) n\left(\theta'\right) h_i^{\text{dr}}\left(\theta'\right). \tag{2.66}$$

This last equation defines the so-called dressing operator, which act on the space of the functions of rapidities:

$$F(\theta) \to F^{\mathrm{dr}}(\theta) = F(\theta) + \int \frac{d\theta'}{2\pi} \varphi\left(\theta - \theta'\right) n\left(\theta'\right) F^{\mathrm{dr}}\left(\theta'\right) \tag{2.67}$$

and, if $\varphi(\theta)$ is symmetric , it satisfies the following identity:

$$\int d\theta \eta(\theta) n(\theta) h^{\mathrm{dr}}(\theta) = \int d\theta \eta^{\mathrm{dr}}(\theta) n(\theta) h(\theta) \tag{2.68}$$

Now we want to express the average of the conserved densities q_i in the rapidities space in terms of the distribution $\rho^{(r)}(\theta)$. In this context the latter is referred to as *spectral particle density* and to lighten the notation we shall denote it simply $\rho_p(\theta)$. We get:

$$(2\pi)\rho_p(\theta) = \left(p'\right)^{\mathrm{dr}}(\theta) n(\theta), \tag{2.69}$$

from which:

$$\mathtt{q}_i \equiv \bar{q}_i = \int \frac{dp}{2\pi} n(\theta) h_i^{\mathrm{dr}}(\theta) = \int \frac{d\theta}{2\pi} p'(\theta) n(\theta) h_i^{\mathrm{dr}}(\theta) = \int d\theta \rho_p(\theta) h_i(\theta). \tag{2.70}$$

In order to obtain the generalised form of the Euler equations in terms of the quantities characterizing our model, we need to find an expression for the average currents $\bar{j}_i$. This task is not trivial requires a "trick" based on the so-called crossing symmetry. In every relativistic quantum field theory the crossing symmetry $\mathcal{C}$ is defined as the double Wick rotation:

$$(x, t) \xrightarrow{\mathcal{C}} (-ix, it), \tag{2.71}$$

which translates, in terms of rapidities, as:

$$\theta \xrightarrow{\mathcal{C}} \frac{i\pi}{2} - \theta, \tag{2.72}$$

(Note that: $\mathcal{C}^2 = 1$). The previous equation implies: $(p, e) \xrightarrow{\mathcal{C}} (ie, -ip)$ and we expect a similar behaviour between $\bar{q}_i$ and $\bar{j}_i$. In particular, let $\mathcal{O}$ be a generic (quasi)local operator. We make the following assumption:

$$\langle \mathcal{C}(\mathcal{O}) \rangle_\nu = \langle \mathcal{O} \rangle_{\mathcal{C}\nu}, \tag{2.73}$$

i.e. the average of the transformed operator $\mathcal{C}\mathcal{O}$ characterized by the source term $\nu(\theta)$ is equal to the average of the original operator evaluated in the transformed sources: $\mathcal{C}\nu(\theta) = \nu(i\pi/2 - \theta)$. Let us denote with $q[h]$ and $j[h]$ respectively the energy densities and currents as functions of the one particle eigenvalue $h(\theta)$. We have:

$$\mathcal{C}(j[h]) = iq\left[h^c\right] \tag{2.74}$$

and, by using (2.73), we get:

$$\langle j[h]\rangle_\nu = \langle \mathcal{C}(\mathcal{C}(j[h]))\rangle_\nu = i\left\langle q\left[h^{\mathcal{C}}\right]\right\rangle_{\mathcal{C}\nu} \tag{2.75}$$

By substituting the expression of the average energy density (2.70) we finally arrive at the equation for the average currents:

$$\mathtt{j}_i \equiv \bar{j}_i = \int \frac{de(\theta)}{2\pi} n(\theta) h_i^{\mathrm{dr}}(\theta) = \int \frac{d\theta}{2\pi} \left(e'\right)^{\mathrm{dr}}(\theta) n(\theta) h_i(\theta). \tag{2.76}$$

We now possess all the ingredients to approach the problem of the evolution of the system from the perspective of the GHD.

We can rewrite the relation (2.76) as:

$$\mathtt{j}_i = \int d\theta v^{\mathrm{eff}}(\theta)\rho_p(\theta)h_i(\theta), \tag{2.77}$$

where:

$$v^{\mathrm{eff}}(\theta) = \frac{\left(e'\right)^{\mathrm{dr}}(\theta)}{\left(p'\right)^{\mathrm{dr}}(\theta)}. \tag{2.78}$$

This effective velocity appears in the form of group velocity and takes into account (via the dressing) all the interactions with the quasiparticles. In this perspective, eq. (2.77) has a very natural interpretation: the average current is obtained by integrating the product of the quantity of charge transported by each quasiparticle times the density of quasiparticles times their effective velocity, so that we can also define a *spectral current density*

$$\rho_c(\theta) = v^{\mathrm{eff}}(\theta)\rho_p(\theta). \tag{2.79}$$

By substituting (2.70) and (2.76) into (2.26) we get:

$$\partial_t \rho_p(\theta) + \partial_x \left(v^{\mathrm{eff}}(\theta)\rho_p(\theta)\right) = 0 \tag{2.80}$$

which identifies ρ_p as the conserved fluid density. To find the normal modes we have to study the properties of the diagonalising matrix of the flux Jacobian. This task is performed in detail in [16] and it turns out that:

- $\sum_j A_i^j h_j^{\mathrm{dr}}(\theta) = v^{\mathrm{eff}}(\theta) h_i^{\mathrm{dr}}(\theta)$. The spectrum of the flux Jacobian is given by the effective velocities of the quasiparticles. Thus, the index ℓ from (2.22) labels all the rapidities.

- The occupation functions represent the normal modes of the GHD:

  $$\partial_t n(\theta) + v^{\mathrm{eff}}(\theta)\partial_x n(\theta) = 0 \tag{2.81}$$

  There is one normal mode for every value of the rapidities, in agreement with the continuum spectrum of the flux Jacobian.

2.4 GHD Approach to the Riemann Problem

One of the most iconic examples in which the results of the GHD have been applied with success is the so-called Riemann problem or partitioning protocol. It can be summarised as follows:

- A physical system is partitioned into two semi-infinite halves, which are, initially homogeneous and independently thermalised into different equilibrium states. In $d = 1$, one sub-system extends towards $x < 0$ with inverse temperature β_L, while the other towards $x > 0$ with inverse temperature β_R.
- At a given time, let's say $t = 0$, the two sub-systems are put into contact at $x = 0$, so they can exchange energy or charge. Immediately after the contact has been established, flows of energy and charge are produced. The evolution of the two halves continue according to the Hamiltonian of the physical system under consideration.
- After a long time, relaxation occurs and the flows described above are expected to reach a steady regime, at least in a neighbourhood of the contact point.

Now, following the discussion in [13], we will give a qualitative (yet detailed) description of the whole process when the system under consideration is characterised by a $(1 + 1)$ dimensional conformal field theory. The principal characteristic of $(1 + 1)$ dimensional CFTs is the so-called chiral separation, namely the property according to which emergent quanta of energy or charge may only be either right-movers or left-movers, independent of each other. Moreover their dynamics is trivialised as waves with speeds $\pm v_F$ given by the Fermi velocity of the underlying critical model. One may introduce the mean free path l_e which is the typical distance a particle travels between successive collisions. These collisions yield to momentum relaxation time τ_e with

$$\tau_e = \frac{l_e}{v_f}. \tag{2.82}$$

When the two sub-systems are put into contact, a ballistic, wave-like flow, transporting energy and charge, from one reservoir to the other, occurs. The fronts of these independent waves propagate at the Fermi velocity and they delimitate a domain in which the flow is stable: a Non Equilibrium Steady State (NESS) is produced. At a time t the size of such domain is approximately $2v_F t$, so in order to observe steady behaviours, the size of the observables ℓ_{obs} has to be smaller. Since there is no delay between the

connection and the emergence of the NESS, we have shock fronts propagating along the fronts of the waves, which induce a discontinuity in the expected values of energy and charge. Other observables don't present this behaviour and are in general smooth.

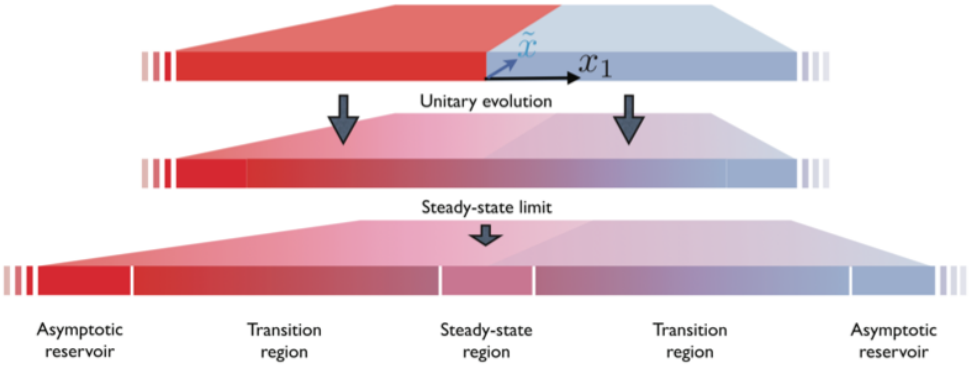

Figure 2.3: Graphic representation of the light cone evolution performed by the system in the Riemann problem. Figure taken from [13].

We can picture the evolution of the system as being described by a light cone (see Fig. 2.3): at large distances we have two reservoirs in which the system state is a Gibbs state, the boundaries of the light cone are represented by shock waves and inside the light cone we have NESS. Since half of the energy is carried by the left-movers and the other half by the right movers, we have the following relation, valid at $\xi = 0$, for the total mean energy density in the NESS [13]:

$$\langle h \rangle_{\text{ness}} = \frac{c\pi}{12} \left(\beta_L^{-2} + \beta_R^{-2} \right), \quad \xi = 0, \tag{2.83}$$

and, if $\beta_L \neq \beta_R$, we have also a non zero mean energy current, given by:

$$\langle j \rangle_{\text{ness}} = \frac{c\pi}{12} \left(\beta_L^{-2} - \beta_R^{-2} \right), \quad \xi = 0. \tag{2.84}$$

We observe that these equations do not depend on the value of the Fermi velocity, thus fully displaying the universality of the result. The previous description is exact if the model under consideration is precisely at the critical point (described by a CFT) and since CFTs are valid only in the low-energy regime, we have to take into account two effects. The first one occurs at microscopic time scales: in fact, when the two sub-systems are put into contact, a very large amount of energy is injected into the system. In principle this discontinuity should break the CFT description (as well as the chiral factorisation), but the decoherence of such process quickly dampens its effects.

This potential issue is therefore invisible at the large time scales of NESS. The second effect is simply related to the fact that in both the sub-systems the temperatures are finite. This should be in contrast with the assumptions of CFT, but, it turns out that even for perturbed CFTs, the previous description remains valid at mesoscopic scales and for times shorter than the momentum relaxation time τ_e. For $t > \tau_e$, the shock fronts become smoother as time increases and a crossover from ballistic transport to diffusive transport occurs inside the light cone domain. At times much larger than τ_e full equilibration and thermalisation is expected provided that the size of the system is finite. An exception of the latter behaviour may take place in integrable models. In fact, the presence of parity-odd conserved quantities that overlap with the energy current, may guarantee the stability of dressed right/left-moving energy quanta. In such a case, even in the diffusive regime, thermalisation may never occur (see [9]) and the steady flows may always exist.

Let us now turn to a quantitative description of the problem. First we observe that the Euler equation (2.81) is invariant under a rescaling of the spacetime coordinates. This implies that its solutions must depend only on the ratio $x/t = \xi$ (i.e. they are constant on each light-cone "ray"). Secondly, we will choose the occupation functions $n(\theta)$ to fully characterise the states of the system. Since those functions represent the normal modes of the GHD, they identify a privileged frame in which the Euler equation assumes the simplified form (3.61). With these considerations, the Riemann problem can be translated into the equations:

$$\left(v^{\text{eff}}(\theta) - \xi\right) \partial_\xi n(\theta, \xi) = 0 \tag{2.85}$$

with boundary conditions:

$$\lim_{\xi \to \pm\infty} n(\theta, \xi) = n^{R/L}(\theta) \tag{2.86}$$

where we denoted with $n^L(\theta)$ and $n^R(\theta)$ the occupation functions corresponding to the initial thermal states with inverse temperatures β_L and β_R respectively as shown in Fig. 2.4.

We observe that eq.(3.64) is trivially solved by all the occupation functions that are independent on the ray ξ, except for a specific value ξ^*, in which the first term vanishes:

$$v^{\text{eff}}\ (\theta^*) = \xi^* = \xi\,(\theta^*) \tag{2.87}$$

Therefore, the solution can be written in terms of Θ step-functions as:

$$n(\theta, \xi) = n^L(\theta)\Theta\left(v^{\text{eff}} - \xi\right) + n^R(\theta)\Theta\left(\xi - v^{\text{eff}}\right) \tag{2.88}$$

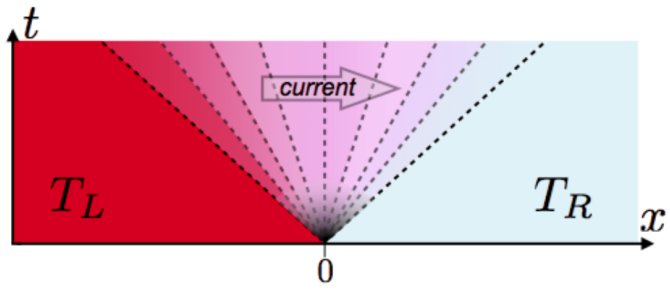

Figure 2.4: The partitioning protocol with two reservoirs at temperaturs $T_{L/R} = \beta_{L/R}^{-1}$. With ballistic transport, a current emerges after a transient period. Dotted lines represent different values of $\xi = x/t$. If a maximal velocity exists initial reservoirs are unaffected beyond it (light-cone effect). The steady state lies at $\xi = 0$ [50].

and, when $v^{\text{eff}}(\theta)$ is a monotonously increasing function of θ for all ξ, we have:

$$n(\theta, \xi) = n^L(\theta)\Theta(\theta - \theta^*) + n^R(\theta)\Theta(\theta - \theta^*) \tag{2.89}$$

The physical interpretation of this solution is clear: due to the two-body elastic scattering, quasi-particles propagate at the effective velocity v^{eff}. They carry, along the ray ξ, information of the left reservoir if their velocity is greater than ξ, otherwise they carry information of the right reservoir. Once the solution $n(\theta)$ is determined, the average values of the energy density and current are given by the relations (2.70) and (2.76).

3

The Staircase Model: Massless Flows and Hydrodynamics

GHD framework has been generalised in many ways to adapt to increasingly complex physical situations such as force terms [68–70], diffusive and higher corrections [55, 71–73], noise [74] and integrability-breaking terms [75–77]. It has been shown to be superior to conventional hydrodynamics in describing the results of experiments on an atom chip [78] and to qualitatively reproduce the phenomenology of Newton's cradle experiment [79]. Impressive as these developments are, an aspect of the original formalism that has only become apparent recently is that, even when used in equilibrium situations, the hydrodynamic picture sheds new light into the physics of IQFTs. Put another way, well-known equilibrium features can be analysed from a different viewpoint by looking at hydrodynamic functions, such as the effective velocities of quasi-particles. This has become apparent in two recent studies of IQFTs with unstable particles in their spectrum [80, 81]. These studies have shown that the presence of unstable particles in the theory, even if they are not part of the asymptotic particle spectrum, leads to recognisable signatures in the effective velocity profile and particle density of their stable constituents. One may for instance identify a particle density ascribable to the unstable particles.

In this chapter we apply GHD to the study of the staircase model (SM), introduced by Al. B. Zamolodchikov [82] by generalising the sinh-Gordon IQFT scattering matrix. The SM has features which make it comparable to the model studied in [80, 81]. Namely, similar to the case of unstable particles, the two-body scattering matrix of the theory has poles in the unphysical sheet and the presence of these extra poles has an enormous effect on the physics of the theory. In particular, the monotonicity properties of typical hydrodynamic quantities such as the effective velocity are markedly different from those

of any model studied so far and, as is typical of the model, are heavily influenced by the interplay between the value of a coupling θ_0 and the value of the temperature (in a Gibbs ensemble) or temperatures (in the partitioning protocol set-up). Various generalizations of the SM construction were proposed in [83–87].

This chapter is organised as follows: In Sec. 3.1 we introduce the SM and its TBA structure. In Sec. 3.2 we investigate several hydrodynamic quantities in the SM at equilibrium and identify unique features associated to this model: the spectral particle density and spectral particle current have generally many local maxima while the effective velocity displays intricate square-wave patterns [88]. We present an explanation of these properties based on the $\mathcal{M}A_k^{(+)}$ model, which provides an effective description of massless flows between consecutive unitary minimal models. In Sec. 3.3 we extend our investigation to the out-of-equilibrium situation where we consider the partitioning protocol and compute higher spin currents and densities. In Appendix A we review some standard results for the SM following the derivations presented in [84, 85]. In particular, we present the constant TBA analysis that allows us to obtain equations for the height of individual plateaux of the TBA L-functions and derive the central charges of unitary minimal models. In Appendix B we present an explicit computation of higher spin currents in CFT as derived from a thermal TBA in the Ising model. We see that even for such a simple theory, the dependence on spin is relatively intricate.

3.1 The Staircase Model

3.1.1 The Model

The staircase model is constructed starting with the sinh-Gordon model. The sinh-Gordon model is the simplest interacting IQFT in one spatial dimension. It is defined by the Lagrangian [89, 90]:

$$\mathcal{L}_{\text{shG}} = \frac{1}{2}(\partial_\mu \phi)^2 - \frac{m^2}{g^2}\cosh(g\phi), \tag{3.1}$$

where ϕ is the bosonic sinh-Gordon field, m is the bare mass of the single particle in the spectrum and g is the coupling constant. The two-particle scattering matrix associated to this model is given by [91–93]

$$S(\theta) = \frac{\tanh\frac{1}{2}\left(\theta - \frac{\mathrm{i}\pi B}{2}\right)}{\tanh\frac{1}{2}\left(\theta + \frac{\mathrm{i}\pi B}{2}\right)}. \tag{3.2}$$

The parameter $B \in [0, 2]$ is the effective coupling constant which is related to the coupling constant g in the lagrangian by

$$B(g) = \frac{2g^2}{8\pi + g^2}. \tag{3.3}$$

The S-matrix is obviously invariant under the transformation $B \mapsto 2 - B$, a symmetry which is also referred to as weak-strong coupling duality, as it corresponds to $B(g) \to B(g^{-1})$ in (3.3). The point $B = 1$ is known as the self-dual point.

In [82] it was observed that when analytically continuing the coupling constant B from the self-dual point to the complex plane via the transformation

$$B \mapsto 1 + i\frac{2\theta_0}{\pi} \qquad \text{with} \qquad \theta_0 \in \mathbb{R}^+, \tag{3.4}$$

the resulting scattering matrix

$$S(\theta) = \tanh\frac{1}{2}\left(\theta - \theta_0 - \frac{i\pi}{2}\right)\tanh\frac{1}{2}\left(\theta + \theta_0 - \frac{i\pi}{2}\right), \tag{3.5}$$

still satisfies all physical requirements, such as unitarity and crossing, while being distinct from the sinh-Gordon S-matrix. In particular, it has poles in the unphysical sheet at $\theta = \pm\theta_0 - \frac{i\pi}{2}$. In order to investigate the properties of this new theory, the paper [82] carried out a detailed TBA study of the model and discovered several unusual features. These observations were later generalised to the whole family of affine Toda field theories[84, 85], of which the sinh-Gordon model is the simplest example. We review the key ideas in the next subsection.

3.1.2 Thermodynamic Bethe Ansatz and Scaling Function

The TBA approach provides a description of IQFTs at finite temperature [62–64] as introduced in section 2.2. This description can be easily generalised to GGEs, as discussed in [94] (even though the generalisation had already been used in [95]). The TBA equations describing the SM at thermal equilibrium take a very simple form. In fact, given that there is a single particle in the theory and that scattering is diagonal, there is a single equation to start with. The non-trivial interaction that is present in the model enters the TBA equation through the kernel or two-body scattering phase $\varphi(\theta)$ which is defined as

$$\varphi(\theta) = -i\frac{d}{d\theta}\ln S(\theta) = \frac{1}{\cosh(\theta - \theta_0)} + \frac{1}{\cosh(\theta + \theta_0)}. \tag{3.6}$$

This is a function that is peaked around $\theta = \pm\theta_0$. This means that interaction is maximal when the rapidity difference between interacting particles takes these values and greatly reduced otherwise. This feature plays a key role in the shape of some of the functions we will study later in the paper, specially the spectral particle density and spectral particle current.

We recall that for finite temperature $T = 1/\beta$ the pseudoenergies $\varepsilon(\theta)$ satisfy the nonlinear integral equation (TBA-equation)

$$\varepsilon(\theta) = \beta \cosh\theta - (\varphi \star L)(\theta), \tag{3.7}$$

where we have taken the mass $m = 1$ and $\star$ denotes the rapidity convolution

$$(\varphi \star L)(\theta) = \frac{1}{2\pi} \int d\theta' \varphi(\theta - \theta') L(\theta'). \tag{3.8}$$

Since $S(0) = -1$ the TBA system is of fermionic type [62–64] and therefore

$$L = \ln\bigl(1 + e^{-\varepsilon(\theta)}\bigr). \tag{3.9}$$

The ground state energy is given by

$$E(\beta) = -\frac{1}{2\pi} \int L(\theta) \cosh\theta \, d\theta = -\frac{\pi c(y)}{6\beta}, \tag{3.10}$$

where $c(y)$ is the TBA scaling function introduced by (2.59) and

$$y = \ln \frac{2}{\beta} \tag{3.11}$$

is a new, more convenient variable in terms of which the infrared (IR) or low temperature limit corresponds to $y \to -\infty$ and the ultraviolet (UV) or high temperature limit corresponds to $y \to \infty$. The scaling function flows from the UV value $c(\infty) = 1$ corresponding to the central charge of a free massless boson, to the IR value $c(-\infty) = 0$. So far, this behaviour is identical to that of the sinh-Gordon theory. The unusual features of the model become only apparent when the dependence of the L-function and the scaling function on the parameter θ_0 is explored in detail. These have been discussed in the original paper [82] and in [84, 85] but it is worth recalling the main ideas, as they will play a role in the hydrodynamic picture.

Let us examine the change in the function $L(\theta)$ as we increase y towards the deep UV regime. We take $\theta_0 \gg 1$ in order to have two well separated bumps in the kernel (3.6). We have the following regimes:

- For $y > 0$, $L(\theta)$ develops a plateau of height $\ln 2$ in the region $-y < \theta < y$, that is the usual free fermion UV behaviour. As y increases the plateau broadens. At the same time, the scaling functions $c(y)$ reaches the value $c = 1/2$ corresponding to a massless free fermion or the Ising model. This is the first of the series of unitary minimal models and we denote it by $\mathcal{M}_3$ for reasons that become clear below. This L-function is shown in the top-right of Fig. 3.5.

- When y reaches the value $\theta_0/2$, the plateau's edges start interacting via the kernel in equation (3.7). The interaction can be described by two separate interacting integral equations for two separate pseudoenergies $\varepsilon_\pm(\theta) = \varepsilon(\theta \pm \frac{\theta_0}{2})$. The resulting system coincides with the description of the massless flow between the critical ($\mathcal{M}_3$) and tricritical ($\mathcal{M}_4$) Ising models given in [96]. This relation is explored in later sections. As y increases the scaling function grows from $c = 1/2$ to $c = 7/10$, as expected, while the L-function develops two higher plateaux at values $2\ln\big(2\cos\frac{\pi}{5}\big)$, which rise above the main plateau at $\ln 2$. This L-function is shown in the top-right of Fig. 3.6. This specific flow has also being studied using form factor techniques in [97].

- Similarly, when y reaches θ_0 we have a new transition from $c = 7/10$ to $c = 4/5$ which again describes the massless flow between two unitary minimal models, in this case the tricritical and the tetracritical Ising model ($\mathcal{M}_5$). This L-function is shown in the top-right of Fig. 3.7.

- In general, every time $y \sim k\theta_0/2$, with $k = 1, 2, 3, \ldots$ the scaling function flows (or roams) from the value

$$c_{k+2} = 1 - \frac{6}{(k+2)(k+3)}, \qquad k = 1, 2, \ldots \tag{3.12}$$

  that is, the central charge of $\mathcal{M}_{k+2}$, to the value c_{k+3} corresponding to $\mathcal{M}_{k+3}$. Simultaneously, the L-function acquires new plateaux, emerging symmetrically in θ in pairs. In summary, for $\theta_0 \gg 1$ the function $c(y)$ exhibits a staircase behaviour roaming through the value c_{k+2} inside every interval $(k-1)\theta_0/2 < y < k\theta_0/2$ and finally settling on the UV value $c = \lim_{k\to\infty} c_k = 1$. The scaling function $c(y)$ is depicted in Fig. 3.1 for three different values of the parameter θ_0.

The values (3.12) are not only observed numerically when evaluating $c(y)$ through the definition (3.10), but they can also be obtained analytically by studying the constant TBA system associated with the SM. That is, the set of TBA equations that are obtained in the UV limit. This is discussed in detail in Appendix A.

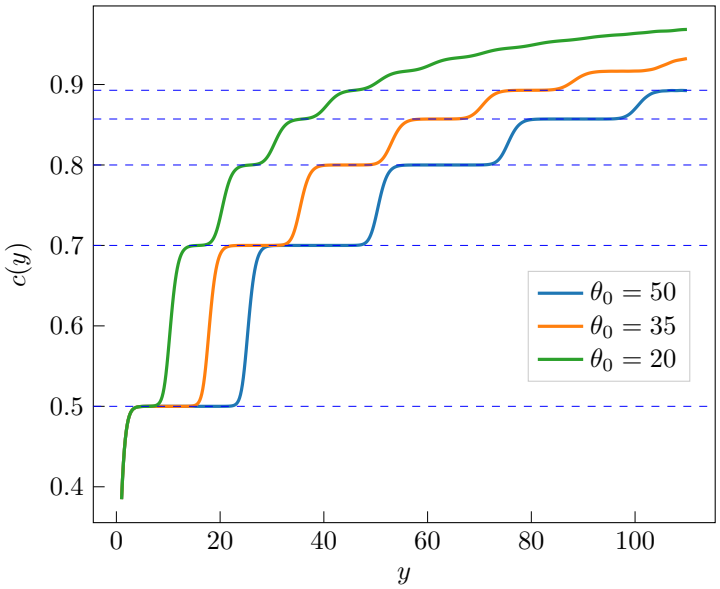

Figure 3.1: Scaling function of the SM for $\theta_0 = 20, 35, 50$. The central charges c_{k+2} (dashed horizontal lines for $k = 1, 2, 3, 4, 5$) are approached by $c(y)$ at different values of y, as the crossover points are at $y \sim k\theta_0/2$.

3.1.3 $\mathcal{M}A_k^{(+)}$ Massless Flows

As we have seen, the SM is associated with an RG flow which visits the vicinity of all unitary minimal models. In particular, each pair of successive fixed points $\mathcal{M}_{k+2}$ and $\mathcal{M}_{k+1}$ are connected by RG trajectories corresponding to a massless interpolating field theory whose UV limit is $\mathcal{M}_{k+2}$, while the IR limit is controlled by $\mathcal{M}_{k+1}$. The associated RG flow is generated from the UV fixed point by perturbing with the relevant operator Φ_{13} and negative coupling [96, 98, 99]. More details can be found at this end of this Section.

Much as the example discussed earlier of the flow between critical and tricritical Ising, which can be described by a pair of TBA equations for shifted pseudoenergies, the interpolating flow between generic fixed points $\mathcal{M}_{k+2}$ and $\mathcal{M}_{k+1}$ can be described by a set of TBA equations associated with the A_k Dynkin diagram [96, 98, 99].
They take the form

$$\varepsilon_i(\theta) = \omega_i(\theta) - \sum_{j=1}^{k} (\hat{\varphi}_{ij} \star L_j)(\theta) \qquad \text{with} \qquad \hat{\varphi}_{ij}(\theta) = \frac{I_{ij}}{\cosh\theta} \tag{3.13}$$

and $I_{ij} = \delta_{i,j+1} + \delta_{i,j-1}$ is the adjacency matrix of the A_k algebra (see Fig. 3.2). The

driving terms $\omega_i(\theta)$ are given by

$$\omega_i(\theta) = \frac{\beta}{2}(e^{-\theta}\delta_{i,1} + e^{\theta}\delta_{i,k}). \tag{3.14}$$

Note that the driving terms associated to nodes 1 and k are usually exchanged in the literature, but this is a more suitable prescription in order to relate the $\mathcal{M}A_k^{(+)}$ model to the SM.

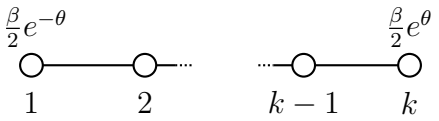

Figure 3.2: A_k Dynkin diagram showing driving terms associated to the massless TBA (3.13).

In the $\mathcal{M}A_k^{(+)}$ model, each node in the Dynkin diagram and each TBA equation can be interpreted as associated to a different particle species, with non-trivial scattering only between nearest neighbouring nodes. Only two nodes in the Dynkin diagrams couple to non-vanishing driving terms. The source terms $\frac{\beta}{2}e^{\pm\theta}$ correspond to right- and left-moving i.e. (RM) and (LM) particles, whose one-particle energy and momentum are

$$e_\pm(\theta) = e^{\pm\theta - y} \quad \text{and} \quad p_\pm(\theta) = \pm e^{\pm\theta - y}\,, \tag{3.15}$$

respectively (y is the variable defined in (3.11)). The other nodes in the Dynkin diagram correspond to magnons, which describe internal degrees of freedom of the quasi-particle excitations. It is important to note that although the magnonic excitations themselves may be regarded as quasi-particles, they have zero one-particle eigenvalues with respect to the conserved charge operators, hence quantities such as the energy or momentum are carried only by the RM and LM species. In particular the scaling function

$$c(y) = \frac{3\beta}{\pi^2}\sum_{j=1}^{k}\int_{-\infty}^{\infty} d\theta\, p_j'(\theta)L_j(\theta)\,, \tag{3.16}$$

only receives equal contributions from the LM and RM. A GHD study of this and other massless theories was carried out in [100].

It is worth saying a little more about the origins of this massless model. The $\mathcal{M}A_k^{(+)}$ models can be seen as perturbations of $\mathcal{M}_{k+2}$ by the field Φ_{13} ($k = 1, 2, 3\ldots$). There are however two families of theories with different properties depending on whether or not the perturbing parameter is positive. These two families were named $\mathcal{M}A_k^{(\pm)}$ in [98].

The family $\mathcal{M}A_k^{(-)}$ is massive, and the S-matrix has been written by various authors [98, 101, 102]. It corresponds to a restriction of the sine-Gordon model (that is, the

sine-Gordon model at a specific k-dependent value of the coupling constant) which is also related to the restricted solid-on-solid $(\mathrm{RSOS})_k$ lattice models. The scattering in these theories is non-diagonal but the associated TBA system can be diagonalised resulting into an A_k-based system of k TBA equations where the driving terms are $\omega_1(\theta) = \cosh\theta$, $\omega_i(\theta) = 0$ for $i > 1$. Thus the A_k-system in this case describes a massive particle and $k-1$ magnons.

The perturbation of interest in the context of the SM is $\mathcal{M}A_k^{(+)}$ which was studied in [96]. These models are massless (although non conformal, there is a fundamental scale in the theory) and describe a crossover between the unitary minimal models $\mathcal{M}_{k+2}$ and $\mathcal{M}_{k+1}$. This flow was studied perturbatively for large k some years before [103, 104]. The TBA description which was then conjectured is given by the equations (3.13).

3.1.4 SM L-function from the $\mathcal{M}A_k^{(+)}$ Model

A remarkable feature of the effective description of massless flows provided by the $\mathcal{M}A_k^{(+)}$ model is that it is possible to carry out both a quantitative and qualitative comparison between solutions of (3.7) and (3.13) by introducing ad hoc shifts (in θ space) of the solutions of (3.13). This procedure amounts to "cutting an pasting" the solutions for the L-functions of the $\mathcal{M}A_k^{(+)}$ model in such a way as to reproduce the SM L-function corresponding to a fixed finite value of the dimensionless parameter α defined by

$$\alpha = \frac{y}{\theta_0}, \qquad \text{for } y, \theta_0 \to \infty. \tag{3.17}$$

An illustration of this approach is presented in Fig. 3.3. As can be seen in the example, such engineered L-function clearly matches the L-function structure of the SM for $\frac{1}{2} < \alpha < 1$.

This procedure allows us to see each step of the scaling function of the SM as two different limits, encoded in the two sets of decoupled equations (A.13) for the values of the pseudoenergy at the centres of the plateaux found in Appendix A: if the RG trajectory flows very close to the fixed point $\mathcal{M}_{k+2}$, the latter can be seen both as the UV limit of the A_k flow and as the IR limit of the A_{k+1} flow of the massless TBA (3.13). This is illustrated in Fig. 3.4.

3.2 The SM at Equilibrium

Let us now solve the TBA-equation for the SM at some inverse temperature β, obtain $n(\theta)$ and compute from this the quantities:

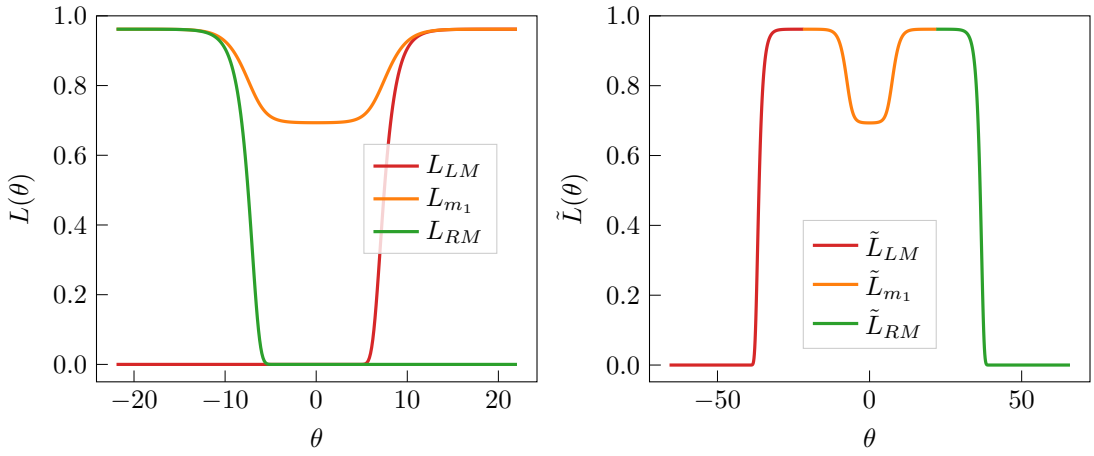

Figure 3.3: *Left*: L-functions for the $\mathcal{M}A_3^{(+)}$ model, showing solutions for three functions corresponding to the RM, the LM and the magnon. *Right*: Same functions shifted in rapidity space to reconstruct the single L-function of the SM.

$$\begin{aligned} \rho_p(\theta) &= e^{\mathrm{dr}}(\theta) n(\theta) && \text{spectral particle density,} \\ v^{\mathrm{eff}}(\theta) &= \frac{(e')^{\mathrm{dr}}(\theta)}{(p')^{\mathrm{dr}}(\theta)} && \text{effective velocity,} \\ \rho_c(\theta) &= \rho_p(\theta) v^{\mathrm{eff}}(\theta) && \text{spectral particle current.} \end{aligned} \tag{3.18}$$

As expected, the form of these functions, similar to the L-functions, will very much depend on the parameter α defined by (3.17). This is illustrated in Figs. 3.5, 3.6, 3.7 and 3.8, all of which show the scaling function (highlighting one specific temperature) and the L-function, spectral particle density, spectral particle current and effective velocity for the same temperature.

Sitting on a step of the scaling function defined by an integer k such that $\frac{k-1}{2} < \alpha < \frac{k}{2}$, the L-function has $2k$ kinks. At the same positions, the spectral particle density and spectral particle current exhibit $2k$ bumps (local maxima). Except for two outer-most bumps which are centered around $\pm y$, all other bumps are centered at values of θ whose distance from one of the outer-most bumps is a multiple of θ_0. This is due to the structure of the scattering phase which maximises interaction precisely for such distances. Thus, from a scattering viewpoint, we can think of each pair of peaks of the spectral particle density whose mutual distance is θ_0 as describing densities of mutually interacting particles. In fact, it is this interaction that makes the particle density increase with respect to the non-interacting (free fermion) case shown in Fig. 3.5. A similar structure was found in [80]. In all figures for this section we have introduced

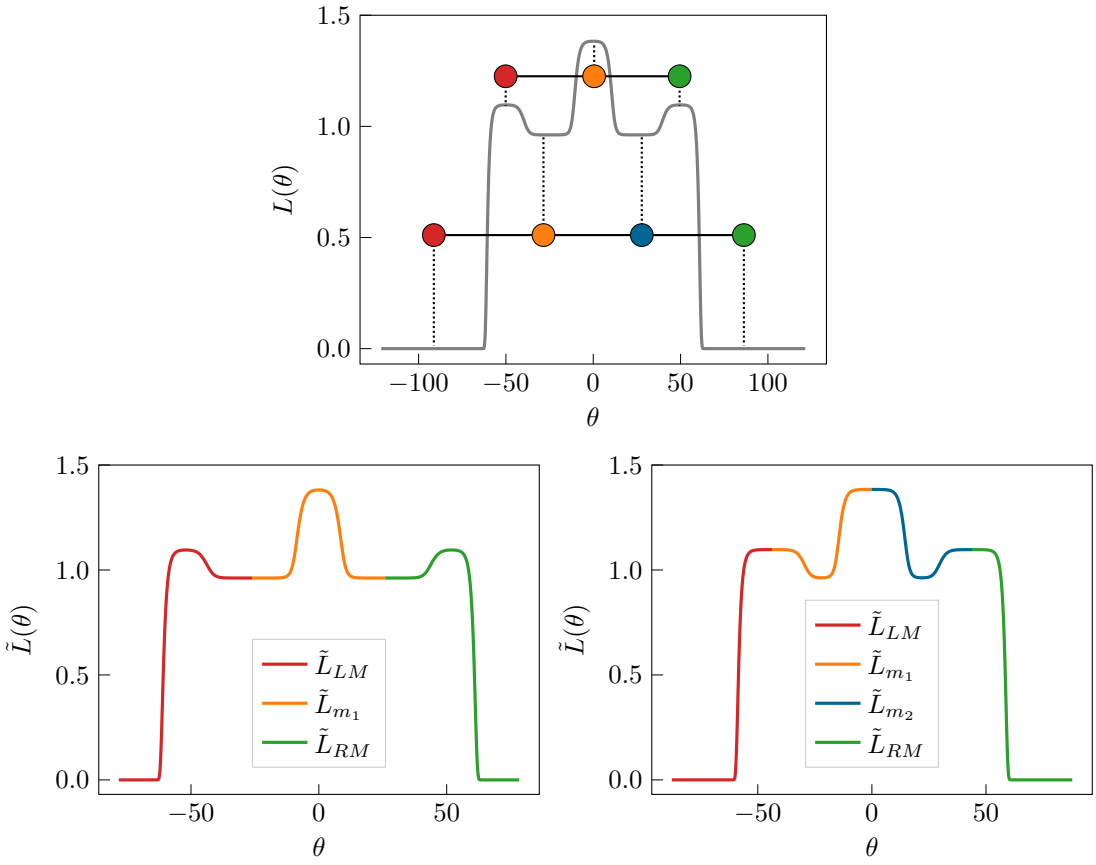

Figure 3.4: *Top*: L-function of the SM for $1 < \alpha < 3/2$ ($k = 3$) highlighting the $2k + 1 = 7$ plateaux' mid-points z_i and $2k$ kinks K_i as discussed in Appendix A. *Bottom, Left*: L-functions of the $\mathcal{M}A_3^{(+)}$ model in the UV limit, reproducing the odd-labelled plateaux of the SM model and matching the colour scheme of the top panel. *Bottom, Right*: L-functions of the $\mathcal{M}A_4^{(+)}$ model in the IR limit, reproducing the even-labelled plateaux of the SM model and matching the colour scheme of the top panel.

the convenient definitions:

$$\tilde{\rho}_{p/c}(\theta) = \frac{\rho_{p/c}(\theta)}{\max \rho_{p/c}(\theta)}\,, \tag{3.19}$$

which are the scaled spectral particle density (p) and current (c).

A simple example of this phenomenology is provided in Fig. 3.6. Here the two pairs of bumps centered at $\pm y$ and $\pm(y - \theta_0)$ describe densities of particles that are mutually interacting and also co-moving, as their effective velocities are the same.

Following the considerations of [80], if we actually compute the particle density associated to one of the larger maxima (say the right-most peak centered at $\theta = y$) and subtract from it the density associated with the corresponding peak of a free fermion

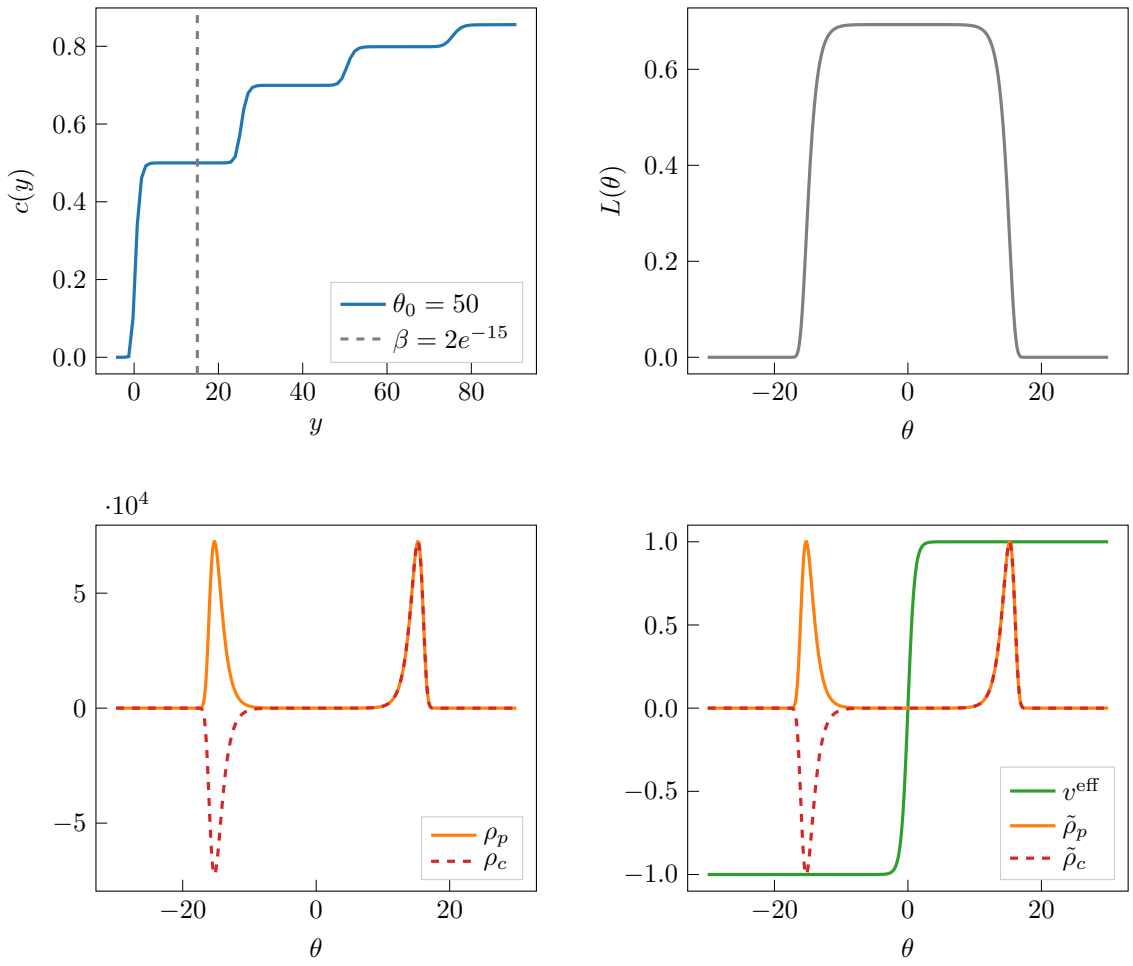

Figure 3.5: Free fermion regime for $k = 1$. *Top*: Scaling function and L-function for $\beta = 2e^{-15}$ and $\theta_0 = 50$, hence $\alpha = 3/10 < \frac{1}{2}$. *Bottom Left*: Spectral density (solid orange line) and spectral particle current (dashed red line). *Bottom Right*: Effective velocity (green) versus scaled spectral particle functions $\tilde{\rho}_{p/c}(\theta)$. Since we are in the free fermion regime, the effective velocity is simply $\tanh\theta$ and the spectral particle densities exhibit two separate bumps corresponding to equal densities of right- and left-moving fermions.

solution at the same temperature, we find that the difference exactly matches the area of the smaller peak centered at $\theta = y - \theta_0$. We can say that the increase in the particle density with respect to the free theory is directly linked to the interaction with a smaller density of particles at distance θ_0 in phase space. In other words, we can identify a stable density of interacting particles corresponding exactly to the area of the smaller peak. These particles are both interacting and co-moving as the two peaks of the spectral density also correspond to the same effective velocities (+1 in this example).

The situation is similar but a bit more complicated in Figs. 3.7 and 3.8. For instance,

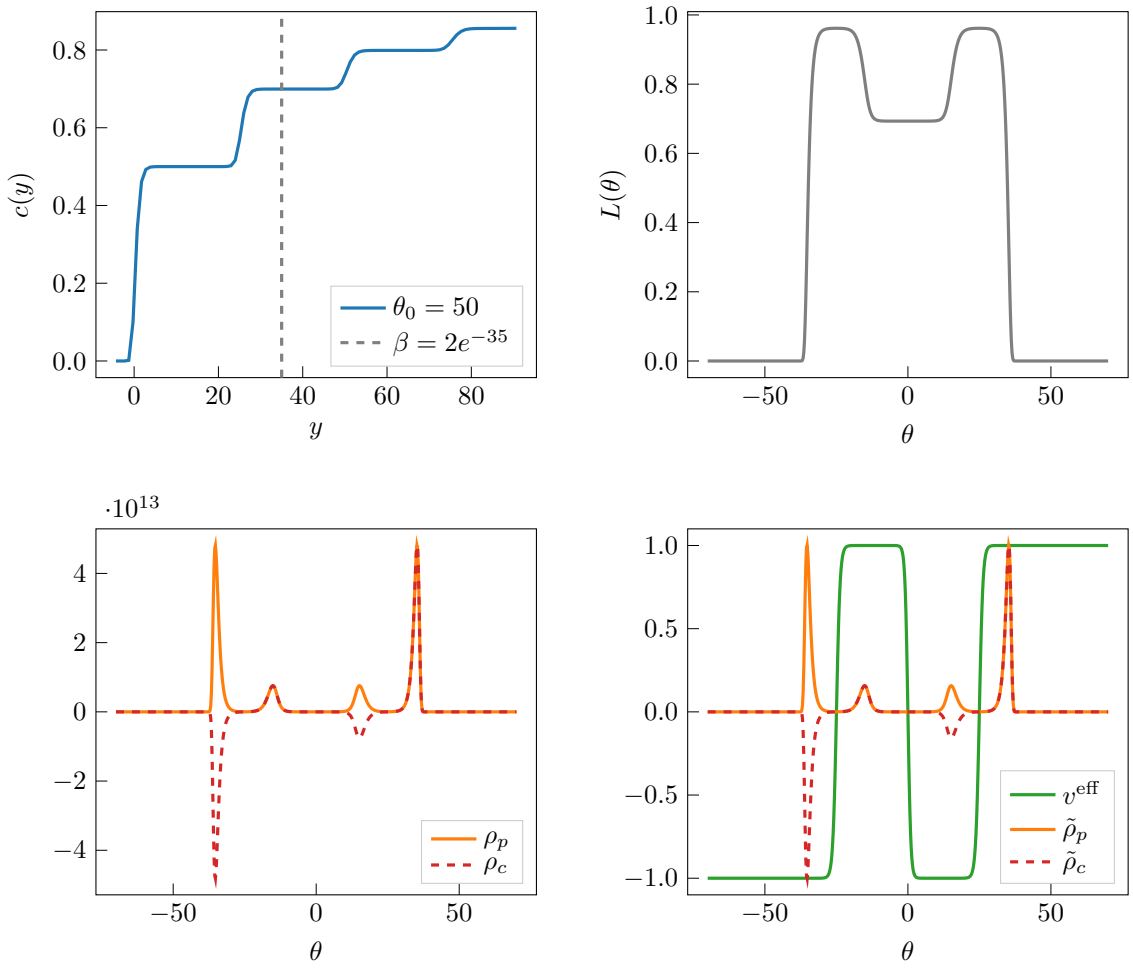

Figure 3.6: Tricritical Ising for $k = 2$: *Top*: Scaling function and L-function for $\beta = 2e^{-35}$ and $\theta_0 = 50$, hence $\frac{1}{2} < \alpha = 7/10 < 1$. *Bottom Left*: Spectral density (solid orange line) and spectral particle current (dashed red line). *Bottom Right*: Effective velocity (green) versus scaled spectral particle functions (3.19). Note that the effective velocity is now non-monotonic and has $2k - 1 = 3$ zeroes.

in Fig. 3.7 the spectral particle density and current have six local maxima, which can be seen as describing three pairs of densities of mutually interacting particles centered around $\pm y$, $\pm(y-\theta_0)$ and $\pm(y-2\theta_0)$. Again, interacting particles are associated with a fixed increase in particle density and are in all cases co-moving so that they can be easily identified by following the twists and turns of the effective velocity profile. Once more, the increase in the particle density can be attributed to interaction. This can be quantified by comparing the particle density associated to one of the larger maxima, say at $\theta = y$, with that of the same peak in the free fermion spectral particle density at the same temperature. The difference in areas coincides with the combined areas of peaks at $y-\theta_0$ and $y-2\theta_0$, both of which are mutually interacting with each other. Reflecting the interaction structure of the $\mathcal{M}A_3^{(+)}$ model, the peak at $y-\theta_0$ also interacts with the one at y.

As α is further increased more pairs of these local maxima will emerge, until infinitely many are present in the deep UV limit. This behaviour is similar but distinct from what is observed in the $SU(3)_2$-HSG model studied in [80]. The main difference arises from parity breaking in the HSG-model which for each particle type makes interaction maximal for some finite value of θ but not for its opposite. The effect of this lack of symmetry is that the spectral particle density of each particle never develops more than three local maxima.

Unlike for the L-functions where a constant TBA analysis allows us to determine the exact height of each plateau, the definition of the effective velocities makes such an analysis difficult. However, their complex structure can be well understood by mapping the SM to the corresponding $\mathcal{M}A_k^{(+)}$ model described in the previous section. In particular we can reinterpret the multiple peaks of the spectral particle densities in terms of the LM, RM and magnonic excitations of the massless theory. This is shown in Fig. 3.9 and 3.10 and is similar in spirit to the reconstruction of the L-function that we saw in Fig. 3.4.

The structure of the effective velocity is far more peculiar. For $k > 1$, $v^{\text{eff}}(\theta)$ becomes strongly non monotonic and develops k plateaux at velocity $v^{\text{eff}}(\theta) = 1$ and the same number at the opposite velocity. The $2k-1$ zeros of $v^{\text{eff}}(\theta)$ are at the midpoints of the L-function's internal plateaux, that is the points z_i given by (A.6). This can be argued from the definitions (3.7) and (2.66), as these imply that

$$\varepsilon'(\theta) = \beta\, p^{\text{dr}}(\theta)\,, \tag{3.20}$$

and therefore the simple zeros of the effective velocity are at the points where $\varepsilon'(\theta)$ (and therefore $L'(\theta)$) vanishes. See Fig. 3.5, Fig. 3.6, Fig. 3.7 and Fig. 3.8 for some

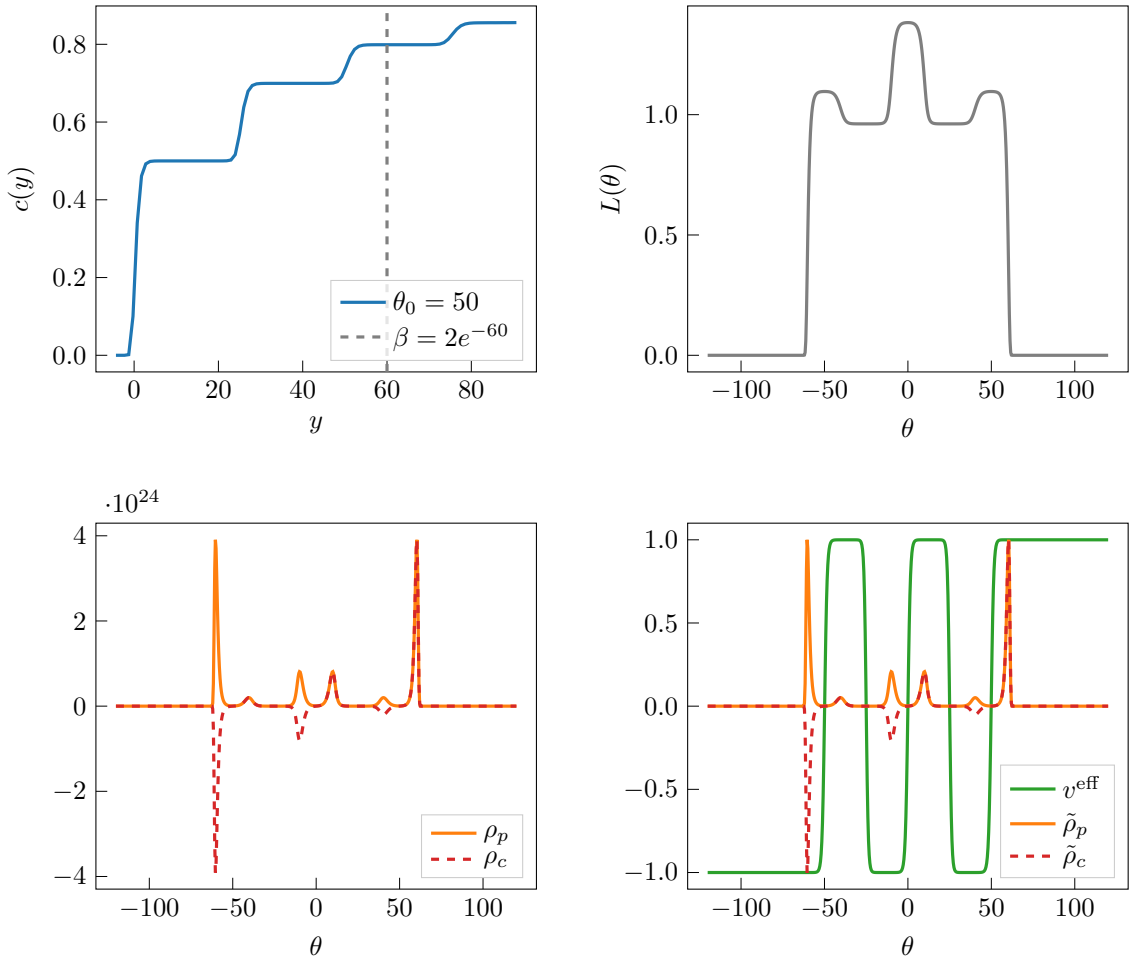

Figure 3.7: Tetracritical Ising model for $k = 3$: *Top*: Scaling function and L-function for $\beta = 2e^{-60}$ and $\theta_0 = 50$, hence $1 < \alpha = \frac{6}{5} < \frac{3}{2}$ *Bottom Left*: Spectral density (solid orange line) and spectral particle current (dashed red line). *Bottom Right*: Effective velocity (green) versus scaled spectral particle functions (3.19). The effective velocity exhibits three plateaux with $v^{\text{eff}}(\theta) = 1$ and three plateaux with $v^{\text{eff}}(\theta) = -1$. Therefore the effective velocity changes sign at $2k - 1 = 5$ points.

summarising plots.

In Fig. 3.9 and 3.10 we reconstruct the effective velocity of the SM for $k = 2$ and $k = 3$, respectively with the same procedure used for the L-function in section A.2. Notice that both the description as UV limit of the $\mathcal{M}A_2^{(+)}$ and IR limit of the $\mathcal{M}A_3^{(+)}$ model are valid. In the former case we have only two excitations with two peaks each in the spectral particle density; in the latter, LM and RM have only one peak while the others are described by the magnons. Nonetheless, both scenarios are valid and all peaks are at the same values of the effective velocity.

How the intricate features of the spectral particle density, current and effective velocity change with temperature can be best seen in the video [88] which provides a visual summary of all results in this Section.

3.3 SM and the Partitioning Protocol

In Section (2.4) we introduced the main ideas behind the partitioning protocol. In this section we focus on the average currents (2.76) and densities (2.70) for spins $s > 1$. Unlike for the energy current and density studied in [65–67, 105], it is not known precisely how higher spin currents and densities behave in the UV limit. That is, unlike for the energy, there is no existing CFT computation of these quantities. There are however some features that are to be expected at UV fixed points: holomorphic/antiholomorphic factorisation should guarantee a structure involving differences/sums of appropriate powers of the temperatures for the currents/densities and dimensional analysis imposes that such power should be $s+1$ for a spin s current/density. In the absence of a CFT derivation, the present model allows us to study these quantities starting from the GHD equations and considering their UV limit. In this context, the SM is an ideal theory to consider, as we are able to access multiple UV fixed points. A special feature of the SM is that the equation $v^{\text{eff}}(\theta;\xi)$ may have multiple solutions depending on ξ and $\beta_{L/R}$, therefore the function $n(\theta)$ has multiple discontinuities as shown in Fig. 3.11.

3.3.1 Higher Spin Currents and Densities

Consider the one-particle eigenvalues (2.62) and their associated average current and density (2.70) and (2.76) with $n(\theta)$ given by (2.88). We are interested in the non-equilibrium steady state at ray $\xi = 0$ and in the situation in which the left and right subsystem both tend in the UV limit to the same minimal model, that is, defining

$$y_{\text{R}} := \log \frac{2}{\beta_{\text{R}}}\,, \qquad y_{\text{L}} := \log \frac{2}{\beta_{\text{L}}} \qquad \text{and} \qquad \sigma := \frac{\beta_{\text{R}}}{\beta_{\text{L}}}\,, \tag{3.21}$$

we will consider

$$\frac{(k-1)\theta_0}{2} < y_{\text{R}} < y_{\text{L}} < \frac{k\theta_0}{2}, \tag{3.22}$$

that is, $\sigma > 1$. If $y_{\text{L/R}}$ lie in the same range (3.22) and σ is not too large then the occupation functions of the right and left subsystems are very similar and one can numerically check that the zeroes of the effective velocity are still very close to their

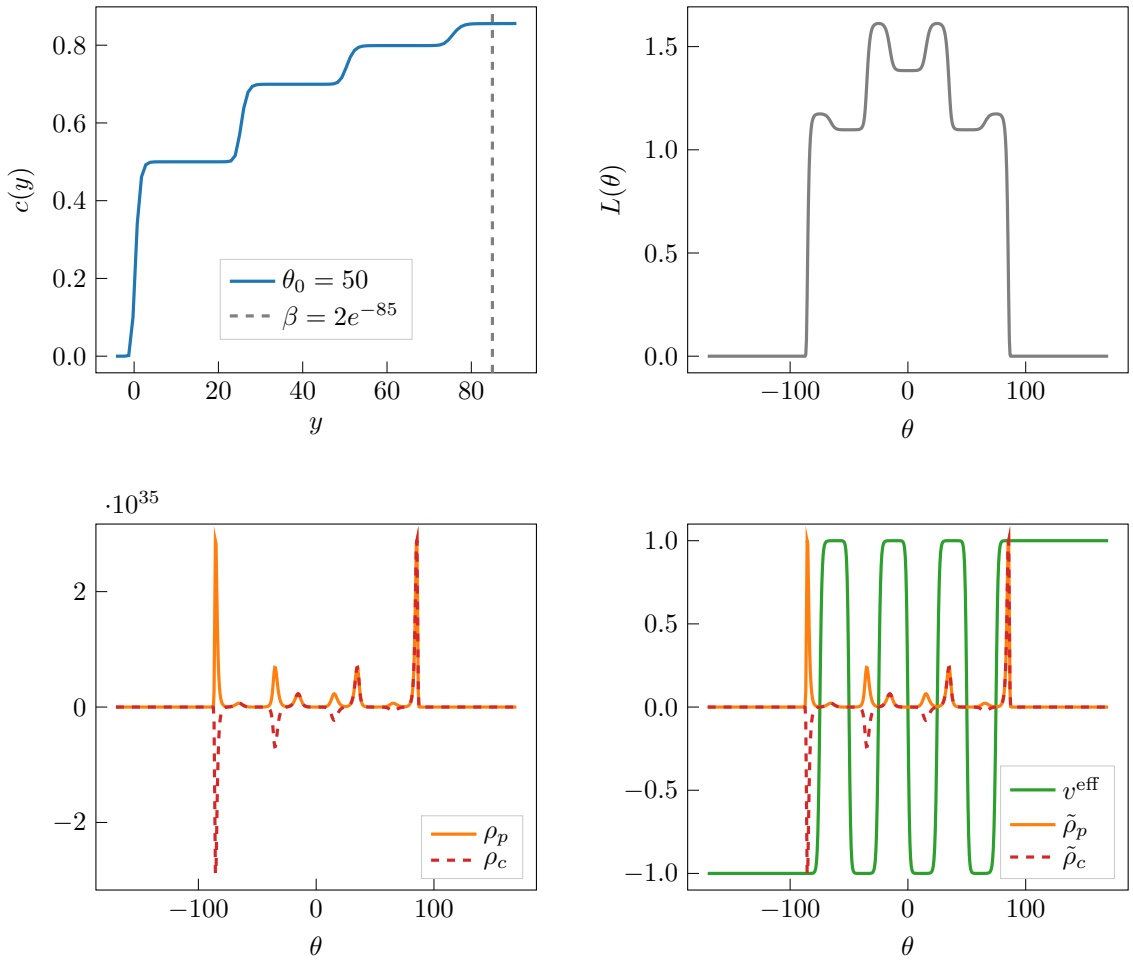

Figure 3.8: Minimal model $\mathcal{M}_6$: *Top*:Scaling function and L-function for $\beta = 2e^{-85}$ and $\theta_0 = 50$, hence $\frac{3}{2} < \alpha = 1.7 < 2$. *Bottom Left*: Spectral density (solid orange line) and spectral particle current (dashed red line). *Bottom Right*: Effective velocity (green) versus scaled spectral particle functions (3.19). As in previous figures, we see that the effective velocity changes sign at $2k - 1 = 7$ points and exhibits eight plateaux at alternating values ± 1.

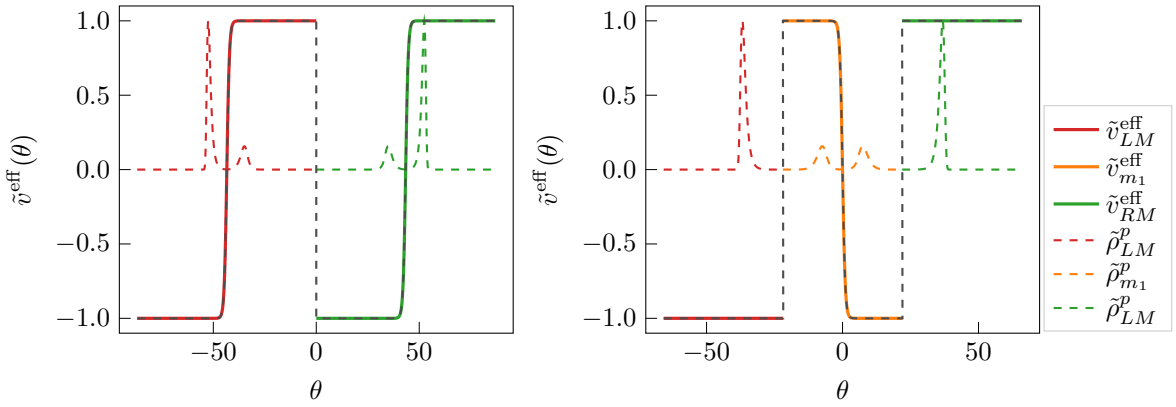

Figure 3.9: Effective velocities and spectral particle density of the $\mathcal{M}A_2^{(+)}$ and $\mathcal{M}A_3^{(+)}$ models shifted according to the analysis in (A.11)-(A.12). *Left*: UV limit of the $\mathcal{M}A_2^{(+)}$ model. We have two bumps of the spectral particle density for the RM and two bumps for the LM. One peak is at $v^{\text{eff}}(\theta) = 1$ (RM) and one at $v^{\text{eff}}(\theta) = -1$ (LM). *Right*: IR limit of the $\mathcal{M}A_3^{(+)}$ model. LM (RM) each have one peak in their spectral particle density at $v^{\text{eff}}(\theta) = \pm 1$, respectively. The single magnon in the theory has two symmetric peaks (these are the two smaller peaks in each figure). The overall effective velocity has the same features as the previous case and both descriptions match qualitatively the SM behaviour. The reconstructed functions reproduce all features of the functions presented in Fig. 3.6 for the case $k = 2$.

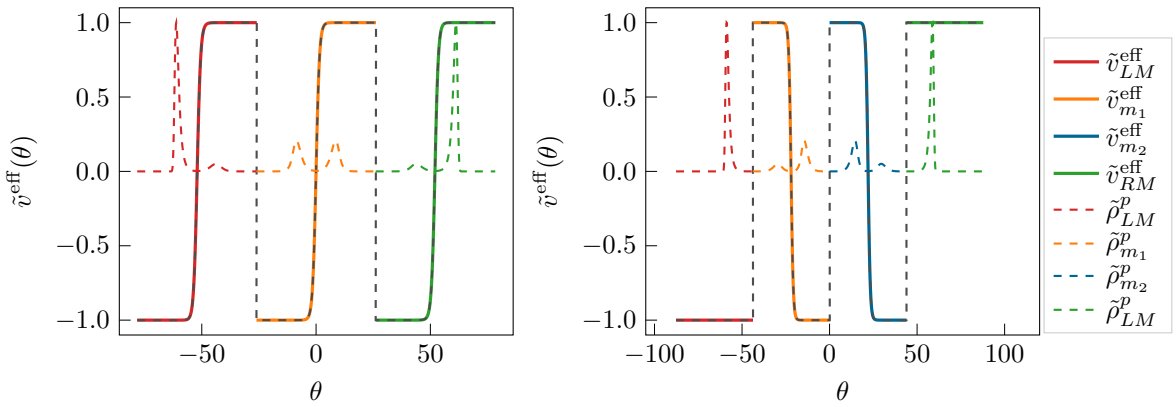

Figure 3.10: Effective velocities and spectral particle density of the $\mathcal{M}A_3^{(+)}$ and $\mathcal{M}A_4^{(+)}$ models shifted according to the analysis in (A.11)-(A.12). *Left*: UV limit of the $\mathcal{M}A_3^{(+)}$ model. We have two bumps of the spectral particle density for each excitation. All peaks (for all excitations) are at $v^{\text{eff}}(\theta) = \pm 1$. *Right*: IR limit of the $\mathcal{M}A_4^{(+)}$ model. The reconstructed functions reproduce all features of the functions presented in Fig. 3.7 for the case $k = 3$.

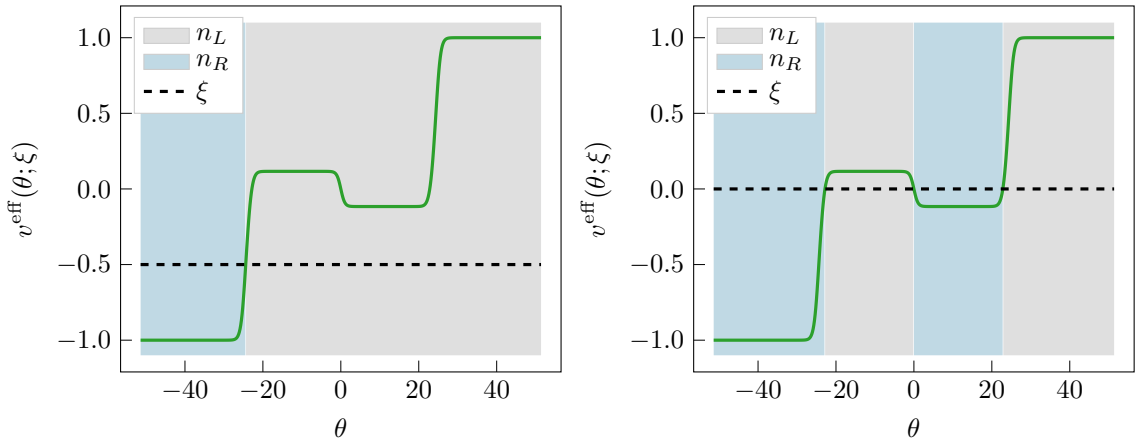

Figure 3.11: A sketch of the effective velocity in the region $\frac{1}{2} < \alpha < 1$ ($k = 2$, second plateau of $c(y)$). As we can see, depending on the ray we can have multiple solutions to $v^{\text{eff}}(\theta;\xi) = \xi$ and every time the velocity changes sign, so does $n(\theta)$ alternate between the right (blue) and left (gray) solutions.

equilibrium values. Given (2.88) we can therefore define the total currents $\mathtt{j}_{2s-1}$ (and $\mathtt{j}_{2s}$) for the joint system as the sum of contributions from the two subsystems:

$$\mathtt{j}_{2s-1} = \mathtt{j}^R_{2s-1} + \mathtt{j}^L_{2s-1}, \tag{3.23}$$

with

$$\mathtt{j}^{L/R}_{2s-1} = \int_{L/R} \frac{d\theta}{2\pi} p^{\text{dr}}(\theta) n_{L/R}(\theta) h_{2s-1}(\theta)\,, \tag{3.24}$$

and integration regions defined by

$$\begin{aligned} R &\equiv]-\infty, z_1] \cup [z_2, z_3] \cup \cdots \cup [z_{2k-2}, z_{2k-1}] \\ L &\equiv [z_1, z_2] \cup [z_3, z_4] \cup \cdots \cup [z_{2k-1}, +\infty[. \end{aligned} \tag{3.25}$$

Now we use the fact that if $\varepsilon_{L/R}(\theta)$ are the solutions of the TBA equations for the two Gibbs ensembles, from (3.20) it follows that

$$\varepsilon'_{L/R}(\theta) = \beta_{L/R}\, p^{\text{dr}}(\theta). \tag{3.26}$$

We emphasise that the dressing of $p(\theta)$ in (3.26) is performed with $n_L(\theta)$ in the left reservoir and with $n_L(\theta)$ in the right one. In contrast, in (3.24) it is the the joint occupation function $n(\theta)$ which enters the definition of the dressing. However, as long as (3.21) holds and σ is small we can assume that also in (3.24) the dressing is performed with $n_{L/R}(\theta)$. This assumption is supported by numerical results.

Therefore, since $\varepsilon'_{L/R}(\theta)n_{L/R}(\theta) = -L'_{L/R}(\theta)$, we have

$$\mathtt{j}^{L/R}_{2s-1} = -\frac{T^{s+1}_{L/R}}{2\pi}\int_R L'_{L/R}(\theta)\beta^s_{R/L}h_{2s-1}(\theta)\,. \tag{3.27}$$

We will see in a few lines why this rewriting of $T_{L/R} = T^{s+1}_{L/R}\beta^s_{L/R}$ is useful. To proceed we can take $\theta_0, y_{R/L} \gg 1$ in order to exploit the correspondence between the SM and the $\mathcal{M}A^{(+)}_k$ model explained in the previous section. In this approximation the expression (3.27) is slightly simpler, and is replaced by the massless limit

$$\begin{aligned}\mathtt{j}^{L}_{2s-1} &= -\frac{T^{s+1}_{L}}{2^{2-s}\pi}\int_{K_{2k}} d\theta\, e^{-s(y_L-\theta)}L'_L(\theta)\\ \mathtt{j}^{R}_{2s-1} &= -\frac{T^{s+1}_{R}}{2^{2-s}\pi}\int_{K_1} d\theta\, e^{-s(y_R+\theta)}L'_R(\theta)\,.\end{aligned} \tag{3.28}$$

The same considerations can be done when considering $\mathtt{j}_{2s}$ and it is straightforward that $\mathtt{j}^L_{2s}$ can be computed with the same expression given in (3.28), while $\mathtt{j}^R_{2s}$ differs from its odd counterpart for an overall sign. Integrating by parts and considering $y_{R,/L}$ sufficiently large, boundary terms vanish (as for large temperature, the L-functions exhibit a double-exponential decay) and we end up with

$$\begin{aligned}\mathtt{j}_{2s-1} &= \frac{s}{2^{2-s}\pi}(\mathcal{C}^s_L T^{s+1}_L - \mathcal{C}^s_R T^{s+1}_R)\\ \mathtt{j}_{2s} &= \frac{s}{2^{2-s}\pi}(\mathcal{C}^s_L T^{s+1}_L + \mathcal{C}^s_R T^{s+1}_R),\end{aligned} \tag{3.29}$$

where

$$\mathcal{C}^s_R = \int_{K_1} d\theta e^{-s(y_R+\theta)}L_R(\theta), \qquad \mathcal{C}^s_L = \int_{K_{2k}} d\theta e^{-s(y_L-\theta)}L_L(\theta). \tag{3.30}$$

Since both the L-functions and the kinks K_1 and K_{2k} are symmetric with respect to the origin we can write $\mathcal{C}^s_{L/R} := \mathcal{C}^s(y_{L/R})$ with

$$\mathcal{C}^s(y) = \int_{K_{2k}} d\theta e^{-s(y-\theta)}L(\theta)\,. \tag{3.31}$$

Note that for $s = 1$ and $(k-1)\theta_0/2 < y < k\theta_0/2$, we recover the known result [65–67]

$$\lim_{y,\theta_0\to+\infty}\mathcal{C}^1(y) = \frac{\pi^2}{6}c_{k+2}\,, \tag{3.32}$$

with c_{k+2} given in (3.12). A very similar result can be obtained for $\mathtt{j}_{2s}$ by simply replacing the minus sign by a plus sign in (3.29).

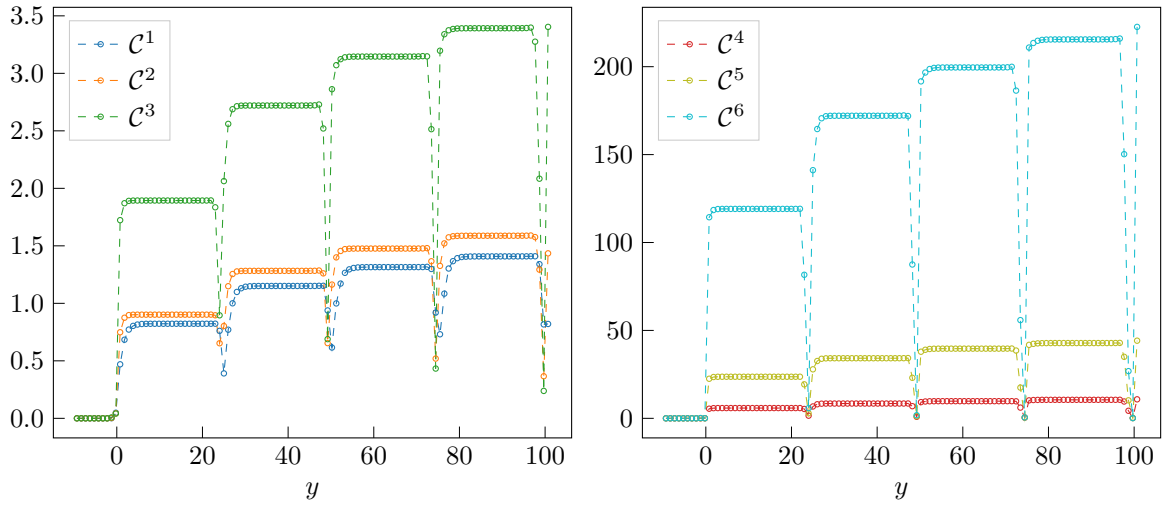

Figure 3.12: $\mathcal{C}^s(y)$ for spin $s = 1, 2, 3, 4, 5$ and 6 from Eq. (3.31). Here $\theta_0 = 50$.

The same considerations can be applied to the charge densities $\mathtt{q}_{2s-1}$ and $\mathtt{q}_{2s}$. Again, the only contributions to the integrals come from K_1 and K_{2k} and at a finite but large temperature one obtains:

$$\mathtt{q}_{2s-1} \approx \mathtt{j}_{2s} \qquad \text{and} \qquad \mathtt{q}_{2s} \approx \mathtt{j}_{2s-1}. \tag{3.33}$$

where the symbol $\approx$ indicates equality up to terms of order $O(e^{-y})$, thus becomes exact in the UV limit. Notice however that because of relativistic invariance $\mathtt{q}_2 = \mathtt{j}_1$ at any finite temperature.

Unfortunately, for $s > 1$ the coefficients $\mathcal{C}^s(y)$ do not admit an obvious simple form. However we can at least perform some analysis based on numerics. Since it is only the value of the ratio $\alpha = \frac{y}{\theta_0}$ that fixes the UV limit of the theory, we expect that $\mathcal{C}^s(y_L) = \mathcal{C}^s(y_R)$ as long as the condition (3.22) is satisfied. This is indeed verified by the numerical evaluation of the function $\mathcal{C}^s(y)$ which shows that it is constant in the central regions of $[(k-1)\theta_0/2, k\theta_0/2]$ (see Fig. 3.12).

Looking at the plots in Fig. 3.12 we also observe that when α approaches a half-integer value the function $\mathcal{C}^s(y)$ has a sudden fall. This is consistent with the definition of $\mathcal{C}^s(y)$ in (3.31): it is easy to show that

$$L(z_{2k}) \leq \lim_{\alpha \to k/2} \mathcal{C}^s(y) \leq L(z_{2k-1})\,, \tag{3.34}$$

where $L(z_{2k}) \simeq 0$ and $L(z_{2k-1}) \simeq 1$. In the central plateau regions, to a first approximation $\mathcal{C}^s(y)$ depends linearly on the central charge and exponentially on the spin. To see

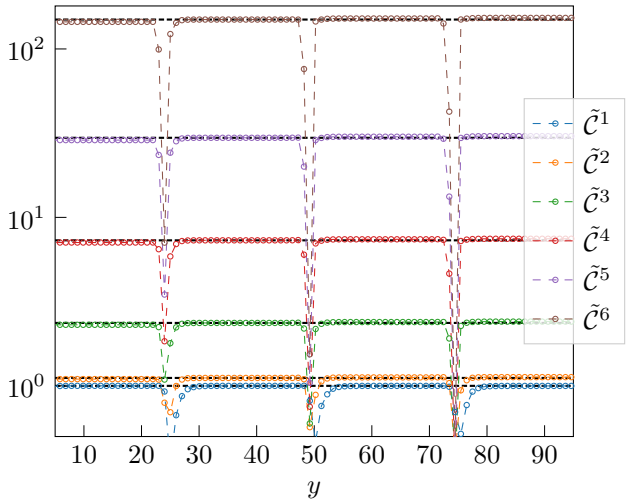

Figure 3.13: The function $\tilde{\mathcal{C}}^s(y)$ defined in (3.37) for spin $s = 1, 2, 3, 4, 5$ and 6 from Eq. (3.31) and $\theta_0 = 50$. For each spin all plateaux are almost the same height, which strongly suggests the coefficient of the currents is very nearly proportional to the central charge c_{k+2}. However there are small deviations for spin $s > 1$.

this we can treat s as a continuous variable and differentiate $\mathcal{C}^s(y)$ with respect to s. We obtain a differential equation for $\mathcal{C}^s(y)$ which is solved with the initial condition (3.32):

$$\mathcal{C}^s(y) = \frac{\pi^2}{6} c_{k+2} \exp\left\{ \int_1^s ds' \, \langle \theta \rangle_{s'} - (s-1)y \right\}, \tag{3.35}$$

where

$$\langle \theta \rangle_s \equiv \frac{\int_{K_{2k}} d\theta \theta e^{s\theta} L(\theta)}{\int_{K_{2k}} d\theta e^{s\theta} L(\theta)}. \tag{3.36}$$

Writing $\mathcal{C}^s(y)$ in this form gives a complicated dependence on the spin but has the advantage that the central charge is factored out and corrections to linearity are encoded in the exponential. In Fig. 3.13 we show the scaled functions

$$\tilde{\mathcal{C}}^s_k(y) = \frac{6\,\mathcal{C}^s(y)}{\pi^2 c_{k+2}}, \tag{3.37}$$

for the first few integer values of s. As is clear from the figure, these functions have almost the same values at every plateau and deviations from linearity in c_k are very small, but non-zero when $s > 1$. It would be interesting to investigate these corrections in more detail as well as the explicit dependence on the spin. The latter can be obtained exactly at the free fermion point, which is instructive. We show the calculation in Appendix B.

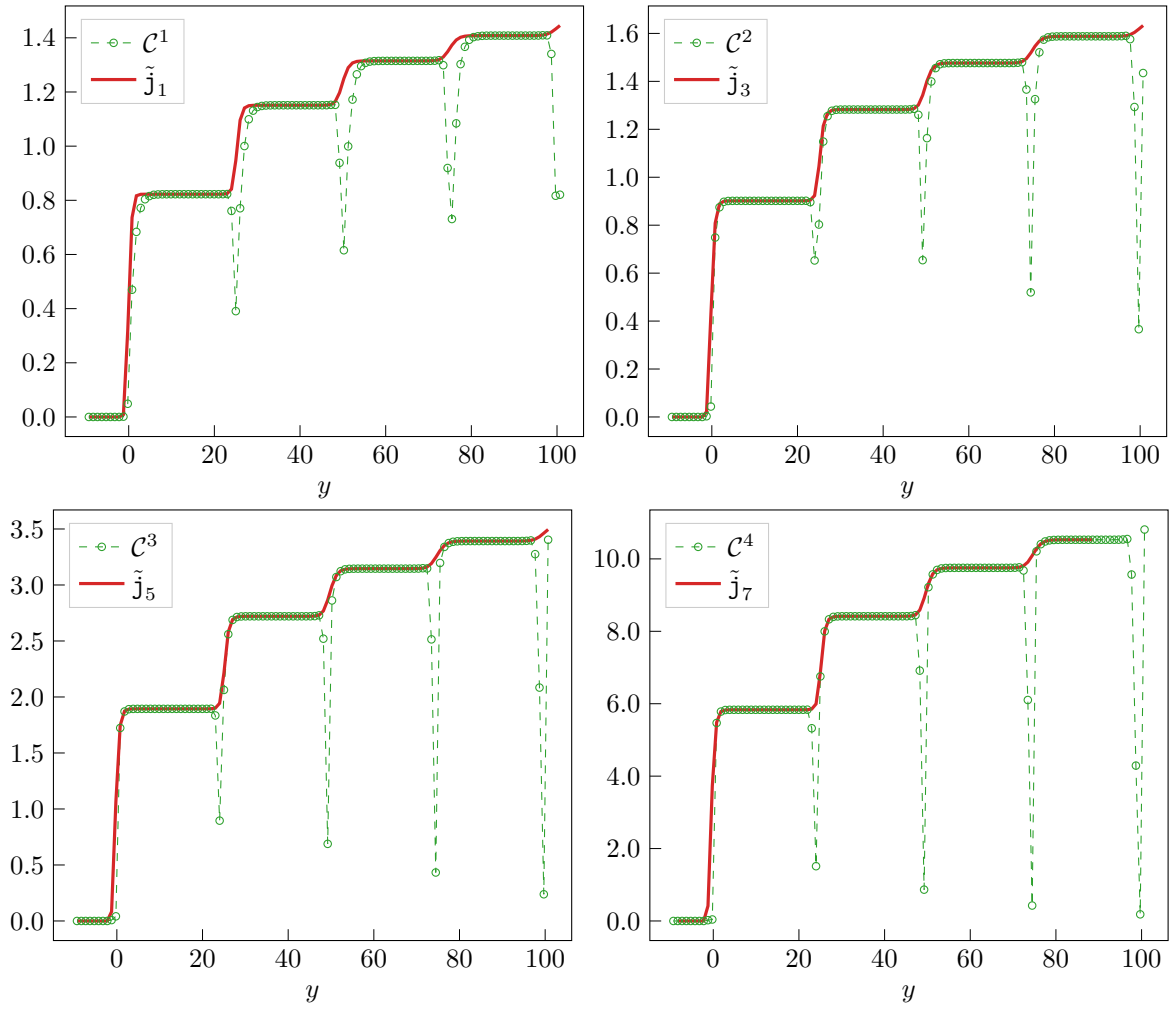

Figure 3.14: Scaled currents $\tilde{\mathtt{j}}_{2s-1}$ versus values of $\mathcal{C}^s(y)$ obtained from (3.31) for $s = 1, 2, 3, 4$. We see very good agreement in all plateau regions. All data are for $\theta_0 = 50$ and $\sigma = e$.

Another numerical check of (3.31) is presented in Fig. 3.14 where we look instead at the scaled currents:

$$\tilde{\mathtt{j}}_{2s-1} = \frac{\pi\,\beta_R^{s+1}}{s\,2^{s-2}(\sigma^{s+1}-1)}\mathtt{j}_{2s-1}\,, \tag{3.38}$$

as functions of $-y_L$ for fixed $\sigma = e$ along with the coefficients $\mathcal{C}^s(y)$ as obtained from (3.31). As expected, we find good agreement in all the plateau regions.

4

Introduction to quantum quenches

Another paradigmatic protocol for taking a quantum many-body system out of equilibrium is provided by a quantum quench, which corresponds to sudden change in the Hamiltonian. It is a protocol routinely engineered in cold-atom experiments [9, 28, 29, 106–111] and provides a fruitful starting point to study non-equilibrium time evolution of isolated quantum systems. When both the pre- and post-quench Hamiltonians are translationally invariant, a quench starting from an equilibrium (e.g. ground) state of the pre-quench system corresponds to a situation with a uniform non-zero energy density under the post-quench Hamiltonian, which is a highly excited configuration that can be considered as a source of quasi-particle excitations [112]. The subsequent time evolution can be considered as dynamics driven by the quasi-particles created in the quench; the post-quench excitations determine the spreading of correlation and entanglement in the system.

We start by properly defining the protocol in Sec. 4.1, while in sections 4.2 and 4.3 we analise how the quasi-particle pictures determines time evolution for correlators and entanglement entropy respectively. We finish the chapter in Sec. 4.4 by reviewing the results for the quench protocol in the paradigmatic Transverse Field Ising model.

4.1 Definition of a quantum quench

We now introduce the concept of *quantum quench* [112]. First suppose we have a quantum system prepared in an eigenstate $|\psi_{n,0}\rangle$ of the hamiltonian function H at time $t = 0$. For $t > 0$ we make H time dependent and we ask how the initial state evolves. Since the hermiticity of the Hamiltonian is preserved, at each t we have an instantaneous

orthonormal basis of eigenvector

$$H_t \left|\psi_{n,t}\right\rangle = \left|\psi_{n,t}\right\rangle E_{n,t} \qquad \left\langle\psi_{n,t}|\psi_{m,t}\right\rangle = \delta_{n,m} \qquad \sum_n \left|\psi_{n,t}\right\rangle \left\langle\psi_{n,t}\right| = \mathbb{1} \ \ \forall t \tag{4.1}$$

Integrating the time dependent Schrödinger equation

$$i\frac{\partial}{\partial t}\left|\psi_{n,t}\right\rangle = H_t \left|\psi_{n,t}\right\rangle = E_{n,t}\left|\psi_{n,t}\right\rangle, \tag{4.2}$$

one finds

$$\left|\psi_{n,t}(t)\right\rangle = e^{i\theta_n(t)}\left|\psi_{n,t}\right\rangle, \tag{4.3}$$

where $\theta_n(t)$ is the so called *dynamical phase factor*:

$$\theta_n(t) = -\int_0^t dt' E_{n,t'}. \tag{4.4}$$

Thanks to the completness relation the initial state can be expressed in terms of the instantaneous eigenstates and evolved

$$\left|\psi_{n,0}(t)\right\rangle = \sum_m c_{m,t} e^{i\theta_m(t)}\left|\psi_{m,t}\right\rangle \qquad c_{m,0} = \delta_{n,m}. \tag{4.5}$$

The coefficients $c_{n,t}$ can be found substituting the latter expression in the time dependent Schrödinger equation:

$$i\sum_m e^{i\theta_m(t)}\{\dot{c}_{m,t}\left|\psi_{m,t}\right\rangle + i\dot{\theta}_m(t)c_{m,t}\left|\psi_{m,t}\right\rangle + c_{m,t}\left|\dot{\psi}_{m,t}\right\rangle\} = \sum_m e^{i\theta_m(t)}c_{m,t}E_{m,t}\left|\psi_{m,t}\right\rangle, \tag{4.6}$$

which implies

$$\dot{c}_{l,t} = -\sum_m e^{-i\int_0^t dt'(E_{m,t'}-E_{l,t'})}c_{m,t}\left\langle\psi_{l,t}\right|\left.\dot{\psi}_{m,t}\right\rangle. \tag{4.7}$$

An expression for $\left\langle\psi_{l,t}\right|\left.\dot{\psi}_{m,t}\right\rangle$ is found by differentiating the eigenvalues equation in (4.1) and projecting on $\left|\psi_{l,t}\right\rangle$:

$$\left\langle\psi_{l,t}\right|\dot{H}_t\left|\psi_{m,t}\right\rangle + E_{l,t}\left\langle\psi_{l,t}\right|\left.\dot{\psi}_{m,t}\right\rangle = \dot{E}_{m,t}\delta_{l,m} + E_{m,t}\left\langle\psi_{l,t}\right|\left.\dot{\psi}_{m,t}\right\rangle. \tag{4.8}$$

Equation (4.7) then becomes

$$\dot{c}_{m,t} = -c_{m,t}\left\langle\psi_{m,t}\right|\left.\dot{\psi}_{m,t}\right\rangle - \sum_{l\neq m} e^{-i\int_0^t dt'(E_{m,t'}-E_{l,t'})}c_{l,t}\frac{\left\langle\psi_{m,t}\right|\dot{H}_t\left|\psi_{l,t}\right\rangle}{E_{l,t}-E_{m,t}}. \tag{4.9}$$

From here it follows that if

$$\left|\left\langle\psi_{m,t}\right|\dot{H}_t\left|\psi_{l,t}\right\rangle\right| \ll \left|E_{l,t}-E_{m,t}\right| \qquad \forall l,m \tag{4.10}$$

then

$$c_{m,t} = e^{i\alpha_m(t)} c_{m,0}, \tag{4.11}$$

where $\alpha_m(t)$ is called *geometric phase*:

$$i\alpha_m(t) = -\int_0^t dt' \left\langle \psi_{m,t'} \middle| \dot{\psi}_{m,t'} \right\rangle . \tag{4.12}$$

Note that $\alpha_m(t)$ is real since

$$0 = \frac{d}{dt} \langle \psi_{m,t'} | \psi_{m,t'} \rangle = \left\langle \psi_{m,t'} \middle| \dot{\psi}_{m,t'} \right\rangle + \overline{\left\langle \psi_{m,t'} \middle| \dot{\psi}_{m,t'} \right\rangle}. \tag{4.13}$$

The evolution of the initial state is eventually given by

$$|\psi_{n,0}(t)\rangle = e^{i\alpha_n(t)} e^{i\theta_n(t)} |\psi_{n,0}\rangle . \tag{4.14}$$

This is essentially the *adiabatic theorem* by Max Born and Vladimir Fock [113]: if (4.10) holds (the Hamiltonian varies slowly with respect to the gap between the $E_{n,t}$ and the rest of the energy spectrum), the initial state evolves without changing quantum numbers and picking up phase factors. The phase factor $\alpha_n(t)$ can also be cancelled out by an appropriate choice of gauge (if the adiabatic evolution is not cyclic, otherwise it becomes a gauge invariant physical quantity known as Berry phase [114]).

A quantum quench occurs when the adiabatic aproximation (4.10) is not valid. This can happen either when the Hamiltonian variation rate is not small enough, or when there is no gap between the energy eigenvalue of the initial state and the rest of the spectrum. In both cases there isn't a precise theoretical approach to the problem and perturbation theory cannot be applied since the change in the Hamiltonian isn't small in general. Seminal works on quantum quenches ([112, 115–118]) investigated different ways of taking the system out of equilibrium. In this thesis we concentrate on a standard procedure which is called *sudden quench*.

In a sudden quench the many-body system is prepared in a pure state which is an eigenstate of the initial Hamiltonian, the latter depending on a set of parameters $\{g_i^0\}$:

$$H(\{g_i^0\}) |\psi_0\rangle = |\psi_0\rangle E \tag{4.15}$$

At $t = 0$ we suddenly quench the set of parameters to new values $\{g_i\}$ and, since the system remains isolated, consider the unitary time evolution with the new Hamiltonian $H(\{g_i\})$. At times $t > 0$ the state of the system is found solving the time-dependent Schrödinger equation

$$|\psi(t)\rangle = e^{iH(\{g_i\})t} |\psi_0\rangle . \tag{4.16}$$

Furthermore, the quench is said to be *global* if the change of the coupling constants $\{g_i^0\}$ is the same in the whole chain.

A crucial property of a global quantum quench is that energy is conserved at all $t > 0$ and the post-quench energy density is larger than the ground state energy per site. This means that through the quantum quench we explore a region of Hilbert space that is macroscopically different from the sector containing the ground state and low-lying excitations [7].

4.2 Spreading of correlations after a quantum quench

How does the system behave after a quantum quench? And what is the theoretical picture that allows to compute expectation values of local operators? Let's consider an integrable quantum system. Suppose that the latter is mappable into a free fermion model, hence both the pre-quench and the post-quench Hamiltonians can be put in the diagonal form

$$\begin{aligned} \text{Pre-quench:} \qquad & H(\{g_i^0\}) = \sum_k \epsilon_{\{g_i^0\}}(k)\tilde{\eta}_k^\dagger \tilde{\eta}_k + E_0(\{g_i^0\}) \\ \text{Post-quench:} \qquad & H(\{g_i\}) = \sum_k \epsilon_{\{g_i\}}(k)\eta_k^\dagger \eta_k + E_0(\{g_i\}), \end{aligned} \tag{4.17}$$

with the corresponding vacua, satisfying

$$\begin{aligned} \tilde{\eta}_k \left|0; \{g_i^0\}\right\rangle &= 0 \qquad \forall k \\ \eta_k \left|0; \{g_i\}\right\rangle &= 0 \qquad \forall k \end{aligned} \tag{4.18}$$

with fermionic commutation relations

$$\{\eta_k, \eta_p^\dagger\} = \delta_{k,p}. \tag{4.19}$$

It is possible to put in relation the two sets of creation and annihilation operators through a Bogoliubov transformation:

$$\begin{aligned} \tilde{\eta}_p &= \sum_k (\Theta_{pk}\eta_k + \Omega_{pk}\eta_k^\dagger) \\ \tilde{\eta}_p^\dagger &= \sum_k (\Theta_{kp}^*\eta_k^\dagger + \Omega_{kp}^*\eta_k). \end{aligned} \tag{4.20}$$

The physical interpretation of Ω is the following: suppose one desires to compute the number of quasi-particles excitations of the pre-quench Hamiltonian on the vacuum

of the quenched system $\langle 0;\{g_i\}|\,\tilde{\eta}_p^\dagger\tilde{\eta}_p\,|0;\{g_i\}\rangle$. Taking (4.18) and (4.20) into account:

$$\tilde{\eta}_p\,|0;\{g_i\}\rangle = \sum_k(\Theta_{pk}\eta_k + \Omega_{pk}\eta_k^\dagger)\,|0;\{g_i\}\rangle = \sum_k \Omega_{pk}\,|1_k;\{g_i\}\rangle\,, \tag{4.21}$$

so that

$$\langle 0;\{g_i\}|\,\tilde{\eta}_p^\dagger\tilde{\eta}_p\,|0;\{g_i\}\rangle = \sum_k |\Omega_{pk}|^2. \tag{4.22}$$

Hence the new vacuum is filled with quasi-particle of the pre-quench Hamiltonian (and viceversa). Indeed, since both sets of quasi-particles can be used to generate the Fock space, we can express the ground state of the pre-quench Hamiltonian as excited states of the quenched system. We can define this relation by taking (4.18) into account:

$$\tilde{\eta}_p\,\big|0;\{g_i^0\}\big\rangle = 0 = \sum_k(\Theta_{pk}\eta_k + \Omega_{pk}\eta_k^\dagger)\,\big|0;\{g_i^0\}\big\rangle\,. \tag{4.23}$$

Multiplying this expression by $\sum_p \Theta^{-1}_{ip}$ we find the equation

$$\eta_i\,\big|0;\{g_i^0\}\big\rangle = \sum_k \aleph_{ik}\eta_k^\dagger\,\big|0;\{g_i^0\}\big\rangle\,, \tag{4.24}$$

where

$$\aleph_{ik} = -\sum_p \Theta^{-1}_{ip}\Omega_{pk}. \tag{4.25}$$

The solution of (4.25) is given by

$$\big|0;\{g_i^0\}\big\rangle = \exp\left\{\frac{1}{2}\sum_{ik}\aleph_{ik}\eta_i^\dagger\eta_k^\dagger\right\}|0;\{g_i\}\rangle\,. \tag{4.26}$$

In our models, that are translational invariant, we'll see that

$$\aleph_{ik} = \delta_{i,-k}\aleph_{i,-i} \equiv \delta_{i,-k}\aleph_i, \tag{4.27}$$

that give us an expression of the pre-quench ground state as *boundary state*:

$$\big|0;\{g_i^0\}\big\rangle = \exp\left\{\sum_{k>0}\aleph_k\eta_k^\dagger\eta_{-k}^\dagger\right\}|0;\{g_i\}\rangle\,, \tag{4.28}$$

where the function $\aleph$ is referred as *kernel* of the state.

This gives a precise physical interpretation for what happens after a quantum quench in this case: when changing the set of parameters in the Hamiltonian, the state of the system is a superposition of excited states given by pairs of quasi-particles with

opposite momenta (in such a way the total momentum is conerved). These excitations propagate with a dispertion relation given by the post-quench Hamiltonian $\epsilon_{\{g_i\}}(k)$ and have therefore a maximum velocity of propagation given by

$$v_{\max} = \max_k \left| \frac{d\epsilon_{\{g_i\}}(k)}{dk} \right|. \tag{4.29}$$

This means that even if the models are non-relativistic there exists a maximum velocity of propagation of the information. This feature has a profound impact on time depenence of the expectation values of local operators after a quench.

Suppose we want to calculate the connected correlation function of a local operator $\mathcal{O}$, whose support is a single site of the chain:

$$G_2^c(l;t) = \langle\psi(t)|\,\mathcal{O}_k\mathcal{O}_{k+l}\,|\psi(t)\rangle - \langle\psi(t)|\,\mathcal{O}_k\,|\psi(t)\rangle\,\langle\psi(t)|\,\mathcal{O}_{k+l}\,|\psi(t)\rangle\,. \tag{4.30}$$

At $t = 0$, the state is characterised by a finite correlation length ξ and the correlation function is extremely small at large spatial separations:

$$G_2^c(l;t) \propto e^{-l/\xi}. \tag{4.31}$$

At times $t > 0$ quasi-particles start propagating throughout the system. A measurement at site k will be influenced by quasi-particles within *the backwards light cone* $[k - v_{\max}t, k + v_{\max}t]$. At time

$$t = \frac{l}{2v_{\max}} \tag{4.32}$$

the backwards light cones emanating from site k and site $k+l$ touch and the the average measurements of the two sites become correlated.

This physical interpratation was given by Calabrese and Cardy [116, 117] and light cone effects after quantum quenches have been analysed and observed in various models. In Fig. 4.1 the time dependent part of the connected density-density correlator of a one dimensional fermionic pairing model is displayed.

4.2.1 Relation to Lieb-Robinson bounds

As shown by Lieb and Robinson [119], the velocity of information transfer in quantum spin chains is effectively bounded and there exists a causal structure in commutators of local operators at different times. Given two local operators $\mathcal{O}_X$ and $\mathcal{O}_Y$ having their supports on X and Y respectively that are spatially separated by distance L,

$$||[\mathcal{O}_X(t), \mathcal{O}_Y(0)]|| \leq c\min\{\mu(X), \mu(Y)\}\|\mathcal{O}_X\|\|\mathcal{O}_Y\|e^{-\frac{L-vt}{\xi'}}, \tag{4.33}$$

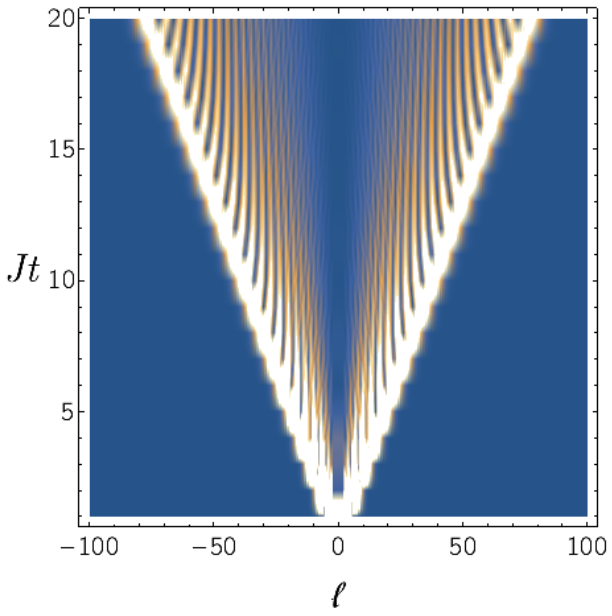

Figure 4.1: Time dependent part of the connected density-density correlator after a quantum quench. A light cone effect is clearly visible [7].

where $\mu(X)$ indicates the numbers of sites in X, $\|.\|$ denotes the operator norm and c, v and ξ' are constants.

The Lieb-Robinson bound has important consequences for quantum quenches starting in initial states with finite correlation lengths and evolving under short-ranged Hamiltonians. It was shown in [120] that (4.33) implies a bound on the connected two point functions

$$\langle\psi(t)|\,\mathcal{O}_X\mathcal{O}_Y\,|\psi(t)\rangle - \langle\psi(t)|\,\mathcal{O}_X\,|\psi(t)\rangle\,\langle\psi(t)|\,\mathcal{O}_Y\,|\psi(t)\rangle \leq c'(\mu(X)+\mu(Y))e^{-\frac{L-2vt}{\chi}}, \tag{4.34}$$

with c' and χ constants.

4.3 Entanglement entropy and evolution after a quantum quench

Many quantum features can be deduce by studying quantities that are non local observables. Entropy is one of these quantities and builds the basis for a statistical description of nature. An isolated quantum system evolves unitarily and if the system is prepared in a pure state it will remain in a pure state with zero entropy.

However we can characterize the entropy of a subsystem, that is generally in a mixed

state, computing the Von Neumann entropy of its reduced density matrix, also called *entanglement entropy*.

The entanglement of a subsystem with the rest of the system measures how the configuration of the former depends on the configuration of the latter and how far it is from being a pure state. To put this into formulae, we first introduce the Schmidt decomposition.

4.3.1 Schmidt decomposition

Let us consider a bipartition of the Hilbert space of a spin chain $\mathcal{H} = \mathcal{H}_L \bigotimes \mathcal{H}_R$ of a $1D$ system, where $\mathcal{H}_L(\mathcal{H}_R)$ describes all the states defined on the left (right) of a given bond.

Any pure state $|\psi\rangle$ defined on the whole system can be written as

$$|\psi\rangle = \sum_{ij} \Psi_{ij} |i\rangle_L \otimes |j\rangle_R , \tag{4.35}$$

where $\{|i\rangle_L\}$ and $\{|j\rangle_R\}$ are orthonormal bases of $\mathcal{H}_L$ and $\mathcal{H}_R$ with dimensions N_L and N_R respectively. From this representation we can introduce the reduced density operator of a part of the system tracing out the degrees of freedom of the other part

$$\rho_{L/R} = \mathrm{Tr}_{R/L} |\psi\rangle \langle\psi| , \tag{4.36}$$

which expressed with respect to the orthonormal bases take the form

$$\rho_L = \Psi\Psi^\dagger \qquad \rho_R = \Psi^\dagger\Psi \tag{4.37}$$

We can now perform a *singular value decomposition* (SVD) of the matrix Ψ. The SVD guarantees for an arbitrary matrix M of dimension $(n \times m)$ the existence of a decomposition

$$M = USV^\dagger, \tag{4.38}$$

where:

- U is of dimension $(n \times \min(n, m))$ and has orthonormal columns, i.e. $U^\dagger U = \mathbb{1}$; if $n \leq m$, U is then unitary;
- S is of dimension $(\min(n, m) \times \min(n, m))$ and diagonal with non negative entries $S_{aa} \equiv \Lambda_a$. These are the so-called *singular values*. The number r of non-zero singular values is the (*Schmidt*) rank, or bond dimension, of M. Furthermore we choose to put the singular values in descending order;

- V is of dimension $(\min(n,m)\times m)$ and has orthonormal rows, i.e. $VV^\dagger = \mathbb{1}$; if $n \geq m$, V is then unitary;

For practical importance in the following, it is useful to define a topology induced by the inner product $\langle M, N\rangle = \operatorname{Tr} M^\dagger N$. The latter defines the Frobenius norm

$$\|M\|_F^2 = \langle M, M\rangle = \operatorname{Tr} M^\dagger M = \operatorname{Tr}\sum_k (M^\dagger)_{ji} M_{ik} = \sum_{ij} |M_{ij}|^2. \tag{4.39}$$

In this topology the optimal approximation of the matrix M by a matrix M' of rank $r' < r$ is given by [121]

$$M' = US'V^\dagger \qquad S' = diag(s_1, s_2, \dots, s_{r'}, 0, \dots), \tag{4.40}$$

i.e. one sets all but the first r' singular values to be zero.

The SVD is at the basis of a very compact representation of quantum states living in a bipartite universe L/R called the *Schmidt decomposition*.

The pure state $|\psi\rangle$ can be expressed as

$$\begin{aligned} |\psi\rangle &= \sum_{ij} \Psi_{ij} |i\rangle_L \otimes |j\rangle_R = \sum_{ij} \sum_{\alpha=1}^{\min(N_L,N_R)} U_{i\alpha} S_{\alpha\alpha} V^*_{j\alpha} |i\rangle_L \otimes |j\rangle_R \\ &= \sum_{\alpha=1}^{\min(N_L,N_R)} \Lambda_\alpha \Big(\sum_i U_{i\alpha} |i\rangle_L\Big) \otimes \Big(\sum_j V^*_{j\alpha} |j\rangle_R\Big) \\ &= \sum_{\alpha=1}^{\min(N_L,N_R)} \Lambda_\alpha |\alpha\rangle_L \otimes |\alpha\rangle_R \end{aligned} . \tag{4.41}$$

Due to the orthonormality properties of U and $V^\dagger$, the sets $\{|\alpha\rangle_L\}$ and $\{|\alpha\rangle_R\}$ are also orthonormal bases of $\mathcal{H}_L$ and $\mathcal{H}_R$, i.e.,

$$\langle\alpha|\alpha'\rangle_L = \sum_{ii'} {}_L\langle i| U^*_{i\alpha} U_{i'\alpha'} |i'\rangle_L = \sum_{ii'} (U^\dagger)_{\alpha i} U_{i'\alpha'} \delta_{ii'} = \sum_i (U^\dagger)_{\alpha i} U_{i\alpha'} = \delta_{\alpha\alpha'} \tag{4.42}$$

Restricting the sum over the r positive non-zero values of $\{\Lambda_a\}$, we obtain the *Schmidt decomposition*:

$$|\psi\rangle = \sum_{\alpha=1}^{r} \Lambda_\alpha |\alpha\rangle_L \otimes |\alpha\rangle_R \tag{4.43}$$

Furthermore, if the pure state $|\psi\rangle$ is normalised:

$$\sum_{\alpha=1}^{r} \Lambda_\alpha^2 = 1 \tag{4.44}$$

4.3.2 Entanglement Entropy and area law

An important aspect of the Schmidt decomposition is that it gives meaningful information about the *entanglement* between the degrees of freedom in $\mathcal{H}_L$ and $\mathcal{H}_R$ because the values Λ_α give a measure of the overlap between the states of the two subsystems. To better understand their meaning, we analyse two extreme cases. The first one is given by

$$\Lambda_\alpha = \delta_{\alpha,\alpha_0} \qquad |\psi\rangle = |\alpha_0\rangle_L \otimes |\alpha_0\rangle_R \,. \tag{4.45}$$

This state is separable and there is no entanglement. A measure on the L subsystem will not affect a measure on the R subsystem.

Every other state is entangled and the opposite situation to the previous one is when

$$\Lambda_\alpha = \frac{1}{\sqrt{\mathcal{N}}} \qquad |\psi\rangle = \frac{1}{\sqrt{\mathcal{N}}} \sum_\alpha^{\mathcal{N}} |\alpha\rangle_L \otimes |\alpha\rangle_R \,, \tag{4.46}$$

where $\mathcal{N} = \min(N_L, N_R)$. This is the maximally entangled state.

It is important to remark that the Schmidt basis coincides with the eigenbasis of the reduced density matrix of the two subsystems, that share the same spectrum:

$$\begin{aligned} \rho_L &= \sum_\alpha \Lambda_\alpha^2 \, |\alpha\rangle_L \, \langle\alpha|_L \\ \rho_R &= \sum_\alpha \Lambda_\alpha^2 \, |\alpha\rangle_R \, \langle\alpha|_R \end{aligned} \tag{4.47}$$

But what provides a good measure of entanglement? It was proved in [122] that an entanglement measure S is fixed uniquely after imposing the following conditions:

1. S is invariant under local unitary transformations (that implies that S is a function of the Λ_α^2 only);
2. S is continuos;
3. S is additive when several copies of the system are present:

$$S(|\psi\rangle \otimes |\phi\rangle) = S(|\psi\rangle) + S(|\phi\rangle). \tag{4.48}$$

This conditions are satisfied by the von Neumann entropy of the reduced density matrix

$$S(\rho_L) = -\operatorname{Tr}[\rho_L \log \rho_L] = -\sum_\alpha \Lambda_\alpha^2 \log \Lambda_\alpha^2 = S(\rho_R) \equiv S, \tag{4.49}$$

which corresponds to the Shannon entropy with $p_\alpha = \Lambda_\alpha^2$.

Note that as we wanted an unentangled product state, where the pure state is described by only one Schmidt value, has $S = 0$. Conversely, S is maximum for a maximally entangled state.

The definition of entanglement entropy is formally the same of thermal entropy. This similarity though is only apparent since they exhibit different behaviours when the system size is changed. Thermal entropy S_T scales indeed withe the number of microstates. These can be approximated with the volume of the phase space accessible to the system. Since the latter is a direct product of the configuration space with its tangent bundle, it is natural that S_T scales with the volume accessible to the system. In d spatial dimensions

$$S_T \backsimeq l^d, \tag{4.50}$$

where l is a typical length of the system.

The situation is different for entanglement entropy. To see this difference let's consider ground states of local, short range Hamiltonians of a bipartite system in d dimensions. In general we expect that for non degenerate ground states of gapped Hamiltonians, the entangled degrees of freedom are the ones placed near the surface that separates the two subsystems. This is because of the finiteness of the correlation length, suggesting that the entanglement entropy scales with the area of the surface that divides the two subsystems [123]:

$$S \backsimeq \left(\frac{l}{\epsilon}\right)^{(d-1)}, \tag{4.51}$$

where ϵ is a non-universal short-distance cut-off.

For one dimensional systems the previous expression leads to bounded entanglement entropy and the following theorem was indeed proved in [124]:

Theorem 2. *Consider a short range Hamiltonian H with a unique ground state with a gap ΔE to the first excited state. Then, for any bond chosen for the bipartition L/R,*

$$S_L \leq S_{max}, \tag{4.52}$$

where

$$S_{max} = c_0 \xi' \log(\xi') \log(d) 2^{\xi' \log d} \tag{4.53}$$

with c_0 constant and $\xi' = 6\xi = 6 \max(2v/\Delta E, \xi_C)$.

When the Hamiltonian is gapless there is a violation to this law since ξ diverges and for one dimensional critical systems it has been shown [125] that

$$S = \frac{c}{3} \log\left(\frac{l}{\epsilon}\right), \tag{4.54}$$

where c is the *central charge* of the correspondent conformal field theory describing the model [126].

On the other hand, excited states are usually characterised by maximal entanglement and actually follow a volume law. Indeed they resemble classical states, where entanglement entropy reduces to thermodynamic entropy.

In conclusion, in the full Hilbert space of the system, among *typical states*, which follow a volume law, there are untypical rare states (usually represented by ground states) that are slightly entangled and can be described by only a relatively small number of Schmidt values.

This provides an extremely useful approach to compress quantum states by truncating the Schmidt decomposition. It is natural to approximate a state $|\psi\rangle$ by some $|\psi'\rangle$ spanned over state spaces of L and R that have dimension r' only. This problem can be related to the SVD, because the 2-norm of $|\psi\rangle$ is identical to the Frobenius norm of the matrix Ψ. The optimal approximation is therefore given in the 2-norm by the optimal approximation of Ψ by Ψ' in the Frobenius norm, where Ψ' is a matrix of rank r' (4.40).

When $|\psi\rangle$ follows an *area law*, we can therefore always truncate the Schmidt decomposition at some finite χ. That is $\forall \epsilon > 0$, $\exists \chi$ finite such that

$$\left\| |\psi\rangle - \sum_{\alpha=1}^{\chi} \Lambda_\alpha |\alpha\rangle_L \otimes |\alpha\rangle_R \right\| < \epsilon, \tag{4.55}$$

being χ non extensive.

This particular property of area law states is intimately related to the MPS representation of one dimensional quantum states, which is at the basis of the iTEBD algorithm (see Appendix C) used throughout the thesis.

4.3.3 Time evolution

How does entanglement entropy evolve after a sudden quench? We showed with the quasi-particle description that after a quench from the ground state, whose entanglement entropy follows an area law, the new state for $t > 0$ is given by a boundary state, obtained as superposition of excited states. Hence one should expect that in the long time limit entanglement entropy follows a volume law.

It was actually proved in [116] that entanglement in one dimensional models between the degrees of freedom in an interval A of length l and its complement $\bar{A}$, starting from a pure state which is not an eigenstate of the Hamiltonian that determines time evolution, increases linearly with time t up to $t^* = l/2v$, after which it saturates at a value proportional to l.

This result was obtained using path integral methods of quantum field theory as well as with explicit computations for the transverse Ising spin chain, but it is believed to hold in a wider class of systems, since it can be derived by causality arguments with the quasi-particle description already introduced.

The initial state $|\psi_0\rangle$ has an extensively high energy relative to the ground state of the post-quenched Hamiltonian and therefore acts as a source of quasiparticle excitations, emitted in pairs from any point of the initial state. Those quasi-particles originating from different points (further apart than the correlation length ξ typical of the initial state) are incoherent, but pairs of particles originating from the same point or from points within ξ are highly entangled. Suppose that the cross section for producing such a pair of particles of momenta p' and p'' from a certain point in space is $\sigma(p', p'')$ and that since they separate they move classically, with no interaction between them.

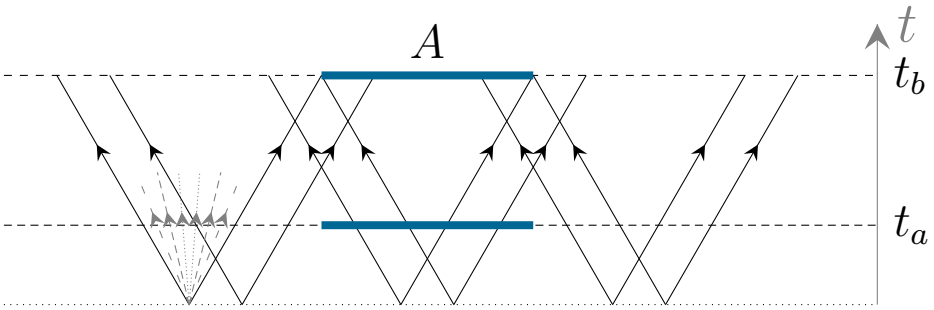

Figure 4.2: Space-time picture illustrating how oppositely moving correlated quasi-particles increase entanglement between an interval A and the rest of the system.

The classical velocity is given by $v(p) = d\epsilon/dp$, where $\epsilon(p)$ is the dispersion relation and we fix the maximum allowed speed to 1, that is $|v(p)| \leq 1$. A quasi-particle generated at $(x, t = 0)$ is therefore at $x + v(p)t$ at time t. Consider these quasi-particles as they reach either A or $\bar{A}$ at time t. The entanglement between the two sets increases if a pair of entangled particles emitted from a point x arrives simultaneously at $x' \in A$ and $x'' \in \bar{A}$ (Fig. 4.2). The entanglement entropy between x' and x'' is proportional to the length of the interval in x for which this can be satisfied. Thus the total entanglement

entropy is

$$S_A(t) \simeq \int_{x' \in A} dx' \int_{x'' \in \bar{A}} dx'' \int_{-\infty}^{\infty} dx \int dp' dp'' \sigma(p', p'') \delta(x' - x - v(p')t) \delta(x'' - x - v(p'')t) \quad (4.56)$$

Considering now that A is an interval of length l then the total entanglement is twice that between A and the real axis to the right of A, which corresponds to taking $p' < 0$, $p'' > 0$ in the above. The integration over the coordinates then gives $\max((v(p') + v(p''))t, l)$ (see Fig. 4.3), so that

$$\begin{aligned} S_A(t) \simeq 2t \int_{-\infty}^{0} dp' \int_{0}^{\infty} dp'' \sigma(p', p'') \{v(-p') + v(p'')\} \theta(l - [v(-p') + v(p'')]t) \\ + 2l \int_{-\infty}^{0} dp' \int_{0}^{\infty} dp'' \sigma(p', p'') \theta([v(-p') + v(p'')]t - l), \end{aligned} \quad (4.57)$$

where $\theta(x)$ is the Heaviside step function. Since $|v(p)| \leq 1$, the second term cannot contribute if $t < t* = l/2$ so that $S_A(t)$ is strictly proportional to t. On the other hand, as $t \to \infty$, the first term is negligible and S_A is asymptotically proportional to l.

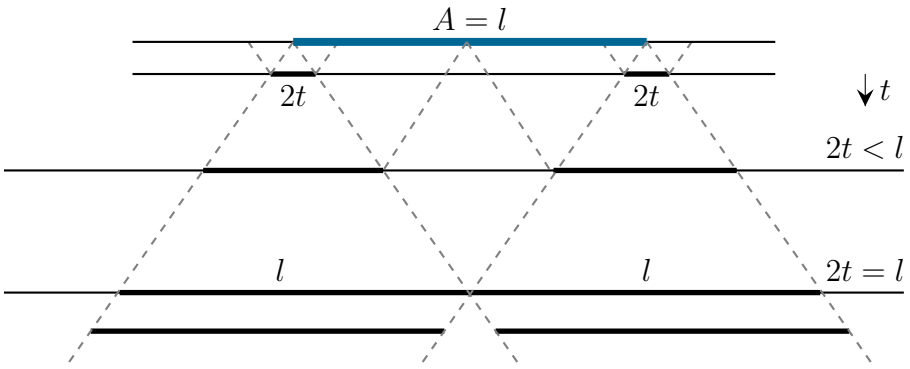

Figure 4.3: Space-time picture of the entanglement entropy dynamics. For times such that $2t < l$ the entanglement entropy increases linearly with time; for later times it saturates to a value proportional to the lenght l of the subsystem considered.

However, unless $|v| = 1$ everywhere (as in the conformal field theory case), S_A is not strictly proportional to l for $t > t^*$ and there is a slow increase towards the asymptotic value. This can be understood since, on the lattice, there are quasi-particles excitations which travel with a group velocity that is less than the maximum allowed value.

4.4 Quantum Quenches in the Transverse Field Ising Chain

As an example of the general statements of the the previous sections we review some results, following [7], obtained in a paradigmatic model: the Transverse Field Ising Chain (TFIC), whose Hamiltonian is given by

$$H(h) = -J \sum_{\ell=1}^{L} \sigma_\ell^x \sigma_{\ell+1}^x + h\sigma_\ell^z \,. \tag{4.58}$$

Here we impose periodic boundary conditions $\sigma_{L+1}^\alpha \equiv \sigma_1^\alpha$, L even, $h \geq 0$ and $J > 0$. We note that the signs of h and J can be reversed by unitary transformations with respectively

$$U_1 = \prod_{\ell=1}^{L} \sigma_\ell^x \;, \quad U_2 = \prod_{\ell=1}^{L/2} \sigma_{2\ell-1}^x \sigma_{2\ell}^y. \tag{4.59}$$

The Hamiltonian (4.58) has a $\mathbb{Z}_2$ symmetry of rotations by π around the z-axis. The ground state phase diagram of the TFIC features a paramagnetic (for $h > 1$) and a ferromagnetic (for $h < 1$) phase, in which the $\mathbb{Z}_2$ symmetry is spontaneously broken. The two phases are separated by a quantum critical point at $h = 1$, which is described by the Ising conformal field theory with central charge $c = 1/2$.

It is well known that the TFIC admits a representation in terms of non-interacting fermions by a Jordan-Wigner transformation

$$\sigma_\ell^z = i a_{2\ell} a_{2\ell-1} \;, \quad \sigma_\ell^x = \left(\prod_{j=1}^{\ell-1} (i a_{2j} a_{2j-1}) \right) a_{2\ell-1} \;, \quad \sigma_\ell^y = \left(\prod_{j=1}^{\ell-1} (i a_{2j} a_{2j-1}) \right) a_{2\ell}, \tag{4.60}$$

where a_ℓ are Majorana fermions satisfying the anti-commutation relations $\{a_\ell, a_n\} = 2\delta_{\ell n}$. The usual spinless fermions are obtained by taking linear combinations $c_\ell^\dagger = (a_{2\ell-1} + i a_{2\ell})/2$. It is now straightforward to see that spin-spin correlation functions map onto expectation values of strings of fermions, e.g.

$$\langle \sigma_\ell^x \rangle = (-i)^{\ell-1} \left\langle \prod_{j=1}^{2\ell-1} a_j \right\rangle \qquad \left\langle \sigma_\ell^x \sigma_{\ell+n}^x \right\rangle = (-i)^n \left\langle \prod_{j=2\ell}^{2\ell+2n-1} a_j \right\rangle . \tag{4.61}$$

Application of the Jordan-Wigner transformation to the TFIC Hamiltonian (4.58) results

in a fermion Hamiltonian of the form

$$\begin{aligned} H &= \frac{\mathrm{I}-e^{i\pi\mathcal{N}}}{2}H_{\mathrm{R}}+\frac{\mathrm{I}+e^{i\pi\mathcal{N}}}{2}H_{\mathrm{NS}}\,, \\ H_{\mathrm{NS/R}} &= iJ\sum_{j=1}^{L-1}a_{2j}\left[a_{2j+1}-ha_{2j-1}\right]-iJa_{2L}\left[ha_{2L-1}\mp a_1\right]. \end{aligned} \tag{4.62}$$

Here $e^{i\pi\mathcal{N}}$ is the fermion parity operator with eigenvalues ± 1

$$e^{i\pi\mathcal{N}}=\prod_{\ell=1}^{L}\sigma_\ell^z=(-i)^L\prod_{j=1}^{2L}a_j\ , \qquad e^{i\pi\mathcal{N}}a_j=-a_je^{i\pi\mathcal{N}}\,. \tag{4.63}$$

$H_{\mathrm{R,NS}}$ commute with the fermion parity operator, and the full Hamiltonian (4.62) is therefore block-diagonal: H_{R} (H_{NS}) describes the action on states with an odd (even) number of fermions.

The Hamiltonians $H_{\mathrm{NS/R}}$ can be diagonalised by Bogoliubov transformations to canonical momentum space fermion operators b_p.

$$H_{\mathrm{a}}(h)=\sum_{p\in\mathrm{a}}\varepsilon_h(p)\left(b_p^\dagger b_p-\frac{1}{2}\right), \quad \mathrm{a}=\mathrm{R},\ \mathrm{NS}\ , \tag{4.64}$$

where the single-particle energy is given by

$$\varepsilon_h(k)=2J\sqrt{1+h^2-2h\cos k}. \tag{4.65}$$

The difference between R and NS sectors enters via the allowed values of the momenta, which are $p=\frac{\pi n}{L}$, where n are even/odd integers for R and NS fermions respectively. The ground states of $H_{\mathrm{R,NS}}(h)$ are the fermionic vacua

$$b_p|GS\rangle_{\mathrm{a}}=0\ \forall p\in\mathrm{a}\ , \quad \mathrm{a}=\mathrm{R},\mathrm{NS}. \tag{4.66}$$

These vacuum states are also eigenstates of the fermion parity operator

$$e^{i\pi\mathcal{N}}\left|GS\right\rangle_{\mathrm{NS}}=\left|GS\right\rangle_{\mathrm{NS}}\ , \qquad e^{i\pi\mathcal{N}}\left|GS\right\rangle_{\mathrm{R}}=\mathrm{sgn}(h-1)\left|GS\right\rangle_{\mathrm{R}}\ . \tag{4.67}$$

From (4.62) it follows that in the ferromagnetic phase $h<1$ both fermion vacua are eigenstates of the full Hamiltonian H. Their respective energies are exponentially (in system size) close, and they become degenerate in the thermodynamic limit. Spin-flip symmetry then gets spontaneously broken, and the ground state is either the symmetric or the antisymmetric combination of the two vacuuum states. In the paramagnetic phase $h>1$ the ground state of H is given by the NS vacuum state. In summary, we have

$$\left|GS\right\rangle=\begin{cases}\frac{\left|GS\right\rangle_{\mathrm{NS}}\pm\left|GS\right\rangle_{\mathrm{R}}}{\sqrt{2}} & h<1\\ \left|GS\right\rangle_{\mathrm{NS}} & h>1\,.\end{cases} \tag{4.68}$$

Quench protocol

We now consider the following quench protocol. We prepare the system in the ground state of $H(h_0)$, and at time $t = 0$ quench the transverse field to a new value h. At times $t > 0$ we time evolve with the new Hamiltonian $H(h)$. We now turn to the dynamics of spin correlations.

One-point functions

The longitudinal spin operator $\sigma_j^x = (-i)^{\ell-1} \prod_{j=1}^{2\ell-1} a_j$ is the simplest and most important example. Its expectation value is the order parameter in the ferromagnetic phase. As we are dealing with an odd operator, its expectation value is identically zero for quenches originating in the paramagnetic phase. For quenches from the ferromagnetic phase ($h_0 < 1$) it was shown in [127] that

$$\langle \Psi(t)|\sigma_j^x|\Psi(t)\rangle \simeq C^x(t) e^{-t/\tau_x}\,, \qquad h_0 < 1\,, \tag{4.69}$$

where the inverse decay time is given by

$$\tau_x^{-1} = \int_0^\pi \frac{\mathrm{d}k}{\pi} \varepsilon_h'(k) \ln \left| \frac{1 - K^2(k)}{1 + K^2(k)} \right| . \tag{4.70}$$

Here the function $iK(k)$ correponds to the kernel $\aleph_k$ in (4.25) and in this case satisfies $K(k) = \tan \Delta_k/2$, with

$$\cos \Delta_k = \frac{hh_0 - (h + h_0)\cos k + 1}{\sqrt{1 + h^2 - 2h\cos k}\sqrt{1 + h_0^2 - 2h_0 \cos k}}\,. \tag{4.71}$$

The prefactor $C^x(t)$ was calculated in [127] and reads

$$C^x(t) = \begin{cases} \sqrt{\frac{1 - hh_0 + \sqrt{(1-h^2)(1-h_0^2)}}{2\sqrt{1-hh_0}(1-h_0^2)^{\frac{1}{4}}}} & h < 1 \\ \left[\frac{h\sqrt{1-h_0^2}}{h+h_0}\right]^{\frac{1}{4}} \left[1 + \cos(2\varepsilon_h(k_0)t + \alpha) + \ldots\right]^{\frac{1}{2}} & h > 1\,, \end{cases} \tag{4.72}$$

where the dots stand for higher orders in the post-quench quasiparticle density.

At first sight the exponential decay (4.69) of the order parameter for quenches within the ferromagnetic phase may look surprising. Even a very small quench will lead to the eventual disappearance of the order parameter. A simple way of understanding this is to note that the ferromagnetic order persists only at zero temperature $T = 0$, and melts for any $T > 0$. By means of our quantum quench we deposit a finite energy density into the system, which is very similar to imposing a finite temperature. This

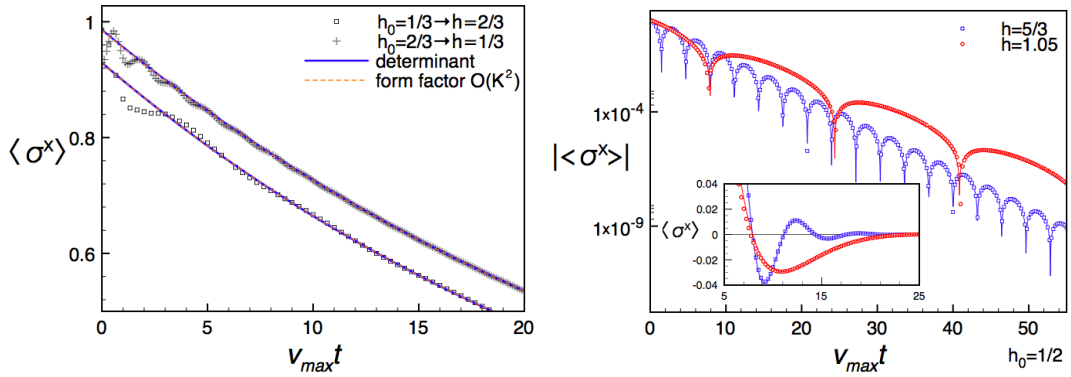

Figure 4.4: Expectation value of the order parameter after two quenches within the ferromagnetic phase (left) and two quenches across the critical point (right). Numerical results obtained in the thermodynamic limit are compared with the asymptotic predictions (4.69) (labelled as "determinant"). In the left panel analytic results obtained by form factor methods[127] are shown as well (labelled as "form factor"). Figures taken from [127].

consideration provides an intuitive explanation for why even small quenches wipe out the long range order present in the initial state. We note that this behaviour is specific to one dimensional systems, where discrete symmetries can be spontaneously broken only at $T = 0$.

We remark that a more recent result for (4.69) is presented in [128] where, with a different approach, they obtained the same result for the decay time τ_x while they found a different C coefficient, known to second order in the post-quench quasiparticle density.

Spin-spin correlators

A particularly useful way of describing the time dependence of two-point functions after a quantum quench is by considering an asymptotic expansion around the so-called *space-time scaling limit* [127]. The latter refers to the behaviour along a particular ray in space-time

$$t, \ell \to \infty \ , \quad \frac{v_{\max} t}{\ell} = \kappa = \text{fixed}. \tag{4.73}$$

Here $v_{\max} = \max_k \frac{d\varepsilon_h(k)}{dk}$ is the maximal group velocity of elementary excitations of the post-quench Hamiltonian.

In the space-time scaling limit the order parameter two-point function $\rho^{xx}(\ell, t)$ takes the form

$$\rho^{xx}(\ell, t) \simeq \mathcal{C}^x(\ell, t) \exp\Big[\int_0^\pi \frac{\mathrm{d}k}{\pi} \ln \Big| \frac{1 - K^2(k)}{1 + K^2(k)} \Big| \min\big(2\varepsilon_h'(k)t, \ell\big) \Big] . \tag{4.74}$$

The function $\mathcal{C}^x(\ell,t)$ has been determined in Ref. [127]:

- For quenches within the ferromagnetic phase, $h_0, h < 1$, $\mathcal{C}^x(\ell,t)$ equals the constant

$$C^x(\ell) \equiv \mathcal{C}^x_{\mathrm{FF}} = \frac{1 - hh_0 + \sqrt{(1-h^2)(1-h_0^2)}}{2\sqrt{1-hh_0}\sqrt[4]{1-h_0^2}}\,. \tag{4.75}$$

  For times smaller than the Fermi time

$$t_F = \frac{\ell}{2v_{\max}}\,, \tag{4.76}$$

  (4.74) equals the square of the one-point function (4.69). Thus, in the space-time scaling limit, connected correlations *vanish identically* for times $t < t_F$ and begin to form only after the Fermi time. We stress that this does not imply that the connected correlations are exactly zero for $t < t_F$: in any model, both on the lattice or in the continuum there are exponentially suppressed terms (in ℓ), which however vanish in the scaling limit.

  Also for this case in [128] they present the result

$$\begin{aligned} \rho^{xx}(\ell,t) &\simeq C \exp\left(-2\int_{-\pi}^{\pi} \rho(x)(1+2\pi\rho(x))|t\varepsilon'(x) - \ell| dx\right), \\ C &= \xi \exp\left(-2\int_{-\pi}^{\pi}\int_{-\pi}^{\pi} \frac{\rho(y)\rho'(x)}{\tan\left(\frac{x-y}{2}\right)} dxdy\right) \end{aligned} \tag{4.77}$$

  with $\rho(x) = \frac{1-\cos\Delta k}{4\pi}$ and $\xi = (1-h^2)^{1/4}$.

- For quenches from the ferromagnetic phase to the paramagnetic phase the prefactor is given by

$$\mathcal{C}^x(\ell,t) = \mathcal{C}^x_{\mathrm{FP}}\Big[1 + \theta_H(t_F - t)\Big(\cos(2\varepsilon_h(k_0)t + \alpha) + \dots\Big)\Big]\,, \tag{4.78}$$

  where $\mathcal{C}^x_{\mathrm{FP}}$ is given by

$$\mathcal{C}^x_{\mathrm{FP}} = \sqrt{\frac{h\sqrt{1-h_0^2}}{h+h_0}}, \tag{4.79}$$

  while k_0 and α are the constants appearing in the one-point function (4.72). Again, the dots stand for higher orders in the post-quench quasiparticle density. For $t < t_F$, (4.74) is simply the square of the corresponding one-point function, which ensures that connected correlations vanish for $t < t_F$ in the space-time scaling regime. We note that the expression for $t < t_F$ is a conjecture [127].

- For quenches within the paramagnetic phase one has

$$\mathcal{C}^x(\ell,t) \simeq \mathcal{C}^x_{\rm PP}(\ell) + (h^2-1)^{\frac{1}{4}}\sqrt{4J^2h}\int_{-\pi}^{\pi}\frac{dk}{\pi}\frac{K(k)}{\varepsilon_k}\sin(2t\varepsilon_k - k\ell) + \dots\,, \tag{4.80}$$

  where $\mathcal{C}^x_{\rm PP}(\ell)$ is the function defined by

$$C^x(\ell) \equiv \mathcal{C}^x_{\rm PP}(\ell) = \begin{cases} -\frac{h_0\sqrt{h}\left(hh_0-1+\sqrt{(h^2-1)(h_0^2-1)}\right)^2}{4\sqrt{\pi}(h_0^2-1)^{3/4}(h_0h-1)^{3/2}(h-h_0)}\ \ell^{-3/2} & \text{if } 1<h_0<h\,, \\ \sqrt{\frac{h(h_0-h)\sqrt{h_0^2-1}}{(h+h_0)(hh_0-1)}} & \text{if } 1<h<h_0. \end{cases} \tag{4.81}$$

  Eq. (4.80) constitutes the leading order in a low-density expansion computed within the form-factor formalism. The exact expression for a generic (not small) quench is not known.

- For quenches from the paramagnetic to the ferromagnetic phase, for $t > t_F$, $\mathcal{C}^x(\ell,t)$ is independent of time and is given by

$$C^x(\ell) \equiv \mathcal{C}^x_{\rm PF}(\ell) = \sqrt{\frac{h_0-h}{\sqrt{h_0^2-1}}}\cos\Big(\ell\arctan\frac{\sqrt{(1-h^2)(h_0^2-1)}}{1+h_0h}\Big)\,. \tag{4.82}$$

  For $t < t_F$ the correlator is exponentially small and, to the best of our knowledge, there are no analytic predictions for its behaviour.

Entanglement entropy

We now turn to the entanglement entropy introduced in section 4.3.2 through (4.49).

Exact results for the evolution of the entanglement entropy after quenches in the transverse field Ising chain [129] are in accordance with the structure suggested by the quasi-particle picture introduce in section 4.3. In the limit $1 \ll \ell, Jt$, the entanglement entropy of a block of ℓ neighbouring spins is

$$S[\rho_B] \simeq \int_{\pi}^{\pi}\frac{\mathrm{d}k}{2\pi}\ w(\langle\Psi(0)|n(k)|\Psi(0)\rangle)\ \min\Big(\ell, 2|\varepsilon'(k)|t\Big) + o(\ell)\,, \tag{4.83}$$

where $w(x) = -x\log x - (1-x)\log(1-x)$ is the entropy per site and $\langle\Psi(0)|n(k)|\Psi(0)\rangle$ is the (conserved) density of elementary excitations of the post-quench Hamiltonian H with momentum k at times $t > 0$. It is given by

$$\langle\Psi(0)|n(k)|\Psi(0)\rangle = \frac{K^2(k)}{1+K^2(k)}\,, \tag{4.84}$$

where $K^2(k)$ was defined through (4.71). It follows from (4.83) that the entanglement entropy increases linearly until the Fermi time (4.76), and then slowly approaches its stationary value set by the GGE. The latter equals the entropy per site of the GGE for the *entire* system [130]

$$\int_{\pi}^{\pi} \frac{\mathrm{d}k}{2\pi}\, w(\langle\Psi(0)|n(k)|\Psi(0)\rangle) = \lim_{L\to\infty} \frac{1}{L} S[\rho^{\mathrm{GGE}}]\,. \tag{4.85}$$

5

Quasi-particle Spectrum, Entropy Generation and Post-quench Relaxation in Quantum Spin Chains

As seen in the previous chapter, entanglement entropy is an important characteristics of the non-equilibrium evolution and the stationary state resulting after a quench. Therefore has been studied extensively in recent years [129–144]. The growth of entanglement also has important implications for the efficiency of computer simulations of the time evolution [145–149]. Recently it has become possible to measure entanglement entropy and its temporal evolution in condensed matter systems [106, 150, 151].

For systems where interactions have a suitable fall-off with distance, the quasi-particle propagation is limited by the existence of a maximum speed $v_{\max}$ called the Lieb-Robinson bound [119]. For the entanglement entropy S_ℓ of a subsystem of length ℓ with the rest of system this results in an overall linear growth of entanglement entropy $S_\ell(t) \sim t$ for times $t < \ell/2v_{\max}$, after which it becomes saturated as the subsystem approaches its stationary state [116]. The late time asymptotic value of entanglement entropy of a large subsystem can also be interpreted as the usual thermodynamic entropy [106, 116, 152–154] and consequently the growth of entanglement entropy can be interpreted as a signal of the approach to equilibrium. In the regime dominated by the linear growth, entanglement generation can be characterised by the mean entanglement entropy production rate $\overline{\partial_t S}$, which naturally depends on the post-quench spectrum and its quasi-particle content.

A more general set of entanglement measures are the so-called Rényi entropies

$$S^{(n)}(t) = \frac{1}{1-n} \log \operatorname{Tr} \rho^n(t)\,, \tag{5.1}$$

which in the limit $n \to 1$ converge to the von Neumann entropy $S_A(t)$; the $n = 2$ case

is also known as the purity of the reduced density matrix $\rho_A(t)$. At present there is no generalisation of the approach of [152, 155] to compute the time evolution of Rényi entropies in integrable models and only the stationary values are known [156–158]. In contrast to the von Neumann entanglement entropy the Rényi entropies are not related directly to the thermodynamics of the system. Nevertheless, the quasi-particle picture suggests that the evolution of the Rényi entropies tracks closely that of the von-Neumann entanglement entropy, including the initial linear growth and later saturation. Contrary to the von Neumann entanglement entropy, the Rényi entropies can also be directly accessed by experiment [106, 151].

Much less is known about entanglement dynamics in quenches governed by non-integrable post-quench dynamics. In the case of the quantum Ising chain it was shown in recent studies that switching on an integrability breaking longitudinal magnetic field h leads to non-trivial dynamical phenomena. The dependence of the mean entanglement entropy production rate $\overline{\partial_t S}$ on the quench parameter h shows an anomalous behaviour in the paramagnetic phase: a sudden increase setting at the threshold value of h where a new quasi-particle excitation appears in the spectrum [159]. Using the physical interpretation of the asymptotic entanglement of a large subsystem as the thermodynamic entropy of the stationary (equilibrium) state, this can be recognised as arising from the contribution of mixing entropy between the particle species, and so the effect can be interpreted as a non-equilibrium manifestation of the Gibbs paradox.

The approach to equilibrium can also be characterised by the rates of relaxation of physical observables, such as order parameters. It is natural to expect a close correspondence between the entropy growth rates $S_A^{(n)}(t)$ and the relaxation rates of expectation values of order parameters after the quench. Indeed, in the transverse field Ising spin chain it is possible to compute the Rényi entropy growth rates [129] and the magnetisation relaxation rate [127] explicitly, and for small post-quench density they are related by simple proportionality factors. The same relation between entropy growth and relaxation rates was found in the scaling Ising field theory in [160] when comparing Rényi entropy growth rates to the magnetisation relaxation rate computed in [161].

The relation between entropy growth and relaxation is interesting since magnetisation relaxation rates have a straightforward physical meaning and can be measured much more directly. Therefore it is interesting to study how the behaviour of entanglement entropy growth is reflected in Rényi entropy and especially relaxation rates. In the next chapter we also discuss a recent example of such a relation, where it was observed that dynamical confinement can limit entropy growth, which is accompanied by apparently undamped oscillations in magnetisation [162].

In the case of non-equilibrium manifestation of the Gibbs paradox, magnetisation relaxation rates provide an experimental signature of the effect instead of the entanglement entropy which is not directly observable.

Motivated by the above considerations, the aim of this chapter is to demonstrate the manifestation of the Gibbs paradox mechanism in the quantum Potts spin chain and to analyse the relation between entropy growth and relaxation in quantum quenches in the quantum Ising and Potts spin chains.

The outline of the chapter is as follows:

- In the first part we demonstrate the manifestation of the Gibbs paradox mechanism in the quantum Potts spin chain. Quenches in the paramagnetic phase are considered first in Sec. 5.1, where it is shown that the effect observed in [159] generalises from the Ising to the Potts case. The determination and analysis of spectrum in the paramagnetic phase are presented in Sec. 5.2. Sec. 5.3 analyses the relation between the time evolution and the quasi-particle spectrum, arguing that the scenario proposed in [159] holds for the Potts case as well, and also discussing specific aspects where the Potts model differs from the Ising case considered in [159];
- In the second part we study the relation between relaxation and entropy growth. In Sec. 5.4 we recall exact results for quenches in the transverse field Ising spin chain, also introduced in Sec. 4.4, and exhibit the exact ratios of Rényi entropy rates to the magnetisation relaxation rate for small post-quench density. Sec. 5.5 proceeds to the transverse field Potts spin chain which is non-integrable, therefore we approach it via numerical simulation. For small quenches the ratios of Rényi entropy rates to the magnetisation relaxation rate again turn out to be universal rational numbers, related to the symmetry properties of the order parameter and the replica symmetry underlying the computation of the Rényi entropy. Sec. 5.6 turns to quenches in the paramagnetic phase corresponding to switching on a longitudinal magnetic field, demonstrating that the relaxation rate provides a direct way for observation of the "dynamical Gibbs effect".

5.1 Quenches in the quantum potts spin chain

The 3-state Potts quantum spin chain is defined on the Hilbert space

$$\mathcal{H} = \bigotimes_{i=1}^{L} \left(\mathbb{C}^3\right)_i \tag{5.2}$$

where i labels the sites of the chain of length L. The quantum space $\mathbb{C}^3$ at site i has the basis $|\alpha\rangle$ with $\alpha = 0, 1, 2$ corresponding to the spin degrees of freedom. The dynamics is defined by the Hamiltonian

$$H = -J \sum_{i=1}^{L} \left[\sum_{\alpha=0}^{2} \left(P_i^\alpha P_{i+1}^\alpha + h_\alpha P_i^\alpha \right) + g \tilde{P}_i \right] \tag{5.3}$$

where

$$\begin{aligned} P^\alpha &= |\alpha\rangle\langle\alpha| - \frac{1}{3}\mathbf{1}_{3\times 3} \\ \tilde{P} &= \frac{1}{3} \sum_{\alpha,\alpha'=0}^{2} (1 - \delta_{\alpha\alpha'}) \, |\alpha\rangle\langle\alpha'| \end{aligned} \tag{5.4}$$

and we assume periodic boundary conditions

$$P_{L+1}^\alpha \equiv P_1^\alpha \quad , \quad \tilde{P}_{L+1} \equiv \tilde{P}_1 \tag{5.5}$$

The parameters h_α and g are dimensionless, while energy (and by implication, time) units are specified by J. In all of our subsequent numerical calculations we use units with $J = 1$ and also $\hbar = 1$.

In the absence of the "longitudinal" magnetic fields h_α, the chain is invariant under the $\mathbb{S}_3$ permutation symmetry of the three spin states $\alpha = 0, 1, 2$ and it has a critical point at $g = 1$ corresponding to a phase transition between a paramagnetic (PM) $g > 1$ and ferromagnetic (FM) $g < 1$ case. In the PM phase, there is a single $\mathbb{S}_3$ invariant vacuum, while in the FM phase there are three vacua that become degenerate in the infinite length limit. The order parameter for the transition is given by the magnetisations $m^{(\alpha)} = \langle P_i^\alpha \rangle$ and the quantum critical point separating the phases can be described with a conformal field theory (CFT) with central charge $c = 4/5$.

5.1.1 The quench protocol and the simulation procedure

The non-equilibrium time evolution we study is defined by the following quench protocol. The initial state is the ground state $|\Psi(0)\rangle$ of the pre-quench Hamiltonian

$$H_{\text{pre}} = -J \sum_{i=1}^{L} \left[\sum_{\alpha=0}^{2} \left(P_i^\alpha P_{i+1}^\alpha \right) + g \tilde{P}_i \right] \tag{5.6}$$

which is unique in the paramagnetic phase $g > 1$. We consider four values $g = 1.25,\ 1.5,\ 1.75$ and 2.0, and the time evolution is given by

$$|\Psi(t)\rangle = e^{-iHt} |\Psi(0)\rangle$$

where the post-quench Hamiltonian is given by (5.11):

$$H = -J \sum_{i=1}^{L} \left(\sum_{\alpha=0}^{2} P_i^{\alpha} P_{i+1}^{\alpha} + h P_i^0 + g \tilde{P}_i \right) \tag{5.7}$$

and we consider the time evolution as a function of h which is taken to be non-negative.

The time evolution is computed using the infinite volume time evolving block decimation (iTEBD) algorithm [163]. Using translational invariance, the many-body state is represented as the Matrix Product State (MPS)

$$|\Psi\rangle = \sum_{\ldots,s_j,s_{j+1},\ldots} \cdots \Lambda_o \Gamma_o^{s_j} \Lambda_e \Gamma_e^{s_{j+1}} \cdots | \ldots, s_j, s_{j+1}, \ldots \rangle \ ,$$

where s_j spans the local 3-dimensional spin Hilbert space, $\Gamma^s_{o/e}$ are $\chi \times \chi$ matrices associated with the odd/even lattice site; $\Lambda_{o/e}$ are diagonal $\chi \times \chi$ matrices with the singular values corresponding to the bipartition of the system at the odd/even bond as their entries. The many-body state is initialised to the product state $|\Psi_0\rangle = \bigotimes \frac{1}{\sqrt{3}}(|0\rangle + |1\rangle + |2\rangle)$. The ground state $|\Psi(0)\rangle$ was obtained by time-evolving the initial state $|\Psi_0\rangle$ in imaginary time by the pre-quench Hamiltonian (5.6), using a second-order Suzuki-Trotter decomposition of the evolution operator with imaginary time Trotter step $\tau = 10^{-3}$. Due to the presence of an energy gap, an auxiliary dimension $\chi_0 = 81$ was sufficient to have a very accurate result for the ground state.

The post-quench time evolution was obtained by evolving $|\Psi(0)\rangle$ with the post-quench Hamiltonian (5.7) in real time, again using a second-order Suzuki-Trotter decomposition of the evolution operator with real time Trotter step $\delta t = 0.005$. To keep the truncation error small the auxiliary dimension was allowed to grow up to $\chi_{\max} = 243$ which was sufficient to reach a maximum time $T = 40$. For more on the iTEBD algorithm see Appendix C.

5.1.2 Entanglement growth rate

The central issue of this analysis concerns the evolution of the half-system entanglement entropy $S(t)$. This is defined by cutting the system into two halves $\mathcal{H}$ and $\bar{\mathcal{H}}$ and introducing the reduced density matrix

$$\rho_{\mathcal{H}}(t) = \mathrm{Tr}_{\bar{\mathcal{H}}} |\Psi(t)\rangle\langle\Psi(t)|$$

Then the half-system entanglement entropy is given by

$$S(t) = -\mathrm{Tr}_{\mathcal{H}} \rho_{\mathcal{H}}(t) \log \rho_{\mathcal{H}}(t) \, .$$

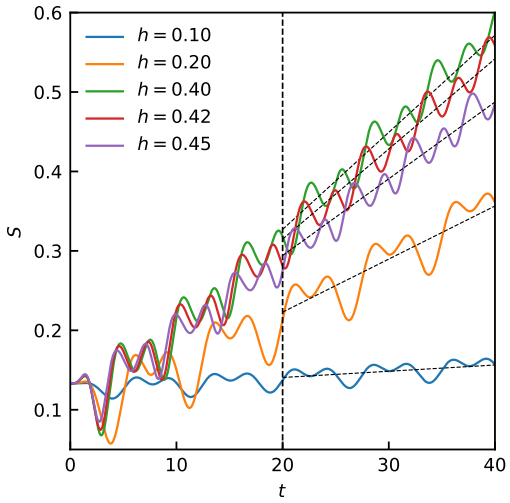

Figure 5.1: The time evolution of $S(t)$ for $g = 1.75$ and $h = 0.10$, 0.20, 0.40, 0.42 and 0.45, where time is measured in units of $1/J$. The vertical line drawn at time t shows the limit above which the average slope was extracted, the corresponding fits are shown by the black dotted lines.

As illustrated in Fig. 5.1 after a relatively short transient $S(t)$ shows a linear trend (with some slowly decaying oscillations) as expected after a global quantum quench. A numerical estimation of the mean entanglement entropy production rate $\overline{\partial_t S}$ was obtained by a linear fit of the iTEBD data in the time window $20 \leq t \leq 40$. The dependence of $\overline{\partial_t S}$ on h for the values of the transverse field $g = 1.25,\ 1.5,\ 1.75$ and 2.0 is shown in Fig. 5.2. It can be seen clearly that $\overline{\partial_t S}$ has a local minimum at a value $h_{\min}$, the values of which are summarised in the following table:

g	1.25	1.5	1.75	2.0
$h_{\min}$	0.10	0.28	0.49	0.72

This very peculiar, non-monotonous behaviour of $\overline{\partial_t S}$ was previously seen for quenches in the paramagnetic Ising spin chain [159] where it was explained by the effect of the quasi-particle spectrum on the entanglement entropy production. In the following we investigate the detailed dynamics of the Potts model to see whether it confirms the scenario proposed in [159], which posited that the reversal of the decreasing trend in $\overline{\partial_t S}$ at $h_{\min}$ is due to the appearance of a new quasi-particle excitation in the spectrum, which enhances entropy production by increasing the number of species available.

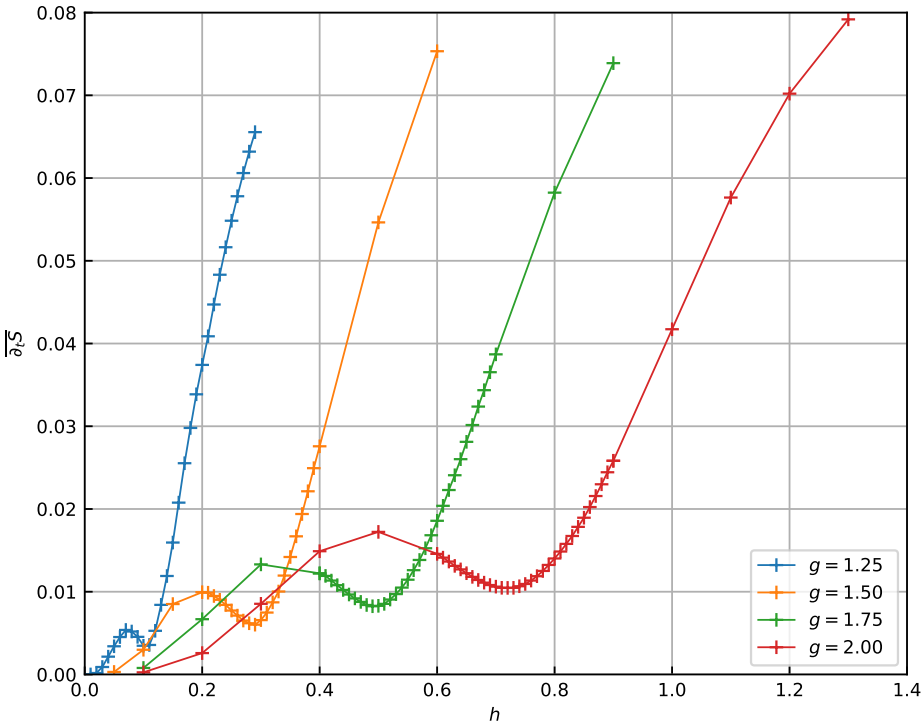

Figure 5.2: The mean entanglement entropy production rate $\overline{\partial_t S}$ as a function of h for $g = 1.25,\ 1.5,\ 1.75$ and 2.0.

5.2 Spectrum of the paramagnetic Potts spin chain

5.2.1 The case $h_\alpha = 0$

In the ferromagnetic phase the quasi-particle spectrum of the chain consists of kink excitations $K_{\alpha\beta}$ connecting the vacua according to the adjacency condition

$$\alpha - \beta = \pm 1 \mod 3 \tag{5.8}$$

with an obvious action of the permutation symmetry.

In the paramagnetic phase the quasi-particle spectrum consists of doubly degenerate magnons. Choosing two generators $\mathcal{C}$ and $\mathcal{T}$ for the group $\mathbb{S}_3$ which satisfy the relations

$$\mathcal{T}^3 = 1 \quad , \quad \mathcal{C}^2 = 1 \quad , \quad \mathcal{C}\mathcal{T}\mathcal{C} = \mathcal{T}^{-1} \tag{5.9}$$

one can introduce a basis in the magnonic space with one-particle states at fixed momentum given by $|A(k)\rangle$and $|\bar{A}(k)\rangle$. They form the two-dimensional irreducible

representation of $\mathbb{S}_3$ defined by the relations:

$$\begin{aligned}\mathcal{T}|A(k)\rangle &= e^{2\pi i/3}|A(k)\rangle \\ \mathcal{T}|\bar{A}(k)\rangle &= e^{-2\pi i/3}|\bar{A}(k)\rangle \\ \mathcal{C}|A(k)\rangle &= |\bar{A}(k)\rangle\end{aligned} \tag{5.10}$$

For more information regarding the quasi-particle spectrum of the chain we refer the interested reader to the work [164] and references therein.

5.2.2 The case $h_\alpha \neq 0$

Switching on one or more longitudinal magnetic fields h_α leads to an explicit breaking of the symmetry group $\mathbb{S}_3$. In the ferromagnetic case this results in confinement which is well-studied in the scaling limit [165–169]. However, in this work we are interested in the paramagnetic phase, and consider switching on one of the fields $h_0 = h \neq 0$ and keeping $h_{1,2} = 0$. Therefore our Hamiltonian is

$$H = -J\sum_{i=1}^{L}\left(\sum_{\alpha=0}^{2} P_i^\alpha P_{i+1}^\alpha + hP_i^0 + g\tilde{P}_i\right) \tag{5.11}$$

This partially breaks the symmetry $\mathbb{S}_3$, leaving only a $\mathbb{Z}_2$ subgroup intact. We choose the generator $\mathcal{C}$ to correspond to the unbroken subgroup, which in this case is generated by the transformation swapping the spin directions 1 and 2. Then for $h = 0$ one can introduce the quasi-particle basis corresponding to the eigenstates of $\mathcal{C}$

$$|A_\pm(k)\rangle = \frac{1}{\sqrt{2}}\left(|A(k)\rangle \pm |\bar{A}(k)\rangle\right) \tag{5.12}$$

For $h = 0$ they are degenerate, but for a non-zero h the degeneracy is lifted. As shown below, similarly to the case of the Ising spin chain [159], for any fixed $g > 1$ there is some critical value h_{crit} above which two A_+ quasi-particles form a $\mathcal{C}$-even bound state B which can formally be written as a two-particle state with imaginary relative momentum

$$|B(k)\rangle \propto |A_+(k/2 + i\kappa/2)A_+(k/2 - i\kappa/2)\rangle\,. \tag{5.13}$$

It is likely that the spectrum shows a larger variation when considering the whole range of parameters h_α and g (in the Ising case, there also exist another bound state for larger values of h: cf. [159] for the spin chain, and [170] for the scaling field theory). However, in this work we restrict ourselves to the regions $0 \leq h \leq h_{\text{crit}}$ and $h_{\text{crit}} \lesssim h$, and leave a more complete exploration of the parameter space for the future.

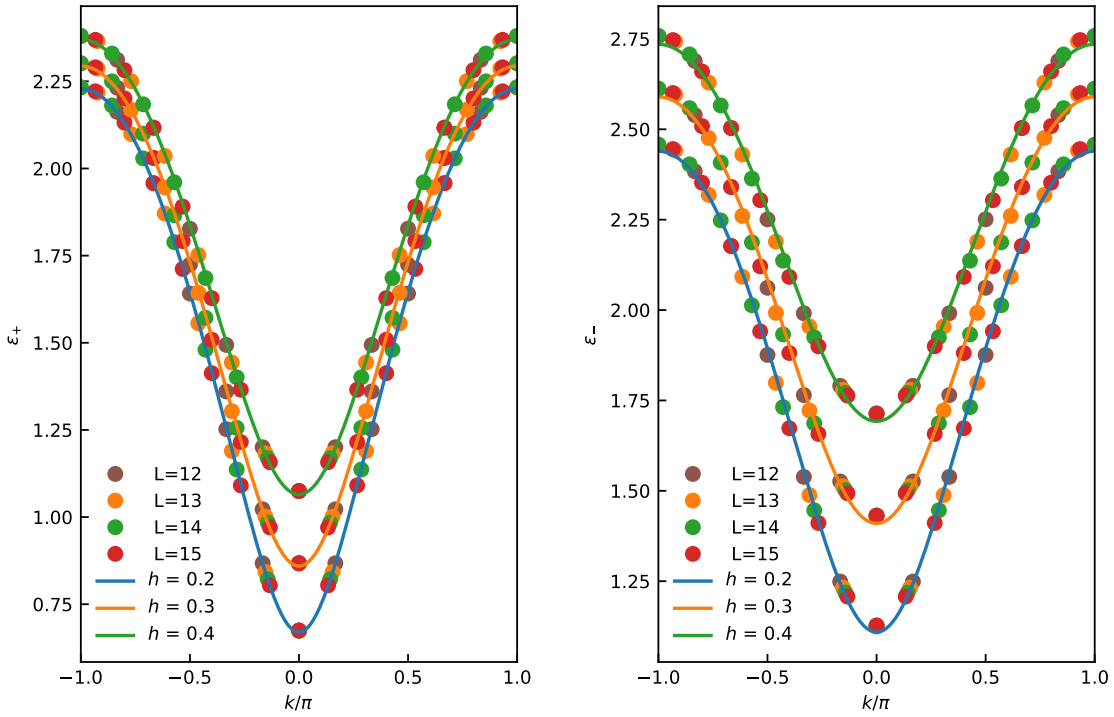

(a) A_+ **(b)** A_-

Figure 5.3: Dispersion relations for A_+ and A_- for $g = 1.5$ and $h = 0.2$, 0.3 and 0.4. Energies are shown in units of J, while momentum is shown in units of $1/a$, where a is the lattice spacing.

5.2.3 Quasi-particle dispersion relations for $h > 0$

We determined the quasi-particle dispersion relations applying exact diagonalisation of the Hamiltonian (5.11). After determining a few hundred states at the bottom of the spectrum, they were sorted into bins containing energy levels that are degenerate within numerical precision. Most of the eigenvalues appear in degenerate pairs of states with opposite total momentum k and $-k$, with the exception of singlets with momenta $k = 0$ and $k = \pi$. Momenta of states can be obtained by diagonalising the shift operator $\mathcal{S}$ mapping site i to site $i+1$ mod L within the bins. In the paramagnetic phase, the ground state is an isolated singlet, followed by two branches of one particle states corresponding to momenta

$$k_n = n\frac{2\pi}{L}\ ,\ n = \left[-\frac{L}{2}\right] + 1, \ldots, \left[\frac{L}{2}\right] \tag{5.14}$$

where the two branches are distinguished by the eigenvalue of $\mathcal{C}$ which corresponds to the unbroken $\mathbb{Z}_2$. We computed the quasi-particle branches for chain lengths L from 12

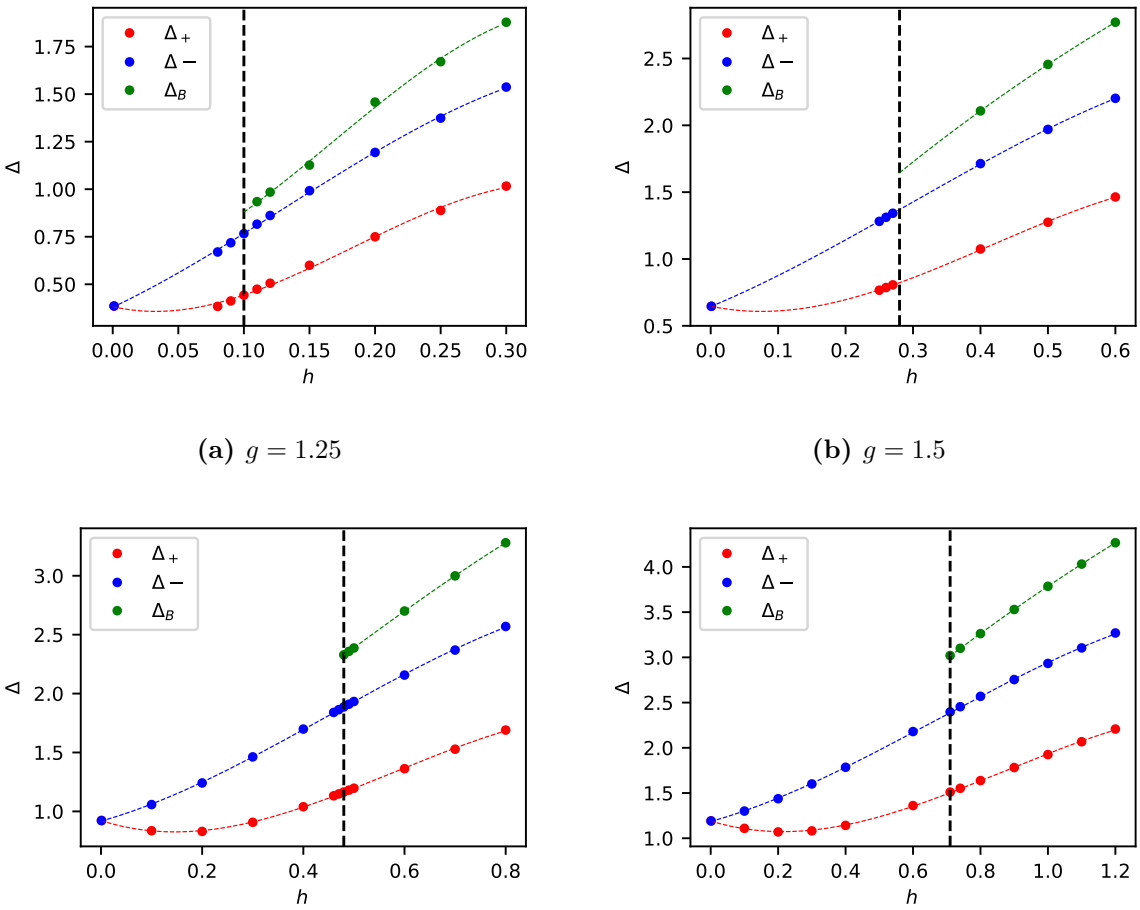

(a) $g = 1.25$ **(b)** $g = 1.5$

(c) $g = 1.75$ **(d)** $g = 2$

Figure 5.4: Quasi-particle gaps $\Delta_\pm$ and Δ_B (in units of J) as functions of h. The vertical dashed line shows the threshold value of h above which the bound state quasi-particle B exists.

to 15. An example result is shown in Fig. 5.3.

It turns out that dependence on the finite size L is very weak, so one can treat the results from different chain lengths L as sampling the same (infinite volume) dispersion relations $\epsilon_\pm(k)$. In addition, the fitting functions

$$\epsilon_\pm(k) = \sqrt{a_\pm + b_\pm \cos k} \tag{5.15}$$

inspired by the free fermion dispersion relation provide an excellent description of the numerical data. The fits can be used to determine both the gaps

$$\Delta_\pm = \sqrt{a_\pm + b_\pm} \tag{5.16}$$

and the Lieb-Robinson (LR) velocities

$$v_{\max\pm} = \max_k \frac{\partial \epsilon_\pm}{\partial k} \tag{5.17}$$

To find the bound state threshold, we use a different approach for the determination of the gap that leads to a much more precise result. Note that for each chain length one can obtain the value of the gap $\Delta_\pm(L)$ from the energy of the first/second zero momentum excited state relative to the ground state. Using the theory of finite size effects [171] one can then extrapolate these to infinite volume using the fitting functions

$$\Delta_\pm(L) = \Delta_\pm + \gamma_\pm e^{-\mu_\pm L} \tag{5.18}$$

For the choices of the transverse field $g = 1.25,\ 1.5,\ 1.75$ and 2.0, the dependence of the gaps and LR velocities on the longitudinal field h are shown in Figs. 5.4 and 5.5, respectively.

5.2.4 Bound state threshold

Determination of $h_{\mathbf{crit}}$

For $h < h_{\rm crit}$, the part of the spectrum above the two quasi-particle branches consists of many-particle states called the continuum. Since $\Delta_+ < \Delta_-$ for $h > 0$, the lowest lying levels are two-particle states[1]

$$|A_+(k/2+q/2)A_+(k/2-q/2)\rangle$$

of total momentum k taking the values (5.14), while q is their relative momentum, which is quantised differently due to interaction effects involving the scattering phase shift [172]. The lowest lying even state above $|A_+(0)\rangle$ corresponds to a zero-momentum state

$$|A_+(q_{\min}/2)A_+(-q_{\min}/2)\rangle$$

where $q_{\min}$ is the smallest allowed value for the relative momentum q. When h approaches $h_{\rm crit}$, $q_{\min}$ goes to 0 and for $h > h_{\rm crit}$ it turns imaginary according to the standard quantum mechanical relation between scattering and bound states, with the state becoming identical to

$$|B(0)\rangle$$

[1] In fact, this state can hybridise with A_-A_- two-particle states, but it does not change the subsequent considerations and so we omit this term for simplicity.

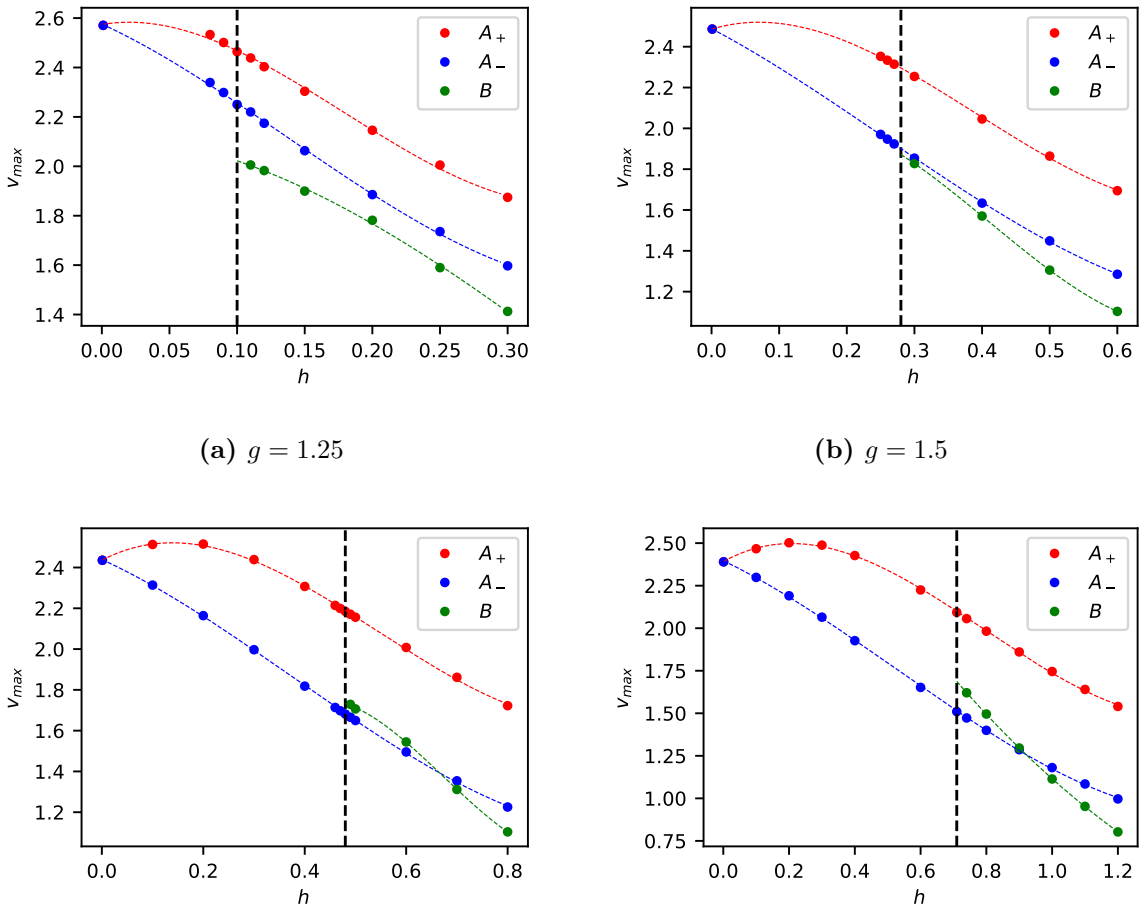

(a) $g = 1.25$ **(b)** $g = 1.5$

(c) $g = 1.75$ **(d)** $g = 2$

Figure 5.5: Lieb-Robinson velocities $v_{\max\pm}$ and $v_{\max B}$ as functions of h. The vertical dashed line shows the threshold value of h above which the bound state quasi-particle B exists. Velocities are shown in units of Ja, where a is the lattice spacing.

i.e. a zero-momentum level with a single B quasi-particle. Denoting the energy gap of this level by Δ_B one has

$$\begin{aligned} \Delta_B &> 2\Delta_+ \quad h < h_{\text{crit}} \\ \Delta_B &= 2\Delta_+ \quad h = h_{\text{crit}} \\ \Delta_B &< 2\Delta_+ \quad h > h_{\text{crit}} \end{aligned} \tag{5.19}$$

which makes possible the determination of h_{crit}.

Finite size effects can be eliminated using the exponential extrapolation according

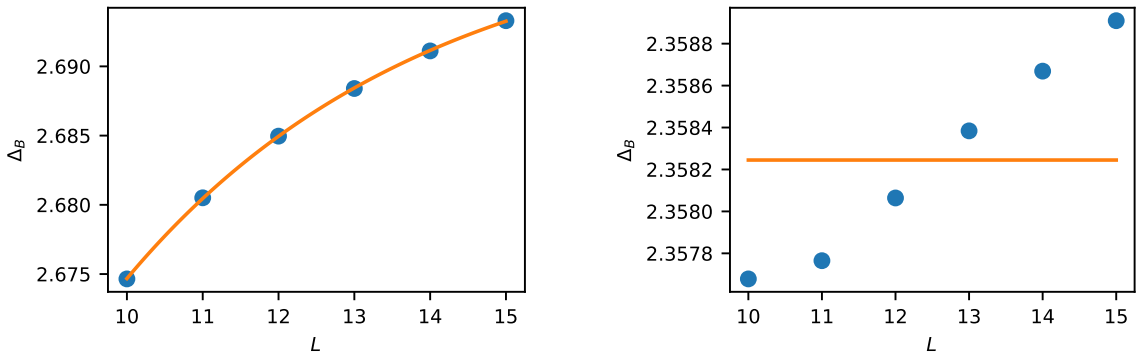

(a) $h = 0.6$ **(b)** $h = 0.49$

Figure 5.6: Finite size extrapolation for the gap Δ_B (in units of J). Note that well above the threshold value of $h \approx 0.49$ the exponential fit works very well (a), while at the threshold it completely misses (b). However, comparing (a) abd (b) shows that the range of variation of Δ_B is much smaller when at the threshold, corresponding to the vanishing of the leading order finite size correction.

to the leading order finite size dependence predicted in [171]

$$\Delta_B(L) = \Delta_B + \gamma_B e^{-\mu_B L} \tag{5.20}$$

when $h > h_{\text{crit}}$. Here $1/\mu_B$ is a length scale corresponding to the spatial extension of the A_+A_+ bound state wave function, which diverges at $h = h_{\text{crit}}$ and so the simple exponential extrapolation prescribed by (5.20) becomes impossible in the vicinity of the threshold h_{crit}, as illustrated in Fig. 5.6. However, in that case γ_B vanishes as well since it corresponds to the effective coupling between two A_+ particles which changes sign from attractive to repulsive and so vanishes at the threshold, so the finite volume dependence is much weaker as it is determined by subleading corrections.

For $h < h_{\text{crit}}$ the energy level is a scattering state and volume dependence is different (decaying as a power in L) and much better numerical data are necessary in order to describe it in terms of scattering characteristics [172]. However, since we are not interested in finding the actual value of the energy level in that range we can simply fit it by the same function (5.20) to keep our procedure uniform.

The value of h_{crit} can be determined by plotting Δ_B/Δ_+ as a function of h and finding the value where it crosses 2, as shown in Fig. 5.7.

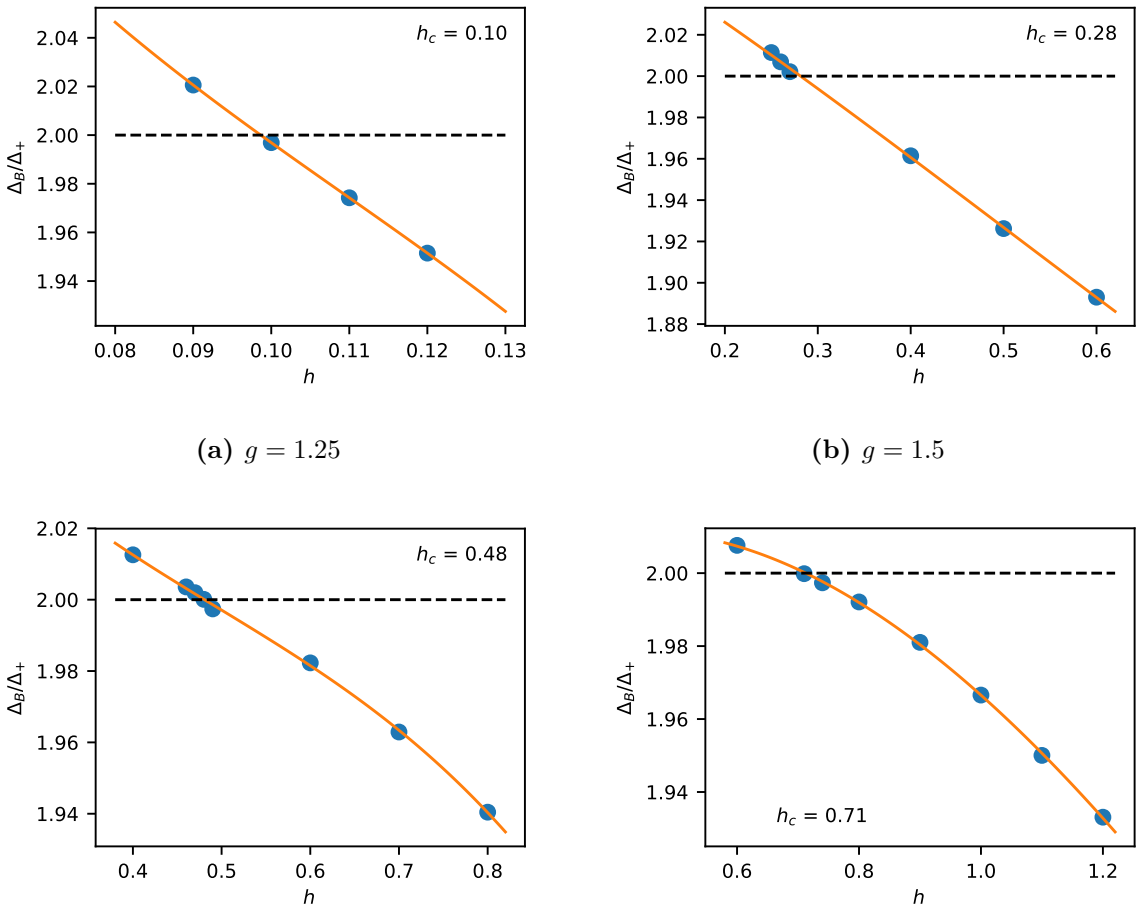

(a) $g = 1.25$ **(b)** $g = 1.5$

(c) $g = 1.75$ **(d)** $g = 2$

Figure 5.7: Determining h_{crit} from Δ_B/Δ_+ as a function of h.

Dispersion relation for B

In the regime $h > h_{\text{crit}}$ the states with momenta (5.14) lying just above the two quasi-particle branches $A_\pm$ correspond to single-quasi-particle states $|B(k_n)\rangle$, and their energies allow the determination of the dispersion relation of B as shown in Fig. 5.8. Just as it was noted in the case of the Ising chain [159], the dispersion relation can be fitted well with the function

$$\epsilon_B(k) = \sqrt{a_B + b_B \cos k + c_B \cos 2k}$$

from which it is possible to determine both the gap $\Delta_B = \sqrt{a_B + b_B + c_B}$ and the Lieb-Robinson velocity $v_{\max\pm} = \max_k \frac{\partial \epsilon_\pm}{\partial k}$. Just as in the case of the "elementary" quasi-particles $A_\pm$, the gap Δ_B can also be determined using the extrapolation (5.20) which

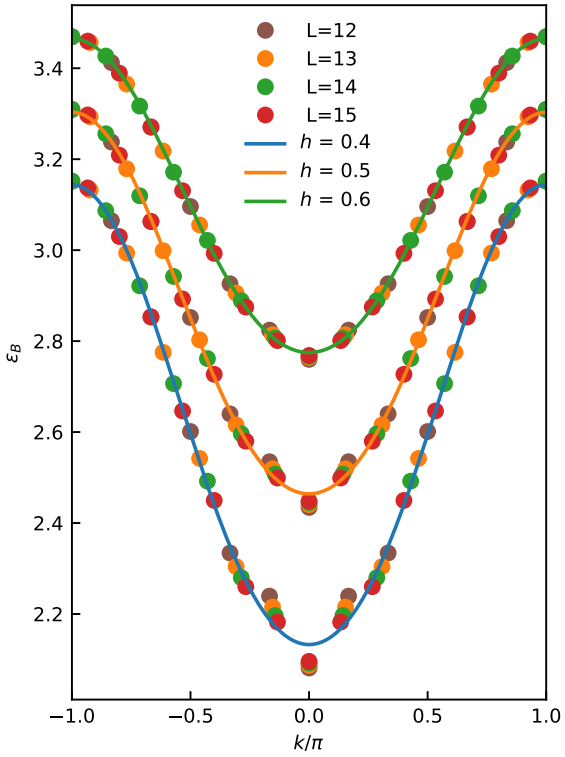

Figure 5.8: Dispersion relation for B at $g = 1.5$ and $h = 0.4$, 0.5 and 0.6. Energies are shown in units of J, while momentum is shown in units of $1/a$, where a is the lattice spacing.

leads to a more accurate result. It is also clear from Fig. 5.8 that moving closer to the threshold i.e. for smaller h, when the quasi-particle B becomes more weakly bound the finite size dependence becomes stronger, which is in fact expected from 5.20 since when the spatial extension of the bound state wave function increases, the exponent μ_B becomes smaller.

5.3 Quasi-particle spectrum and non-equilibrium time evolution

5.3.1 Time evolution of magnetisation

The three components of longitudinal magnetisation can be computed as

$$m_\alpha(t) = \langle \Psi(t) | P_i^\alpha | \Psi(t) \rangle$$

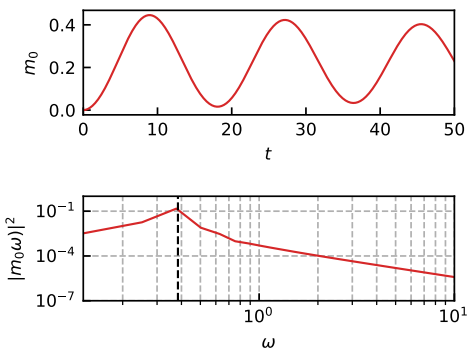

(a) $m_1(t)$ and its FPS for $h = 0.06$

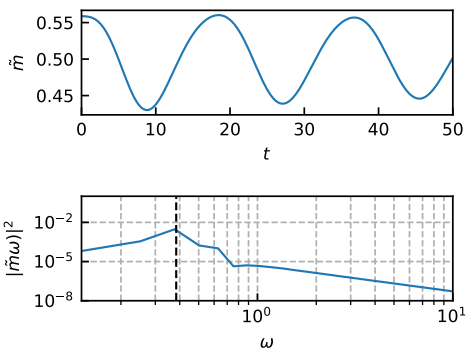

(b) $\tilde{m}(t)$ and its FPS for $h = 0.06$

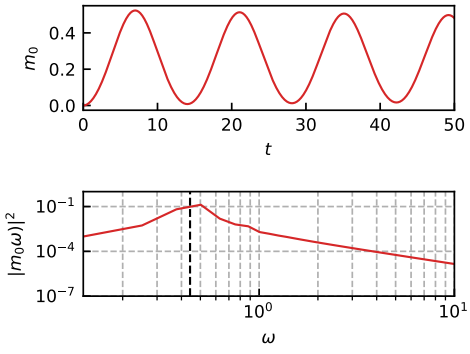

(c) $m_1(t)$ and its FPS for $h = 0.1$

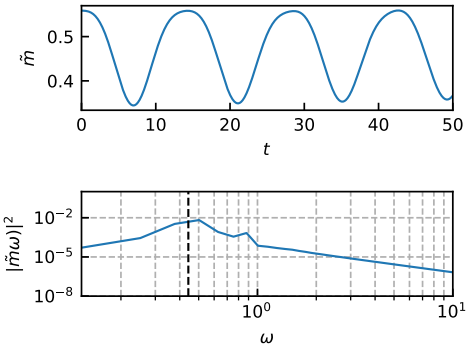

(d) $\tilde{m}(t)$ and its FPS for $h = 0.1$

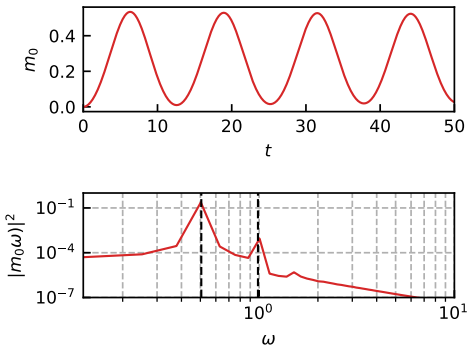

(e) $m_1(t)$ and its FPS for $h = 0.12$

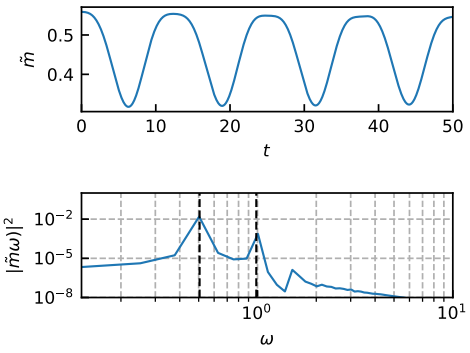

(f) $\tilde{m}(t)$ and its FPS for $h = 0.12$

Figure 5.9: Time evolution of the longitudinal and transverse magnetisations $m_0(t)$ resp. $\tilde{m}(t)$ for $g = 1.25$ and $h = 0.06$, 0.10 and 0.12, showing both the real time dependence and its Fourier power spectrum (FPS). Frequencies are shown in units of J.

Due to translation invariance they are independent of the spatial position i and from the definitions (5.4) and due to the residual symmetry $\mathbb{Z}_2$ they satisfy

$$m_1(t) = m_2(t) = -\frac{m_0(t)}{2} \ .$$

Transverse magnetisation can be defined as

$$\tilde{m}(t) = \langle \Psi(t) | \tilde{P}_i | \Psi(t) \rangle \ .$$

An example of their time evolution is shown in Fig. 5.9. Following [162] and [159], the Fourier spectra of their time series can be used as to determine the post-quench quasi-particle spectrum via a sort of "quench spectroscopy". The power spectra were obtained using FFT with an angular frequency resolution $d\omega = 2\pi/T \simeq .157$ and are also illustrated in Figs. 5.9. They agree well with the predicted quasi-particle gaps; note that due to the $\mathbb{Z}_2$ symmetry of the initial state preserved by the post-quench Hamiltonian (5.7), only $\mathcal{C}$-even states are visible. The second peak in the power spectrum which appears above the critical value of h is the signature of a new bound state, in agreement with the predicted spectrum from exact diagonalisation.

We remark that the post-quench state has a finite energy density, which induces corrections in the quasi-particle spectrum and introduces a finite life-time. The presence of well-defined quasi-particle peaks close to the values extracted from the spectrum of the zero-density system demonstrates that the post-quench dynamics can be described in terms of the quasi-particle picture despite the non-integrability of the system, similarly to the Ising case considered in [159].

5.3.2 Time evolution of entanglement entropy

Now we return to the effect observed in Fig. 5.2. Starting our discussion with the decreasing trend just before $h_{\min}$, we note that while presently a full quantitative understanding is missing, the qualitative picture is clear. The initial increase in $\overline{\partial_t S}$ comes from the energy density of the quench increasing with h as shown in Fig. 5.10. The subsequent decline in $\overline{\partial_t S}$ is consistent with the quasi-particle gaps increasing, and the Lieb-Robinson velocities decreasing with h as demonstrated in Figs. 5.4 and 5.5, respectively. In fact for very large values of h the dynamics of the whole chain stops since the Potts spins are locked in the direction of h, suppressing the propagation of excitations along the chain as shown in the next Subsection.

Now let us consider the reversal of the decreasing trend, which happens at the position $h_{\min}$ of the local minimum in $\overline{\partial_t S}$. The value of $h_{\min}$ can be compared to the threshold h_{crit} for the excited even quasi-particle B:

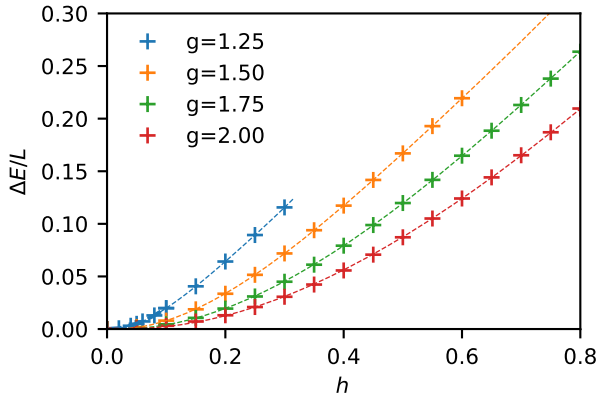

Figure 5.10: Density of energy (in units of J/a, with a denoting the lattice spacing) released by the quench as a function of h.

g	1.25	1.5	1.75	2.0
h_{min}	0.10	0.28	0.49	0.72
h_{crit}	0.10	0.28	0.48	0.71

It is clear that the two positions coincide within numerical accuracy (corresponding to the number of digits shown in the above table) for small values of g, while h_{min} is slightly larger than h_{crit} for larger g. This is the same pattern as observed for the Ising spin chain in [159], and it can be explained in the same way.

Firstly, the appearance of the new quasi-particle species B for $h > h_{\text{crit}}$ leads to a steep increase in the entanglement entropy production due to the contribution of Gibbs mixing entropy arising from species information carried by the post-quench quasi-particles. While a full quantitative description is lacking at the moment, there is a simple argument using quasi-particle pair production rates determined in the scaling Ising field theory that shows that the presence of mixing entropy can lead to an order-of-magnitude increase in entropy production. This argument is presented in [159], and we do not repeat it here in detail.

Secondly, the fact that $h_{\text{min}} - h_{\text{crit}}$ is non-zero and grows with g can also be easily understood. Note that before particle B appears, $\overline{\partial_t S}$ has a decreasing trend which is reversed by the appearance of B. However, the rate of production of pairs containing B is expected to rise only gradually. The reason is when B is only very weakly bound, the finite density post-quench medium easily destabilises it. So the higher the value of h_{crit}, the larger is the quench when B appears, leading to a higher destabilising effect of the post-quench medium to be overcome. Since h_{crit} increases with g, the difference

$h_{\min} - h_{\text{crit}}$ is also expected to increase with g as well. This is indeed what was observed both here in the Potts case, and also the Ising case considered in [159].

5.3.3 Large h behaviour

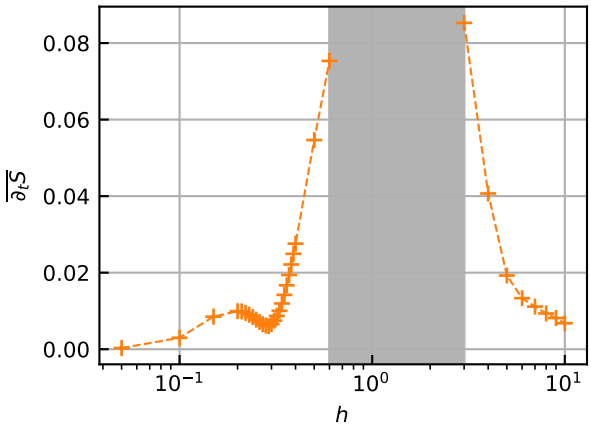

Figure 5.11: Entanglement entropy production rate $\overline{\partial_t S}$ for $g = 1.5$, including the regime of large $h > 0$. The shaded region corresponds to a parameter range where entropy growth was so fast that $\overline{\partial_t S}$ could not be evaluated from iTEBD as it was impossible to follow the dynamics for long enough times.

Recalling the Hamiltonian (5.7) we see that for large $h \gg g$ the spins of the chain are essentially frozen in direction 0. This is consistent with the increasing gaps and decreasing velocities for the excitations shown in Figs. 5.4 and 5.5. For a very large value of h, the dynamics slows down and $\overline{\partial_t S}$ goes to zero, as shown in Fig. 5.11.

5.3.4 The regime $h < 0$

When $h < 0$, no freezing of the dynamics occurs for $h \ll -g$. The reason is that although a large negative h freezes direction 0, the energetically favoured directions 1 and 2 remain degenerate and so the chain effectively enters an Ising regime where $\overline{\partial_t S}$ grows monotonously with the amount of energy injected into the system as shown in Fig. 5.12. Examining the quasi-particle threshold shows that here A_- is lighter than A_+ and there is even a threshold value $h_-(\approx -0.19$ for $g = 1.5)$ below which $\Delta_+ > 2\Delta_-$. Therefore, for $h < h_-$ the excitation A_+ becomes unstable and decays into a pair of A_- particles; as a result, the number of available species decreases.

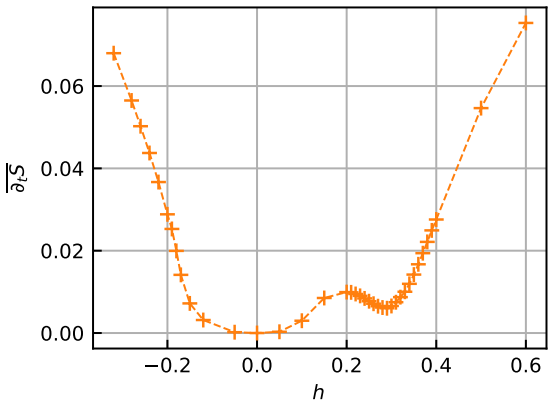

Figure 5.12: Entanglement entropy production rate $\overline{\partial_t S}$ for $g = 1.5$ including the range $h < 0$

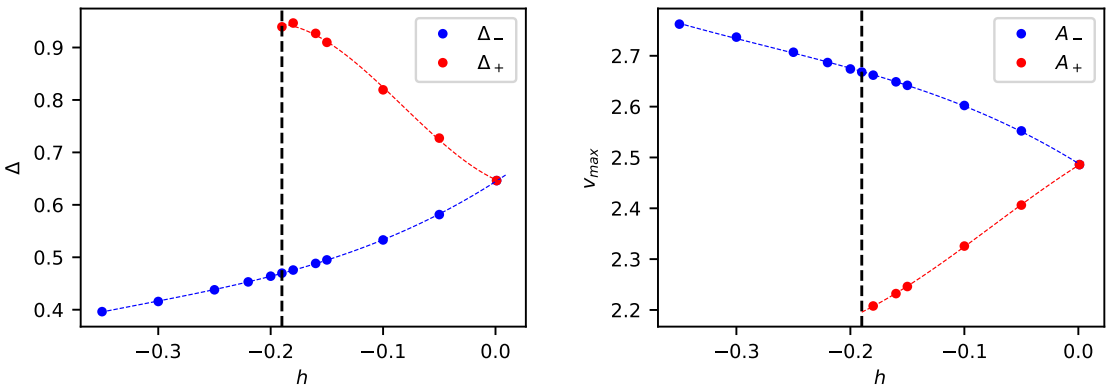

Figure 5.13: Quasi-particle gaps $\Delta_\pm$ (in units of J) and Lieb-Robinson velocities $v_{\max\pm}$ (in units of Ja, where a is the lattice spacing) for $h < 0$ (with $g = 1.5$). The vertical dashed line shows the threshold value $h_- \approx -0.19$ beyond which A_+ becomes unstable and decays into two A_- quasi-particles.

Turning to the details of the quasi-particle spectrum, a direct calculation using exact diagonalisation (as described in Section 5.2) shows that the quasi-particle gap Δ_- rapidly decreases, while the Lieb-Robinson velocities $v_{\max-}$ increases when h becomes more negative as shown in Fig. 5.13. Coupled with the rapid increase of the energy density injected in the quench very similar to the $h > 0$ domain (starting with a quadratic rise and having a linear asymptotics for large $|h|$, cf. Fig. 5.10), this explains the rapid rise in $\overline{\partial_t S}$. Note that even though A_+ becomes unstable at h_-, it barely has any effect on entropy generation. The reason is that the gap and Lieb-Robinson velocity of A_+ behave

in an opposite way compared to A_-, so with h becoming more negative the share of A_+ in the entropy production decreases rapidly. By the point when h passes through h_-, the only observable effect of A_+ becoming unstable is a hint of an inflection point in the dependence of $\overline{\partial_t S}$ on h at the threshold (cf. Fig. 5.12).

We turn now to the discussion on the relation between relaxation and entropy generation in quantum spin chains.

5.4 Quenches in the transverse field Ising spin chain

Due to a slight change of notation, we recall the main concepts already introduced in 4.4 when quenching the Transverse Field Ising Chain, defined by the Hamiltonian

$$H(g) = -J \sum_{j=1}^{N} \left(\sigma_j^x \sigma_{j+1}^x + g \sigma_j^z \right), \tag{5.21}$$

where σ_j^α are the Pauli matrices at site j, and J is taken to be positive. The model can be solved exactly by mapping the spin variables to Majorana fermion modes α_k with momenta $k = 2\pi r/N$ [2] [173, 174], in terms of which the Hamiltonian becomes

$$H(g) = \sum_k \epsilon_g(k) \alpha_k^\dagger \alpha_k + E_0(g), \tag{5.22}$$

with the dispersion relation

$$\epsilon_g(k) = 2J\sqrt{1 + g^2 - 2g\cos k} \tag{5.23}$$

and ground state energy

$$E_0(g) = -\frac{1}{2} \sum_k \epsilon_g(k). \tag{5.24}$$

We consider a quench protocol where the pre-quench Hamiltonian is given by a transverse Ising Hamiltonian with transverse field g_0, and the quench corresponds to switching the transverse field to a new value g at $t = 0$. Then both the pre-quench and the post-quench models are described by free Majorana fermions $\tilde{\alpha}_k$ and α_k, respectively, related by the Bogolyubov transformation

$$\begin{aligned} \tilde{\alpha}_k &= \cos\left(\frac{\Delta_k}{2}\right) \alpha_k + i \sin\left(\frac{\Delta_k}{2}\right) \alpha_{-k}^\dagger, \\ \cos \Delta_k &= \frac{g g_0 - (g + g_0)\cos k + 1}{\sqrt{1 + g^2 - 2g\cos k}\sqrt{1 + g_0^2 - 2g_0 \cos k}}. \end{aligned} \tag{5.25}$$

[2] The momentum quantum number r can take either half-integer or integer values, corresponding to the Neveu-Schwarz and Ramond sectors.

The initial state can be written in terms of the post-quench eigenstates as

$$|\Psi_0\rangle \equiv |0;g_0\rangle = \frac{1}{\mathcal{N}} \exp\left\{ i \sum_k K(k) \alpha_k^\dagger \alpha_{-k}^\dagger \right\} |0;g\rangle \,, \tag{5.26}$$

with

$$K(k) = \tan\left(\frac{\Delta_k}{2}\right) \quad , \quad \cos\Delta_k = \frac{1-K^2(k)}{1+K^2(k)} \,, \tag{5.27}$$

which allows for a detailed evaluation of the time evolution [127].

5.4.1 Magnetisation

For a quench inside the ferromagnetic regime i.e. both $g, g_0 < 1$, the order parameter evolves in time according to [127]

$$m(t) \equiv \langle \Psi_0(t)| \sigma^x |\Psi_0(t)\rangle \simeq (\mathcal{C}_{FF})^{\frac{1}{2}} \exp\left\{ \left[t \int_0^\pi \frac{dk}{\pi} \epsilon_g'(k) \ln|\cos\Delta_k| \right] \right\} , \tag{5.28}$$

where $\mathcal{C}_{FF}$ was conjectured to be

$$\mathcal{C}_{FF} = \frac{1 - gg_0 + \sqrt{(1-g^2)(1-g_0^2)}}{2\sqrt{1-gg_0}(1-g_0^2)^{\frac{1}{4}}} \,, \tag{5.29}$$

which follows by applying the cluster decomposition principle to the two-point function. The two-point function and the validity of (5.29) was recently reconsidered and a new result on $\mathcal{C}_{FF}$ is presented in [128]. Alternatively, a form factor expansion results in

$$m(t) \sim \sqrt{\xi}[1 + I(t) + O(t^{-1})] e^{-\Gamma t} \,, \tag{5.30}$$

where

$$\begin{aligned} \sqrt{\xi} &= (1-g^2)^{1/8} \equiv \langle 0;g| \sigma^x |0;g\rangle \\ I(t) &= A_0 \frac{\cos\left(2\epsilon_g(0)t + \frac{3\pi}{4}\right)}{t^{3/2}} - A_\pi \frac{\cos\left(2\epsilon_g(\pi)t - \frac{3\pi}{4}\right)}{t^{3/2}} + o(t^{-3/2}) \\ \Gamma &= \int_0^\pi \frac{dk}{\pi} K^2(k)[2\epsilon_g'(k)] + O(K^6) \end{aligned} \tag{5.31}$$

with

$$A_k = \frac{hJ^2 K'(k)}{\sqrt{\pi}\epsilon_g(k)^2 \left|\epsilon_g''(k)\right|^{3/2}} \,, \qquad k = 0, \pi \,, \tag{5.32}$$

which is equivalent to (5.28) in the limit where $K^2(k) \ll 1$.

In the scaling limit the relaxation rate Γ in (5.31) is given by [161]

$$\Gamma = 2M \int_0^\infty \frac{d\theta}{\pi} \hat{K}^2(\theta) \sinh\theta \,, \tag{5.33}$$

where $M = 2J|1-h|$ is the fermion mass which is kept fixed in the scaling limit, and

$$i\hat{K}(\theta) = K(\theta) = i \tan\left[\frac{1}{2}\arctan(\sinh\theta) - \frac{1}{2}\arctan\left(\frac{M}{M_0}\sinh\theta\right)\right]. \tag{5.34}$$

with $M_0 = 2J|1-h_0|$ denoting the fermion mass of the pre-quench system.

5.4.2 Rényi entropies vs. relaxation rate

In the scaling limit

Consider a spatial partition of the system into a subsystem A its complement $\bar{A}$, the Rényi entropies are given by

$$S_n := \frac{1}{1-n} \log \mathrm{Tr}\, \rho_A^n \,. \tag{5.35}$$

Its evaluation can be handled by the replica trick where n is the number of replicas and Rényi entropy for an interval can be represented as a correlator of branch-point twist fields [175, 176].

Quenching the transverse field corresponds to changing the mass parameter from a value m_0 to m in the scaling Ising field theory (free Majorana fermion). For the case when the subsystem A spans the (semi-infinite) left/right half of space, the Rényi entropies can be computed as the expectation values of the appropriate branch-point twist fields, which can be evaluated to $O(K^2)$ using form factors resulting in [160]

$$S_n(t) = S_n(0) + \frac{\Gamma n t}{2(n-1)} + \frac{n\mu^2}{64\pi M t(n-1)} + \frac{\mu}{8\sqrt{\pi}n} \frac{\cos\frac{\pi}{2n}}{\sin^2\frac{\pi}{2n}} \frac{\cos\left(2Mt - \frac{\pi}{4}\right)}{(n-1)(Mt)^{3/2}} + O(t^{-3}), \tag{5.36}$$

where

$$\mu = 1 - \frac{M}{M_0} \tag{5.37}$$

parameterises the quench magnitude. We remark that it is unclear at present how to carry out the $n \to 1$ limit to obtain the von Neumann entropy in the scaling field theory.

The result (5.36) implies that in the leading order in μ the following relation holds between the relaxation rate of the magnetisation and the growth rates of the $n > 1$ Rényi entropies:

$$\gamma_n^{TFIM} = \frac{\Gamma_n^{TFIM}}{\Gamma} = \frac{1}{2}\frac{1}{1-1/n} \,. \tag{5.38}$$

On the spin chain

In the case of a finite region A of L number of sites, one can calculate the eigenvalues of the reduced density matrix from a block Toeplitz matrix [116, 177], which allow the computation of the S_n. For long times t, assuming that $L \gg t$ the time evolution of the entropies is given by [129]:

$$S_n(t) \approx 2S_n(0) + 2\Gamma_n^{TFIM} t\,, \tag{5.39}$$

where $2S_n(0)$ is the entropy of the initial state and the growth rates Γ_n^{TFIM} are given as:

$$\Gamma_n^{TFIM} = \frac{1}{1-n}\int_0^\pi \frac{dk}{\pi} |\epsilon_g'(k)| \log(P_n(\cos\Delta_k))\,, \tag{5.40}$$

where $P_n(x) = (\frac{1+x}{2})^n + (\frac{1-x}{2})^n$. The factor of two in (5.39) is related to the number of boundaries between the subsystems A and B, or identically the number of brach-point twist field insertions. This result holds for any transverse quenches regardless of the phase, but in order to compare it to the relaxation of magnetisation we restrict our consideration to the quenches within the ferromagnetic regime in the following.

In Table 5.1 we compute the ratios γ_n^{TFIM} for quenches on the spin chain by numerical integration of (5.28) and (5.40) illustrating the relation (5.38). It is clear that (5.38) only holds approximately, and the agreement is better for smaller quenches. Note that a finite quench in the scaling field theory corresponds to a limit in the spin chain when the quench magnitude goes to zero, so the universal ratio (5.38) continues to hold to the lowest order of the quench amplitude K, i.e. for small post-quench density.

It is possible to show explicitly that (5.38) holds for small quasi-particle density for the discrete chain itself. At $O(K^2)$ we have that $P_n(\cos\Delta_k)$ as a function of K is given by

$$P_n(\cos\Delta_k) = 1 - nK^2 + O(K^4) \tag{5.41}$$

so that (5.40) becomes

$$\Gamma_n^{TFIM} = \frac{n}{n-1}\int_0^\pi \frac{dk}{\pi} |\epsilon_g'(k)| K^2(k) + O(K^4). \tag{5.42}$$

Comparing the latter result with Γ in (5.31) it is clear that the relation (5.38) holds at the leading order in K. Including the first correction leads to

$$\gamma_n^{TFIM} = \frac{1}{2}\frac{1}{1-1/n}\left(1 - \frac{3n+1}{2}\frac{\int_0^\pi \frac{dk}{\pi}|\epsilon_g'(k)|K^4(k)}{\Gamma}\right). \tag{5.43}$$

$g_0 \to g$	γ_1^{TFIM}	γ_2^{TFIM}	γ_3^{TFIM}	γ_4^{TFIM}
$0.3 \to 0.5$	2.85355	1	0.746474	0.66351
$0.5 \to 0.3$	2.85355	1	0.746474	0.66351
$1/3 \to 2/3$	2.18374	1	0.737744	0.6555
$2/3 \to 1/3$	2.18374	1	0.737744	0.6555
$0.5 \to 0.7$	2.56297	1	0.743885	0.661164
$0.7 \to 0.5$	2.56297	1	0.743885	0.661164
$0.6 \to 0.66$	3.74455	1	0.749385	0.666119
$0.6 \to 0.66$	3.74455	1	0.749385	0.666119
$0.6 \to 0.606$	6.10712	1	0.749996	0.666663
$0.1 \to 0.11$	6.03714	1	0.749994	0.666661
$0.1 \to 0.101$	8.34075	1	0.75	0.666666
$0.3 \to 0.4$	3.60792	1	0.749189	0.665945
$0.3 \to 0.2$	3.67499	1	0.74929	0.666035

Table 5.1: Values of γ_n^{TFIM} for a set of transverse quenches in the ferromagnetic phase of the TFIM, in units obtained by setting $J = 1$.

For the von Neumann entropy we have

$$\begin{aligned}\lim_{n\to 1}\frac{1}{1-n}\log P_n(x) &= -\frac{1}{P_1(x)}\frac{\partial P_n(x)}{\partial n}\bigg|_{n=1} \\ &= \frac{1+x}{2}\log\left(\frac{1+x}{2}\right)+\frac{1-x}{2}\log\left(\frac{1-x}{2}\right)\end{aligned} \tag{5.44}$$

resulting in

$$\gamma_1^{TFIM} = \frac{1}{2}\left(1-\frac{\int_0^\pi \frac{dk}{\pi}|\epsilon_g'(k)|K^2(k)\log K^2(k)+O(K^4)}{\Gamma}\right), \tag{5.45}$$

which is K dependent. In agreement with the numerical data, this ratio increases for smaller quenches.

5.5 Transverse quenches on the quantum Potts spin chain

5.5.1 The quantum Potts spin chain

The q-state quantum Potts spin chain consists of a chain of generalised spins having internal quantum states $|\mu\rangle_i$, with i labeling the lattice sites and $\mu = 0, \ldots, q-1$ the possible internal states of the spins, governed by the Hamiltonian

$$H = -J \left(\sum_i \sum_{\mu=0}^{q-1} P_i^\mu P_{i+1}^\mu + g \sum_i P_i \right) . \tag{5.46}$$

The first term of the Hamiltonian contains the traceless projector $P_i^\mu = |\mu\rangle_i \langle\mu|_i$ which tends to align the spin at site i along the direction μ, while the second term is given by the traceless operator $P = |\lambda_0\rangle \langle\lambda_0| - 1/q$, which forces the spin along the direction $|\lambda_0\rangle \equiv \sum_\mu \frac{|\mu\rangle}{\sqrt{q}}$. The relative strength of these two terms is regulated by the transverse magnetic field g: $g > 1$ is the paramagnetic phase with a unique ground state, while $g < 1$ is the ferromagnetic phase with q degenerate ground states, spontaneously breaking the global $\mathbb{S}_q$ symmetry. The case $q = 2$ is the quantum Ising spin chain, while $q = 3$ gives the 3-state quantum Potts spin chain which we call quantum Potts spin chain for short. In both of these cases, the partition function is invariant under the Kramers-Vannier duality $g \to 1/g$ [178], and the two phases are separated by a quantum phase transition at the critical point $g_c = 1$. For the quantum Ising spin chain, the spectral gap is given by $\Delta = 2J|1 - g|$ (exact), while for the quantum Potts spin chain $\Delta \sim J|g - 1|^{5/6}$ (for $g \sim 1$) where the exponent can be extracted from conformal field theory [179].

The quantum Potts spin chain is not integrable apart from the critical point. Nevertheless, its spectrum can easily be guessed, and subsequently verified using perturbation theory for g far away from the critical value [164]. In the ferromagnetic phase, the elementary excitations are domain walls with dispersion relation

$$\epsilon^{\mu,\mu'}(k) = \epsilon_g(k), \tag{5.47}$$

where μ and μ' denote the orientations of domains linked by the excitation, with $\mu - \mu' = \pm 1 \bmod 3$, with the dispersion relation

$$\epsilon_g(k) = J \left(1 - \frac{2g}{3} \cos k \right) + O\left(g^2\right) . \tag{5.48}$$

Conversely, for $g > g_c$ the ground state is non-degenerate and the elementary excitations are two kinds of local spin flips $\lambda = \pm$ with dispersion relation

$$\epsilon^{\lambda}(k) = \tilde{\epsilon}_g(k) \quad , \quad \tilde{\epsilon}_g(k) = 3J\left(1 - \frac{2}{3g}\cos k\right) + O\left(g^{-2}\right) . \tag{5.49}$$

The two excitations are related to each other by the charge conjugation mapping the spin direction μ to $-\mu$ mod 3.

5.5.2 Quenches in the transverse field

We consider quantum quenches starting at time $t = 0$ from the ground state $|\Psi_0\rangle$ of a pre-quench Hamiltonian H_0 corresponding to a pre-quench value of transverse field g_0, evolved for $t > 0$ by the post-quench Hamiltonian H corresponding to transverse field g:

$$|\Psi_0(t)\rangle = e^{-iHt}\,|\Psi_0\rangle \ . \tag{5.50}$$

For the quantum Potts spin chain there are no analytic results for time evolution since the model is not integrable. However, we expect a quench dynamics qualitatively similar to the Ising case, and so considering quenches inside the ferromagnetic phase $g, g_0 < 1$ we can assume that the magnetisation evolves according to

$$m_0(t) \equiv \langle\Psi_0(t)|\,P^0\,|\Psi_0(t)\rangle \simeq (\mathcal{C}_{FF}^{Potts})\exp\{-t\Gamma^{Potts}\}, \tag{5.51}$$

where $\mathcal{C}_{FF}^{Potts}$ and Γ^{Potts} are some positive constants that can be determined fitting the iTEBD data. For Rényi entropies (computed for semi-infinite subsystem) we can again assume that time evolution occurs according to

$$S_n(t) = S_n(0) + \Gamma_n^{Potts} t\,, \tag{5.52}$$

where again Γ_n^{Potts} can be obtained fitting the iTEBD data. Examples are shown in Fig. 5.14, while Table 5.2 summarises the results for the ratios $\gamma_n^{Potts} = \Gamma_n^{Potts}/\Gamma^{Potts}$ for different values of g_0 and g.

5.5.3 Digression: global symmetries, twist fields and replicas

In general, quantum field theories can have global internal symmetry transformations $\{\phi\} \to \{\mathcal{R}\phi\}$ acting on the fields of the field theory. Twist fields, or symmetry fields are defined in the path integral formalism: a twist field insertion $\langle\mathcal{T}_{\mathcal{R}}\ldots|\mathcal{T}_{\mathcal{R}}\ldots\rangle$ changes the

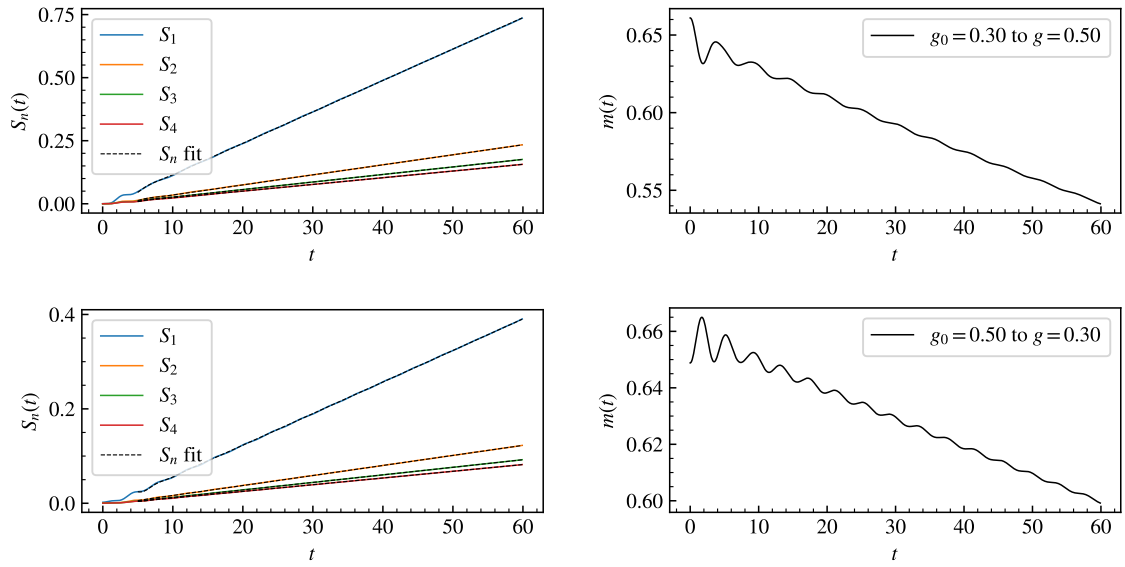

Figure 5.14: Rényi entropies and magnetisation time evolution for the quenches $g_0 = 0.3 \to g = 0.5$ (a) and $g_0 = 0.5 \to g = 0.3$ (b). Time is measured in units of $1/J$, and the initial entropy was subtracted.

$g_0 \to g$	γ_1^{Potts}	γ_2^{Potts}	γ_3^{Potts}	γ_4^{Potts}
$0.3 \to 0.5$	4.20	1.34	1.01	0.89
$0.5 \to 0.3$	4.21	1.34	1.01	0.89
$1/3 \to 2/3$	3.29	1.32	1.00	0.89
$2/3 \to 1/3$	3.34	1.32	1.00	0.89
$0.5 \to 0.7$	3.82	1.32	1.00	0.88
$0.7 \to 0.5$	3.88	1.33	1.00	0.89

Table 5.2: Values of γ_n^{Potts} for various transverse quenches.

boundary condition for the path integral along the cut starting from the insertion point to:

$$\{\phi^+\} = \{\mathcal{R}\phi^-\} \tag{5.53}$$

where $\{\phi^\pm\}$ denote the set of fields on the two sides of the cut. From this definition it is clear that taking a local operator $\mathcal{O}$ around the twist-field insertion results in the change $\mathcal{O} \to \mathcal{R}\mathcal{O}$. Therefore the correlator $\langle \mathcal{T}_\mathcal{R}\mathcal{O}\ldots|\mathcal{T}_\mathcal{R}\mathcal{O}\ldots\rangle$ is not a single valued function if $\mathcal{R}\mathcal{O} \neq \mathcal{O}$, and $\mathcal{O}$ is said to be "semi-local" with respect to $\mathcal{T}_\mathcal{R}$.

The q-state Potts model has the permutation symmetry $\mathbb{S}_q$ of the spins, with the

magnetisation field as order parameter. In the scaling field theory the kink excitations are created by the disorder operators [180] which are semi-local with respect to the magnetisation [181] and the respective symmetry is given by the cyclic subgroup $\mathbb{Z}_q$. Note that the same properties hold for the lattice model [182].

The Rényi entropies can be constructed using the so-called replica trick [116, 125, 175]. Considering the scaling field theory limit, the n-th power of the reduced density matrix of a finite interval can be represented as a path integral over an n-sheeted Riemann surface with each sheet corresponding to a replica of the original QFT. The branching points of the Riemann surface can be represented as the insertion points of branch-point twist-fields. The Rényi entropy of an interval is proportional to the logarithm of a branch-point twist-field two-point function, while the bipartite Rényi entropy of a system cut in two semi-infinite halves can be obtained from a one-point function.

The replica theory has a $\mathbb{S}_n$ replica symmetry in addition to the possible global symmetries acting within the replicas, and the original QFT fields describing observables and creating the particle excitations have a copy inside each replica. These copies are transferred to the next Riemann sheet when taken around a branch-point twist-field, which corresponds to the action by the generator of the cyclic group $\mathbb{Z}_n$ [175]. Therefore the branch-point twist-field acts as a $\mathbb{Z}_n$ twist field for the fields creating the particle excitations, which entirely parallels the situation for the magnetisation and its associated $\mathbb{Z}_q$ symmetry.

5.5.4 Conjecture for the universal ratio

From the numerical results one can form the following conjecture: for $n \neq 1$

$$\gamma_n^{Potts} = \frac{2}{3}\frac{1}{1-1/n}\,, \tag{5.54}$$

in the limit of small quenches. Together with (5.38) this result hints that for a generic q-state quantum Potts spin chain

$$\gamma_n^{(q)} = \frac{1-1/q}{1-1/n}\,. \tag{5.55}$$

This conjecture can be heuristically supported as follows. Note that the Rényi entropy is associated to a replica trick, which has a symmetry $\mathbb{Z}_n$. The replica structure can be implemented by a branch-point twist field, which is semi-local with respect to the intertwining fields creating the particles in the different replicas [175] and the entropy

growth rate itself is nothing else than the relaxation rate of the expectation value of the $\mathbb{Z}_n$ twist field divided by $n-1$.

Turning to the magnetisation, it is a field with $\mathbb{Z}_q$ symmetry. The role of replicas is played by the sectors built upon the q different ground states. In this case the roles are reversed: the magnetisation is a local field acting within a given sector, while the particle excitations are kinks (domain walls) created by disorder operators [165, 183], however their mutual semi-locality properties are analogous to the case of the branch-point twist fields. In fact, the factor $\frac{1}{1-1/q}$ appears in the annihilation pole of the two-kink form factor of the magnetisation [165]. It is exactly the kinematical poles that give rise to the secular terms in the time evolutions which can be resummed to yield the relaxation of the magnetisation [161], which explains the q-dependence in (5.55).

It is then tempting to argue that the full ratio (5.55) is just a result of the symmetry properties, whereby the relaxation rate for the branch-point twist field can be obtained from that of the magnetisation by replacing q with n. There is a caveat, however: the Rényi entropy growth rate depends on its normalisation, i.e. the choice of the prefactor in its definition (5.35). The prefactor is necessary to recover the von Neumann entropy in the limit $n \to 1$, however, it is not so obvious how to argue for $n > 1$. Therefore, the argument can only be made robust by comparing the computation of the relaxation rates of the branch-point twist fields to that of the magnetisation in the q-state Potts model in more detail, and we return to this issue in the Conclusions.

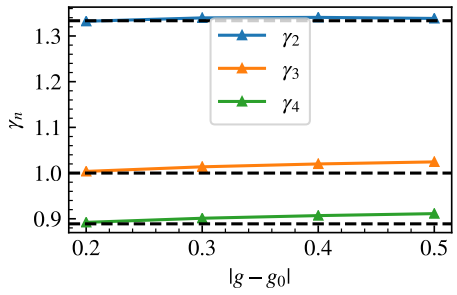

Figure 5.15: Values of γ_n quenching from $g_0 = 0.7$ to $g = 0.5, 0.4, 0.3, 0.2$. The dashed lines represent the conjectured ratios (5.55).

Similarly to the Ising case, the universal ratio (5.55) is only expected to be valid when considering small quenches. To demonstrate this numerically for the 3-state Potts chain, we considered quenches starting from $g_0 = 0.7$ to different values of g (see Fig. 5.15). These results are consistent with the analytic considerations presented for the Ising chain in subsection 5.4.2: the ratios γ_n^{Potts} start to deviate from (5.55) once $|g - g_0|$

(and therefore the post-quench quasi-particle density) is increased.

5.6 Longitudinal quenches in the paramagnetic phase

The other class of quenches we consider corresponds to starting from a transverse spin chain and switching on a *longitudinal* field h. For the quantum Ising spin chain this means a quench from

$$H(g,0) = -J\sum_{j=1}^{N}\left(\sigma_j^x\sigma_{j+1}^x + g\sigma_j^z\right)\,, \tag{5.56}$$

to

$$H(g,h) = -J\sum_{j=1}^{N}\left(\sigma_j^x\sigma_{j+1}^x + g\sigma_j^z + h\sigma_j^x\right)\,. \tag{5.57}$$

In the ferromagnetic phase this leads to confinement [162] which limits entropy growth and prevents equilibration by truncating the spread of correlations; therefore here we only consider these quenches in the paramagnetic phase.

These quenches lead to the dynamical manifestation of the Gibbs mixing entropy observed in [2, 159], resulting in a non-monotonic behaviour of the von Neumann entropy growth rate with the quench magnitude h. We demonstrate that the same behaviour is reflected in the relaxation rate of magnetisation and the Rényi entropy growth rates, which opens the way for an experimental observation of the "dynamical Gibbs effect".

5.6.1 Longitudinal quenches in the Ising spin chain

We present the numerical results for longitudinal quenches in the quantum Ising spin chain with transverse field $g = 1.75$, leaving the transverse field unchanged and quenching the longitudinal field from 0 to h in Fig. 5.16. Some plots for different quenches showing the same behaviour are relegated to Appendix D.

In this case we do not expect that the ratio

$$\gamma_n = \frac{\Gamma_n}{\Gamma} = \frac{1}{2}\frac{1}{1-1/n} \tag{5.58}$$

holds in the limit of small quenches, since the $\mathbb{Z}_2$ symmetry characterising the magnetisation is broken by the longitudinal field h. However, the replica symmetry of the twist fields associated to the Rényi entropies is unaffected, and therefore we expect that

$$\frac{\Gamma_n}{\Gamma_m} = \frac{1-1/m}{1-1/n}\,, \tag{5.59}$$

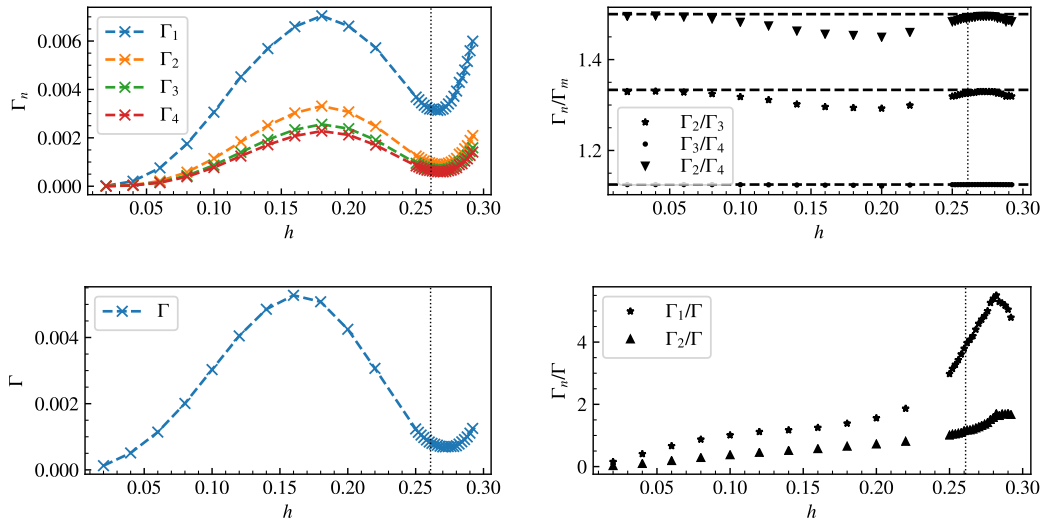

Figure 5.16: Left panels: Entropy growth rates Γ_n (top) and magnetisation relaxation rate Γ (bottom) in units $J = 1$ for longitudinal quenches in the quantum Ising spin chain starting from $g = 1.75$ as a function of the longitudinal coupling. Right: Ratios Γ_n/Γ_m (top) and Γ_n/Γ (bottom). The dashed lines represent the universal ratios (5.59) that are restored in the limit $h \to 0$. The vertical line is drawn at the value h_{crit} where the second quasi-particle appears in the post-quench spectrum.

which is in fact the case as shown in Fig. 5.16.

Note that the characteristic minimum and subsequent fast growths displayed by the von Neumann entropy growth rate Γ_1 is followed very well by the Rényi entropy rates Γ_n, with the maximum and the subsequent minimum at the same location within a very good approximation. We recall that the critical value of the longitudinal field $h \approx 0.4$ where the rates take their minimum, coincides with the threshold for the appearance of a bound state quasi-particle in the spectrum, and the subsequent much faster generation of entropy can be associated to the contribution of Gibbs mixing entropy [159]. Additionally, the magnetisation relaxation rate follows the behaviour of the entropy growth rate, which means that it can be used as an experimental signal for the "dynamical Gibbs effect" .

More precisely, the threshold value h_{crit} where the new quasi-particle appears generally somewhat differs from the position h_{min} of the minimum in the von Neumann entropy rate Γ_1. As already explained in [159] this is mainly due to two effects. Firstly, the bound state threshold value h_{crit} is determined from the excitation spectrum above the ground state, while the post-quench system has a finite energy density which is expected

to induce shifts in the effective quasi-particle masses. Secondly, the contribution which makes Γ_1 grow for $h > h_{\text{crit}}$ must grow sufficiently in size to counteract the one that made it decrease for $h < h_{\text{crit}}$. The latter effect is expected to depend on the quantity considered, i.e. one expects to find slightly different positions of the minima for Γ_n for different n, as well as for the magnetisation relaxation rate Γ. However these differences are quite small and the positions of the local minimum (and similarly that of the local maximum) only depend very mildly on the rate considered.

Another interesting observation is that the quench corresponding to the critical longitudinal field field $h = h_{\text{crit}}$ also seems to be small in the sense that the ratios Γ_n/Γ_m return close to the universal values (5.59) characteristic for small quenches. This indicates that somehow these quenches are also small as indicated by the slow growth of entanglement entropy, and that the proper condition for the universal ratios (5.59) to hold is slow growth of entropy rather than small post-quench density.

Finally we note that simulations for other values of the transverse field lead to the same conclusions, as shown in Appendix D in Figs. D.1, D.2 and D.3 for $g = 1.25$, $g = 1.5$ and $g = 2.00$, respectively.

5.6.2 Longitudinal quenches in the Potts spin chain

In this subsection we present the numerical results for longitudinal quenches in the quantum Potts spin chain. As shown in [2], this model shows effects of changes of the quasi-particle spectrum on the entropy growth rate as observed in the quantum Ising spin chain [159]. Just as for the Ising case, we consider four different values of transverse field ($g = 1.25, 1.50, 1.75, 2.00$) and performed a quench by adding a longitudinal field leaving the transverse field unchanged, i.e. starting from

$$H(g,0) = -J\left(\sum_i \sum_{\mu=0}^{q-1} P_i^\mu P_{i+1}^\mu + g\sum_i P_i\right) \tag{5.60}$$

to

$$H(g,h) = -J\left(\sum_i \sum_{\mu=0}^{q-1} P_i^\mu P_{i+1}^\mu + g\sum_i P_i + \sum_i h P_i^{\mu_0}\right). \tag{5.61}$$

where the direction μ_0 of the longitudinal field h can eventually be chosen arbitrarily among the three possibilities 0, 1 and 2 without altering the physical behaviour.

For $g = 1.75$, the results are shown in 5.17, while the other three cases are presented in Appendix D in Figs. D.4, D.5 and D.6. Apart from difference in quantitative details such as the values of the critical longitudinal field and the numerical values of the rates

themselves, the qualitative features and the essential conclusions are exactly the same as for the quantum Ising spin chain: (1) the universal ratios (5.59) hold both for small values of h and, to a very good approximation for quenches around the critical value corresponding to the appearance of a new quasi-particle; and (2) the magnetisation relaxation rate closely follows the behaviour of the von Neumann and Rényi entropy rates, which can again be used as an observable signature for the "dynamical Gibbs effect".

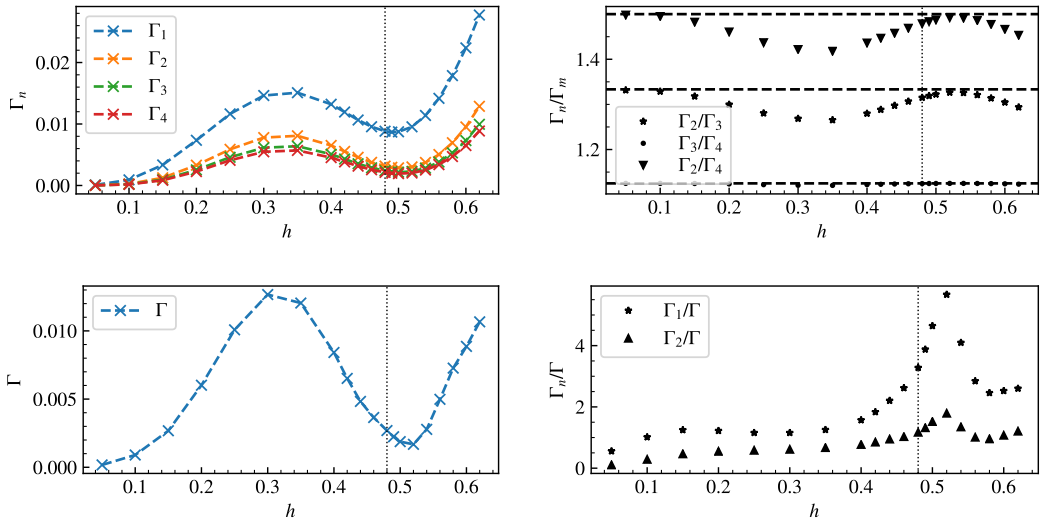

Figure 5.17: Left panels: Entropy growth rates Γ_n (top) and magnetisation relaxation rate Γ (bottom) for longitudinal quenches in the quantum Potts spin chain starting from $g = 1.75$ as a function of the longitudinal coupling, in units with $J = 1$. Right: Ratios Γ_n/Γ_m (top) and Γ_n/Γ (bottom). The dashed lines represent the universal ratios (5.59) that are restored in the limit $h \to 0$. The vertical line is drawn at the value h_{crit} where the second quasi-particle appears in the post-quench spectrum.

5.6.3 Large quenches above the threshold: slow oscillations

Above the bound state threshold, i.e. for $h > h_{\text{crit}}$ there are two quasi-particle species of masses (a.k.a. quasi-particle gaps) m_1 and m_2, and the binding energy $m_2 - 2m_1$ goes to zero when h approaches h_{crit} from above. As a result, the quench dynamics contains slow oscillations with the frequency $m_2 - 2m_1$, similar to those recently observed in the time evolution of entropies and one-point functions in mass quenches in the E_8 field theory [184, 185]. It turns out that in the E_8 case entanglement growth is suppressed and iTEBD numerics can be performed for very long times, which allows to extract the

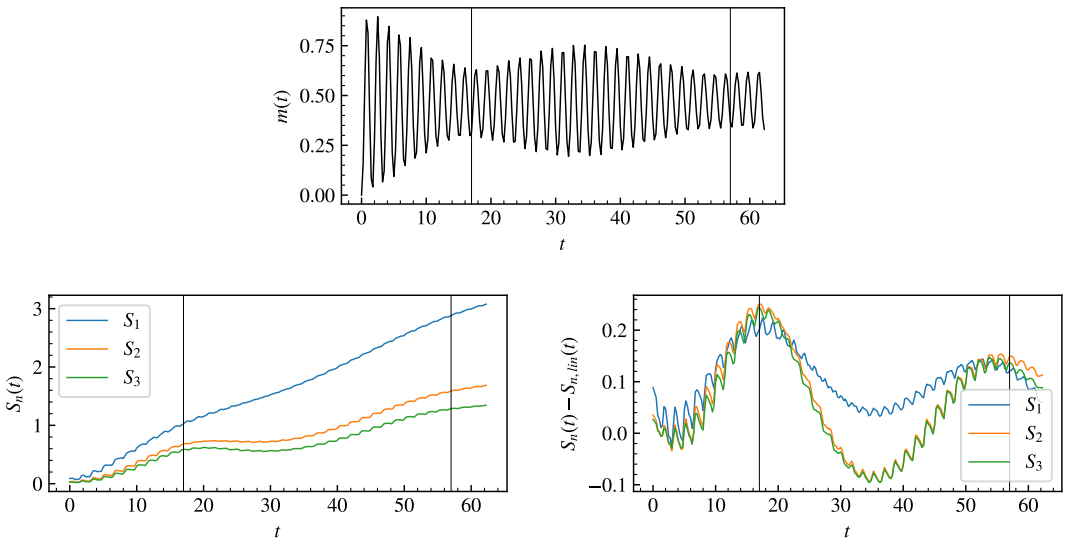

Figure 5.18: Time evolution of various quantities after a large quench $(g_0, h_0) = (2.0, 0.0) \to (g, h) = (2.0, 0.7)$ in the quantum Ising spin chain. The top diagram shows the evolution of magnetisation, the bottom left one the von Neumann entropy (S_1) and two of the Rényi entropies (S_2 and S_3), while the bottom right one shows the entropy evolution with the linear trend subtracted. The vertical lines correspond to a single period of the slow oscillation corresponding to the frequency $2m_1 - m_2$. The first line is drawn at the first minimum of the envelope of the magnetisation oscillations while second is drawn at a distance given by the period $T \approx 40$. Note that their position matches quite well the behaviour of the entropy curves as well. Time is measured in units of $1/J$, and the initial entropy was subtracted.

frequency with a very high precision. For the E_8 theory the source of the long period oscillations is the third quasi-particle, with a mass $m_3 = 1.989\ldots\, m_1$, which is known exactly in terms of the mass m_1 of the lightest quasi-particle due to the integrability of the model [186].

In the longitudinal quenches of the paramagnetic quantum Ising spin chain, entanglement growth is enhanced for $h > h_{\text{crit}}$ by the "dynamical Gibbs effect" , so even observing a single period of the oscillation takes quite some effort. Nevertheless, we were able to demonstrate its presence for a large quench from $g = 2.00, h = 0$ to $g = 2.00, h = 0.7$. Although the model is non-integrable, the quasi-particle masses can be computed with sufficient precision from exact diagonalisation [159] resulting in $2m_1 - m_2 = 0.158$ (in units with $J = 1$), leading to a period $T \approx 40$. As shown in Fig. 5.18 this period matches well the oscillations observed in iTEBD evaluation of the magnetisation and entropy time evolutions. Two other examples of slow oscillations present in large longitudinal

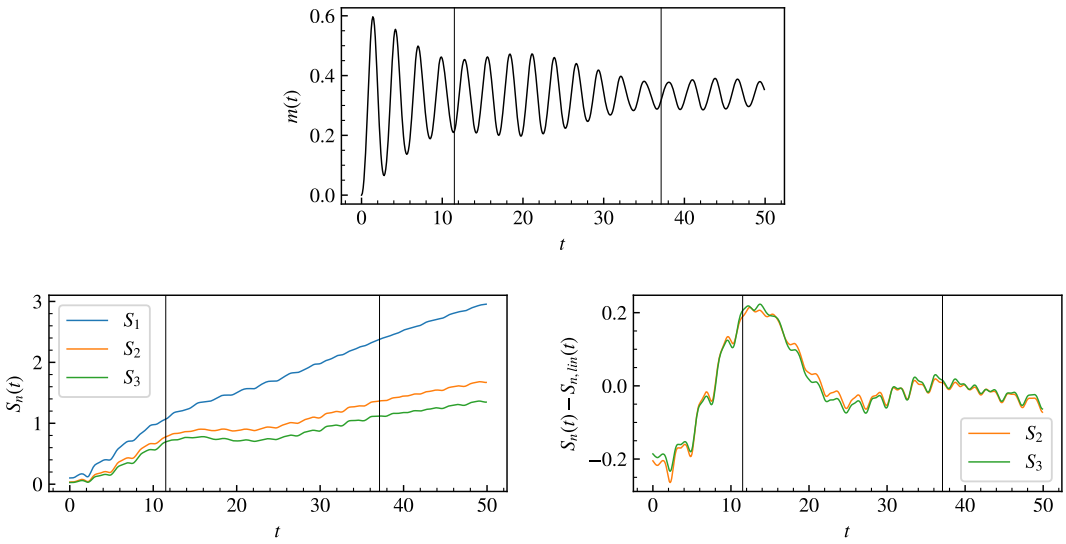

Figure 5.19: Time evolution of various quantities after a large quench $(g_0, h_0) = (2.0, 0.0) \to (g, h) = (2.0, 1.4)$ in the quantum Potts spin chain. The top diagram shows the evolution of magnetisation, the bottom left one the von Neumann entropy (S_1) and two of the Rényi entropies (S_2 and S_3), while the bottom right one shows the entropy evolution with the linear trend subtracted. The vertical lines correspond to a single period of the slow oscillation corresponding to the frequency $2m_1 - m_2$. The first line is drawn at the first minimum of the envelope of the magnetisation oscillations while second is drawn at a distance given by the period $T \approx 25.6$. Note that their position matches quite well the behaviour of the entropy curves as well. Time is measured in units of $1/J$, and the initial entropy was subtracted.

quenches of the quantum Ising spin chain are shown in Appendix D in Figs. D.7 and D.8.

The same effect can also be observed in the quantum Potts spin chain, as shown in Fig. 5.19 for a quench from $g = 2.00, h = 0$ to $g = 2.00, h = 1.4$, where the quasi-particle masses are again determined from exact diagonalisation following [2] with the result $m_1 = 2.480$ and $m_2 = 4.714$, leading to a period $T \approx 25.62$ which matches the signature in the numerical simulation.

6

Confinement and Emergent Bloch oscillations

The decay of the false vacuum is a famous scenario proposed in 1977 by Sidney Coleman to describe the dynamics of phase transitions in quantum field theory [187, 188], which plays an important role in particle physics and cosmology. In such a situation a system stuck in a metastable ('false') vacuum state transitions to the 'true' vacuum state by bubble nucleation and subsequent growth of the bubbles driven by the energy difference between the false and the true vacua. This is a non-equilibrium process, in which the expansion of the bubbles rapidly accelerates to the maximum possible velocity (the speed of light), and thus the true vacuum ultimately replaces the original false vacuum everywhere in space. Quantum bubble formation is, of course, not only relevant in cosmology, but it is the primary mechanism behind first order classical and quantum phase transitions and hysteresis.

Quantum quenches provide a natural environment to test Coleman's scenario in various quantum systems. In fact, in global, translationally invariant quantum quenches, the initial state has a finite uniform energy density with respect to the post-quench Hamiltonian, and the system is therefore in a highly excited state. This highly excited configuration acts as a *source* of quasi-particle excitations, which may collide and thermalise with time. Preparing a system in the false vacuum as an initial state, therefore allows one to test quantum bubble nucleation in the laboratory [189–193].

A primary candidate to perform this experiment is again the quantum Ising spin chain, governed by the Hamiltonian

$$H_{\mathrm{QISC}} = -J \sum_i \left(\sigma_i^z \sigma_{i+1}^z + g\sigma_i^x + h\sigma_i^z \right) \ , \tag{6.1}$$

where g and h denote the transverse and the longitudinal magnetic fields, respectively.

In the ferromagnetic phase, $g < 1$, quasi-particles are domain walls, and the chain's dynamics may be understood in terms of quantum bubble nucleation [cf. Ref. [194] for a recent study in a different setting].

However, light-cone spreading of correlations is not completely generic [162]: confining forces, as a remarkable exception, can suppress the light-cone spreading of correlations. The prediction of *dynamical confinement* has indeed been confirmed recently in numerous systems and settings exhibiting confinement [195–203]. For the model (6.1) dynamical confinement occurs when initialising the system in its $g_0 < 1$ positive (spontaneous) magnetisation ground state with $m = \langle \sigma_i^z \rangle > 0$ and $h_0 = 0$, and then quenching to a Hamiltonian with some $g < 1$ and $h > 0$. In this case, the quench gives rise to oppositely moving domain walls (kink-antikink pairs), with a bubble of false vacuum with negative magnetisation $-m$ stretched between them (see Fig. 6.6a), which costs a potential energy proportional to the distance between the domain walls. The resulting confining force [204] inhibits the propagation of the domain walls to large distances, and prevents thermalisation of the system within all time scales accessible to numerical simulations.

It is intriguing to investigate what happens if we switch on a field in the opposite direction, $h < 0$, thereby initialising the system in the false vacuum of the final Hamiltonian. In this case, according to Coleman's scenario, nucleation must lead to bubbles of the true vacuum appearing inside a sea of false vacuum. The external field now *promotes* the expansion of bubbles, and generates a repulsive force between domain walls forming the bubbles, as illustrated in Fig. 6.6b. As a result, one naively expects that bubbles extend to the whole spin chain and the system rapidly relaxes to an equilibrium or steady state around the true vacuum. In the quantum quench framework, this corresponds to the light-cone spreading of correlations, as predicted by the quasi-particle picture.

In this final chapter, however, we show by detailed simulations that – quite counter-intuitively – Coleman's scenario is violated in the Ising spin chain. We start in Sec. 6.1 by reviewing the results obtained in [162] for the *confining* regime of the Ising chain, where dynamical confinement emerges. In Sec. 6.2 the dynamics of the *anit-confining regime* is introduced. In particular spin-spin correlation function indicates that the true vacuum bubbles do not expand indefinitely. In addition, computing the entanglement entropy between two halves of the system reveals that its initial linear growth is suppressed after a transitional period. For the confining quenches this effect was discovered in [162] and is explained by the suppression of light-cone spreading of correlations due to localisation of the quasi-particles by the confining force; however, in the anti-confining case this is

unexpected in light of the force being repulsive. In Sec. 6.3 we find that the relevant mechanism responsible for the lack of light-cone spreading of bubbles is not dynamical confinement: rather, the repulsive force leads to an oscillatory motion of the domain walls, known as Bloch oscillations. While surprising, these findings are consistent with recent numerical studies of the order parameter statistics in the quantum Ising spin chain [205]. Finally, in 6.4 we present two different ways of probing Bloch oscillations.

6.1 Dynamical confinement in the Ising chain

In [162] it was proposed a mechanism that, through confinement of the elementary excitations, strongly suppresses the light-cone spreading. As in the standard scenario, the initial state acts as a source of quasiparticles. Pairs of quasiparticles move in opposite directions, but due to the confining potential the farther they go apart the stronger is the attractive force they feel, which eventually turns the particles back leading to an oscillatory behaviour, as depicted in Fig. 6.1. In analogy to strong interaction physics, the resulting bound states are called mesons. Confinement is known to take place in the Ising chain with both transverse and longitudinal fields. Switching on a non-zero field h in (6.1) induces a linear attractive potential between pairs of domain walls which enclose a domain of length d and of magnetisation opposite to h. For small h, the potential can be approximated as $V(d) = \chi \cdot d$ with $\chi = 2Jhm$, with $m = (1 - g^2)^{1/8}$. This scenario was first proposed by McCoy and Wu in [204].

The model for $h \neq 0$ is no longer integrable and in [162] to describe out-of-equilibrium dynamics the low-density approximation of Ref. [206] was used. This approximation allows to calculate all the properties of the mesons we need, namely their number, masses, and velocities. We now review the main concepts.

6.1.1 Semiclassical calculation of the meson dispersion relations

When applying a non-zero field h, this lifts the degeneracy of the two ferromagnetic ground states, and in particular, a domain with magnetisation opposite to the external field will have energy proportional to its length. In the lattice system the number of stable mesons and their dispersion relations were computed in Refs. [206].

The external field induces a linear attractive potential between neighbouring domain walls which border a domain having magnetisation in the direction opposite to h. If d is the distance between the domain walls, the potential is $V(d) = \chi \cdot$. Let us now consider

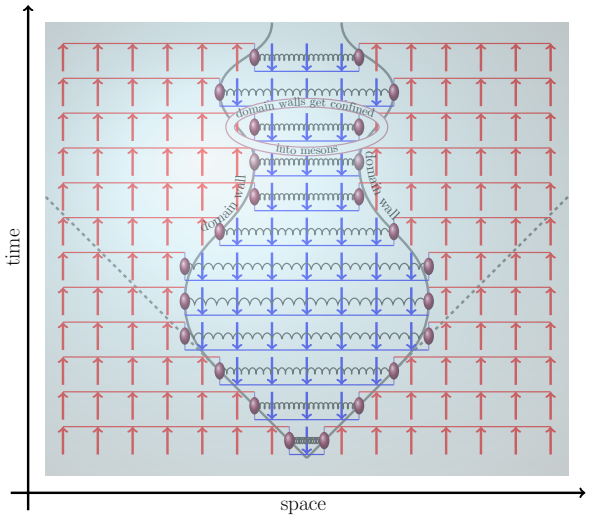

Figure 6.1: Pictorial semiclassical picture of a meson state in the Ising model: two counter-propagating domain walls bounce back and forth because of a confining interaction. Fig. taken from [162].

two fermions moving in one dimension as a classical system with the Hamiltonian

$$\mathcal{H} = \epsilon(\theta_1) + \epsilon(\theta_2) + \chi|x_2 - x_1|\,. \tag{6.2}$$

For simplicity, the coordinates are taken to be real numbers as in a continuum system, but the dispersion relation is taken to be that in the lattice system. θ_1, θ_2 are the canonical conjugate variables. After making the canonical transformation

$$X = \frac{x_1 + x_2}{2}\,, \qquad x = x_2 - x_1\,, \tag{6.3}$$

$$\Theta = \theta_1 + \theta_2\,, \qquad \theta = \frac{\theta_2 - \theta_1}{2}\,, \tag{6.4}$$

the Hamiltonian takes the form

$$\mathcal{H} = \omega(\theta;\Theta) + \chi|x|\,, \tag{6.5}$$

where $\omega(\theta;\Theta) = \epsilon(\theta + \Theta/2) + \epsilon(\theta - \Theta/2)$. The canonical equations of motion are

$$\dot{X}(t) = \frac{\partial\omega(\theta;\Theta)}{\partial\Theta}\,, \qquad \Theta(t) = \Theta = \text{const.}\,, \tag{6.6}$$

$$\dot{x}(t) = \frac{\partial\omega(\theta;\Theta)}{\partial\theta}\,, \qquad \dot{\theta}(t) = -\chi\,\mathrm{sgn}(x(t))\,. \tag{6.7}$$

For a given value of the total momentum Θ, these equations describe the relative motion of two particles. The solution becomes simple if we think of $q = \theta$ as a spatial

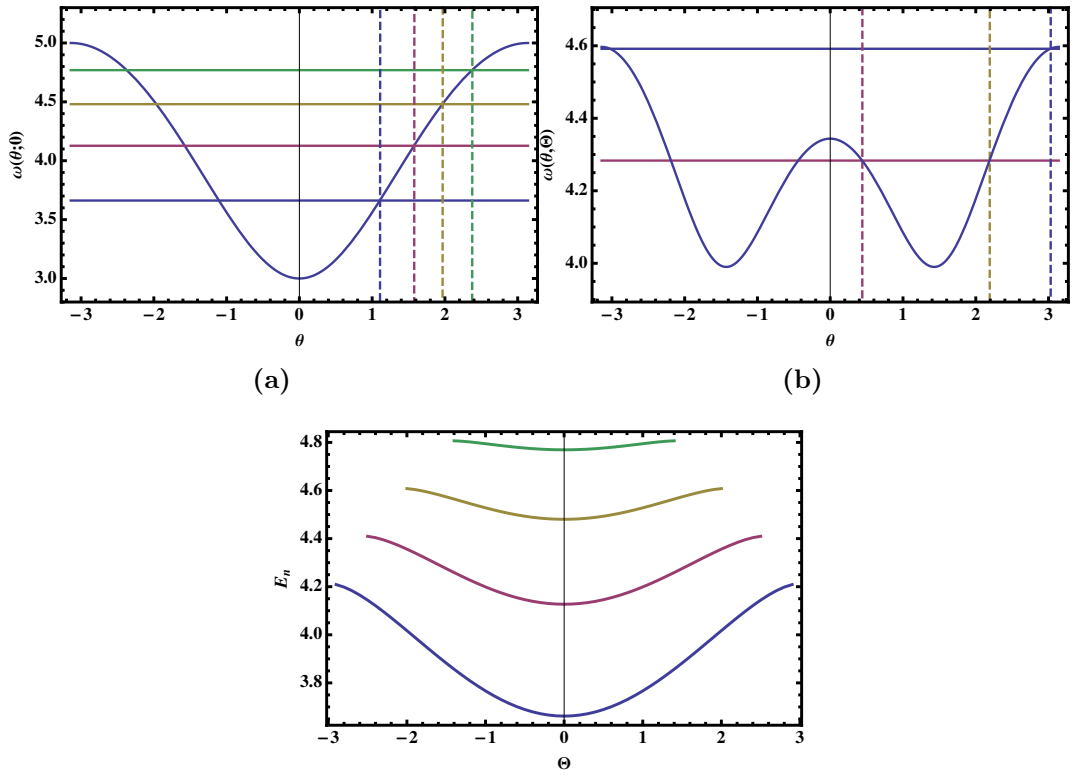

Figure 6.2: Semiclassical bound state energy levels in the "relative potential" $\omega(\theta, \Theta)$ from the solutions of Eqs. (6.8). The dashed vertical lines show the turning points $\theta_{a,b}$.
(a) Bound states for $g = 0.25, h = 0.1, \Theta = 0$. (b) Bound states for $g = 0.5, h = 0.1, \Theta = 3$.
(c) Meson dispersion relations for $g = 0.25, h = 0.1$. Figures taken from the supplementary material of [162].

coordinate and consider $p = -x$ as the conjugate momentum: we have the periodic motion of a particle with "kinetic energy" $\chi|p|$ in the 1D potential $\omega(q; \Theta)$. The energy levels can be obtained by the Bohr–Sommerfeld quantisation condition which becomes more and more accurate as one moves to higher excited states. When $\Theta < 2 \arccos g$ the function $\omega(q; \Theta)$ has only one minimum at $q = 0$) and this leads to [206]

$$2E_n(\Theta)\theta_a - \int_{-\theta_a}^{\theta_a} \mathrm{d}\theta\, \omega(\theta; \Theta) = 2\pi\chi(n - 1/4)\,, \tag{6.8a}$$

where $n = 1, 2, \ldots$ and the turning point $\theta_a = \theta_a(n; \Theta)$ is the solution of the equation

$$\omega(\theta_a(n; \Theta); \Theta) = E_n(\Theta)\,. \tag{6.8b}$$

For $\Theta > 2 \arccos g$ the potential $\omega(\theta; \Theta)$ has two minima. Then for $E > \omega(0; \Theta)$ the

above treatment is unchanged, but if $E < \omega(0;\Theta)$, the classical motion takes place in one of the two separated wells, and the semiclassical energy levels are given by [206]

$$E_n(\Theta)(\theta_a - \theta_b) - \int_{\theta_b}^{\theta_a} \mathrm{d}\theta\, \omega(\theta;\Theta) = \pi\chi(n-1/2)\,, \tag{6.9a}$$

with $n = 1, 2, \ldots$ and

$$\omega(\theta_{a,b}(n;\Theta);\Theta) = E_n(\Theta)\,. \tag{6.9b}$$

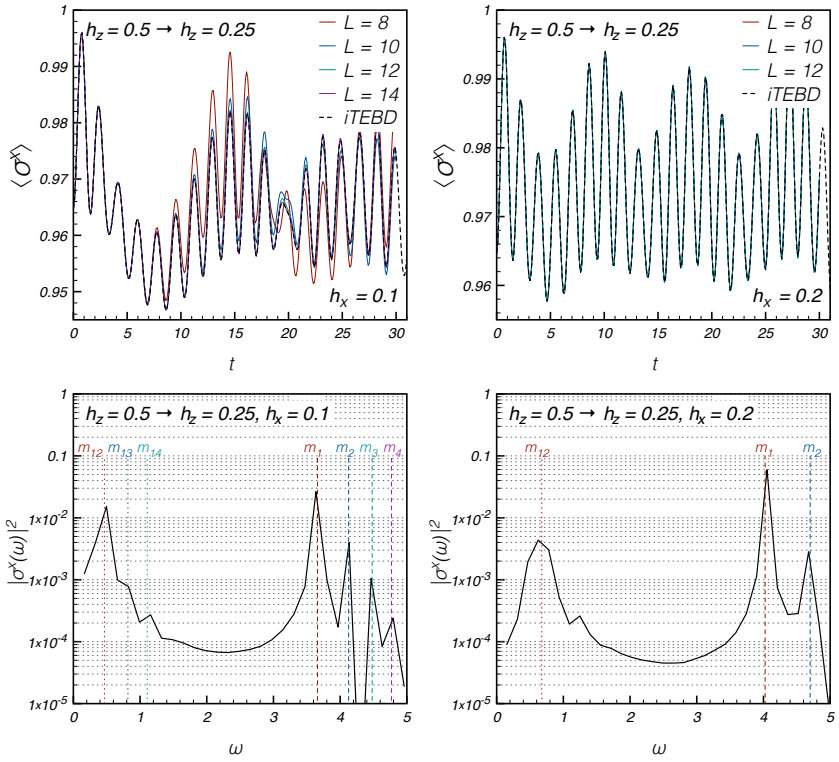

Figure 6.3: Remark: In the original paper [162] the roles of σ^x and σ^z in the Hamiltonian are inverted, so the time evolution represented here corresponds to our order parameter $\langle\sigma^z\rangle$, while h_z corresponds to g and h_x to h.
Upper panels: Time evolution of the longitudinal magnetisation $\langle\sigma^z(t)\rangle$ after quenching from $g = 0.5, h = 0$ to $g = 0.25$ and $h = 0.1, 0.2$. Dots are iTEBD results, lines are exact diagonalisation results for $L = 8, \ldots, 12,$. *Lower panels*: power spectrum of $\langle\sigma^z(t)\rangle$ in which the dashed vertical lines show the meson masses and their differences. Figures taken from [162].

The solutions of Eqs. (6.8,6.9) give the dispersion relations $E_n(\Theta)$ of the bound states (see Fig. 6.2c) The energy gaps give, in particle physics language, the meson masses.

Mesons cannot have arbitrarily large momenta Θ, at least semiclassically, and higher lying mesons have flatter dispersion relations. Since their velocities are given by

$$v_n(\Theta) = \frac{\mathrm{d}E_n(\Theta)}{\mathrm{d}\Theta}\,, \tag{6.10}$$

this means that the heavier mesons move more slowly.

6.1.2 Time evolution

We now see how the presence of mesonic bound states alters dynamics. Starting from time evolution of the magnetisation $\langle\sigma^z(t)\rangle$, we recall from Sec. 4.4 that in the integrable case the order parameter decays to zero exponentially for any quench in the ferromagnetic phase. When switching on the external field h it is evident from Fig. 6.3 that the exponential relaxations turn into an oscillatory behaviour with different frequencies. With a Fourier transform the dominant frequencies in the resulting power spectrum are compatible, to a surprising high degree of accuracy, with the masses of the mesons and their differences obtained as in Sec. 6.1.1.

The two point function is the quantity that shows the strongest effects of confinement. Mesons propagate with a maximal velocity which is smaller than that of the domain walls as shown in 6.1.1.

However, it turns out that the effect of confinement in some cases is even stronger than an already dramatic and non-perturbative change of speed of propagation. In Fig. 6.4 it is shown that for large values of h the region where there is light cone propagation shrinks to an almost invisible portion of the space-time. What happens is that due to the heavy masses of the mesons, the quench only provides sufficient energy to produce them at rest.

It is very important to stress once more that these confinement effects are non-perturbative: a very small perturbation such as $h = 0.025$ is enough to destroy completely the sharp light cone of the integrable model.

Finally, entanglement entropy $S_A = -\mathrm{Tr}\rho_A \ln \rho_A$ is another important probe for the quasi-particle propagation and hence light cone effects. The results are reported for three sets of quenches in Fig. 6.5, two within the ferromagnetic phase and one across the critical point to the ferromagnetic phase. We consider several different final values of the longitudinal fields. In all cases, by turning on the interaction h, the growth of the entanglement entropy is considerably slowed down and practically saturates (during the observation time) for quenches within the ferromagnetic phase. The latter correspond to cases in which the light-cone of the two-point function is

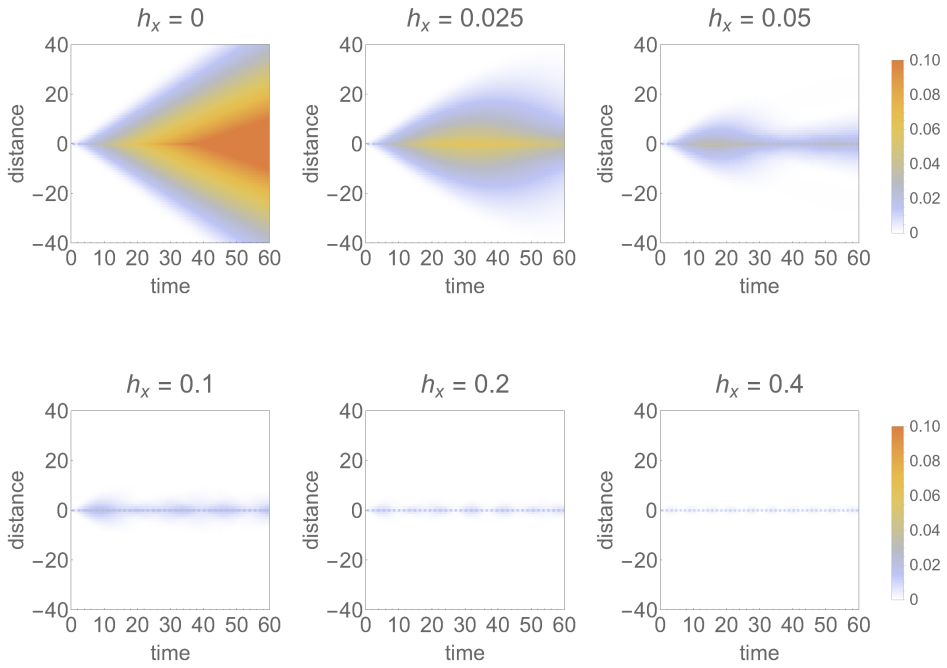

Figure 6.4: Remark: In the original paper [162] the roles of σ^x and σ^z in the Hamiltonian are inverted. h_z corresponds to g and h_x to h.
Connected longitudinal spin-spin correlation function $\langle \sigma_1^z \sigma_{m+1}^z \rangle_c$ after quenching to the ferromagnetic point $g = 0.25$ with a longitudinal magnetic field $h = 0, 0.025, 0.05, 0.1, 0.2, 0.4$. Figures taken from [162].

strongly suppressed. As explained above, this is a consequence of the fact that mesons are predominantly produced at rest and then the entanglement just oscillates around a saturation value, as in the left panel of Fig. 6.5. Actually the small fraction of mesons with non-negligible velocities should produce a very slow increase of the entanglement which however is likely too small to be observed. In the case of a quench across the critical point, the increase of the entanglement entropy is only reduced because of the production of many mesons with non-vanishing velocities. Overall, the data for the entanglement are compatible with the confinement scenario drawn for the correlations.

6.2 Anti-confining quench: setup and subsequent time evolution

We now consider quantum quenches in the ferromagnetic phase of the quantum Ising spin chain (6.1). For simplicity, we start the quench from a fully aligned, positively

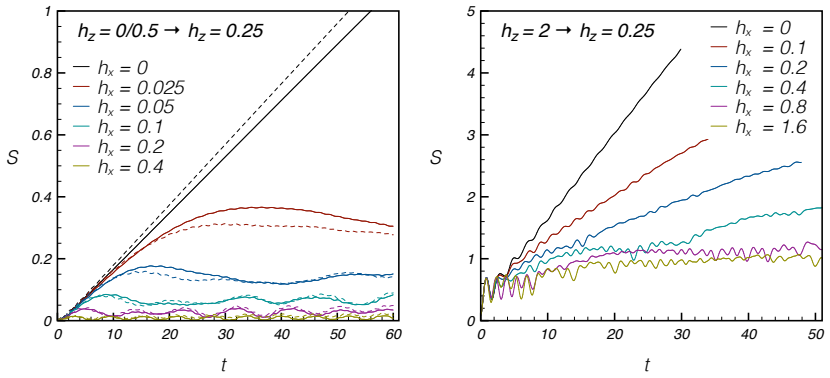

Figure 6.5: Remark: In the original paper [162] h_z corresponds to g and h_x to h.
Time evolution of the half-chain entanglement entropy after a quench to the confining phase. Left: starting from the ferromagnetic phase ($g = 0$). Right: starting from the paramagnetic phase ($g = 2$). Figures taken from [162].

polarised state, i.e. from the ground state with $g_0 = 0$ and $h_0 = 0$. We then quench to a finite transverse field, $g < 1$, and an "anti-confining" longitudinal field $h < 0$. Turning on a finite $g_0 \to g > 0$ creates a gas of domain wall excitations, which then move in the presence of the field $h < 0$.

The time evolution is numerically simulated using the infinite volume time evolving block decimation (iTEBD) method [163] (for more see Appendix C), which we use to compute the time evolution of the connected two-point equal time spin correlation function

$$\begin{aligned} C_z(l,t) &\equiv \langle \sigma_0^z(t)\sigma_l^z(t)\rangle_c \\ &= \langle \sigma_0^z(t)\sigma_l^z(t)\rangle - \langle \sigma_0^z(t)\rangle \langle \sigma_l^z(t)\rangle \ , \end{aligned} \tag{6.11}$$

as well as the entanglement entropy between two halves of the system, say A and $\bar{A}$,

$$S(t) = -\operatorname{Tr} \rho_A(t) \log \rho_A(t) \tag{6.12}$$

where ρ_A is the reduced density matrix of the subsystem A. For the time evolution we used a second order Trotter expansion, with the maximum bond dimension of the matrix product states fixed at 512.

As shown in Figs. 6.6 and 6.7, at a first sight, the time evolutions of the correlation functions $C_z(l,t)$ and the entanglement entropy $S(t)$ look remarkably similar for an anti-confining field, $h < 0$, to the one obtained in the dynamical confinement region, $h > 0$, studied in the previous section: in both cases, the light-cone propagation of correlations and the growth of entropy are suppressed, and oscillations are observed.

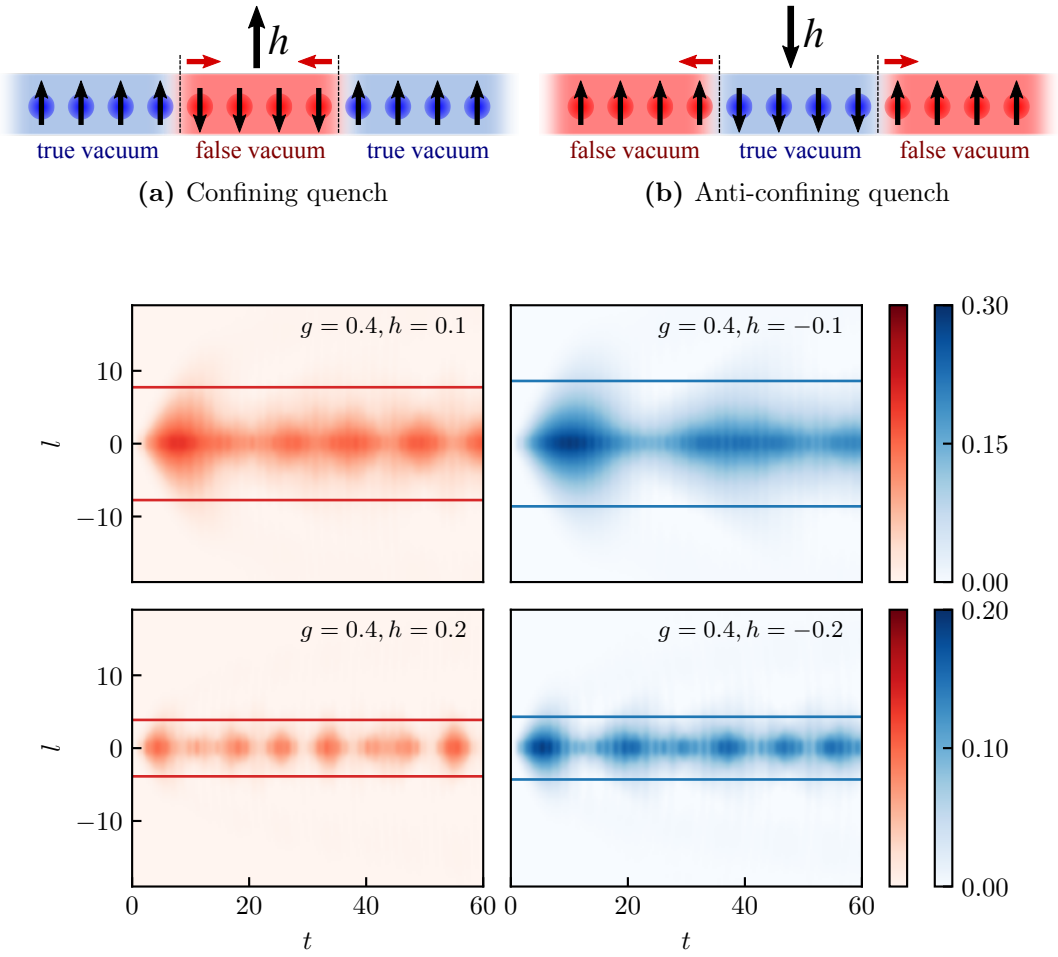

(a) Confining quench **(b)** Anti-confining quench

Figure 6.6: Upper panel: (a) For h parallel to the initial magnetisation, bubbles nucleated during the quench contain the false vacuum. The corresponding attractive forces (red arrows) confine domain walls into 'mesons'. (b) For h opposite to the initial magnetisation, nucleating bubbles contain the true vacuum. The induced repulsive forces (red arrows) accelerate the domain walls. Lower panel: Time evolution of the connected spin-spin correlation function $C_z(l,t) \equiv \langle \sigma_0^z(t)\sigma_l^z(t)\rangle_c$ for $g = 0.4$ in the confining regime, $h > 0$ (left), and in the anti-confining regime, $h < 0$ (right). Red vs. blue lines show average bubble sizes estimated using Eqs. (6.25) and (6.24), respectively.

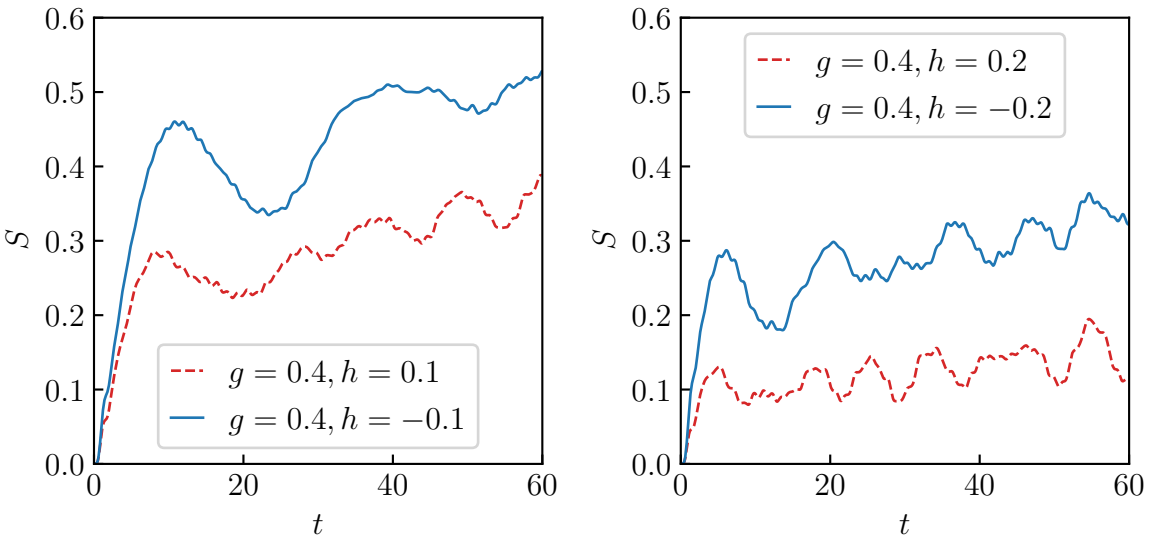

Figure 6.7: Time-dependence of entanglement entropy for the quenches displayed in Fig. 6.6. Note that anti-confining quenches (blue continuous lines) show a suppression of entropy growth similar to the confining case (red dashed lines), albeit with a larger magnitude of entanglement entropy generated during the quench.

Closer examination of the simulation results discerns, however, some important differences between the two cases. While correlations have an oscillatory behaviour in both cases, the corresponding *frequencies* and *amplitudes* are quite different. As discussed in Ref. [162], in the confining case $h > 0$ the frequencies of oscillations scale with $h^{2/3}$ and correspond to bound states of domain walls called "mesons". In contrast, for the anti-confining case the characteristic frequency scales with h, as shown explicitly by the quench spectroscopy discussed in Subsection 6.4.2.

6.3 Bloch oscillations

Consider first a pure transverse field quench with $h = 0$ and $g > 0$. The post-quench state then consists of independent kink-antikink pairs with momenta k and $-k$. These kinks behave as non-interacting fermions with a dispersion relation, $\epsilon(k) = 2J\sqrt{1 + g^2 - 2g\cos k}$, and propagate with the group velocity

$$v(k) = \frac{\partial \epsilon(k)}{\partial k} \,, \tag{6.13}$$

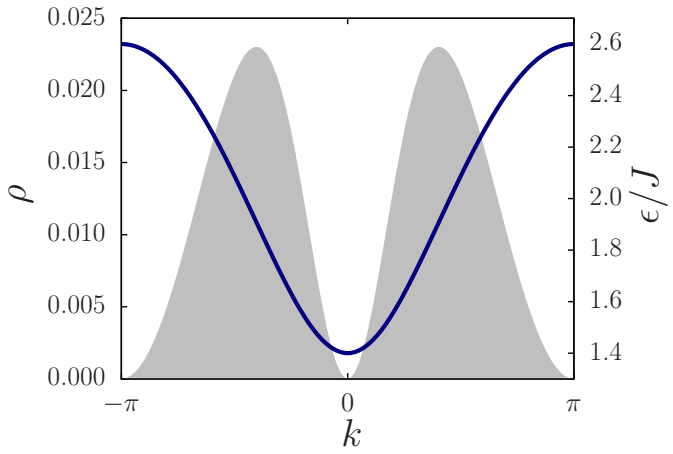

Figure 6.8: The kink dispersion relation $\epsilon(k)$ for $g = 0.3$ (full line) and the initial density $\rho(k)$ (shaded region) for $g_0 = 0$, $g = 0.3$.

limited by the maximum velocity, $v_{\max} = 2J\,g$. The initial density of kinks can be determined following Refs. [127, 207]. Kink-antikink pairs of momentum $\pm k$ are created with a pair creation amplitude, $K(k) = \tan \Delta_k/2$, with

$$\cos \Delta_k = \frac{g g_0 - (g + g_0)\cos k + 1}{\sqrt{1 + g^2 - 2g\cos k}\sqrt{1 + g_0^2 - 2g_0 \cos k}} \,. \tag{6.14}$$

and the density of kink pairs with momentum in the interval $[k, k + dk]$ is given by

$$\rho(k) = \frac{|K(k)|^2}{1 + |K(k)|^2} = \frac{1 - \cos(\Delta_k)}{2} = \sin^2(\Delta_k/2) \,, \tag{6.15}$$

shown in Fig. 6.8. The denominator in this equation simply reflects the fermionic nature of kinks, and the spatial bubble density is just the integral of $\rho(k)$,

$$\rho_{\text{bubble}} = \int_0^\pi \frac{dk}{2\pi} \rho(k) \,. \tag{6.16}$$

Let us consider now a finite longitudinal field $h < 0$. Before entering the issue of bubble dynamics, it is important to discuss the origin of the bubbles. In Coleman's original scenario, the bubbles appear as a result of vacuum tunnelling. The tunnelling probability per lattice site for the Ising spin chain was computed in [208] and in a semi-classical approximation[1] it is given by

$$\gamma = \frac{\pi g m}{9} \exp\left\{ -\frac{1}{mg} \left| f\left(-i \log h\right) \right| \right\} \tag{6.17}$$

[1]We note that the conditions for the semi-classical approximation are that g is sufficiently far away from its critical value $g_c = 1$ and it is valid in the asymptotic limit $h \to 0$, which means that the exponent is large and tunnelling is suppressed.

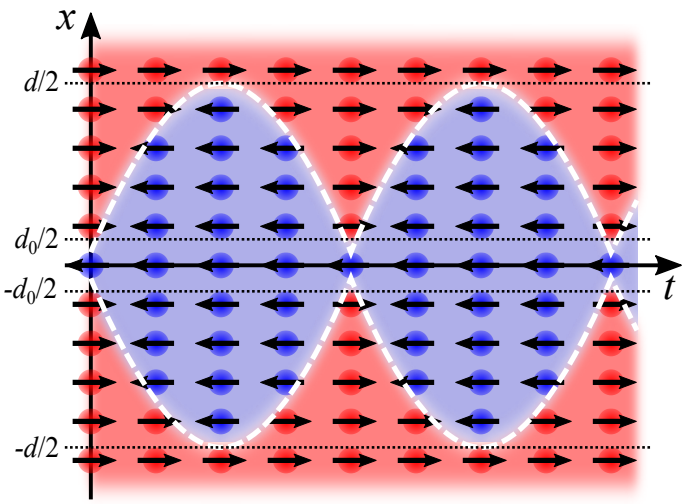

Figure 6.9: Illustration of Bloch oscillation of a bubble with a definite initial momentum of the kinks forming the bubble walls. Arrows indicate dominant spin directions in space and time. Time delays at kink collisions are neglected.

where $m = (1 - g^2)^{1/8}$ is the spontaneous magnetisation for the pure transverse field Ising spin chain with transverse field g and

$$f(x) = 2 \int_0^x \epsilon(k) dk \,. \tag{6.18}$$

For the range of parameters considered in our simulations, the nucleation rate per site estimated from (6.17) is very small, not exceeding 10^{-6}. In fact, the nucleation is heavily suppressed by a mechanism analogous to the Schwinger effect [209] in Quantum Electrodynamics: the creation of the bubbles can also be viewed as spontaneous creation of particle-antiparticle (kink-antikink) pairs in a homogeneous external field (here given by h), which is the same as in continuum field theory. However, the bubbles created in the quenches we consider originate from the finite energy density in the initial state which is not fine-tuned to be the false vacuum itself. Nevertheless, the fate of the bubbles after their appearance is essentially independent of the mechanism responsible for their creation and, as we demonstrate, the suppression of their subsequent expansion is due to Bloch oscillations, which arise from the presence of the lattice.

Bloch oscillations can be described using a simple semi-classical picture, similar to the one used in [206] to describe the spectrum of mesonic excitations due to confinement. This is expected to work under the conditions that (i) the system is apart from the immediate vicinity of the critical point $g_c = 1$, (ii) the mean inter-particle spacing is much larger than the correlation length ξ: $\rho_{\text{bubble}}\xi \ll 1$, where ξ is of order one away

from the vicinity of g_c, and (iii) $|h|$ is sufficiently small. The validity of the latter condition can be seen from the fact that the semi-classical description of the meson spectrum is very accurate for the parameter range considered here [162].

To a first approximation, we can neglect the correction to the dispersion relation $\epsilon(k)$, and treat the dynamics of the bubbles as that of a two-particle system, a kink and an antikink interacting via a repulsive potential

$$V(r) = -\chi\, r, \tag{6.19}$$

where r is the distance between the kinks, and χ the coefficient given by the energy gain of flipping the magnetisation into the external field's direction: $\chi = 2m|h| = 2|h|\,(1-g^2)^{1/8}$. The semi-classical equation of motion of the kinks is then written as

$$\dot{r} = 2\,\frac{\partial\epsilon(k)}{\partial k}, \qquad \dot{k} = -\frac{1}{2}\frac{\partial V}{\partial r} = \frac{\chi}{2}, \tag{6.20}$$

with the factors 2 and 1/2 related to having two mobile kinks. The second equation yields immediately $k(t) = k_0 + \frac{1}{2}\chi t$, and can be used to determine the kink-antikink distance as

$$r(t) = \frac{4}{\chi}\left[\epsilon\left(k_0 + \chi\, t/2\right) - \epsilon\left(k_0\right)\right] + r_0\ , \tag{6.21}$$

with r_0 initial size of the bubble (typically of the order of the lattice spacing), and $\pm k_0$ the initial momenta of the kinks. Let us first consider bubbles where the initial size r_0 can be neglected. Due to the periodicity of $\epsilon(k)$, the kink velocity reverses sign when the momentum k passes the boundary of the Brillouin zone at $k = \pm\pi$, where the kinks turn back. As a result, kinks return to their original position and collide again after a period $T(k_0)$ when the bubble re-collapses ($r(T(k_0)) \approx 0$). This happens when $k_0 + \chi\, T(k_0)/2 = 2\pi - k_0$. At this point, the kink and the antikink are reflected, and start off again with the whole cycle repeating as illustrated in Fig. 6.9, causing the bubbles oscillate in time. The maximum amplitude of these oscillations is obtained when $k_0 = 0$:

$$l_{\max} = \frac{4(\epsilon(\pi) - \epsilon(0))}{\chi} = \frac{8g}{m|h|}\,. \tag{6.22}$$

In contrast to the idealised single-bubble dynamics shown in Fig. 6.9, the observed oscillations shown on the left of Fig. 6.6 result from a large number of bubbles, each having different initial momenta and initial sizes. Nevertheless, these Bloch oscillations still have a characteristic time. As obvious from Fig. 6.8, (and can be indeed verified by direct calculation, for an initial state with $g_0 = 0$) the kink density is highest around momenta corresponding to $v_{\max}$, which determines the front line of the bubbles, and

thus the overall frequency of oscillations via the condition, $\frac{1}{2}\chi T_B = 2k_0 \approx \pi$ for small g-s, yielding

$$\omega \approx \frac{2\pi}{T_B} = \chi \,.$$

The presence of a distribution of domain wall momenta leads, however, to a gradual decay of oscillations due to the dependence of the oscillation period and phase on the initial kink momentum. Bubble collisions have a similar, degrading effect on coherent oscillations.

We close this subsection with some important observations regarding the role of collisions:

- For small bubbles, kink-antikink pairs collide once during every oscillation period. In principle they could annihilate into mesons then; however our numerics shows no such effect in the accessible time frame, which is consistent with recent findings [210] that the inelastic scattering is very ineffective. In this regard we also note that annihilation into mesons would involve string breaking which is heavily suppressed as can be understood via relating it to the Schwinger effect [201].

  These collisions also give rise to a time delay due to the interaction between kinks. In the case of zero longitudinal field, $h = 0$, however, the kink-antikink scattering amplitude is simply -1, and there is no time delay. Therefore any time delay introduced by kink collisions is of order h, which we can neglect in the simple semi-classical picture used here.

- Collisions between different bubbles lead to corrections to the simple motion described above. This effect can be neglected if the average spacing between bubbles is larger than their maximum allowed size, which leads to the condition $\rho_{\text{bubble}} \ll 1/l_{\max}$ requiring the longitudinal field to satisfy $h \gg h_c$, where

$$h_c = \frac{8g}{m}\rho_{\text{bubble}} \,. \tag{6.23}$$

  therefore we always use field values larger than h_c in our simulations. The values of h_c are reported in Table 6.1 for different values of g.

g	0.20	0.25	0.30	0.35	0.40
h_c	0.0041	0.0080	0.0139	0.0223	0.0338

Table 6.1: Values of h_c for different values of g.

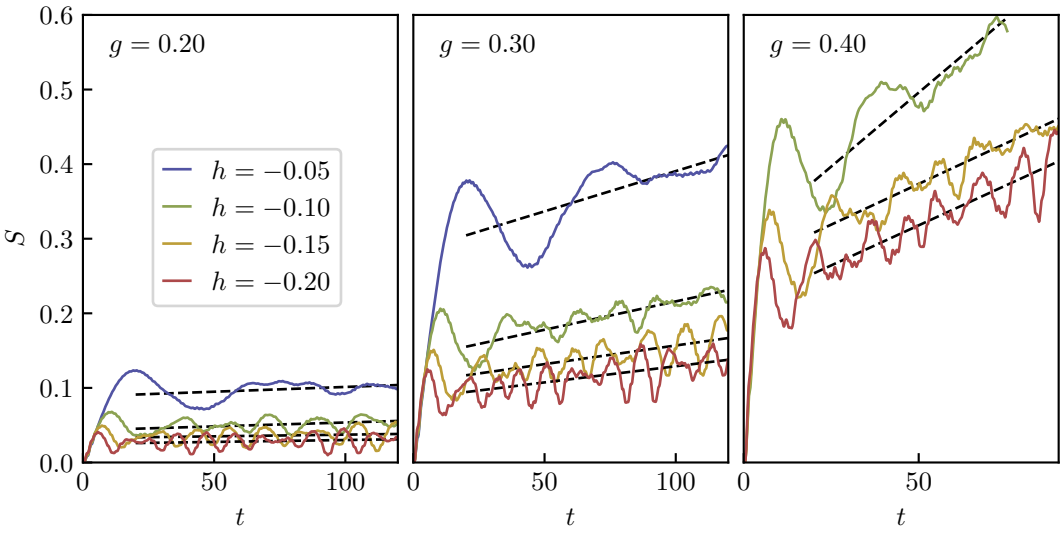

Figure 6.10: Entanglement entropy as a function of time for different values of g and h, with the overall drift indicated by dashed lines.

- For bubbles created with a sufficiently large initial size $r_0 > l_{\max}$, the kinks never collide and instead oscillate around spatially separated positions with frequency given exactly by χ (cf. also [206]). Note that the creation of large bubbles is suppressed, since creating a finite sized bubble of the true vacuum corresponds to a process involving a number of simultaneous spin flips given by the bubble size r_0, with probability suppressed exponentially in r_0. As a result, the contribution of 'collisionless bubbles' (those satisfying $r_0 > l_{\max}$ and therefore oscillating without periodic internal collisions) increases sharply with decreasing $l_{\max}$ i.e. increasing $|h|$, which is consistent with the quench spectroscopy results reported later in Subsection 6.4.2. In addition, to avoid collisions between kinks from different bubbles, the average bubble spacing must be much larger than $l_{\max}$, leading to the same condition $|h| \gg h_c$ as before.

- It is apparent from Fig. 6.7 that even though the growth of entanglement entropy is suppressed, it still shows a slow drift in time in addition to the dominant feature of temporal oscillations. This drift can be understood to originate from bubble collisions, which become less probable as $|h|$ grows compared to h_c. Indeed, Fig. 6.10 demonstrates that the drift is suppressed for other values of g as well when $|h| > h_c$. Note that entanglement entropy grows so fast at $g = 0.4$ for $h = -0.05$ that it was not possible to simulate the evolution in the time scale shown in the figure. As can be seen from Table 6.1, $h_c = 0.0338$ for $g = 0.4$, so bubble collisions

are much less suppressed than for the other two cases $g = 0.2$ and 0.3.

6.4 Probing Bloch oscillations

6.4.1 Verifying average bubble size and scaling

One piece of evidence for the scenario of Bloch oscillations is that it predicts an average bubble size that agrees reasonably well with the spatial extension of the correlations. This is demonstrated in Figure 6.6, where the blue lines depict the estimate for the average bubble size

$$\langle r \rangle_{\text{anti-conf}} \approx \frac{1}{\rho_{\text{bubble}}} \int_0^\pi \frac{dk_0}{2\pi} \rho(k_0) \frac{4}{\chi} \left(\epsilon(\pi) - \epsilon(k_0) \right) \tag{6.24}$$

obtained by neglecting the original bubble size d_0. For the standard confining case, a similar reasoning gives the average bubble size

$$\langle r \rangle_{\text{conf}} \approx \frac{1}{\rho_{\text{bubble}}} \int_0^\pi \frac{dk_0}{2\pi} \rho(k_0) \frac{4}{\chi} \left(\epsilon(k_0) - \epsilon(0) \right) \tag{6.25}$$

since, in this latter case, kink momenta oscillate between k_0 and 0. Note that these estimates depend both on g and h, and give a very good estimate for the spatial extension of the correlations shown in Figure 6.6.

Another tell-tale signal of Bloch oscillations is that their spatial extension is predicted to scale as $\sim 1/h$, while their frequency is proportional to h. This is manifest in the numerically computed time evolution, as demonstrated in Fig. 6.11, where the space-time bubble contour is extracted from the data at $h = -0.1$ and then superimposed on the time evolution obtained for other h values, with time and space rescaled accordingly. Note that the actual distance and time scales vary by a factor of 4, while the correlation profiles remain almost identical when plotted in terms of the scaled variables, $|h|t$ and $|h|l$. This scaling works remarkably well for the first few oscillations. Differences for larger values of time can be attributed to deviations from our simple semi-classical picture such as the presence of localised spin excitations with frequencies much higher than the Bloch oscillations of the bubble walls, as well as distortions due to bubble collisions and the contributions from the periodic kink collisions when bubbles shrink to their minimal size.

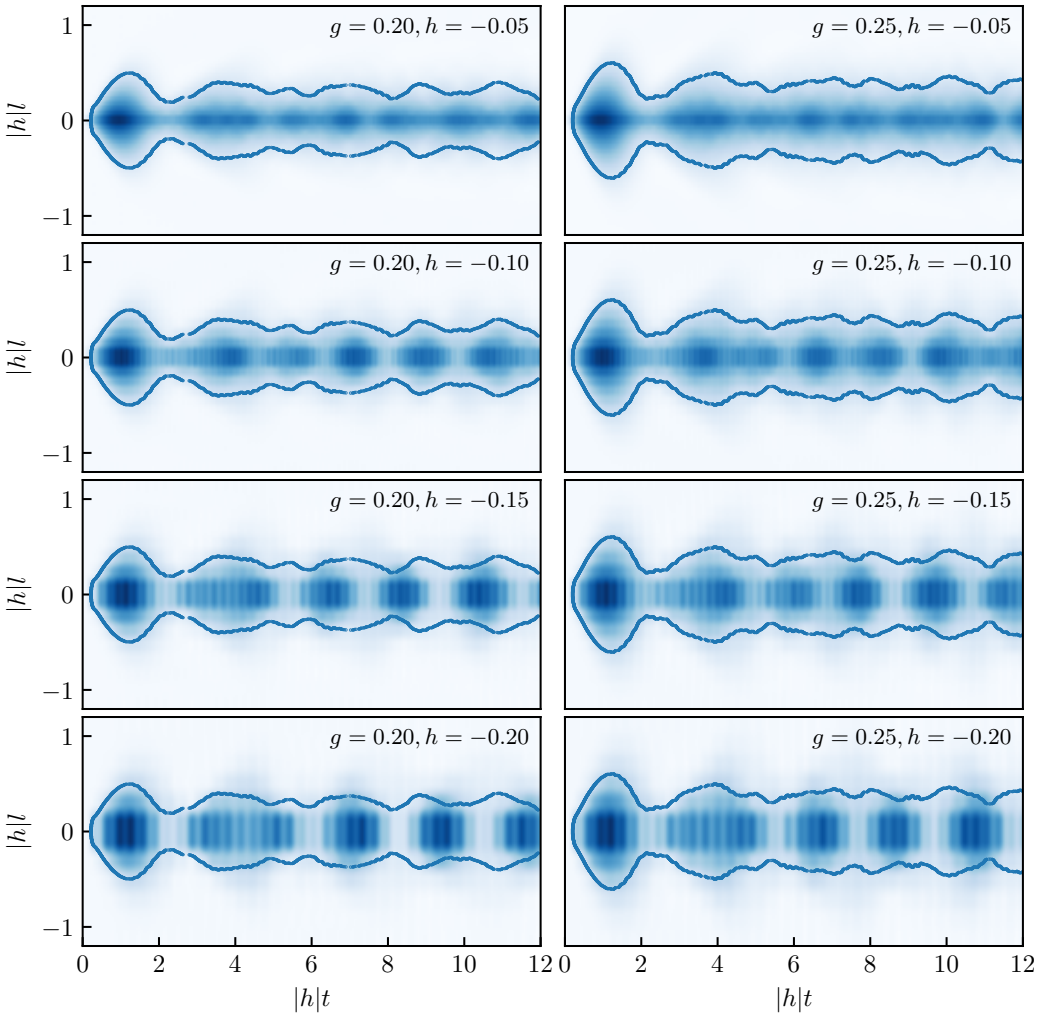

Figure 6.11: Scaling evidence for Bloch oscillations for the transverse field values $g = 0.20$ (left) and $g = 0.25$ (right), with the longitudinal field taking the values $h = -0.05, -0.10, -0.15, -0.20$ for each. The plot shows $\langle \sigma_0^z \sigma_l^z \rangle_c$ as a function of the scaling variables $|h|t$ and $|h|l$. The colour scale is defined by normalising the maximum value of the correlator to 1, while the blue lines show the bubble wall defined by the data with $h = -0.10$ at one fifth of its maximum value. Note that $h = -0.05$ where the scaling is visibly the least perfect, is a small field for which quench spectroscopy (cf. Subsec. 6.4.2) reveals that the system is not yet cleanly dominated by Bloch oscillations.

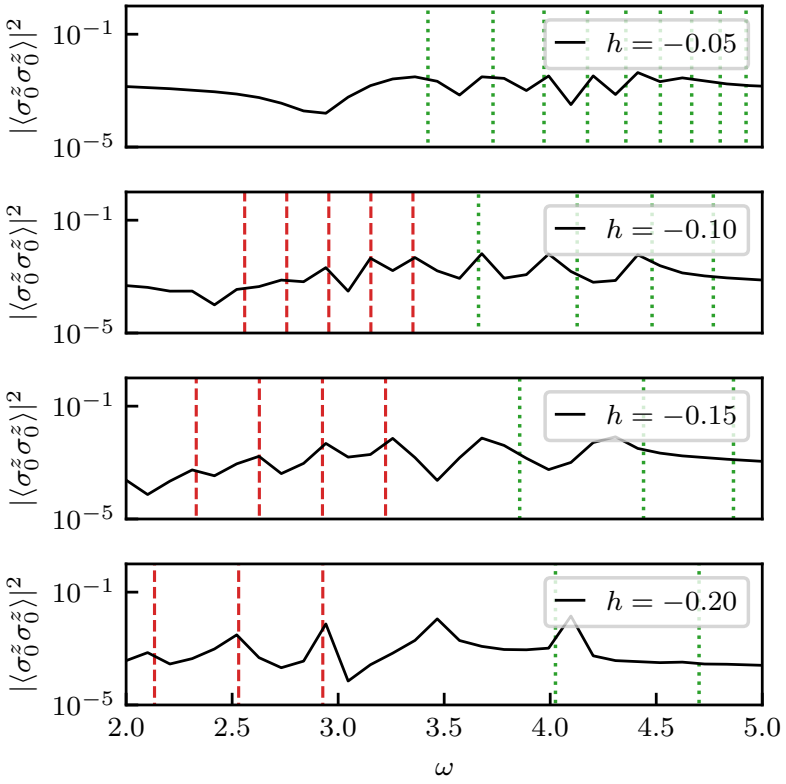

Figure 6.12: Power spectrum of $\langle\sigma_0^z(t)\sigma_l^z(t)\rangle_c$ for $l = 0$ and $g = 0.25$. Green dotted lines show meson frequencies (computed following [162]) - note that they become less and less relevant as $|h|$ grows. Red dashed lines have a spacing $\chi = 2|h|m$, indicating a regular sequence of higher harmonics of the Bloch oscillations, which instead become more prominent for higher values of $|h|$ as $l_{\max}$ becomes smaller. In the cases shown, the minimum size of collisionless bubbles $l_{\max}$ (from top to bottom) are 40.3, 20.2, 13.4 and 10.1, respectively.

6.4.2 Quench spectroscopy

'Quench spectroscopy', presented in Fig. 6.12, i.e. the Fourier analysis of the time evolution after the quench provides a further tool to assess Bloch oscillations. For negative values of h with small magnitude, we only observe frequency peaks corresponding to mesonic bound states, just as for the case of dynamical confinement with $h > 0$ [162]. The energy gap of these mesonic excitations is always larger than twice the kink gap, grows with increasing $|h|$, and can also be computed theoretically using a semi-classical method [206], which we briefly summarise in Section 6.1.1. For longitudinal fields such that $|h|$ is smaller than, or comparable to h_c, we do not observe well-defined frequencies corresponding to Bloch oscillations, as shown by the top plot in Fig. 6.12. This is not

unexpected, since in such a case bubble collisions prevent independent Bloch oscillations.

For larger field values $|h| \gg h_c$, collisions between bubbles become less frequent. In addition, the maximum Bloch oscillation length $l_{\max}$ becomes shorter with increasing h, and the number of collisionless bubbles increases rapidly. This leads to the appearance of regularly spaced frequency peaks well below the threshold of mesonic excitations, corresponding to higher harmonics of the Bloch frequency χ. Indeed, such a series of peaks is seen to coincide with the red lines in the lower three plots in Fig. 6.12, with the distance between them equal to χ. Note that the simulation can only capture higher harmonics, mostly due to the finite time window of the numerical simulations, but also due to low-frequency background which results from the quench time evolution containing frequencies corresponding to all differences between energy levels of the post-quench Hamiltonian. In addition, the energy needed to create mesonic excitations also increases with $|h|$. We therefore expect, and indeed find, that mesonic contributions to the frequency spectrum become less and less pronounced with growing $|h|$. This stands in stark contrast to the case of dynamical confinement, where meson excitations continue to dominate the time evolution even for large values of the longitudinal field h [162].

Conclusions and Outlooks

In Chapter 3 we used the generalised hydrodynamics approach introduced in Chapter 2 to study the paradigmatic staircase model [82]. The SM has a property which is unique among integrable quantum field theories, that is, at thermal equilibrium and high temperature, the theory does not flow to a single ultraviolet fixed point but rather to infinitely many, depending on how the high temperature limit is carried out. More precisely, at temperature T, the key scale in the model is the ratio $\alpha = \frac{y}{\theta_0}$ where $y = \log(2T)$ and θ_0 is a parameter of the scattering matrix. Taking both y and θ_0 to infinity, whilst keeping their ratio fixed and finite, determines the choice of the UV fixed point. The set of all possible UV fixed points is given by the unitary minimal models of conformal field theory. In addition, the flow between consecutive CFTs, ordered according to their central charge, admits an effective description in terms of a massless theory known as the $\mathcal{M}A_k^{(+)}$ model, which we have also studied. The main conclusions of our study can be summarised as follows:

- The evaluation of TBA quantities that have a key hydrodynamic interpretation, such as the spectral particle current and density and the effective velocity gives new insights into the properties of the model, even at thermal equilibrium. The spectral functions of the SM generally exhibit multiple local maxima/minima while the effective velocity has multiple zeroes and plateaux. The number of such maxima, minima, zeroes and plateaux is linked to the scale α introduced above. For $\frac{k-1}{2} < \alpha < \frac{k}{2}$ the spectral particle density has $2k$ maxima and the spectral particle current has k maxima and k minima. The effective velocity has $2k-1$ zeroes, k plateaux at value $+1$ and k plateaux at value -1. The non-monotonicity of the effective velocity is indeed one of the most distinct features of the model. All these properties can be seen in the video [88].

- The massless description of the SM by means of the $\mathcal{M}A_k^{(+)}$ models provides an accurate description of all the functions mentioned above. The agreement between both descriptions can be visualised by contrasting any of the SM functions with a

"cut and paste" arrangement of the corresponding functions found in the massless model. The agreement is particularly striking for the effective velocities, whose intricate square-wave structure is perfectly reproduced.

- Similar properties are found within the partitioning protocol, especially when the right and left temperatures are chosen so as to fall within an interval of values of α associated to the same UV fixed point. In this context, the SM model provides an excellent opportunity to study the averages of conserved currents and densities for higher spins near different UV fixed points. Indeed, it is well-known how the energy current and density scale in CFT [65–67] but a lot less is known for higher spin conserved quantities. We provide a partial answer to this question. We show numerically and analytically that higher spin currents and densities scale with appropriate powers of the temperatures $T_{L/R}$, as expected. More importantly, we also show that the numerical coefficient of these powers is very nearly proportional to the central charge of the UV fixed point. By very nearly we mean that the central charge is not exactly reproduced (except for spin 1, corresponding to the energy), but deviations from it are numerically very small and still to be analytically understood.

These results suggest several future directions of research. First, in line with the last point, it is desirable to have a better analytical understanding of the UV scaling of the averages of higher spin currents and densities. This is a problem of general interest in the context of out-of-equilibrium dynamics in CFT and goes beyond the precise model we have discussed. This analytical understanding could come from two sources: the explicit construction/study of conserved quantities in CFT and the evaluation of their averages and/or the manipulation of the GHD expressions for higher spin currents and densities, so that coefficients such as those presented in (3.30) are analytically evaluated. Second, we would like to generalise these results to other staircase models such as the generalisations constructed in [83–87].

In conclusion, this is a new contribution to a so far small body of work including also [80, 81] which explores how quantities of interest in the context of generalised hydrodynamics can provide, even at thermal equilibrium, new insights into properties of integrable quantum field theory. These insights are especially rich in IQFTs possessing unusual features, such as unstable particles or, as in the present case, an intricate RG physics. In all the models studied, including SM, we find a quantitative relationship between the emergence and area of new local maxima of the spectral particle density and the intensity of the interaction, as described by the two-particle scattering matrix.

We also find that in such models the effective velocities can exhibit extremely intricate and unusual patterns as seen in [88], very far from the standard deformed $\tanh\theta$ shape that is found for most interacting IQFTs.

In the work introduced in Chapter 5 we considered quantum quenches in the paramagnetic phase of the quantum Potts spin chain corresponding to switching on a longitudinal magnetic field. We have demonstrated that the entanglement entropy production rate shows a deep relation with the quasi-particle spectrum. In particular, the mean entanglement entropy production rate $\overline{\partial_t S}$ is greatly enhanced by the appearance of a new quasi-particle species in the spectrum, which is a manifestation of Gibbs mixing entropy corresponding to species information. These findings are completely consistent with the results obtained for the Ising case in [159], showing the general nature of the effect and confirming its interpretation as a non-equilibrium manifestation of the so-called Gibbs paradox. We have also shown that for very large $h > 0$ the entropy production rate decreases towards zero, which can be understood from the freezing of spin chain dynamics.

In contrast with the Ising model, for the Potts case the domain $h < 0$ has a different physics since the spin dynamics does not freeze for any magnitude of h, and indeed in that domain we observed a monotonous increase of $\overline{\partial_t S}$ with $|h|$, the qualitative details of which again could be fully understood from the quasi-particle spectrum.

As we noted, a detailed quantitative description of the entanglement entropy production is not yet available. All the available evidence shows that the quenches considered here are of sufficiently small density to admit an essentially semi-classical quasi-particle description following the picture proposed by Calabrese and Cardy in their seminal works [112, 116]. There has been substantial recent work aiming at extending the quasi-particle description beyond the simple picture of production of independent pairs, such as to cases with no pair structure [211], and initial states with correlated pairs [212].

For a quantitative prediction of entanglement entropy production, the main missing ingredient is sufficiently detailed knowledge of the quasi-particle production rates as functions of the quench parameter h. Presently such information is only available for the Ising case and even there only in the scaling field theory limit [213]. Once the amplitudes are available, one can try to develop a theory for the entanglement entropy production following the lines of [211]. Albeit in contrast to the case in [211] the system we consider has interacting quasi-particles, it seems likely that in the regime of transverse

field g close enough to the critical value 1, the post-quench density is small enough so that effects of interactions between the quasi-particle do not affect substantially the post-quench time evolution once the particles were created, and therefore one could achieve at least a semi-quantitative description if the quasi-particle production rates can be obtained by some means.

Furthermore we analysed the existence of a direct relation between relaxation rates and entropy growth after a quantum quench. This is not just an idea intuitively supported by the quasi-particle picture of the dynamics [112], but a more direct, quantitative relation is suggested by the fact that the growth rate of Rényi entropies can be represented as the relaxation rate for branch-point twist fields related to replica symmetry [160, 185]. In the second part of Chapter 5 we examined this relation in the context of quantum quenches on the quantum Ising and Potts spin chains i.e. q-state Potts spin chains with $q = 2, 3$.

For transversal quenches (i.e. in the absence of explicit breaking of the symmetry $\mathbb{Z}_q$) we found that the ratio of Rényi entropy growth rates to the magnetisation relaxation rates is universal in the small quench limit

$$\frac{\Gamma_n}{\Gamma} = \frac{1 - 1/q}{1 - 1/n} + \dots \,, \quad (n = 2, 3, \dots) \,, \tag{6.26}$$

with the ellipsis denoting corrections for higher post-quench density. This can be proven explicitly using exact results for the Ising chain, and it is also consistent with the above-mentioned expression of Rényi entropy rates as relaxation rates of branch-point twist fields; we also presented numerical evidence using iTEBD simulations. The value of the ratio can be understood heuristically in terms of the symmetries $\mathbb{Z}_q$ of the magnetisation operator and $\mathbb{Z}_n$ of the branch-point twist fields, however, at this point we lack a fully convincing derivation. One possible way to go is to consider the scaling limit of the transverse field 3-state Potts chain, which is an integrable quantum field theory [214], for which the exact S-matrices are known both in the paramagnetic [215] and ferromagnetic [180] phases. In fact, the parameter q can even be generalised to a real variable between 0 and 4. Therefore it must be possible to repeat the field theory derivation of both the relaxation rate and the Rényi entropy growth rates for the transverse quenches for $q \neq 2$, and directly verify that the universal ratio (5.55) is indeed obtained at the leading order in the post-quench quasi-particle density. However, this requires a rather involved and lengthy calculation (cf. [161]) which is beyond the scope of the present work.

Note that there is no similar universal ratio for the von Neumann entropy rate obtained as the limit $n \to 1$, which is not surprising as there is no semi-local operator (such as the twist field) to express it as an expectation value.

For quenches involving the longitudinal field the symmetry $\mathbb{Z}_q$ is explicitly broken. In the ferromagnetic phase when the transverse field $g < 1$ this leads to confinement, which can limit the growth of entropy and at the same time leads to persistent oscillations [162], which is consistent with both the entropy rate and the relaxation rate vanishing.

The behaviour in the paramagnetic regime is more interesting. Here we considered the family of quenches starting from the ground state at a transverse field $g > 1$ and switching the longitudinal field h from zero to a finite value. Since the order parameter symmetry $\mathbb{Z}_q$ is explicitly broken, we expect that the universal ratio above is not valid even for small quenches. However, for the Rényi entropy rates we still predict

$$\frac{\Gamma_n}{\Gamma_m} = \frac{1 - 1/m}{1 - 1/n} + \dots \,, \quad (n, m = 2, 3, \dots) \,, \tag{6.27}$$

which is indeed confirmed by numerical simulations.

Despite the absence of a simple quantitative relation, the growth rates of Rényi entropies and the magnetisation relaxation rate qualitatively follow the behaviour of the growth rate of the von Neumann entropy, as expected from the quasi-particle picture. In particular, all rates show the characteristic non-monotonous behaviour in h due to changes in the quasi-particle spectrum and the consequent "dynamical Gibbs effect". The important implication of our results is that in an experimental implementation of the spin chain the "dynamical Gibbs effect' has a well-defined signature in the behaviour of the magnetisation relaxation rates which is easily observable, in contrast to the entanglement entropy, opening an avenue for the experimental demonstration of the effect.

An interesting observation is that while the ratios of Rényi entropy rates deviate from (6.27) by increasing the quench size parametrised by h, the universal ratio is restored to a good precision in a well defined region. This happens approximately at the threshold h_{crit} for the appearance of the bound state quasi-particles, where the entropy growth is suppressed despite of the finite magnitude of the quench. The theoretical explanation of this finding is an interesting open question.

Finally, in Chapter 6 we demonstrated within the framework of the transverse field Ising model that light-cone time evolution and the decay of the false vacuum can be absent in one-dimensional systems even in a deconfined quench regime, where the formation of bubbles would be energetically favourable. Rather, quite unexpectedly, we observe in this regime spatially confined correlations, oscillating in time, which we identify as Bloch oscillations. These appear due to the underlying lattice and the

periodicity of the quasi-particles' dispersion relation in the momentum variable. The absence of relaxation after the quantum quench can also be considered an effect of the bounded quasi-particle dispersion, due to which the domain walls can only carry away a limited portion of the energy that would be liberated by the expansion of the true vacuum bubble.

This results demonstrate that Bloch oscillations play a key role in inhibiting the growth of bubbles which result from nucleation of the true vacuum in a global quantum quench starting from a translationally invariant initial state dominated by the false vacuum. The effect we observe can also be interpreted as a suppression of thermalisation in a global quench of a spin chain with (anti-)confining dynamics. In this context, we note that Bloch oscillations have been previously found in the dynamics governed by the Hamiltonian (6.1) for an initial state consisting of a single domain wall [197], and later they were argued to slow down entropy growth after starting from a random multi-kink state [201]. Besides the difference from our case in the initial state and the observable signature, in [197, 201] the Bloch oscillations appear in concert with the dynamical confinement mechanism discovered in [162], while in our case the effect of Bloch oscillations is clearly separate and distinct from dynamical confinement. This separation between the two mechanisms is parameterised by relative magnitude of the longitudinal field compared to the field value h_c (cf. Eq. (6.23)) derived from comparing the maximum bubble size to the post-quench bubble density, and is also confirmed by quench spectroscopy. In addition, instead of relying on perturbation theory in the transverse field g, we make use of the semi-classical approach which is valid for any g (albeit not too close to the critical point $g = 1$).

We point out that after our results, the vacuum tunnelling in the Ising spin chain was numerically observed in [216], where the prediction (6.17) was also verified. The observation of the tunnelling was made possible by choosing transverse fields close to the critical value, $g \geq 0.7$ which enhances the transition amplitude (6.17) to magnitudes $10^{-3} - 10^{-1}$, and also by observing the dynamics for times much shorter (at least by an order of magnitude) than the period of Bloch oscillations for the chosen parameters values of g and h. It is an interesting issue to perform simulations for parameter values and time ranges where effects of both Bloch oscillations and vacuum tunnelling can be observed, to see how the two mechanisms interfere. However, these regimes are difficult to access by the present numerical methods.

Our observations of emergent Bloch oscillations are also in agreement with recent results obtained in kinetically constrained Rydberg spin systems [217]. However, while in Ref. [217] a special constraint (fine-tuning) was needed to generate Bloch oscillations,

here they emerge quite generically, without any constraint in a regime where quasi-particle excitations would naively be expected to speed up and spread correlations over the system.

This results are relevant for experimental realisations of the tunnelling decay of the false vacuum such as put forward in Ref. [191]. We predict that in discrete spin chains, the dynamics after bubble nucleation generally leads to Bloch oscillations, in stark contrast to expectations from continuum quantum field theories. We also demonstrate that simple spin chains provide an experimental realisation of Bloch oscillations, which can clearly be identified from the scaling of the space-time dependent spin-spin correlation functions with the applied longitudinal field and from quench spectroscopy.

Today, strongly correlated quantum many-body systems – including the quantum Ising spin chain itself [218] – can be routinely realised using ultra-cold atomic quantum simulators [219–223], or in a digital quantum computers [224]. These advances have triggered recently considerable interest in simulating the decay of the false vacuum [189–193]. Our results, demonstrating the violation of Coleman's scenario and providing directly observable signatures of Bloch oscillations, may be particularly interesting in this context.

APPENDIX A

CONSTANT TBA FOR THE SM

A.1 L-function Kinks and Plateaux

The value of TBA functions in the SM depends very strongly on the interplay between the parameters $y = -\log(\beta/2)$ and θ_0. In fact, the crucial parameter is precisely their ratio

$$\alpha = \frac{y}{\theta_0} \tag{A.1}$$

If this ratio is kept fixed with both y and θ_0 going to infinity, then the scaling function $c(y)$ tends to the central charge of one of the unitary minimal models $\mathcal{M}_{k+2}$. Precisely which one depends on the value α.

As already introduced in section 3.1.2, the general structure is the following. When

$$\frac{k-1}{2} < \alpha < \frac{k}{2} \quad , \qquad k \in \mathbb{N}, \tag{A.2}$$

the L-function has $2k$ kinks at positions $\pm(y - \ell\theta_0)$ with $\ell = 0, 1, \ldots, k-1$. Kinks can be organised into two sequences, depending on whether they originate from the left or from the right. That is, we can order kinks according to

$$\theta_{1,L} < \theta_{1,R} < \theta_{2,L} < \cdots < \theta_{k,L} < \theta_{k,R} \tag{A.3}$$

with

$$\begin{cases} \theta_{\ell,L} = -y + (\ell - 1)\theta_0 \\ \theta_{\ell,R} = y - (k - \ell)\theta_0 \end{cases} \qquad \ell = 1, 2, \ldots, k \tag{A.4}$$

As we have seen, the L-function will develop plateaux in the regions between consecutive kinks. There are therefore $2k + 1$ plateaux, the first and the last being in the regions $\theta < -y$ and $\theta > y$, respectively, where $L(\theta)$ is effectively zero. The internal plateaux

are of alternating width, and so is the distance between two adjacent kinks. We arrange the internal plateaux in two sequences, odd and even, according to:

$$\begin{cases} P_{2\ell-1} = [\theta_{\ell,L}, \theta_{\ell,R}], & \ell = 1, \dots, k \\ P_{2\ell} = [\theta_{\ell,R}, \theta_{\ell+1,L}], & \ell = 1, \dots, k-1, \end{cases} \tag{A.5}$$

with $|P_{2\ell-1}| = 2y - (k-1)\theta_0$ and $|P_{2\ell}| = k\theta_0 - 2y$, where $|P|$ indicates the width of plateau P.

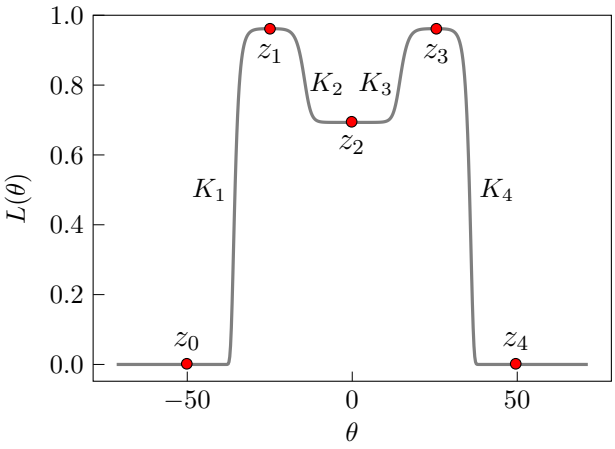

Figure A.1: L-function of the SM for $k = 2$. Points z_ℓ lie at the centre of plateaux, while kinks K_ℓ interpolate between them.

Finally, we define the mid-points of the internal plateaux

$$z_\ell \equiv \frac{(\ell - k)\theta_0}{2}, \qquad 1, \dots, 2k-1, \tag{A.6}$$

and

$$z_0 \equiv -\frac{k\theta_0}{2}, \qquad z_{2k} \equiv \frac{k\theta_0}{2} \tag{A.7}$$

to extend the definition (A.6) to the first and last plateaux where $L(\theta)$ is zero. All these definitions are illustrated in Fig. A.1 for the case $k = 2$. So far we have ignored the fact that the kinks K_i have themselves a finite width. We can see that the ℓ^{th} kink is spread in the interval

$$K_\ell = [z_{\ell-1}, z_\ell], \qquad i = 1, 2, \dots, 2k\,. \tag{A.8}$$

A.2 Constant TBA equations

In this section we derive the so-called constant TBA equations [62–64]. These can be seen as UV limits of the original TBA equation for the SM, whose solutions describe the height of the centres of the plateaux at z_i. Because there are many such plateaux in the SM there are several constant TBA equations, which in effect form a system of coupled equations in much the same spirit as the TBA description of the $\mathcal{M}A_k^{(+)}$ model presented in section 3.1.3. Following the steps used in [84, 85], we want to look at the values of $L(\theta)$ at the midpoints of the plateaux. Let $\varepsilon_i := \varepsilon(z_i)$ be the values of the pseudoenergy at the plateaux' mid-points. The TBA-equation can be expressed as

$$\varepsilon_i = 2e^{-y}\cosh(z_i) - \sum_{i=1}^{2k}\int_{K_i}\frac{d\theta'}{2\pi}L(z_i-\theta')\varphi(\theta')\,, \tag{A.9}$$

where we can reduce our integration region because of the double-exponential fall-off of $L(\theta)$. The driving term is vanishingly small for all i except for regions K_1 and K_{2k}:

$$2e^{-y}\cosh(\theta) \sim \begin{cases} e^{-y-\theta}, & \theta \in K_1 \\ 0, & \theta \in K_2, \ldots, K_{2k-1} \\ e^{-y+\theta}, & \theta \in K_{2k} \end{cases} \tag{A.10}$$

Furthermore the kernel couples only those mid-points which are at distance θ_0 from each other since it is strongly peaked at $\theta' = \pm\theta_0$. Therefore, we can identify $L(z_i \pm \theta_0) := L_{i\pm 2}$. We can also make the standard asumption that underlies all constant TBA derivations, namely that the L-function is effectively constant (with values $L_{i\pm 2}$) over the region where the kernel is non-vanishing. In effect this means that we can take the L-functions outside the convolution (A.9) and just integrate each term in the kernel separately, giving

$$\int_{-\infty}^{\infty}\frac{d\theta}{\cosh(\theta \pm \theta_0)} = \pi\,. \tag{A.11}$$

The equations for plateaux midpoints simplify to:

$$-2\varepsilon_i = L_{i+2} + L_{i-2}, \quad i = 1, \ldots, 2k-1\,, \tag{A.12}$$

with boundary conditions $\varepsilon_{-1} = \varepsilon_0 = \varepsilon_{2k} = \varepsilon_{2k+1} = \infty$. Setting $x_i = \exp\{-\varepsilon_{2i-1}\}$ for $i = 1, \ldots, k$ and $y_i = \exp\{-\varepsilon_{2i-2}\}$ for $i = 2, \ldots, k$ we can rewrite (A.12) as

$$x_i^2 = \prod_{j=1}^{k}(1+x_j)^{I_{ij}} \qquad \text{and} \qquad y_i^2 = \prod_{j=2}^{k}(1+y_j)^{I_{ij}}\,, \tag{A.13}$$

with boundary conditions $x_0 = x_{k+1} = y_1 = y_{k+1} = 0$. These two sets of equations are again reminiscent of an underlying A_n structure and I_{ij} is the incidence matrix of A_n. Solutions to these equations where first given in [63] in their study of the constant TBA of A_n minimal Toda field theory and also in [98] in the study of RSOS models. They were also found in a more general context in [225]

$$x_\ell = \frac{\sin\frac{\pi\ell}{k+3}\sin\frac{\pi(\ell+2)}{k+3}}{\sin^2\frac{\pi}{k+3}}, \qquad y_\ell = \frac{\sin\frac{\pi\ell}{k+2}\sin\frac{\pi(\ell+1)}{k+2}}{\sin^2\frac{\pi}{k+2}}\,. \tag{A.14}$$

The associated UV central charge can be computed in terms of these values in the standard way [62, 63] and gives c_{k+2} as in equation (3.12).

Due to the kink structure of the L-function discussed here (see (A.10)) the SM scaling function (3.10) only receives contributions from the outer-most kinks K_1 and K_{2k}. Writing $c(y,\theta_0) = c_- + c_+$ with

$$c_- = \frac{3}{\pi^2}\int_{K_1} d\theta e^{-y-\theta}L(\theta), \qquad c_+ = \frac{3}{\pi^2}\int_{K_{2k}} d\theta e^{-y+\theta}L(\theta)\,, \tag{A.15}$$

we find that $c_- = c_+$ and the two contributions match exactly the formula (3.16) for the $\mathcal{M}A_k^{(+)}$ model. Their computation is standard and, as expected, for $\frac{k-1}{2} < \alpha < \frac{k}{2}$ we obtain once more c_{k+2} as in (3.12).

APPENDIX B

HIGHER SPIN CURRENTS FOR A FREE FERMION

In the free fermion case we can evaluate explicitly and analytically all the functions (3.23). In particular, in the partitioning protocol we have that

$$\varepsilon_{L/R}(\theta) = \beta_{L/R}\cosh\theta\,, \tag{B.1}$$

and so the even and odd spin currents can be written as

$$\mathtt{j}_{2s-1} = \frac{1}{2\pi}\int_0^\infty \cosh(s\theta)\sinh\theta\left[\frac{1}{1+e^{\beta_L\cosh\theta}} - \frac{1}{1+e^{\beta_R\cosh\theta}}\right], \tag{B.2}$$

$$\mathtt{j}_{2s} = \frac{1}{2\pi}\int_0^\infty \sinh(s\theta)\sinh\theta\left[\frac{1}{1+e^{\beta_L\cosh\theta}} + \frac{1}{1+e^{\beta_R\cosh\theta}}\right]. \tag{B.3}$$

For $\beta > 0$ it is possible to expand the occupation functions as

$$\frac{1}{1+e^{\beta\cosh\theta}} = e^{-\beta\cosh\theta}\sum_{n=0}^{\infty}(-1)^n e^{-n\beta\cosh\theta}\,, \tag{B.4}$$

and to express the CFT limit of the currents above in terms of modified Bessel functions $K_s(x)$. For instance, for the currents $\mathtt{j}_{2s}$ we can use the identity

$$\int_0^\infty \sinh(s\theta)\sinh\theta e^{-\beta\cosh\theta}\,d\theta = \frac{s}{\beta}K_s(\beta)\,, \tag{B.5}$$

to obtain

$$\begin{aligned}
\mathtt{j}_{2s} &= \frac{1}{2\pi}\sum_{n=0}^{\infty}(-1)^n\int_0^{\infty}\sinh(s\theta)\sinh\theta[e^{-\beta_L(n+1)\cosh\theta}+e^{-\beta_R(n+1)\cosh\theta}]d\theta \\
&= \frac{s}{2\pi}\sum_{n=0}^{\infty}\frac{(-1)^n}{n+1}\left[T_L K_s((n+1)\beta_L)+T_R K_s((n+1)\beta_R)\right] \\
&\approx \frac{s}{2\pi}\sum_{n=0}^{\infty}\frac{(-1)^n}{(n+1)}\left[\frac{2^{s-1}\Gamma(s)}{\beta_L^{s+1}(n+1)^s}-\frac{2^{s-1}\Gamma(s)}{\beta_R^{s+1}(n+1)^s}\right] \\
&= \frac{s\Gamma(s)}{2^{2-s}\pi}(T_L^{s+1}+T_R^{s+1})\sum_{n=0}^{\infty}\frac{(-1)^n}{(n+1)^{s+1}} \\
&= \frac{s\Gamma(s)}{4\pi}(2^s-1)\zeta(s+1)(T_L^{s+1}+T_R^{s+1})\,, \qquad \text{(B.6)}
\end{aligned}$$

where we have used the small x expansion of $K_s(x)$ and $\zeta(x)$ is Riemann's zeta function. As discussed in Chapter 3, we expect the coefficients (3.31) to be identical for $\mathtt{j}_{2s-1}$ and $\mathtt{j}_{2s}$ and so from the computation above we can identify

$$\mathcal{C}^s(\infty)=\Gamma(s)\zeta(s+1)(1-2^{-s})\,. \qquad \text{(B.7)}$$

In particular, we have the values

$$\begin{aligned}
\mathcal{C}^1(\infty)&=\frac{\pi^2}{12}=0.822467\,, \quad \mathcal{C}^2(\infty)=\frac{3\zeta(3)}{4}=0.901543\,, \\
\mathcal{C}^3(\infty)&=\frac{7\pi^4}{360}=1.89407\,, \quad \mathcal{C}^4(\infty)=\frac{45\zeta(5)}{8}=5.83272\,. \qquad \text{(B.8)}
\end{aligned}$$

These values are well reproduced by the height of the first plateau in the Figs. 3.12 and 3.14. As we can see in Fig. B.1 this coefficient grows rapidly with the spin s.

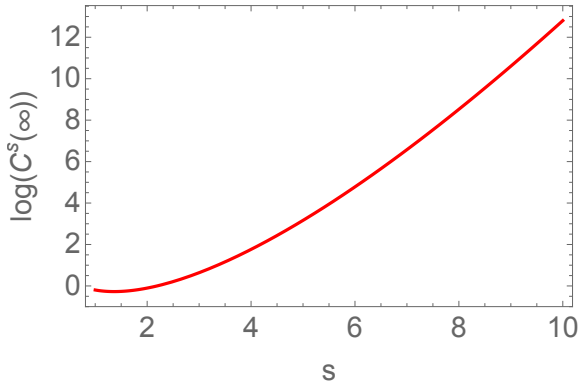

Figure B.1: $\log(\mathcal{C}^s(\infty))$ for the free fermion.

In fact, using Stirling's approximation we have that

$$\log\left(\mathcal{C}^{s+1}(\infty)\right)\approx s\log s-s. \qquad \text{(B.9)}$$

APPENDIX C

THE iTEBD ALGORITHM

The iTEBD algorithm [226] is based on the infinite Matrix Product State (iMPS) description of one dimensional translational invariant lattice models in the thermodynamic limit (thus it is free of any finite size effect). The canonical iMPS representation of a generic many-body state is

$$|\Psi\rangle = \sum_{\{s\}} \mathrm{Tr}[\cdots \mathbf{\Gamma}_o^{s_j} \mathbf{\Lambda}_o \mathbf{\Gamma}_e^{s_{j+1}} \mathbf{\Lambda}_e \cdots] |\cdots s_j s_{j+1} \cdots\rangle, \tag{C.1}$$

where $\mathbf{\Gamma}_{o/e}^{s_j}$ are $\chi \times \chi$ matrices associated with odd/even lattice sites, with s_j spanning the j^{th}-site Hilbert space in the canonical basis $\{|\uparrow_z\rangle, |\downarrow_z\rangle\}$; similarly, $\mathbf{\Lambda}_{o/e}$ are diagonal matrices with entries equal to the singular values associated with the bipartition of the system onto the odd/even bonds.

To achive time evolution, one makes use of the Trotter-Suzuki decomposition, which apporoximates the exponent of a sum of operators with a product of exponents of the same operators. At first order the expansion reads

$$e^{(V+W)\delta} = e^{V\delta} e^{W\delta} + O(\delta^2). \tag{C.2}$$

We can decompose the Hamiltonian as a sum

$$\begin{aligned} H &= H_{\text{odd}} + H_{\text{even}} \\ &= \sum_{r \text{ odd}} h^{[r,r+1]} + \sum_{r \text{ even}} h^{[r,r+1]}. \end{aligned} \tag{C.3}$$

In this way each term consistes of a sum of commuting operators.

We now divide the time into small time slices $\delta t \ll 1$ and expand the $U(t)$ operator as a sequence of small two-site gates

$$U^{[r,r+1]}(\delta t) = \exp\big(-i h^{[r,r+1]} \delta t\big), \tag{C.4}$$

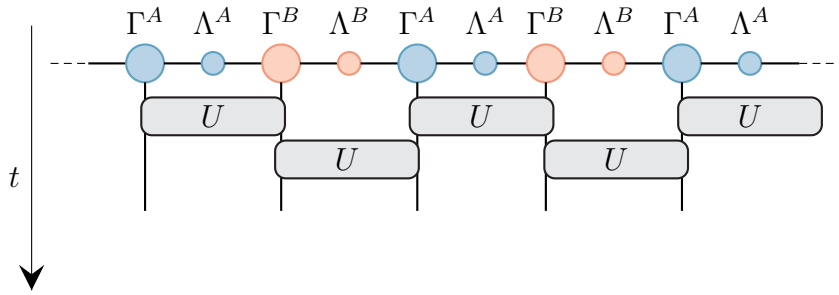

Figure C.1: In iTEBD eash time step δt of a time evolution is approximated using a Trotter-Suzuki decomposition. The evolved state is obtained by subsequent applications of U gates.

which we arrange into gates U^{AB} and U^{BA},

$$U^{AB}(\delta t) = \bigotimes_{r\in\mathbb{Z}} U^{[2r,2r+1]}(\delta t), \qquad U^{BA}(\delta t) = \bigotimes_{r\in\mathbb{Z}} U^{[2r-1,2r]}(\delta t). \tag{C.5}$$

At first order $U(\delta t)$ is given by

$$U(\delta t) = U^{AB}(\delta t)U^{AB}(\delta t). \tag{C.6}$$

We partially break translational symmetry to simulate the action of gates (C.5) on $|\psi_0\rangle$:

$$\begin{aligned} \Gamma^{[2r]} &= \Gamma^A & \Lambda^{[2r]} &= \Lambda^A \\ \Gamma^{[2r+1]} &= \Gamma^B & \Lambda^{[2r+1]} &= \Lambda^B. \end{aligned} \tag{C.7}$$

The decomposition of the time evolution operator is shown pictorially in Fig. C.1. The simulation of the time evolution is achieved by updating the MPS by repated application of gates U^{AB} and U^{BA}. The update procedure for two-site transformation action on two neighboring sites n and $n+1$ is shown in Fig. C.2. We focus on an update with a U^{AB} gate. The inequivalent BA bonds are updated similarly by exchanging A and B.

The wave function of a generic state $|\psi\rangle$ can be expressed in the basis spanned by the left Schmidt states on bond $n-1:n$, the local Hilbert space of sites n and $n+1$, and the right Schmidt states on bond $n+1:n+2$:

$$|\psi\rangle = \sum_{\alpha,j,k,\gamma} \Theta^{j,k}_{\alpha\gamma} |\alpha_{n-1}\rangle_L |j_n\rangle |k_{n+1}\rangle |\gamma_{n+1}\rangle_R , \tag{C.8}$$

where the wave function coefficients Θ are given by (step (i) in Fig. C.2)

$$\Theta^{j,k}_{\alpha\gamma} = \sum_{\beta} \Lambda^B_\alpha \Gamma^{A,j}_{\alpha\beta} \Lambda^A_\beta \Gamma^{B,k}_{\beta\gamma} \Lambda^B_\gamma . \tag{C.9}$$

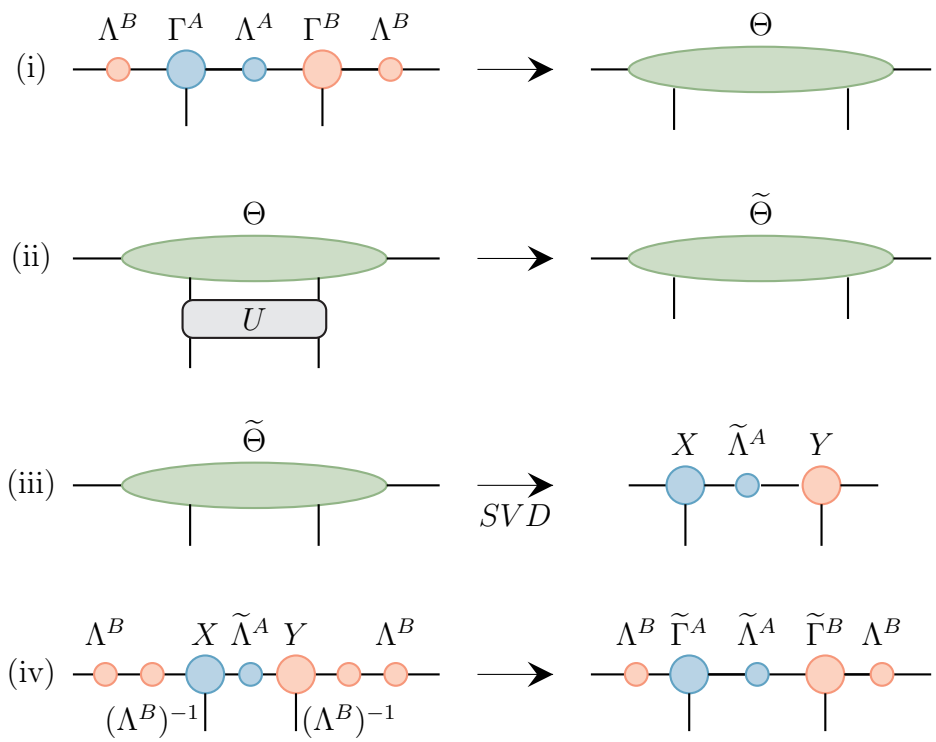

Figure C.2: The iTEBD update scheme for unitary two-site transformation of a two-site unit cell MPS in canonical form.

Physical indices j, k can take d values while bond indices α, γ have ξ values. The local unitary update of the algorithm is given by (step (ii) in Fig. C.2) :

$$\tilde{\Theta}^{j,k}_{\alpha\gamma} = \sum_{j'k'} U^{jk}_{j'k'} \Theta^{j',k'}_{\alpha\gamma}. \tag{C.10}$$

Next we have to extract the updated tensor $\tilde{\Gamma}^A$, $\tilde{\Gamma}^B$ and $\tilde{\Lambda}^A$ from the transformed tensor $\tilde{\Theta}$. We first reshape the tensor $\tilde{\Theta}$ by combining indices to obtain a $d\chi \times d\chi$ dimensional matrix $\tilde{\Theta}_{j\alpha;k\gamma}$. Because the basis $|\alpha_{n-1}\rangle_L |j_n\rangle$ is orthonormal, as for the right, it is natural to decompose the matrix using a SVD into

$$\tilde{\Theta}_{j\alpha;k\gamma} = \sum_{\beta} X_{j\alpha;\beta} D_{\beta}\beta Y_{\beta;k\gamma} \tag{C.11}$$

(step (iii) in Fig. C.2).The matrix X relates to the new Schmidt states $|\beta_n\rangle_L$ to the combined bases $|\alpha_{n-1}\rangle_L |j_n\rangle$. The Schmidt states for the right site are obtained from the matrix Y in the same way. Thus the diagonal matrix D contains the Schmidt values of the updated state:

$$\tilde{\Lambda}^A = D. \tag{C.12}$$

The new tensors $\tilde{\Gamma}^A$ and $\tilde{\Gamma}^B$ can be obtained extracting the old matrices Λ^β (see step (iv) in Fig. C.2):

$$\begin{aligned} \tilde{\Gamma}^{A,j}_{\alpha\beta} &= (\Lambda^B)^{-1}_\alpha X_{j\alpha;\beta} \\ \tilde{\Gamma}^{B,j}_{\beta\gamma} &= Y_{\beta;k\gamma}(\Lambda^B)^{-1}_\gamma \end{aligned} \tag{C.13}$$

The update of n sites the TEBD algorithm requires $O(nd\chi^2)$ space to store an MPS and $O(nd^3\chi^3)$ time to simulate a small evolution $\exp(-iH\delta t)$, but for an infinite chain the action of the gates preserves the invariance of the evolved state under shift by two sites. In other words for $n = \infty$ the iTEBD requires computational space and time that scale hust as $O(d\chi^2)$ and $O(d^3\chi^3)$.

APPENDIX D

FURTHER SIMULATIONS OF LONGITUDINAL QUENCHES

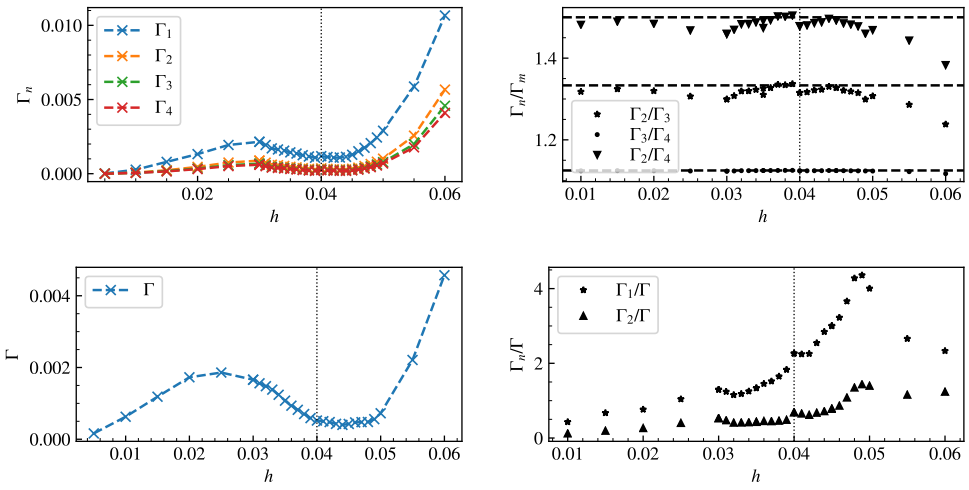

Figure D.1: Left panels: Entropy growth rates Γ_n (top) and magnetisation relaxation rate Γ (bottom) for longitudinal quenches in the Ising chain starting from $g = 1.25$ as a function of the longitudinal coupling. Right: Ratios Γ_n/Γ_m (top) and Γ_n/Γ (bottom). The dashed lines represent the universal ratios (5.59) that are restored in the limit $h \to 0$. The vertical line is drawn at the value h_{crit} where the second quasi-particle appears in the post-quench spectrum.

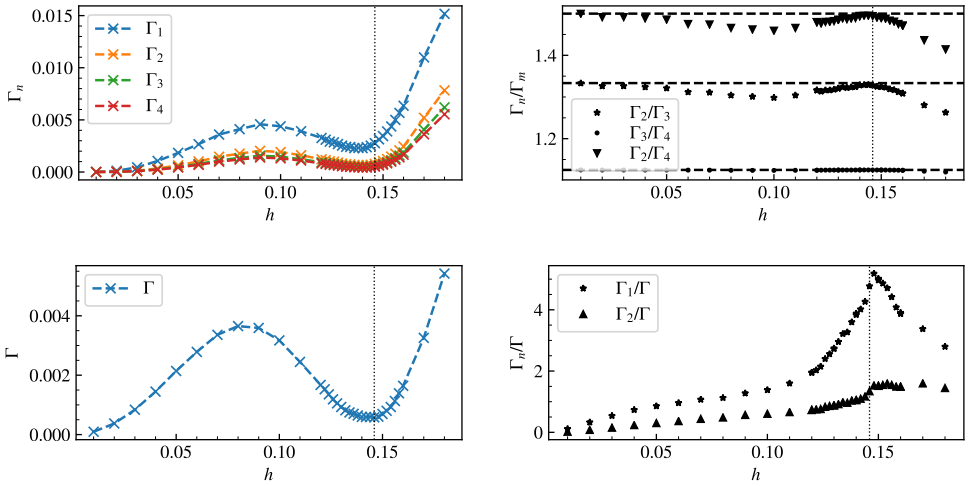

Figure D.2: Left panels: Entropy growth rates Γ_n (top) and magnetisation relaxation rate Γ (bottom) for longitudinal quenches in the Ising chain starting from $g = 1.5$ as a function of the longitudinal coupling. Right: Ratios Γ_n/Γ_m (top) and Γ_n/Γ (bottom). The dashed lines represent the universal ratios (5.59) that are restored in the limit $h \to 0$. The vertical line is drawn at the value h_{crit} where the second quasi-particle appears in the post-quench spectrum.

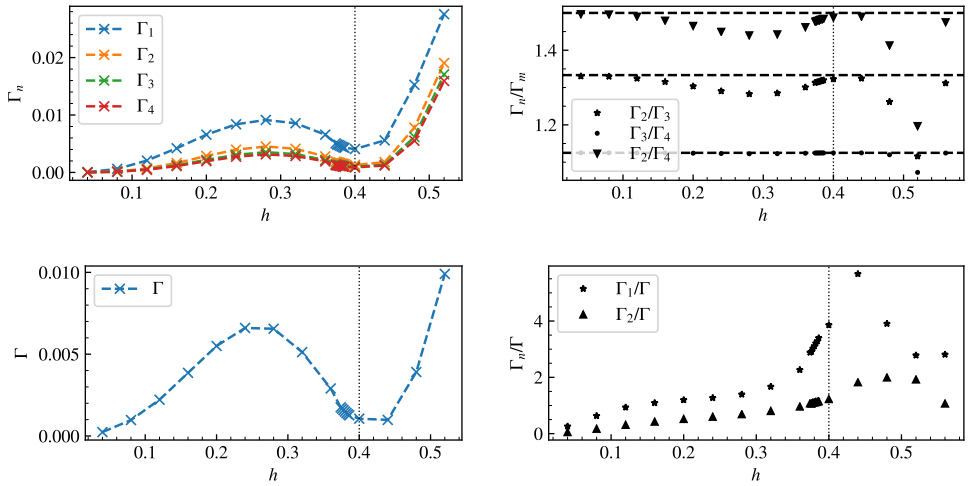

Figure D.3: Left panels: Entropy growth rates Γ_n (top) and magnetisation relaxation rate Γ (bottom) in units $J = 1$ for longitudinal quenches in the quantum Ising spin chain starting from $g = 2.0$ as a function of the longitudinal coupling. Right: Ratios Γ_n/Γ_m (top) and Γ_n/Γ (bottom). The dashed lines represent the universal ratios (5.59) that are restored in the limit $h \to 0$. The vertical line is drawn at the value h_{crit} where the second quasi-particle appears in the post-quench spectrum.

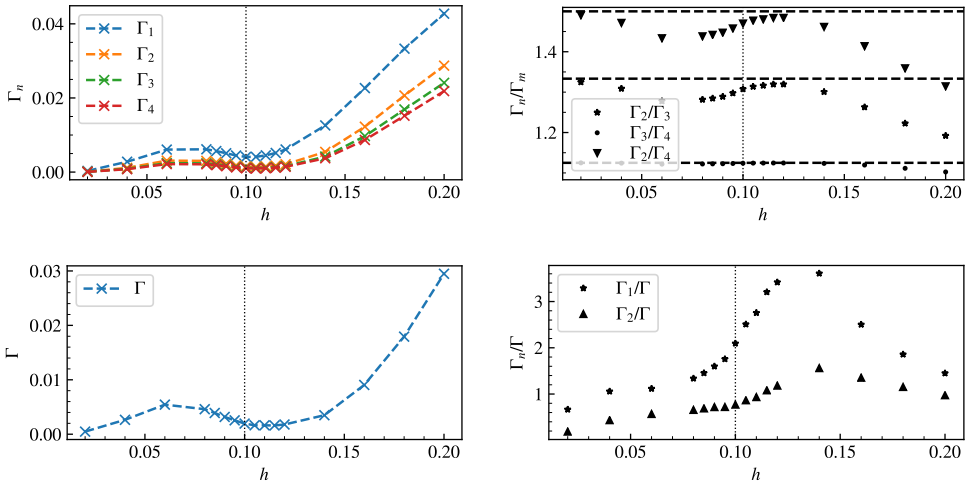

Figure D.4: Left panels: Entropy growth rates Γ_n (top) and magnetisation relaxation rate Γ (bottom) in units $J = 1$ for longitudinal quenches in the quantum Potts spin chain starting from $g = 1.25$ as a function of the longitudinal coupling. Right: Ratios Γ_n/Γ_m (top) and Γ_n/Γ (bottom). The dashed lines represent the universal ratios (5.59) that are restored in the limit $h \to 0$. The vertical line is drawn at the value h_{crit} where the second quasi-particle appears in the post-quench spectrum.

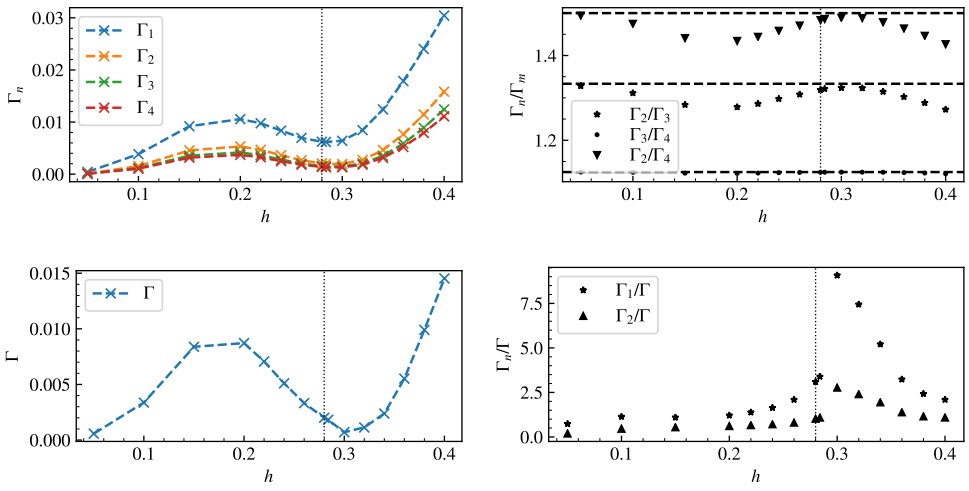

Figure D.5: Left panels: Entropy growth rates Γ_n (top) and magnetisation relaxation rate Γ (bottom) in units $J = 1$ for longitudinal quenches in the quantum Potts spin chain starting from $g = 1.5$ as a function of the longitudinal coupling. Right: Ratios Γ_n/Γ_m (top) and Γ_n/Γ (bottom). The dashed lines represent the universal ratios (5.59) that are restored in the limit $h \to 0$. The vertical line is drawn at the value h_{crit} where the second quasi-particle appears in the post-quench spectrum.

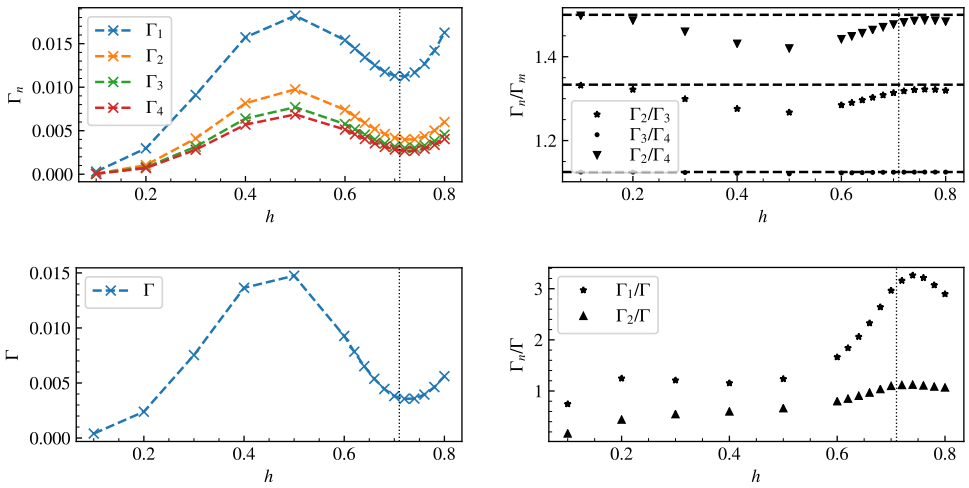

Figure D.6: Left panels: Entropy growth rates Γ_n (top) and magnetisation relaxation rate Γ (bottom) in units $J = 1$ for longitudinal quenches in the quantum Potts spin chain starting from $g = 2.0$ as a function of the longitudinal coupling. Right: Ratios Γ_n/Γ_m (top) and Γ_n/Γ (bottom). The dashed lines represent the universal ratios (5.59) that are restored in the limit $h \to 0$. The vertical line is drawn at the value h_{crit} where the second quasi-particle appears in the post-quench spectrum.

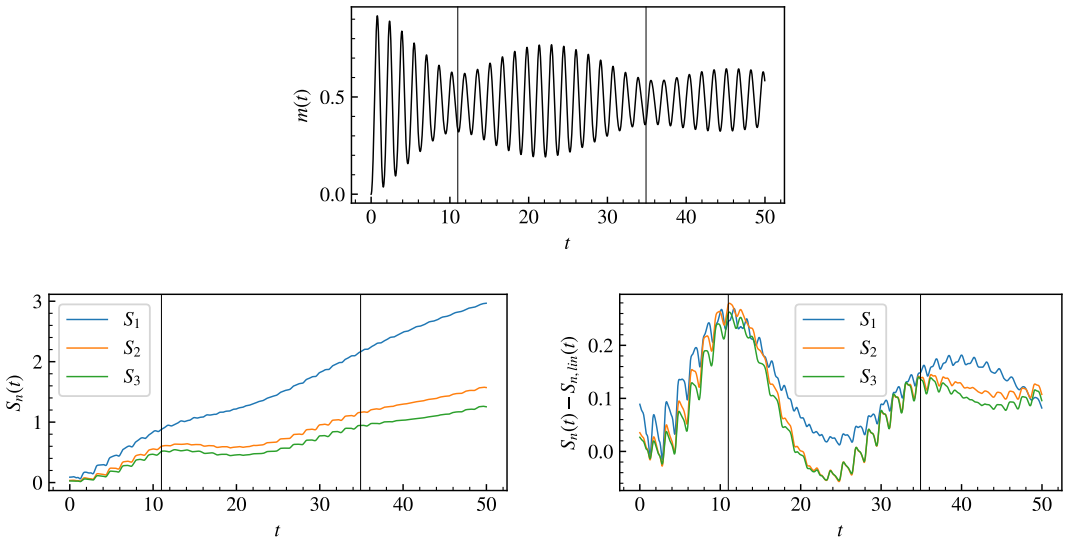

Figure D.7: Time evolution of various quantities after a large quench $(g_0, h_0) = (2.0, 0.0) \to (g, h) = (2.0, 0.8)$ in the quantum Ising spin chain. The top diagram shows the evolution of magnetisation, the bottom left one the von Neumann entropy (S_1) and two of the Rényi entropies (S_2 and S_3), while the bottom right one shows the entropy evolution with the linear trend subtracted. The vertical lines correspond to a single period of the slow oscillation corresponding to the frequency $2m_1 - m_2$. The first line is drawn at the first minimum of the envelope of the magnetisation oscillations while second is drawn at a distance given by the period $T \approx 23.9$. Note that their position also matches the behaviour of the entropy curves quite well. Time is measured in units of $1/J$, and the initial entropy was subtracted.

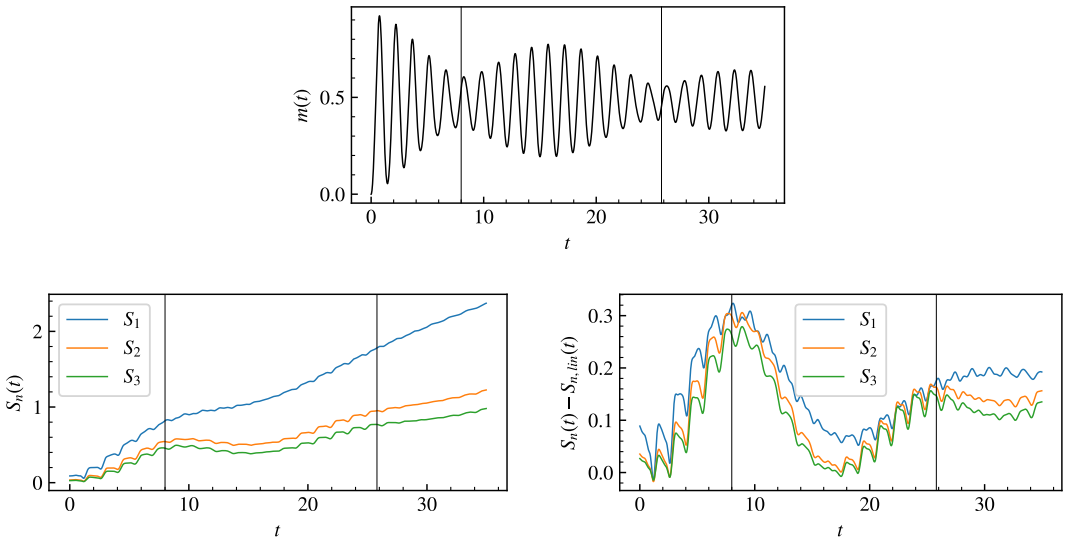

Figure D.8: Time evolution of various quantities after a large quench $(g_0, h_0) = (2.0, 0.0) \to (g, h) = (2.0, 0.9)$ in the quantum Ising spin chain. The top diagram shows the evolution of magnetisation, the bottom left one the von Neumann entropy (S_1) and two of the Rényi entropies (S_2 and S_3), while the bottom right one shows the entropy evolution with the linear trend subtracted. The vertical lines correspond to a single period of the slow oscillation corresponding to the frequency $2m_1 - m_2$. The first line is drawn at the first minimum of the envelope of the magnetisation oscillations while second is drawn at a distance given by the period $T \approx 17.8$. Note that their position also matches the behaviour of the entropy curves quite well. Time is measured in units of $1/J$, and the initial entropy was subtracted.

Bibliography

[1] Michele Mazzoni, Octavio Pomponio, Olalla A Castro-Alvaredo, and Francesco Ravanini. "The staircase model: massless flows and hydrodynamics". In: *Journal of Physics A: Mathematical and Theoretical* 54.40 (Sept. 2021), p. 404005. DOI: 10.1088/1751-8121/ac2141. URL: https://doi.org/10.1088/1751-8121/ac2141.

[2] O. Pomponio, L. Pristyák, and G. Takács. "Quasi-particle spectrum and entanglement generation after a quench in the quantum Potts spin chain". In: *Journal of Statistical Mechanics: Theory and Experiment* 1.1 (Jan. 2019), p. 013104. DOI: 10.1088/1742-5468/aafa80. arXiv: 1810.05539 [cond-mat.stat-mech].

[3] Máté Lencses, Octavio Pomponio, and Gabor Takacs. "Relaxation and entropy generation after quenching quantum spin chains". In: *SciPost Physics* 9.1, 011 (July 2020), p. 011. DOI: 10.21468/SciPostPhys.9.1.011. arXiv: 2004.09550 [cond-mat.stat-mech].

[4] Octavio Pomponio, Miklós Antal Werner, Gergely Zaránd, and Gabor Takacs. "Bloch oscillations and the lack of the decay of the false vacuum in a one-dimensional quantum spin chain". In: *SciPost Physics* 12.2, 061 (Feb. 2022), p. 061. DOI: 10.21468/SciPostPhys.12.2.061. arXiv: 2105.00014 [cond-mat.stat-mech].

[5] Anatoli Polkovnikov, Krishnendu Sengupta, Alessandro Silva, and Mukund Vengalattore. "Colloquium: Nonequilibrium dynamics of closed interacting quantum systems". In: *Reviews of Modern Physics* 83.3 (July 2011), pp. 863–883. DOI: 10.1103/RevModPhys.83.863. arXiv: 1007.5331 [cond-mat.stat-mech].

[6] J Eisert, M Friesdorf, and C Gogolin. "Quantum many-body systems out of equilibrium". In: *Nat. Phys.* 11 (2015), p. 124. DOI: 10.1038/nphys3215. URL: https://doi.org/10.1038/nphys3215.

[7] F H L Essler and M Fagotti. "Quench dynamics and relaxation in isolated integrable quantum spin chains". In: *J. Stat. Mech.* (2016). DOI: 10.1088/1742-5468/2016/06/064002. URL: https://doi.org/10.1088/1742-5468/2016/06/064002.

[8] R Zwanzig. *Non-equilibrium Statistical Physics*. New York: Oxford University Press, 2001.

[9] Toshiya Kinoshita, Trevor Wenger, and David S. Weiss. "A quantum Newton's cradle". In: *Nature* 440.7086 (Apr. 2006), pp. 900–903. DOI: 10.1038/nature04693.

[10] M Rigol, V Dunjko, V Yurovsky, and M Olshanii. "Relaxation in a completely integrable many-body quantum system: an ab initio study of the dynamics of the highly excited states of 1D lattice hard-core bosons". In: *Phys. Rev. Lett.* 98 (2007). DOI: 10.1103/physrevlett.98.050405. URL: https://doi.org/10.1103/physrevlett.98.050405.

[11] R Vasseur and J E Moore. "Nonequilibrium quantum dynamics and transport: from integrability to many-body localization". In: *J. Stat. Mech.* (2016). DOI: 10.1088/1742-5468/2016/06/064010. URL: https://doi.org/10.1088/1742-5468/2016/06/064010.

[12] E Ilievski, M Medenjak, T Prosen, and L Zadnik. "Quasilocal charges in integrable lattice systems". In: *J. Stat. Mech.* (2016). DOI: 10.1088/1742-5468/2016/06/064008. URL: https://doi.org/10.1088/1742-5468/2016/06/064008.

[13] D Bernard and B Doyon. "Conformal field theory out of equilibrium: a review". In: *J. Stat. Mech.* (2016). DOI: 10.1088/1742-5468/2016/06/064005. URL: https://doi.org/10.1088/1742-5468/2016/06/064005.

[14] Luca D'Alessio, Yariv Kafri, Anatoli Polkovnikov, and Marcos Rigol. "From quantum chaos and eigenstate thermalization to statistical mechanics and thermodynamics". In: *Advances in Physics* 65.3 (May 2016), pp. 239–362. DOI: 10.1080/00018732.2016.1198134. arXiv: 1509.06411 [cond-mat.stat-mech].

[15] C Gogolin and J Eisert. "Equilibration, thermalisation, and the emergence of statistical mechanics in closed quantum systems". In: *Rep. Prog. Phys.* 79 (2016). DOI: 10.1088/0034-4885/79/5/056001. URL: https://doi.org/10.1088/0034-4885/79/5/056001.

[16] B Doyon. "Lecture notes on generalised hydrodynamics". In: *SciPost Phys. Lect. Notes* 18 (2020). DOI: 10.21468/scipostphyslectnotes.18. URL: https://doi.org/10.21468/scipostphyslectnotes.18.

[17] Pasquale Calabrese, Fabian H L Essler, and Giuseppe Mussardo. "Introduction to 'Quantum Integrability in Out of Equilibrium Systems'". In: *Journal of Statistical Mechanics: Theory and Experiment* 2016.6 (June 2016), p. 064001. DOI: 10.1088/1742-5468/2016/06/064001. URL: https://doi.org/10.1088/1742-5468/2016/06/064001.

[18] E. T. Jaynes. "Information Theory and Statistical Mechanics". In: *Phys. Rev.* 106 (4 May 1957), pp. 620–630. DOI: 10.1103/PhysRev.106.620. URL: https://link.aps.org/doi/10.1103/PhysRev.106.620.

[19] E. T. Jaynes. "Information Theory and Statistical Mechanics. II". In: *Phys. Rev.* 108 (2 Oct. 1957), pp. 171–190. DOI: 10.1103/PhysRev.108.171. URL: https://link.aps.org/doi/10.1103/PhysRev.108.171.

[20] Sandu Popescu, Anthony J. Short, and Andreas Winter. "Entanglement and the foundations of statistical mechanics". In: *Nature Physics* 2.11 (Nov. 2006), pp. 754–758. DOI: 10.1038/nphys444. arXiv: quant-ph/0511225 [quant-ph].

[21] Maurizio Fagotti and Fabian H. L. Essler. "Reduced density matrix after a quantum quench". In: *Phys. Rev. B* 87.24, 245107 (June 2013), p. 245107. DOI: 10.1103/PhysRevB.87.245107. arXiv: 1302.6944 [cond-mat.stat-mech].

[22] M. Cramer, C. M. Dawson, J. Eisert, and T. J. Osborne. "Exact Relaxation in a Class of Nonequilibrium Quantum Lattice Systems". In: *Phys. Rev. Lett.* 100.3, 030602 (Jan. 2008), p. 030602. DOI: 10.1103/PhysRevLett.100.030602. arXiv: cond-mat/0703314 [cond-mat.stat-mech].

[23] M. Cramer and J. Eisert. "A quantum central limit theorem for non-equilibrium systems: exact local relaxation of correlated states". In: *New Journal of Physics* 12.5, 055020 (May 2010), p. 055020. DOI: 10.1088/1367-2630/12/5/055020. arXiv: 0911.2475 [quant-ph].

[24] V. I. Arnol'd. *Mathematical methods of classical mechanics*. 1978.

[25] John von Neumann. "Proof of the Ergodic Theorem and the H-Theorem in Quantum Mechanics". In: *arXiv e-prints* (Mar. 2010), arXiv:1003.2133. arXiv: 1003.2133 [physics.hist-ph].

[26] Marcos Rigol, Vanja Dunjko, and Maxim Olshanii. "Thermalization and its mechanism for generic isolated quantum systems". In: *Nature* 452.7189 (Apr. 2008), pp. 854–858. DOI: 10.1038/nature06838.

[27] Marcos Rigol. "Breakdown of Thermalization in Finite One-Dimensional Systems". In: *Phys. Rev. Lett.* 103.10, 100403 (Sept. 2009), p. 100403. DOI: 10.1103/PhysRevLett.103.100403. arXiv: 0904.3746 [cond-mat.stat-mech].

[28] S. Trotzky, Y. -A. Chen, A. Flesch, I. P. McCulloch, U. Schollwöck, J. Eisert, and I. Bloch. "Probing the relaxation towards equilibrium in an isolated strongly correlated one-dimensional Bose gas". In: *Nature Physics* 8.4 (Apr. 2012), pp. 325–330. DOI: 10.1038/nphys2232. arXiv: 1101.2659 [cond-mat.quant-gas].

[29] Marc Cheneau, Peter Barmettler, Dario Poletti, Manuel Endres, Peter Schauß, Takeshi Fukuhara, Christian Gross, Immanuel Bloch, Corinna Kollath, and Stefan Kuhr. "Light-cone-like spreading of correlations in a quantum many-body system". In: *Nature* 481.7382 (Jan. 2012). DOI: 10.1038/nature10748. arXiv: 1111.0776 [cond-mat.quant-gas].

[30] Marcos Rigol and Mark Srednicki. "Alternatives to Eigenstate Thermalization". In: *Phys. Rev. Lett.* 108.11, 110601 (Mar. 2012), p. 110601. DOI: 10.1103/PhysRevLett.108.110601. arXiv: 1108.0928 [cond-mat.stat-mech].

[31] J. M. Deutsch. "Quantum statistical mechanics in a closed system". In: *Phys. Rev. A* 43 (4 Feb. 1991), pp. 2046–2049. DOI: 10.1103/PhysRevA.43.2046. URL: https://link.aps.org/doi/10.1103/PhysRevA.43.2046.

[32] Mark Srednicki. "Chaos and quantum thermalization". In: *Phys. Rev. E* 50.2 (Aug. 1994), pp. 888–901. DOI: 10.1103/PhysRevE.50.888. arXiv: cond-mat/9403051 [cond-mat].

[33] Mark Srednicki. "The approach to thermal equilibrium in quantized chaotic systems". In: *Journal of Physics A Mathematical General* 32.7 (Feb. 1999), pp. 1163–1175. DOI: 10.1088/0305-4470/32/7/007. arXiv: cond-mat/9809360 [cond-mat.stat-mech].

[34] J. Sirker, N. P. Konstantinidis, F. Andraschko, and N. Sedlmayr. "Locality and thermalization in closed quantum systems". In: *Phys. Rev. A* 89.4, 042104 (Apr. 2014), p. 042104. DOI: 10.1103/PhysRevA.89.042104. arXiv: 1303.3064 [cond-mat.stat-mech].

[35] David Pekker, Gil Refael, Ehud Altman, Eugene Demler, and Vadim Oganesyan. "Hilbert-Glass Transition: New Universality of Temperature-Tuned Many-Body Dynamical Quantum Criticality". In: *Phys. Rev. X* 4 (1 Mar. 2014), p. 011052. DOI: 10.1103/PhysRevX.4.011052. URL: https://link.aps.org/doi/10.1103/PhysRevX.4.011052.

[36] P. Dirac. *The principles of quantum mechanics*. 1947.

[37] B. Sutherland. *Beautiful Models: 70 Years of Exactly Solved Quantum Many-body Problems*. World Scientific, 2004. ISBN: 9789812388971. URL: https://books.google.it/books?id=PA0xV0XxZIwC.

[38] J. Mossel and J.-S. Caux. "Exact time evolution of space- and time-dependent correlation functions after an interaction quench in the one-dimensional Bose gas". In: *New Journal of Physics* 14.7, 075006 (July 2012), p. 075006. DOI: 10.1088/1367-2630/14/7/075006. arXiv: 1201.1885 [cond-mat.stat-mech].

[39] B. Doyon and Olalla Castro-Alvaredo. "The Bologna Lectures on Entanglement and Non-Equilibrium Physics in Extended Quantum Systems". In: (Dec. 2016). DOI: https://thebolognalectures.weebly.com/uploads/2/6/7/1/26714966/notes-bologna.pdf.

[40] H. Bethe. "Zur Theorie der Metalle". In: *Zeitschrift für Physik* 71.3 (Mar. 1931), pp. 205–226. ISSN: 0044-3328. DOI: 10.1007/BF01341708. URL: https://doi.org/10.1007/BF01341708.

[41] Maurizio Fagotti. "On conservation laws, relaxation and pre-relaxation after a quantum quench". In: *Journal of Statistical Mechanics: Theory and Experiment* 2014.3, 03016 (Mar. 2014), p. 03016. DOI: 10.1088/1742-5468/2014/03/P03016. arXiv: 1401.1064 [cond-mat.stat-mech].

[42] John Cardy. "Quantum Quenches to a Critical Point in One Dimension: some further results". In: *arXiv e-prints*, arXiv:1507.07266 (July 2015), arXiv:1507.07266. arXiv: 1507.07266 [cond-mat.stat-mech].

[43] Benjamin Doyon. "Thermalization and Pseudolocality in Extended Quantum Systems". In: *Communications in Mathematical Physics* 351.1 (Apr. 2017). DOI: 10.1007/s00220-017-2836-7. arXiv: 1512.03713 [math-ph].

[44] B. Wouters, J. De Nardis, M. Brockmann, D. Fioretto, M. Rigol, and J.-S. Caux. "Quenching the Anisotropic Heisenberg Chain: Exact Solution and Generalized Gibbs Ensemble Predictions". In: *Phys. Rev. Lett.* 113 (11 Sept. 2014), p. 117202. DOI: 10.1103/PhysRevLett.113.117202. URL: https://link.aps.org/doi/10.1103/PhysRevLett.113.117202.

[45] B. Pozsgay, M. Mestyán, M. A. Werner, M. Kormos, G. Zaránd, and G. Takács. "Correlations after Quantum Quenches in the XXZ Spin Chain: Failure of the Generalized Gibbs Ensemble". In: *Phys. Rev. Lett.* 113 (11 Sept. 2014), p. 117203. DOI: 10.1103/PhysRevLett.113.117203. URL: https://link.aps.org/doi/10.1103/PhysRevLett.113.117203.

[46] Toma ž Prosen. "Open XXZ Spin Chain: Nonequilibrium Steady State and a Strict Bound on Ballistic Transport". In: *Phys. Rev. Lett.* 106 (21 May 2011), p. 217206. DOI: 10.1103/PhysRevLett.106.217206. URL: https://link.aps.org/doi/10.1103/PhysRevLett.106.217206.

[47] Toma ž Prosen and Enej Ilievski. "Families of Quasilocal Conservation Laws and Quantum Spin Transport". In: *Phys. Rev. Lett.* 111 (5 Aug. 2013), p. 057203. DOI: 10.1103/PhysRevLett.111.057203. URL: https://link.aps.org/doi/10.1103/PhysRevLett.111.057203.

[48] Enej Ilievski, Marko Medenjak, and Toma ž Prosen. "Quasilocal Conserved Operators in the Isotropic Heisenberg Spin-1/2 Chain". In: *Phys. Rev. Lett.* 115 (12 Sept. 2015), p. 120601. DOI: 10.1103/PhysRevLett.115.120601. URL: https://link.aps.org/doi/10.1103/PhysRevLett.115.120601.

[49] E. Ilievski, J. De Nardis, B. Wouters, J.-S. Caux, F. H. L. Essler, and T. Prosen. "Complete Generalized Gibbs Ensembles in an Interacting Theory". In: *Phys. Rev. Lett.* 115 (15 Oct. 2015), p. 157201. DOI: 10.1103/PhysRevLett.115.157201. URL: https://link.aps.org/doi/10.1103/PhysRevLett.115.157201.

[50] Olalla A. Castro-Alvaredo, Benjamin Doyon, and Takato Yoshimura. "Emergent Hydrodynamics in Integrable Quantum Systems Out of Equilibrium". In: *Physical Review X* 6.4, 041065 (Oct. 2016), p. 041065. DOI: 10.1103/PhysRevX.6.041065. arXiv: 1605.07331 [cond-mat.stat-mech].

[51] Bruno Bertini, Mario Collura, Jacopo De Nardis, and Maurizio Fagotti. "Transport in Out-of-Equilibrium X X Z Chains: Exact Profiles of Charges and Currents". In: *Phys. Rev. Lett* 117.20, 207201 (Nov. 2016), p. 207201. DOI: 10.1103/PhysRevLett.117.207201. arXiv: 1605.09790 [cond-mat.stat-mech].

[52] M Fagotti. "Charges and currents in quantum spin chains: late-time dynamics and spontaneous currents". In: *J. Phys. A: Math. Theor.* 50 (2016). DOI: 10.1088/1751-8121/50/3/034005. URL: https://doi.org/10.1088/1751-8121/50/3/034005.

[53] A Urichuk, Y Oez, A Klümper, and J Sirker. "The spin Drude weight of the XXZ chain and generalized hydrodynamics". In: *SciPost Phys* 6 (2019), p. 005. DOI: 10.21468/scipostphys.6.1.005. URL: https://doi.org/10.21468/scipostphys.6.1.005.

[54] D-L Vu and T Yoshimura. "Equations of state in generalized hydrodynamics". In: *SciPost Phys.* 6 (2019), p. 023. DOI: 10.21468/scipostphys.6.2.023. URL: https://doi.org/10.21468/scipostphys.6.2.023.

[55] J De Nardis, D Bernard, and B Doyon. "Diffusion in generalized hydrodynamics and quasiparticle scattering". In: *SciPost Phys.* 6 (2019), p. 049. DOI: 10.21468/scipostphys.6.4.049. URL: https://doi.org/10.21468/scipostphys.6.4.049.

[56] Z Bajnok and I Vona. "Exact finite volume expectation values of conserved currents". In: *Phys. Lett. B* 805 (2020). DOI: 10.1016/j.physletb.2020.135446. URL: https://doi.org/10.1016/j.physletb.2020.135446.

[57] H Spohn. "Collision rate ansatz for the classical Toda lattice". In: *Phys. Rev.* 101 (2020). DOI: 10.1103/physreve.101.060103. URL: https://doi.org/10.1103/physreve.101.060103.

[58] T Yoshimura and H Spohn. "Collision rate ansatz for quantum integrable systems". In: *SciPost Phys.* 9 (2020), p. 040. DOI: 10.21468/scipostphys.9.3.040. URL: https://doi.org/10.21468/scipostphys.9.3.040.

[59] M Borsi, B Pozsgay, and L Pristyák. "Current operators in Bethe ansatz and generalized hydrodynamics: an exact quantum-classical correspondence". In: *Phys. Rev.* 10 (2020). DOI: 10.1103/physrevx.10.011054. URL: https://doi.org/10.1103/physrevx.10.011054.

[60] B Pozsgay. "Current operators in integrable spin chains: lessons from long range deformations". In: *SciPost Phys.* 8 (2020), p. 016. DOI: 10.21468/scipostphys.8.2.016. URL: https://doi.org/10.21468/scipostphys.8.2.016.

[61] B Pozsgay. "Algebraic construction of current operators in integrable spin chains". In: *Phys. Rev. Lett.* 125 (2020). DOI: 10.1103/physrevlett.125.070602. URL: https://doi.org/10.1103/physrevlett.125.070602.

[62] Al. B. Zamolodchikov. "Thermodynamic Bethe ansatz in relativistic models: Scaling 3-state potts and Lee-Yang models". In: *Nuclear Physics B* 342.3 (Oct. 1990), pp. 695–720. DOI: 10.1016/0550-3213(90)90333-9.

[63] Timothy R. Klassen and Ezer Melzer. "Purely elastic scattering theories and their ultraviolet limits". In: *Nuclear Physics B* 338.3 (July 1990), pp. 485–528. DOI: 10.1016/0550-3213(90)90643-R.

[64] Timothy R. Klassen and Ezer Melzer. "The thermodynamics of purely elastic scattering theories and conformal perturbation theory". In: *Nuclear Physics B* 350.3 (Feb. 1991), pp. 635–689. DOI: 10.1016/0550-3213(91)90159-U.

[65] D Bernard and B Doyon. "Energy flow in non-equilibrium conformal field theory". In: *J. Phys. A: Math. Theor.* 45 (2012). DOI: 10.1088/1751-8113/45/36/362001. URL: https://doi.org/10.1088/1751-8113/45/36/362001.

[66] D Bernard and B Doyon. "Time-reversal symmetry and fluctuation relations in non-equilibrium quantum steady states". In: *J. Phys. A: Math. Theor.* 46 (2013). DOI: 10.1088/1751-8113/46/37/372001. URL: https://doi.org/10.1088/1751-8113/46/37/372001.

[67] D Bernard and B Doyon. "Non-equilibrium steady states in conformal field theory". In: *Ann. Henri Poincaré* 16 (2014), pp. 113–161. DOI: 10.1007/s00023-014-0314-8. URL: https://doi.org/10.1007/s00023-014-0314-8.

[68] B Doyon and T Yoshimura. "A note on generalized hydrodynamics: inhomogeneous fields and other concepts". In: *SciPost Phys.* 2 (2017), p. 014. DOI: 10.21468/scipostphys.2.2.014. URL: https://doi.org/10.21468/scipostphys.2.2.014.

[69] A Bastianello and A De Luca. "Integrability-protected adiabatic reversibility in quantum spin chains". In: *Phys. Rev. Lett.* 122 (2019). DOI: 10.1103/physrevlett.122.240606. URL: https://doi.org/10.1103/physrevlett.122.240606.

[70] A Bastianello, V Alba, and J-S Caux. "Generalized hydrodynamics with space-time inhomogeneous interactions". In: *Phys. Rev. Lett.* 123 (2019). DOI: 10.1103/physrevlett.123.130602. URL: https://doi.org/10.1103/physrevlett.123.130602.

[71] J De Nardis, D Bernard, and B Doyon. "Hydrodynamic diffusion in integrable systems". In: *Phys. Rev. Lett.* 121 (2018). DOI: 10.1103/physrevlett.121.160603. URL: https://doi.org/10.1103/physrevlett.121.160603.

[72] S Gopalakrishnan, D A Huse, V Khemani, and R Vasseur. "Hydrodynamics of operator spreading and quasiparticle diffusion in interacting integrable systems". In: *Phys. Rev. B* 98 (2018). DOI: 10.1103/physrevb.98.220303. URL: https://doi.org/10.1103/physrevb.98.220303.

[73] M Fagotti. "Locally quasi-stationary states in noninteracting spin chains". In: *SciPost Phys.* 8 (2020), p. 048. DOI: 10.21468/scipostphys.8.3.048. URL: https://doi.org/10.21468/scipostphys.8.3.048.

[74] A Bastianello, J De Nardis, and A De Luca. "Generalized hydrodynamics with dephasing noise". In: *Phys. Rev. B* 102 (2020). DOI: 10.1103/physrevb.102.161110. URL: https://doi.org/10.1103/physrevb.102.161110.

[75] X Cao, V B Bulchandani, and J E Moore. "Incomplete thermalization from trap-induced integrability breaking: lessons from classical hard rods". In: *Phys. Rev. Lett.* 120 (2018). DOI: 10.1103/physrevlett.120.164101. URL: https://doi.org/10.1103/physrevlett.120.164101.

[76] A J Friedman, S Gopalakrishnan, and R Vasseur. "Diffusive hydrodynamics from integrability breaking". In: *Phys. Rev. B* 101 (2020). DOI: 10.1103/physrevb.101.180302. URL: https://doi.org/10.1103/physrevb.101.180302.

[77] Joseph Durnin, M. J. Bhaseen, and Benjamin Doyon. "Nonequilibrium Dynamics and Weakly Broken Integrability". In: *Phys. Rev. Lett* 127.13, 130601 (Sept. 2021), p. 130601. DOI: 10.1103/PhysRevLett.127.130601. arXiv: 2004.11030 [cond-mat.stat-mech].

[78] M Schemmer, I Bouchoule, B Doyon, and J Dubail. "Generalized hydrodynamics on an atom chip". In: *Phys. Rev. Lett.* 122 (2019). DOI: 10.1103/physrevlett.122.090601. URL: https://doi.org/10.1103/physrevlett.122.090601.

[79] J-S Caux, B Doyon, J Dubail, R Konik, and T Yoshimura. "Hydrodynamics of the interacting Bose gas in the quantum Newton cradle setup". In: *SciPost Phys.* 6 (2019), p. 070. DOI: 10.21468/scipostphys.6.6.070. URL: https://doi.org/10.21468/scipostphys.6.6.070.

[80] O A Castro-Alvaredo, C De Fazio, B Doyon, and F Ravanini. "On the hydrodynamics of unstable excitations". In: *J. High Energy Phys.* (2020). DOI: 10.1007/jhep09(2020)045. URL: https://doi.org/10.1007/jhep09(2020)045.

[81] Olalla A. Castro-Alvaredo, Cecilia De Fazio, Benjamin Doyon, and Aleksandra A. Ziółkowska. "Tails of Instability and Decay: a Hydrodynamic Perspective". In: *arXiv e-prints*, arXiv:2103.03735 (Mar. 2021), arXiv:2103.03735. arXiv: 2103.03735 [hep-th].

[82] A B Zamolodchikov. "Resonance factorized scattering and roaming trajectories". In: *J. Phys. A: Math. Gen.* 39 (2006), pp. 12847–12861. DOI: 10.1088/0305-4470/39/41/s08. URL: https://doi.org/10.1088/0305-4470/39/41/s08.

[83] M J Martins. "Renormalization-group trajectories from resonance factorized S matrices". In: *Phys. Rev. Lett.* 69 (1992), p. 2461. DOI: 10.1103/physrevlett.69.2461. URL: https://doi.org/10.1103/physrevlett.69.2461.

[84] P Dorey and F Ravanini. "Staircase models from affine Toda field theory". In: *Int. J. Mod. Phys. A* 08 (1993), pp. 873–893. DOI: 10.1142/s0217751x93000333. URL: https://doi.org/10.1142/s0217751x93000333.

[85] Patrick Dorey and Francesco Ravanini. "Generalising the staircase models". In: *Nuclear Physics B* 406.3 (Oct. 1993), pp. 708–726. DOI: 10.1016/0550-3213(93)90007-C. arXiv: hep-th/9211115 [hep-th].

[86] M J Martins. "Exact resonance ADE S-matrices and their renormalization group trajectories". In: *Nucl. Phys. B* 394 (1993), p. 339. DOI: 10.1016/0550-3213(93)90018-k. URL: https://doi.org/10.1016/0550-3213(93)90018-k.

[87] M J Martins. "Analysis of asymptotic conditions in resonance functional hierarchies". In: *Phys. Lett. B* 304 (1993), p. 111. DOI: 10.1016/0370-2693(93)91408-f. URL: https://doi.org/10.1016/0370-2693(93)91408-f.

[88] M Mazzoni, O Pomponio, O A Castro-Alvaredo, and F Ravanini. *Staircase model: spectral densities and effective velocity*. 2021. URL: https://youtu.be/rI6KTxLZz_8.

[89] A E Arinshtein, V A Fateev, and A B Zamolodchikov. "Quantum S-matrix of the (1 + 1)-dimensional todd chain". In: *Phys. Lett. B* 87 (1979), pp. 389–392. DOI: 10.1016/0370-2693(79)90561-6. URL: https://doi.org/10.1016/0370-2693(79)90561-6.

[90] A V Mikhailov, M A Olshanetsky, and A M Perelomov. "Two-dimensional generalized Toda lattice". In: *Commun. Math. Phys.* 79 (1981), pp. 473–488. DOI: 10.1007/bf01209308. URL: https://doi.org/10.1007/bf01209308.

[91] I Arafeva and V Korepin. "Scattering in two-dimensional model with Lagrangian $\mathcal{L} = \gamma^{-1}[1/2(\partial_\mu u)^2 + m^2(\cos u - 1)]$". In: *Pis'ma Zh. Eksp. Teor. Fiz.* 20 (1974), p. 680.

[92] S Vergeles and V Gryanik. "Two-dimensional quantum field theories having exact solutions". In: *Yad. Fiz.* 23 (1976), pp. 1324–1334.

[93] B Schroer, T T Truong, and P Weisz. "Towards an explicit construction of the sine-Gordon field theory". In: *Phys. Lett. B* 63 (1976), pp. 422–424. DOI: 10.1016/0370-2693(76)90386-5. URL: https://doi.org/10.1016/0370-2693(76)90386-5.

[94] J Mossel and J-S Caux. "Generalized TBA and generalized Gibbs". In: *J. Phys. A: Math. Theor.* 45 (2012). DOI: 10.1088/1751-8113/45/25/255001. URL: https://doi.org/10.1088/1751-8113/45/25/255001.

[95] D Fioretto and G Mussardo. "Quantum quenches in integrable field theories". In: *New J. Phys.* 12 (2010). DOI: 10.1088/1367-2630/12/5/055015. URL: https://doi.org/10.1088/1367-2630/12/5/055015.

[96] Al. B. Zamolodchikov. "From tricritical Ising to critical Ising by thermodynamic Bethe ansatz". In: *Nuclear Physics B* 358.3 (July 1991), pp. 524–546. DOI: 10.1016/0550-3213(91)90423-U.

[97] D X Horváth, P E Dorey, and G Takács. "Roaming form factors for the tricritical to critical Ising flow". In: *J. High Energy Phys.* (2016). DOI: 10.1007/jhep07(2016)051. URL: https://doi.org/10.1007/jhep07(2016)051.

[98] Al. B. Zamolodchikov. "Thermodynamic Bethe ansatz for RSOS scattering theories". In: *Nuclear Physics B* 358.3 (July 1991), pp. 497–523. DOI: 10.1016/0550-3213(91)90422-T.

[99] Al. B. Zamolodchikov. "TBA equations for integrable perturbed SU(2) $_k \times$ {SU(2) $_l$}/{SU(2) $_{k+1}$} coset models". In: *Nuclear Physics B* 366.1 (Nov. 1991), pp. 122–132. DOI: 10.1016/0550-3213(91)90054-2.

[100] D X Horváth. "Hydrodynamics of massless integrable RG flows and a non-equilibrium c-theorem". In: *J. High Energy Phys.* (). DOI: 10.1007/jhep10(2019)020. URL: https://doi.org/10.1007/jhep10(2019)020.

[101] André Leclair. "Restricted sine-Gordon theory and the minimal conformal series". In: *Physics Letters B* 230.1-2 (Oct. 1989), pp. 103–107. DOI: 10.1016/0370-2693(89)91661-4.

[102] Denis Bernard and André Leclair. "Residual quantum symmetries of the Restricted sine-Gordon theories". In: *Nuclear Physics B* 340.2 (Aug. 1990), pp. 721–751. DOI: 10.1016/0550-3213(90)90466-Q.

[103] A B Zamolodchikov. "Renormalization group and perturbation theory near fixed points in two-dimensional field theory". In: *Sov. J. Nucl. Phys.* 46 (1987), p. 1090.

[104] Andreas W. W. Ludwig and John L. Cardy. "Perturbative evaluation of the conformal anomaly at new critical points with applications to random systems". In: *Nuclear Physics B* 285 (Jan. 1987), pp. 687–718. DOI: 10.1016/0550-3213(87)90362-2.

[105] K Gawedzki, E Langmann, and P Moosavi. "Finite-time universality in nonequilibrium CFT". In: *J. Stat. Phys.* 172 (2018), pp. 353–378. DOI: 10.1007/s10955-018-2025-x. URL: https://doi.org/10.1007/s10955-018-2025-x.

[106] Adam M. Kaufman, M. Eric Tai, Alexander Lukin, Matthew Rispoli, Robert Schittko, Philipp M. Preiss, and Markus Greiner. "Quantum thermalization through entanglement in an isolated many-body system". In: *Science* 353.6301 (Aug. 2016), pp. 794–800. DOI: 10.1126/science.aaf6725. arXiv: 1603.04409 [quant-ph].

[107] S. Hofferberth, I. Lesanovsky, B. Fischer, T. Schumm, and J. Schmiedmayer. "Non-equilibrium coherence dynamics in one-dimensional Bose gases". In: *Nature* 449.7160 (Sept. 2007), pp. 324–327. DOI: 10.1038/nature06149. arXiv: 0706.2259 [cond-mat.other].

[108] Tim Langen, Sebastian Erne, Remi Geiger, Bernhard Rauer, Thomas Schweigler, Maximilian Kuhnert, Wolfgang Rohringer, Igor E. Mazets, Thomas Gasenzer, and Jörg Schmiedmayer. "Experimental observation of a generalized Gibbs ensemble". In: *Science* 348.6231 (Apr. 2015), pp. 207–211. DOI: 10.1126/science.1257026. arXiv: 1411.7185 [cond-mat.quant-gas].

[109] F. Meinert, M. J. Mark, E. Kirilov, K. Lauber, P. Weinmann, A. J. Daley, and H. -C. Nägerl. "Quantum Quench in an Atomic One-Dimensional Ising Chain". In: *Phys. Rev. Lett* 111.5, 053003 (Aug. 2013), p. 053003. DOI: 10.1103/PhysRevLett.111.053003. arXiv: 1304.2628 [cond-mat.quant-gas].

[110] Takeshi Fukuhara, Peter Schauß, Manuel Endres, Sebastian Hild, Marc Cheneau, Immanuel Bloch, and Christian Gross. "Microscopic observation of magnon bound states and their dynamics". In: *Nature* 502.7469 (Oct. 2013), pp. 76–79. DOI: 10.1038/nature12541. arXiv: 1305.6598 [cond-mat.quant-gas].

[111] T. Langen, R. Geiger, M. Kuhnert, B. Rauer, and J. Schmiedmayer. "Local emergence of thermal correlations in an isolated quantum many-body system". In: *Nature Physics* 9.10 (Oct. 2013), pp. 640–643. DOI: 10.1038/nphys2739. arXiv: 1305.3708 [cond-mat.quant-gas].

[112] Pasquale Calabrese and John Cardy. "Time Dependence of Correlation Functions Following a Quantum Quench". In: *Phys. Rev. Lett* 96.13, 136801 (Apr. 2006), p. 136801. DOI: 10.1103/PhysRevLett.96.136801. arXiv: cond-mat/0601225 [cond-mat.stat-mech].

[113] M. Born and V. Fock. "Beweis des Adiabatensatzes". In: *Zeitschrift fur Physik* 51.3-4 (Mar. 1928), pp. 165–180. DOI: 10.1007/BF01343193.

[114] B. A. Bernevig and T. L. Hughes. *Topological Insulators and Topological Superconductors*. Ed. by Princeton University Press. 2013, p. 247.

[115] K. Sengupta, Stephen Powell, and Subir Sachdev. "Quench dynamics across quantum critical points". In: *Phys. Rev. A* 69.5, 053616 (May 2004), p. 053616. DOI: 10.1103/PhysRevA.69.053616.

[116] Pasquale Calabrese and John Cardy. "Evolution of entanglement entropy in one-dimensional systems". In: *Journal of Statistical Mechanics: Theory and Experiment* 2005.4 (Apr. 2005), p. 04010. DOI: 10.1088/1742-5468/2005/04/P04010. arXiv: cond-mat/0503393 [cond-mat.stat-mech].

[117] Pasquale Calabrese and John Cardy. "Quantum quenches in extended systems". In: *Journal of Statistical Mechanics: Theory and Experiment* 2007.6 (June 2007), p. 06008. DOI: 10.1088/1742-5468/2007/06/P06008. arXiv: 0704.1880 [cond-mat.stat-mech].

[118] J. Berges, Sz. Borsányi, and C. Wetterich. "Prethermalization". In: *Phys. Rev. Lett.* 93 (14 Sept. 2004), p. 142002. DOI: 10.1103/PhysRevLett.93.142002. URL: https://link.aps.org/doi/10.1103/PhysRevLett.93.142002.

[119] Elliott H. Lieb and Derek W. Robinson. "The finite group velocity of quantum spin systems". In: *Communications in Mathematical Physics* 28.3 (Sept. 1972), pp. 251–257. DOI: 10.1007/BF01645779.

[120] S. Bravyi, M. B. Hastings, and F. Verstraete. "Lieb-Robinson Bounds and the Generation of Correlations and Topological Quantum Order". In: *Phys. Rev. Lett.* 97.5, 050401 (Aug. 2006), p. 050401. DOI: 10.1103/PhysRevLett.97.050401. arXiv: quant-ph/0603121 [quant-ph].

[121] Ulrich Schollwöck. "The density-matrix renormalization group in the age of matrix product states". In: *Annals of Physics* 326.1 (Jan. 2011), pp. 96–192. DOI: 10.1016/j.aop.2010.09.012. arXiv: 1008.3477 [cond-mat.str-el].

[122] Guifre Vidal. "On the characterization of entanglement". In: *J. Mod. Opt.* 47 (2000), p. 355. DOI: 10.1080/09500340008244048. arXiv: quant-ph/9807077 [quant-ph].

[123] J. Eisert, M. Cramer, and M. B. Plenio. "Colloquium: Area laws for the entanglement entropy". In: *Reviews of Modern Physics* 82.1 (Jan. 2010), pp. 277–306. DOI: 10.1103/RevModPhys.82.277. arXiv: 0808.3773 [quant-ph].

[124] M. B. Hastings. "An area law for one-dimensional quantum systems". In: *Journal of Statistical Mechanics: Theory and Experiment* 2007.8 (Aug. 2007), p. 08024. DOI: 10.1088/1742-5468/2007/08/P08024. arXiv: 0705.2024 [quant-ph].

[125] Pasquale Calabrese and John Cardy. "Entanglement entropy and quantum field theory". In: *Journal of Statistical Mechanics: Theory and Experiment* 2004.6 (June 2004), p. 06002. DOI: 10.1088/1742-5468/2004/06/P06002. arXiv: hep-th/0405152 [hep-th].

[126] P. Di Francesco, P. Mathieu, and D. Sénéchal. *Conformal Field Theory*. Graduate texts in contemporary physics. Island Press, 1996. ISBN: 9781461222576. URL: https://books.google.it/books?id=mcMbswEACAAJ.

[127] Pasquale Calabrese, Fabian H. L. Essler, and Maurizio Fagotti. "Quantum quench in the transverse field Ising chain: I. Time evolution of order parameter correlators". In: *Journal of Statistical Mechanics: Theory and Experiment* 2012.7 (July 2012), p. 07016. DOI: 10.1088/1742-5468/2012/07/P07016. arXiv: 1204.3911 [cond-mat.quant-gas].

[128] Etienne Granet, Maurizio Fagotti, and Fabian Essler. "Finite temperature and quench dynamics in the Transverse Field Ising Model from form factor expansions". In: *SciPost Physics* 9.3, 033 (Sept. 2020), p. 033. DOI: 10.21468/SciPostPhys.9.3.033. arXiv: 2003.09014 [cond-mat.stat-mech].

[129] Maurizio Fagotti and Pasquale Calabrese. "Evolution of entanglement entropy following a quantum quench: Analytic results for the XY chain in a transverse magnetic field". In: *Phys. Rev. A* 78.1, 010306 (July 2008), p. 010306. DOI: 10.1103/PhysRevA.78.010306. arXiv: 0804.3559 [cond-mat.stat-mech].

[130] Mario Collura, Márton Kormos, and Pasquale Calabrese. "Stationary entanglement entropies following an interaction quench in 1D Bose gas". In: *Journal of Statistical Mechanics: Theory and Experiment* 2014.1, 01009 (Jan. 2014), p. 01009. DOI: 10.1088/1742-5468/2014/01/P01009. arXiv: 1310.0846 [cond-mat.quant-gas].

[131] V. Eisler and I. Peschel. "Entanglement in a periodic quench". In: *Annalen der Physik* 520.6 (June 2008), pp. 410–423. DOI: 10.1002/andp.200810299. arXiv: 0803.2655 [cond-mat.stat-mech].

[132] M. Ghasemi Nezhadhaghighi and M. A. Rajabpour. "Entanglement dynamics in short- and long-range harmonic oscillators". In: *Phys. Rev. B* 90.20, 205438 (Nov. 2014), p. 205438. DOI: 10.1103/PhysRevB.90.205438. arXiv: 1408.3744 [cond-mat.stat-mech].

[133] Márton Kormos, Leda Bucciantini, and Pasquale Calabrese. "Stationary entropies after a quench from excited states in the Ising chain". In: *EPL (Europhysics Letters)* 107.4, 40002 (Aug. 2014), p. 40002. DOI: 10.1209/0295-5075/107/40002. arXiv: 1406.5070 [cond-mat.stat-mech].

[134] Leda Bucciantini, Márton Kormos, and Pasquale Calabrese. "Quantum quenches from excited states in the Ising chain". In: *Journal of Physics A Mathematical General* 47.17, 175002 (May 2014), p. 175002. DOI: 10.1088/1751-8113/47/17/175002. arXiv: 1401.7250 [cond-mat.stat-mech].

[135] Lucas Hackl, Eugenio Bianchi, Ranjan Modak, and Marcos Rigol. "Entanglement production in bosonic systems: Linear and logarithmic growth". In: *Phys. Rev. A* 97.3, 032321 (Mar. 2018), p. 032321. DOI: 10.1103/PhysRevA.97.032321. arXiv: 1710.04279 [hep-th].

[136] Gabriele DeChiara, Simone Montangero, Pasquale Calabrese, and Rosario Fazio. "Entanglement entropy dynamics of Heisenberg chains". In: *Journal of Statistical Mechanics: Theory and Experiment* 2006.3 (Mar. 2006), p. 03001. DOI: 10.1088/1742-5468/2006/03/P03001. arXiv: cond-mat/0512586 [cond-mat.mes-hall].

[137] Andreas M. Läuchli and Corinna Kollath. "Spreading of correlations and entanglement after a quench in the one-dimensional Bose Hubbard model". In: *Journal of Statistical Mechanics: Theory and Experiment* 2008.5 (May 2008), p. 05018. DOI: 10.1088/1742-5468/2008/05/P05018. arXiv: 0803.2947 [cond-mat.other].

[138] Hyungwon Kim and David A. Huse. "Ballistic Spreading of Entanglement in a Diffusive Nonintegrable System". In: *Phys. Rev. Lett* 111.12, 127205 (Sept. 2013), p. 127205. DOI: 10.1103/PhysRevLett.111.127205. arXiv: 1306.4306 [quant-ph].

[139] Maurizio Fagotti and Mario Collura. "Universal prethermalization dynamics of entanglement entropies after a global quench". In: *arXiv e-prints*, arXiv:1507.02678 (July 2015), arXiv:1507.02678.

[140] Anton S. Buyskikh, Maurizio Fagotti, Johannes Schachenmayer, Fabian Essler, and Andrew J. Daley. "Entanglement growth and correlation spreading with variable-range interactions in spin and fermionic tunneling models". In: *Phys. Rev. A* 93.5, 053620 (May 2016), p. 053620. DOI: 10.1103/PhysRevA.93.053620. arXiv: 1601.02106 [cond-mat.quant-gas].

[141] Irénée Frérot, Piero Naldesi, and Tommaso Roscilde. "Multispeed Prethermalization in Quantum Spin Models with Power-Law Decaying Interactions". In: *Phys. Rev. Lett* 120.5, 050401 (Jan. 2018), p. 050401. DOI: 10.1103/PhysRevLett.120.050401. arXiv: 1704.04461 [cond-mat.quant-gas].

[142] Jerome Dubail, Jean-Marie Stéphan, Jacopo Viti, and Pasquale Calabrese. "Conformal field theory for inhomogeneous one-dimensional quantum systems: the example of non-interacting Fermi gases". In: *SciPost Physics* 2.1, 002 (Feb. 2017), p. 002. DOI: 10.21468/SciPostPhys.2.1.002. arXiv: 1606.04401 [cond-mat.str-el].

[143] Andrea Coser, Erik Tonni, and Pasquale Calabrese. "Entanglement negativity after a global quantum quench". In: *Journal of Statistical Mechanics: Theory and Experiment* 2014.12, 12017 (Dec. 2014), p. 12017. DOI: 10.1088/1742-5468/2014/12/P12017. arXiv: 1410.0900 [cond-mat.stat-mech].

[144] Jordan S. Cotler, Mark P. Hertzberg, Márk Mezei, and Mark T. Mueller. "Entanglement growth after a global quench in free scalar field theory". In: *Journal of High Energy Physics* 2016.11, 166 (Nov. 2016), p. 166. DOI: 10.1007/JHEP11(2016)166. arXiv: 1609.00872 [hep-th].

[145] Norbert Schuch, Michael M. Wolf, Frank Verstraete, and J. Ignacio Cirac. "Entropy Scaling and Simulability by Matrix Product States". In: *Phys. Rev. Lett* 100.3, 030504 (Jan. 2008), p. 030504. DOI: 10.1103/PhysRevLett.100.030504. arXiv: 0705.0292 [quant-ph].

[146] N. Schuch, M. M. Wolf, K. G. H. Vollbrecht, and J. I. Cirac. "On entropy growth and the hardness of simulating time evolution". In: *New Journal of Physics* 10.3, 033032 (Mar. 2008), p. 033032. DOI: 10.1088/1367-2630/10/3/033032. arXiv: 0801.2078 [quant-ph].

[147] Álvaro Perales and Guifré Vidal. "Entanglement growth and simulation efficiency in one-dimensional quantum lattice systems". In: *Phys. Rev. A* 78.4, 042337 (Oct. 2008), p. 042337. DOI: 10.1103/PhysRevA.78.042337. arXiv: 0711.3676 [cond-mat.str-el].

[148] Philipp Hauke, Fernando M. Cucchietti, Luca Tagliacozzo, Ivan Deutsch, and Maciej Lewenstein. "Can one trust quantum simulators?" In: *Reports on Progress in Physics* 75.8, 082401 (Aug. 2012), p. 082401. DOI: 10.1088/0034-4885/75/8/082401. arXiv: 1109.6457 [quant-ph].

[149] J. Dubail. "Entanglement scaling of operators: a conformal field theory approach, with a glimpse of simulability of long-time dynamics in 1 + 1d". In: *Journal of Physics A Mathematical General* 50.23, 234001 (June 2017), p. 234001. DOI: 10.1088/1751-8121/aa6f38. arXiv: 1612.08630 [cond-mat.str-el].

[150] A. J. Daley, H. Pichler, J. Schachenmayer, and P. Zoller. "Measuring Entanglement Growth in Quench Dynamics of Bosons in an Optical Lattice". In: *Phys. Rev. Lett* 109.2, 020505 (July 2012), p. 020505. DOI: 10.1103/PhysRevLett.109.020505. arXiv: 1205.1521 [cond-mat.quant-gas].

[151] Rajibul Islam, Ruichao Ma, Philipp M. Preiss, M. Eric Tai, Alexander Lukin, Matthew Rispoli, and Markus Greiner. "Measuring entanglement entropy in a quantum many-body system". In: *Nature* 528.7580 (Dec. 2015), pp. 77–83. DOI: 10.1038/nature15750.

[152] Vincenzo Alba and Pasquale Calabrese. "Entanglement and thermodynamics after a quantum quench in integrable systems". In: *Proceedings of the National Academy of Science* 114.30 (July 2017), pp. 7947–7951. DOI: 10.1073/pnas.1703516114. arXiv: 1608.00614 [cond-mat.str-el].

[153] J. M. Deutsch, Haibin Li, and Auditya Sharma. "Microscopic origin of thermodynamic entropy in isolated systems". In: *Phys. Rev. E* 87.4, 042135 (Apr. 2013), p. 042135. DOI: 10.1103/PhysRevE.87.042135. arXiv: 1202.2403 [quant-ph].

[154] W. Beugeling, A. Andreanov, and Masudul Haque. "Global characteristics of all eigenstates of local many-body Hamiltonians: participation ratio and entanglement entropy". In: *Journal of Statistical Mechanics: Theory and Experiment* 2015.2, 02002 (Feb. 2015), p. 02002. DOI: 10.1088/1742-5468/2015/02/P02002. arXiv: 1410.7702 [cond-mat.stat-mech].

[155] Vincenzo Alba and Pasquale Calabrese. "Entanglement dynamics after quantum quenches in generic integrable systems". In: *SciPost Physics* 4.3, 017 (Mar. 2018), p. 017. DOI: 10.21468/SciPostPhys.4.3.017. arXiv: 1712.07529 [cond-mat.stat-mech].

[156] Vincenzo Alba and Pasquale Calabrese. "Quench action and Rényi entropies in integrable systems". In: *Phys. Rev. B* 96.11, 115421 (Sept. 2017), p. 115421. DOI: 10.1103/PhysRevB.96.115421. arXiv: 1705.10765 [cond-mat.stat-mech].

[157] Vincenzo Alba and Pasquale Calabrese. "Rényi entropies after releasing the Néel state in the XXZ spin-chain". In: *Journal of Statistical Mechanics: Theory and Experiment* 11.11 (Nov. 2017), p. 113105. DOI: 10.1088/1742-5468/aa934c. arXiv: 1709.02193 [cond-mat.stat-mech].

[158] Márton Mestyán, Vincenzo Alba, and Pasquale Calabrese. "Rényi entropies of generic thermodynamic macrostates in integrable systems". In: *Journal of Statistical Mechanics: Theory and Experiment* 8.8 (Aug. 2018), p. 083104. DOI: 10.1088/1742-5468/aad6b9. arXiv: 1806.00624 [cond-mat.stat-mech].

[159] M. Collura, M. Kormos, and G. Takacs. "Dynamical manifestation of Gibbs paradox after a quantum quench". In: *arXiv e-prints*, arXiv:1801.05817 (Jan. 2018), arXiv:1801.05817. arXiv: 1801.05817 [cond-mat.stat-mech].

[160] Olalla A. Castro-Alvaredo, Máté Lencsés, István M. Szécsényi, and Jacopo Viti. "Entanglement dynamics after a quench in Ising field theory: a branch point twist field approach". In: *Journal of High Energy Physics* 2019.12, 79 (Dec. 2019), p. 79. DOI: 10.1007/JHEP12(2019)079. arXiv: 1907.11735 [hep-th].

[161] Dirk Schuricht and Fabian H. L. Essler. "Dynamics in the Ising field theory after a quantum quench". In: *Journal of Statistical Mechanics: Theory and Experiment* 2012.4 (Apr. 2012), p. 04017. DOI: 10.1088/1742-5468/2012/04/P04017. arXiv: 1203.5080 [cond-mat.str-el].

[162] Marton Kormos, Mario Collura, Gabor Takács, and Pasquale Calabrese. "Real-time confinement following a quantum quench to a non-integrable model". In: *Nature Physics* 13.3 (Mar. 2017), pp. 246–249. DOI: 10.1038/nphys3934. arXiv: 1604.03571 [cond-mat.stat-mech].

[163] Guifré Vidal. "Efficient Simulation of One-Dimensional Quantum Many-Body Systems". In: *Phys. Rev. Lett* 93.4, 040502 (July 2004), p. 040502. DOI: 10.1103/PhysRevLett.93.040502. arXiv: quant-ph/0310089 [quant-ph].

[164] Ákos Rapp, Peter Schmitteckert, Gábor Takács, and Gergely Zaránd. "Asymptotic scattering and duality in the one-dimensional three-state quantum Potts model on a lattice". In: *New Journal of Physics* 15.1, 013058 (Jan. 2013). DOI: 10.1088/1367-2630/15/1/013058.

[165] Gesualdo Delfino and Paolo Grinza. "Confinement in the q-state Potts field theory". In: *Nuclear Physics B* 791.3 (Mar. 2008), pp. 265–283. DOI: 10.1016/j.nuclphysb.2007.09.003. arXiv: 0706.1020 [hep-th].

[166] L. Lepori, G. Z. Tóth, and G. Delfino. "The particle spectrum of the three-state Potts field theory: a numerical study". In: *Journal of Statistical Mechanics: Theory and Experiment* 2009.11 (Nov. 2009), p. 11007. DOI: 10.1088/1742-5468/2009/11/P11007. arXiv: 0909.2192 [hep-th].

[167] S. B. Rutkevich. "Two-kink bound states in the magnetically perturbed Potts field theory at $T < T_c$". In: *Journal of Physics A Mathematical General* 43.23, 235004 (June 2010), p. 235004. DOI: 10.1088/1751-8113/43/23/235004. arXiv: 0907.3697 [cond-mat.stat-mech].

[168] S. B. Rutkevich. "Baryon masses in the three-state Potts field theory in a weak magnetic field". In: *Journal of Statistical Mechanics: Theory and Experiment* 2015.1, 01010 (Jan. 2015), p. 01010. DOI: 10.1088/1742-5468/2015/01/P01010. arXiv: 1408.1818 [cond-mat.stat-mech].

[169] M. Lencsés and G. Takács. "Confinement in the q-state Potts model: an RG-TCSA study". In: *Journal of High Energy Physics* 2015, 146 (Sept. 2015), p. 146. DOI: 10.1007/JHEP09(2015)146. arXiv: 1506.06477 [hep-th].

[170] Alexander Zamolodchikov. "Ising Spectroscopy II: Particles and poles at T>Tc". In: *arXiv e-prints*, arXiv:1310.4821 (Oct. 2013), arXiv:1310.4821. arXiv: 1310.4821 [hep-th].

[171] M. Lüscher. "Volume dependence of the energy spectrum in massive quantum field theories: I. Stable particle states". In: *Communications in Mathematical Physics* 104.2 (June 1986), pp. 177–206. DOI: 10.1007/BF01211589.

[172] M. Lüscher. "Volume dependence of the energy spectrum in massive quantum field theories: II. Scattering states". In: *Communications in Mathematical Physics* 105.2 (June 1986), pp. 153–188. DOI: 10.1007/BF01211097.

[173] Elliott Lieb, Theodore Schultz, and Daniel Mattis. "Two soluble models of an antiferromagnetic chain". In: *Annals of Physics* 16.3 (Dec. 1961), pp. 407–466. DOI: 10.1016/0003-4916(61)90115-4.

[174] Pierre Pfeuty. "The one-dimensional Ising model with a transverse field". In: *Annals of Physics* 57.1 (Mar. 1970), pp. 79–90. DOI: 10.1016/0003-4916(70)90270-8.

[175] J. L. Cardy, O. A. Castro-Alvaredo, and B. Doyon. "Form Factors of Branch-Point Twist Fields in Quantum Integrable Models and Entanglement Entropy". In: *Journal of Statistical Physics* 130.1 (Jan. 2008), pp. 129–168. DOI: 10.1007/s10955-007-9422-x. arXiv: 0706.3384 [hep-th].

[176] Olalla A. Castro-Alvaredo and Benjamin Doyon. "Bi-partite entanglement entropy in massive (1+1)-dimensional quantum field theories". In: *Journal of Physics A Mathematical General* 42.50, 504006 (Dec. 2009), p. 504006. DOI: 10.1088/1751-8113/42/50/504006. arXiv: 0906.2946 [hep-th].

[177] G. Vidal, J. I. Latorre, E. Rico, and A. Kitaev. "Entanglement in Quantum Critical Phenomena". In: *Phys. Rev. Lett* 90.22, 227902 (June 2003), p. 227902. DOI: 10.1103/PhysRevLett.90.227902. arXiv: quant-ph/0211074 [quant-ph].

[178] L. Mittag and M. J. Stephen. "Dual Transformations in Many-Component Ising Models". In: *Journal of Mathematical Physics* 12.3 (Mar. 1971), pp. 441–450. DOI: 10.1063/1.1665606.

[179] A. A. Belavin, A. M. Polyakov, and A. B. Zamolodchikov. "Infinite conformal symmetry in two-dimensional quantum field theory". In: *Nuclear Physics B* 241.2 (July 1984), pp. 333–380. DOI: 10.1016/0550-3213(84)90052-X.

[180] Leung Chim and Alexander Zamolodchikov. "Integrable Field Theory of the q-STATE Potts Model with 0<q<4". In: *International Journal of Modern Physics A* 7.21 (Jan. 1992), pp. 5317–5335. DOI: 10.1142/S0217751X9200243X.

[181] A. B. Zamolodchikov and V. A. Fateev. "Nonlocal (parafermion) currents in two-dimensional conformal quantum field theory and self-dual critical points in ZN-symmetric statistical systems". In: *Soviet Journal of Experimental and Theoretical Physics* 62.2 (Aug. 1985), p. 215.

[182] Roger S. K. Mong, David J. Clarke, Jason Alicea, Netanel H. Lindner, and Paul Fendley. "Parafermionic conformal field theory on the lattice". In: *Journal of Physics A Mathematical General* 47.45, 452001 (Nov. 2014), p. 452001. DOI: 10.1088/1751-8113/47/45/452001. arXiv: 1406.0846 [cond-mat.stat-mech].

[183] G. Delfino and J. L. Cardy. "Universal amplitude ratios in the two-dimensional q-state Potts model and percolation from quantum field theory". In: *Nuclear Physics B* 519.3 (May 1998), pp. 551–578. DOI: 10.1016/S0550-3213(98)00144-8. arXiv: hep-th/9712111 [hep-th].

[184] Kristóf Hódsági, Márton Kormos, and Gábor Takács. "Perturbative post-quench overlaps in quantum field theory". In: *Journal of High Energy Physics* 2019.8, 47 (Aug. 2019), p. 47. DOI: 10.1007/JHEP08(2019)047. arXiv: 1905.05623 [cond-mat.stat-mech].

[185] Olalla A. Castro-Alvaredo, Máté Lencsés, István M. Szécsényi, and Jacopo Viti. "Entanglement Oscillations near a Quantum Critical Point". In: *Phys. Rev. Lett* 124.23, 230601 (June 2020), p. 230601. DOI: 10.1103/PhysRevLett.124.230601. arXiv: 2001.10007 [cond-mat.stat-mech].

[186] A. B. Zamolodchikov. "Integrals of Motion and S-Matrix of the (scaled) T = T_c Ising Model with Magnetic Field". In: *International Journal of Modern Physics A* 4.16 (Jan. 1989), pp. 4235–4248. DOI: 10.1142/S0217751X8900176X.

[187] S. Coleman. "Fate of the False Vacuum: Semiclassical Theory". In: *The Early Universe: Reprints*. Ed. by Edward W. Kolb and Michael S. Turner. 1988, p. 483.

[188] Curtis G. Callan and Sidney Coleman. "Fate of the false vacuum. II. First quantum corrections". In: *Phys. Rev. D* 16 (6 Sept. 1977), pp. 1762–1768. DOI: 10.1103/PhysRevD.16.1762. URL: https://link.aps.org/doi/10.1103/PhysRevD.16.1762.

[189] Thomas P. Billam, Ruth Gregory, Florent Michel, and Ian G. Moss. "Simulating seeded vacuum decay in a cold atom system". In: *Phys. Rev. D* 100.6, 065016 (Sept. 2019), p. 065016. DOI: 10.1103/PhysRevD.100.065016. arXiv: 1811.09169 [hep-th].

[190] Thomas P. Billam, Kate Brown, and Ian G. Moss. "Simulating cosmological supercooling with a cold-atom system". In: *Phys. Rev. A* 102.4, 043324 (Oct. 2020), p. 043324. DOI: 10.1103/PhysRevA.102.043324. arXiv: 2006.09820 [cond-mat.quant-gas].

[191] Steven Abel and Michael Spannowsky. "Quantum-Field-Theoretic Simulation Platform for Observing the Fate of the False Vacuum". In: *PRX Quantum* 2 (1 Mar. 2021), p. 010349. DOI: 10.1103/PRXQuantum.2.010349. URL: https://link.aps.org/doi/10.1103/PRXQuantum.2.010349.

[192] King Lun Ng, Bogdan Opanchuk, Manushan Thenabadu, Margaret Reid, and Peter D. Drummond. "The fate of the false vacuum: Finite temperature, entropy and topological phase in quantum simulations of the early universe". In: *arXiv e-prints*, arXiv:2010.08665 (Oct. 2020), arXiv:2010.08665. arXiv: 2010.08665 [quant-ph].

[193] Thomas P. Billam, Kate Brown, Andrew J. Groszek, and Ian G. Moss. "Simulating cosmological supercooling with a cold atom system II". In: *arXiv e-prints*, arXiv:2104.07428 (Apr. 2021), arXiv:2104.07428. arXiv: 2104.07428 [cond-mat.quant-gas].

[194] Aritra Sinha, Titas Chanda, and Jacek Dziarmaga. "Nonadiabatic dynamics across a first-order quantum phase transition: Quantized bubble nucleation". In: *Phys. Rev. B* 103.22, L220302 (June 2021), p. L220302. DOI: 10.1103/PhysRevB.103.L220302. arXiv: 2103.04762 [cond-mat.stat-mech].

[195] Giuseppe Magnifico, Marcello Dalmonte, Paolo Facchi, Saverio Pascazio, Francesco V. Pepe, and Elisa Ercolessi. "Real Time Dynamics and Confinement in the $\mathbb{Z}_n$ Schwinger-Weyl lattice model for 1+1 QED". In: *arXiv e-prints*, arXiv:1909.04821 (Sept. 2019), arXiv:1909.04821. arXiv: 1909.04821 [quant-ph].

[196] W. L. Tan, P. Becker, F. Liu, G. Pagano, K. S. Collins, A. De, L. Feng, H. B. Kaplan, A. Kyprianidis, R. Lundgren, W. Morong, S. Whitsitt, A. V. Gorshkov, and C. Monroe. "Domain-wall confinement and dynamics in a quantum simulator". In: *Nature Physics* 17.6 (Jan. 2021), pp. 742–747. DOI: 10.1038/s41567-021-01194-3. arXiv: 1912.11117 [quant-ph].

[197] Paolo Pietro Mazza, Gabriele Perfetto, Alessio Lerose, Mario Collura, and Andrea Gambassi. "Suppression of transport in nondisordered quantum spin chains due to confined excitations". In: *Phys. Rev. B* 99.18, 180302 (May 2019), p. 180302. DOI: 10.1103/PhysRevB.99.180302. arXiv: 1806.09674 [cond-mat.stat-mech].

[198] Neil J. Robinson, Andrew J. A. James, and Robert M. Konik. "Signatures of rare states and thermalization in a theory with confinement". In: *Phys. Rev. B* 99.19, 195108 (May 2019), p. 195108. DOI: 10.1103/PhysRevB.99.195108. arXiv: 1808.10782 [cond-mat.str-el].

[199] Andrew J. A. James, Robert M. Konik, and Neil J. Robinson. "Nonthermal States Arising from Confinement in One and Two Dimensions". In: *Phys. Rev. Lett* 122.13, 130603 (Apr. 2019), p. 130603. DOI: 10.1103/PhysRevLett.122.130603. arXiv: 1804.09990 [cond-mat.stat-mech].

[200] Fangli Liu, Rex Lundgren, Paraj Titum, Guido Pagano, Jiehang Zhang, Christopher Monroe, and Alexey V. Gorshkov. "Confined Quasiparticle Dynamics in Long-Range Interacting Quantum Spin Chains". In: *Phys. Rev. Lett* 122.15, 150601 (Apr. 2019), p. 150601. DOI: 10.1103/PhysRevLett.122.150601. arXiv: 1810.02365 [cond-mat.quant-gas].

[201] Alessio Lerose, Federica M. Surace, Paolo P. Mazza, Gabriele Perfetto, Mario Collura, and Andrea Gambassi. "Quasilocalized dynamics from confinement of quantum excitations". In: *Phys. Rev. B* 102.4, 041118 (July 2020), p. 041118. DOI: 10.1103/PhysRevB.102.041118. arXiv: 1911.07877 [cond-mat.stat-mech].

[202] Titas Chanda, Jakub Zakrzewski, Maciej Lewenstein, and Luca Tagliacozzo. "Confinement and Lack of Thermalization after Quenches in the Bosonic Schwinger Model". In: *Phys. Rev. Lett* 124.18, 180602 (May 2020), p. 180602. DOI: 10.1103/PhysRevLett.124.180602. arXiv: 1909.12657 [cond-mat.stat-mech].

[203] Zhi-Cheng Yang, Fangli Liu, Alexey V. Gorshkov, and Thomas Iadecola. "Hilbert-Space Fragmentation from Strict Confinement". In: *Phys. Rev. Lett* 124.20, 207602 (May 2020), p. 207602. DOI: 10.1103/PhysRevLett.124.207602. arXiv: 1912.04300 [cond-mat.str-el].

[204] Barry M. McCoy and Tai Tsun Wu. "Two-dimensional Ising field theory in a magnetic field: Breakup of the cut in the two-point function". In: *Phys. Rev. D* 18 (4 Aug. 1978), pp. 1259–1267. DOI: 10.1103/PhysRevD.18.1259. URL: https://link.aps.org/doi/10.1103/PhysRevD.18.1259.

[205] Riccardo Javier Valencia Tortora, Pasquale Calabrese, and Mario Collura. "Relaxation of the order-parameter statistics and dynamical confinement". In: *arXiv e-prints*, arXiv:2005.01679 (May 2020), arXiv:2005.01679. arXiv: 2005.01679 [cond-mat.stat-mech].

[206] S. B. Rutkevich. "Energy Spectrum of Bound-Spinons in the Quantum Ising Spin-Chain Ferromagnet". In: *Journal of Statistical Physics* 131.5 (June 2008), pp. 917–939. DOI: 10.1007/s10955-008-9495-1.

[207] Pasquale Calabrese, Fabian H. L. Essler, and Maurizio Fagotti. "Quantum Quench in the Transverse-Field Ising Chain". In: *Phys. Rev. Lett* 106.22, 227203 (June 2011), p. 227203. DOI: 10.1103/PhysRevLett.106.227203. arXiv: 1104.0154 [cond-mat.str-el].

[208] S. B. Rutkevich. "Decay of the metastable phase in $d = 1$ and $d = 2$ Ising models". In: *Phys. Rev. B* 60 (21 Dec. 1999), pp. 14525–14528. DOI: 10.1103/PhysRevB.60.14525. URL: https://link.aps.org/doi/10.1103/PhysRevB.60.14525.

[209] Julian Schwinger. "On Gauge Invariance and Vacuum Polarization". In: *Phys. Rev.* 82 (5 June 1951), pp. 664–679. DOI: 10.1103/PhysRev.82.664. URL: https://link.aps.org/doi/10.1103/PhysRev.82.664.

[210] Ashley Milsted, Junyu Liu, John Preskill, and Guifre Vidal. "Collisions of false-vacuum bubble walls in a quantum spin chain". In: arXiv:2012.07243 (Dec. 2020), arXiv:2012.07243.

[211] Bruno Bertini, Elena Tartaglia, and Pasquale Calabrese. "Entanglement and diagonal entropies after a quench with no pair structure". In: *Journal of Statistical Mechanics: Theory and Experiment* 6.6 (June 2018), p. 063104. DOI: 10.1088/1742-5468/aac73f. arXiv: 1802.10589 [cond-mat.stat-mech].

[212] Alvise Bastianello and Pasquale Calabrese. "Spreading of entanglement and correlations after a quench with intertwined quasiparticles". In: *SciPost Physics* 5.4, 033 (Oct. 2018), p. 033. DOI: 10.21468/SciPostPhys.5.4.033. arXiv: 1807.10176 [cond-mat.stat-mech].

[213] Kristóf Hódsági, Márton Kormos, and Gábor Takács. "Quench dynamics of the Ising field theory in a magnetic field". In: *SciPost Physics* 5.3, 027 (Sept. 2018), p. 027. DOI: 10.21468/SciPostPhys.5.3.027. arXiv: 1803.01158 [cond-mat.stat-mech].

[214] A. B. Zamolodchikov. "Integrals of Motion in Scaling 3-STATE Potts Model Field Theory". In: *International Journal of Modern Physics A* 3.3 (Jan. 1988), pp. 743–750. DOI: 10.1142/S0217751X88000333.

[215] R. Köberle and J. A. Swieca. "Factorizable Z(N) models". In: *Physics Letters B* 86.2 (Sept. 1979), pp. 209–210. DOI: 10.1016/0370-2693(79)90822-0.

[216] Gianluca Lagnese, Federica Maria Surace, Márton Kormos, and Pasquale Calabrese. "False vacuum decay in quantum spin chains". In: *Phys. Rev. B* 104 (20 Nov. 2021), p. L201106. DOI: 10.1103/PhysRevB.104.L201106. URL: https://link.aps.org/doi/10.1103/PhysRevB.104.L201106.

[217] Matteo Magoni, Paolo P. Mazza, and Igor Lesanovsky. "Emergent Bloch Oscillations in a Kinetically Constrained Rydberg Spin Lattice". In: *Phys. Rev. Lett* 126.10, 103002 (Mar. 2021), p. 103002. DOI: 10.1103/PhysRevLett.126.103002. arXiv: 2010.07825 [cond-mat.quant-gas].

[218] Ren Liao, Fangyu Xiong, and Xuzong Chen. "Simulating an exact one-dimensional transverse Ising model in an optical lattice". In: *Phys. Rev. A* 103.4, 043312 (Apr. 2021), p. 043312. DOI: 10.1103/PhysRevA.103.043312. arXiv: 2003.02411 [cond-mat.quant-gas].

[219] A. Friedenauer, H. Schmitz, J. T. Glueckert, D. Porras, and T. Schaetz. "Simulating a quantum magnet with trapped ions". In: *Nature Physics* 4.10 (2008), pp. 757–761. DOI: 10.1038/nphys1032. URL: https://doi.org/10.1038/nphys1032.

[220] B. P. Lanyon, C. Hempel, D. Nigg, M. Müller, R. Gerritsma, F. Zähringer, P. Schindler, J. T. Barreiro, M. Rambach, G. Kirchmair, M. Hennrich, P. Zoller, R. Blatt, and C. F. Roos. "Universal Digital Quantum Simulation with Trapped Ions". In: *Science* 334.6052 (Oct. 2011), p. 57. DOI: 10.1126/science.1208001. arXiv: 1109.1512 [quant-ph].

[221] Christian Gross and Immanuel Bloch. "Quantum simulations with ultracold atoms in optical lattices". In: *Science* 357.6355 (Sept. 2017), pp. 995–1001. DOI: 10.1126/science.aal3837.

[222] Hannes Bernien, Sylvain Schwartz, Alexander Keesling, Harry Levine, Ahmed Omran, Hannes Pichler, Soonwon Choi, Alexander S. Zibrov, Manuel Endres, Markus Greiner, Vladan Vuletić, and Mikhail D. Lukin. "Probing many-body dynamics on a 51-atom quantum simulator". In: *Nature* 551.7682 (Nov. 2017), pp. 579–584. DOI: 10.1038/nature24622. arXiv: 1707.04344 [quant-ph].

[223] C. Monroe, W. C. Campbell, L. -M. Duan, Z. -X. Gong, A. V. Gorshkov, P. W. Hess, R. Islam, K. Kim, N. M. Linke, G. Pagano, P. Richerme, C. Senko, and N. Y. Yao. "Programmable quantum simulations of spin systems with trapped ions". In: *Reviews of Modern Physics* 93.2, 025001 (Apr. 2021), p. 025001. DOI: 10.1103/RevModPhys.93.025001. arXiv: 1912.07845 [quant-ph].

[224] Joseph Vovrosh and Johannes Knolle. "Confinement and entanglement dynamics on a digital quantum computer". In: *Scientific Reports* 11, 11577 (Jan. 2021), p. 11577. DOI: 10.1038/s41598-021-90849-5.

[225] A Kuniba, T Nakanishi, and J Suzuki. "T-systems and Y-systems in integrable systems". In: *J. Phys. A: Math. Theor.* 44 (2011). DOI: 10.1088/1751-8113/44/10/103001. URL: https://doi.org/10.1088/1751-8113/44/10/103001.

[226] G. Vidal. "Classical Simulation of Infinite-Size Quantum Lattice Systems in One Spatial Dimension". In: *Phys. Rev. Lett* 98.7, 070201 (Feb. 2007), p. 070201. DOI: 10.1103/PhysRevLett.98.070201.